Università degli Studi di Palermo
AREA RICERCA E TRASFERIMENTO TECNOLOGICO
SETTORE DOTTORATI E CONTRATTI PER LA RICERCA
U. O. DOTTORATI DI RICERCA

Corso di Dottorato in Ingegneria MECHANICAL, MANUFACTURING, MANAGEMENT,
AND AEROSPACE INNOVATION (D086).
Dipartimento di Ingegneria
IIND-04/A - Tecnologie e Sistemi di lavorazione

COMPUTER AIDED ENGINEERING FOR SOLID BONDING RECYCLING PROCESSES

IL DOTTORE
ING. RICCARDO PULEO

IL COORDINATORE
CHIA.MA PROF. GIOVANA LO NIGRO

IL TUTOR
CHIA.MO PROF. LIVAN FRATINI

CO TUTOR
CHIA.MO PROF. GIUSEPPE INGARAO

CICLO XXXVIII
ANNO CONSEGUIMENTO TITOLO 2024-2025

Table of Contents

List of figures

List of Tables

Acknowledgment

I would like to thank my tutor, Prof. Livan Fratini, my co-tutor, Prof. Giuseppe Ingarao, my R-tutor, Gianluca Buffa, and all the other professors of our research group Prof. Rosa Di Lorenzo, Prof. Dina Palmeri, and Prof. Davide Campanella, Prof. Giulia Marcon, Prof. Emanuela La Fata for supporting me all the time, and for the academic experiences we shared. I will always carry your advice with me. (Prof. Ingarao always TOP).

I would like to extend my thanks to my colleagues Dr. Gaetano Pollara, Dr. Mohammad Adnan, Dr. Abdul Latif, Simone Amantia, Gloria Trapani, Kirill Kalasnikov, Rosalinda, Rosanna, Fabrizio, Roberta, Silvia, Daniele for the laughs and the time spent together. You made these three years truly enjoyable. Moreover, I want to say thank you to Bari's crew and to the great Gigant machine that made me spend lots of days in Bari.

I want to express my gratitude to all the people I met during my participation in conferences Sara, Chiara, Iacopo, Mauro, Erica, Federico, and Francesco who made these events worth attending. Special thanks go to Chenyang, Ziguang, and Yuchen, who, with their amazing personalities, supported me in learning Chinese.

I express my deepest appreciation to Prof. Daniel R. Cooper, who hosted me during my research period abroad at the University of Michigan, Ann Arbor. A very special thanks goes to my colleagues Peter Fabe, Zhuoer Li, Muhammad Umar Farooq, Alissa Tsai, Dr. Ala'aldin Alafaghani, Jiankan Liao, Ziqi Yin, Opeyemi Akinniyi, Dr. Yongxian Zhu, Dr. Seyed Mohammadreza Heidari, and my friends Joe Trzaska, Joseph Beckett, Max Nyffenegger, Catherine Kinman, Youngrok Lee, and Xirong Liu in Ann Arbor, who warmly welcomed me and made me feel at home. Best wishes to Peter and Catherine, I hope you will have a beautiful life together with your daughter, Maria.

I am grateful to all my new and old friends in Palermo Gabriele, Simone, Davide, Giulio, Irene, Giorgia, Elena (and her second personality, Mel'Hell), Manfredi, Gabriele, Roberta, Irene, and all the others I'm not mentioning who made my life worth living.

Finally, just as the roots sustain a tree from the bottom, I want to say thank you to my family, here, at the bottom. I am the person I am today thanks to the motivation, encouragement, and support you have always given me. I love you, mom, dad, and my beloved sister. Also, thank you Marcella, Maurizio, Roberto, Fabrizio, and all my relatives.

List of journal papers

- Muhammad A., Puleo R., Buffa G., Fratini L., Ingarao G. (*Under review*). **Unlocking the Potential of Friction Stir Extrusion as a Sole Manufacturing Step for Producing Sustainable Tubes from Aluminum Chips**.
- Puleo, R., Mohammad, A., Ingarao, G., & Fratini, L. (*Submitted*). **Mechanical And Microstructural Characterization of Friction Stir Extruded Bimetallic Tube**.
- Micari, F., Amantia, S., Puleo, R., & Ingarao, G. (2025). **Application of innovation theory to metal forming modelling: FEM sunset and AI dawn??**. International Journal of Material Forming, 18(4), 79.
- Alafaghani, A. A., Puleo, R., Adams, L., Dong, P., & Cooper, D. (2025). **A study on internal quenching of hollow extrusions to reduce distortion and increase the energy to failure of aluminum profiles**. International Journal of Material Forming, 18(1), 19.
- Puleo, R., Latif, A., Ingarao, G., & Fratini, L. (2024). **A generalized parametric model for the bonding occurrence prediction in friction stir consolidation of aluminum alloys chips**. Journal of Manufacturing Processes, 131, 604-618.
- Amantia, S., Campanella, D., Puleo, R., Buffa, G., & Fratini, L. (2024). **Effect of process parameters on the mechanical properties of wires produced from A356 aluminum alloy chips by Continuous Friction Stir Extrusion: Experiments and numerical simulation**. CIRP Journal of Manufacturing Science and Technology, 54, 28-42.
- Puleo, R., Latif, A., Ingarao, G., Di Lorenzo, R., & Fratini, L. (2023). **Solid bonding criteria design for aluminum chips recycling through Friction Stir Consolidation**. Journal of Materials Processing Technology, 319, 118080.

List of conference papers

- Russo, S., Puleo, R., G., Buffa, G., & Fratini, L. (*Submitted*). **Exploiting the SPH meshless approach potential for Tube Friction Stir Extrusion: insights into process mechanics, grain size, and micro-mechanical properties**. 54th North American Manufacturing Research Conference (NAMRC 54).
- Puleo, R., Adnan, M., Ingarao, G., Buffa, G., & Fratini, L. (2025). **Investigating the tube production via friction stir extrusion of aluminum chips**. Italian Manufacturing Association Conference: XVII AITeM (p. 352). Materials Research Forum LLC.
- Di Bella, G., Chairi, M., Campanella, D., Puleo, R., & Buffa, G. (2025) **Friction stir welding of AA6082 and AA5083 T-joints for naval applications: Finite element modeling and experimental analysis of material flow**. Materials Research Proceedings, 57.
- Puleo, R., Ingarao, G., & Fratini, L. (2025). **Friction stir consolidation of aluminium chips: A new approach to overcome the inhomogeneous properties of the consolidated billet**. Materials Research Proceedings, 54.
- Adnan, M., Amantia, S., Puleo, R., Ingarao, G., & Fratini, L. (2025). **Recycling magnesium alloy AZ31B chips via friction stir consolidation: A sustainable approach**. Materials Research Proceedings, 54.
- Latif, A., Puleo, R., Ingarao, G., Micari, F., & Fratini, L. (2024). **Material flow analysis in friction stir consolidation during recycling aluminum alloy chips**. Metal Forming 2024, 44, 158.
- Latif, A., Puleo, R., Ingarao, G., & Fratini, L. (2023). **An insight into friction stir consolidation process mechanics through advanced numerical model development**. Materials Research Proceedings, 35.

Abstract

In most sectors of the automotive and aerospace industries, a combination of high strength and low weight is essential to meet the requirements of modern products. In this context, aluminium and its alloys are increasingly replacing conventional steels thanks to their low density and superior strength-to-weight ratio. However, despite the mechanical advantages, aluminium's primary production has a significant environmental impact. The extraction and synthesis of aluminium from ores result in extremely high greenhouse gas (GHG) emissions and high energy consumption compared to other traditional metals. To mitigate GHG emissions, several international frameworks have been established. For instance, the United Nations Framework Convention on Climate Change (UNFCCC) led to the Kyoto Protocol (2005–2012), which imposed emission reduction targets for participating nations, and the Paris Agreement (2015), which set the goal of limiting the global temperature rise to well below 2 °C by the end of the century. In response to the growing need for sustainable goals, recycling strategies have gained increasing attention. Among these, the conventional remelting process has been developed to enable the reuse of aluminium scrap generated during industrial manufacturing, bypassing the high energy-intensive stages of auminium production (primary production). Nevertheless, remelting has significant drawbacks: it requires substantial energy input, and oxidation of the molten metal leads to unavoidable losses, often reaching 15–20% of the processed material. To address these drawbacks, researchers have developed innovative recycling methods that avoid melting the metal scraps, known as solid-state recycling (SSR) processes. These methods are capable of recycling machining swarf through the combined action of pressure, temperature, and contact time, thereby reducing both energy demand and material loss. Based on this background, this dissertation provides a comprehensive investigation of aluminium alloy recycling using a specific group of solid-state recycling (SSR) techniques: friction stir-based processes. Specifically, friction stir consolidation and friction stir extrusion were employed to turn machining chips into consolidated billets and extruded tubes, respectively. Particular focus was given to understanding the solid bonding phenomena governing friction stir-based recycling, through a dedicated methodology combining experimental investigations, numerical simulations, and analytical modelling within the MATLAB environment. Furthermore, the study examined process dynamics and their influence on the resulting microstructure and mechanical properties, thereby enhancing the understanding of these processes. Finally, the main challenges associated with FSC and FSE were critically assessed, and innovative solutions were developed to overcome their current limitations.

Motivation and structure of the dissertation

The present research was initially motivated by several questions that emerged from a thorough review of the state of the art on solid bonding criteria: "*What are the limitations of the existing criteria?*", "*Are they suitable for friction stir consolidation (FSC) processes?*", and "*Can a versatile tool be developed for different materials?*"

Accordingly, the objective of this thesis was to design an effective and accurate tool to predict bonding occurrence in FSC, while overcoming the limitations of existing approaches.

To address these questions, a new solid bonding criterion was developed through a combination of numerical simulations, experimental campaigns, and Matlab-based calculations. Furthermore, a generalized model was proposed to demonstrate the applicability of the criterion to different materials.

The investigation of FSC also provided deeper insight into process dynamics, raising further questions such as: "*How can the mechanical properties of consolidated billets be improved?*", "*Which variables are primarily responsible for sound bonding?*", and "*How can the bonding mechanism itself be enhanced in FSC?*". Answering these questions, the role of material flow, temperature, and strain in friction stir-based processes was analyzed. In addition, a new process setup was proposed to improve the quality of the FSCed billet.

Once a comprehensive understanding of bonding phenomena in FSC was achieved, focus moved to another friction stir-based technique: friction stir extrusion (FSE).

This part of the study aimed to demonstrate the suitability and sustainability of FSE for manufacturing tubes from machining chips. In this regard, new questions were posed: "*Is FSE a viable method for tube extrusion?*" and "*Is it more sustainable compared to conventional techniques?*". A feasibility study was therefore carried out to validate tube production through solid-state recycling and to determine the optimal process parameters for achieving soundly consolidated tubes.

Finally, the traditional FSE process was further explored, questioning "*Given the discontinuous nature of this process, is it possible to design a continuous route for extruding consolidated wires?*"

Consequently, continuous wire production via FSE was studied using a specifically designed machine, developed by the University of Palermo.

In summary, this dissertation provides a general overview of research conducted in the field of metal recycling, especially focusing on numerical simulation approaches and solid boning investigations. The dissertation is organized into five chapters. Following an introduction to the state of the art and the strategies currently adopted for recycling metal swarf, the main research questions that have driven this dissertation are described and discussed for introducing the chapters dedicated to the research results. Finally, a summary of the main findings along with an outline of future research perspectives will be presented.

A graphical view of the dissertation's structure is proposed in Figure 1, while a brief description of the chapters will be given in the following lines.

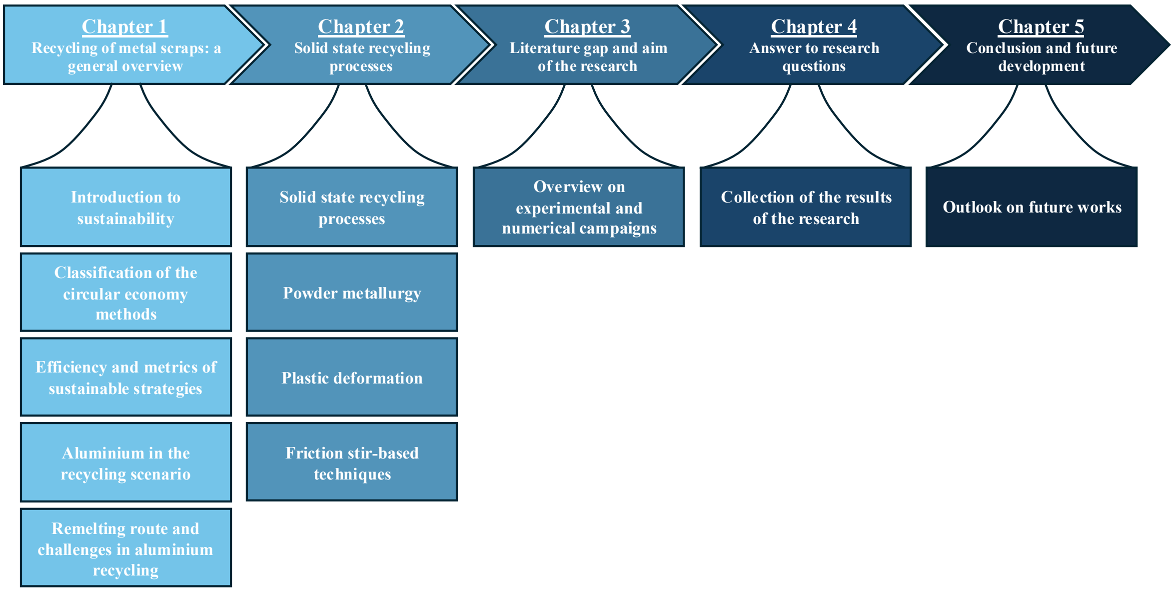

***Figure 1**. Dissertation structure scheme.*

Chapter 1, titled "Recycling of metal: a general view", provides a general overview of the state of the art of metal recycling. Specifically, in this chapter, an introduction to traditional aluminium production, along with the concept of sustainability and circular economy strategies, is proposed, aiming to provide a comprehensive view of the current global scenario. Additionally, a brief description of the common recycling processes is provided.

Chapter 2, titled "Solid state recycling processes", explores the technologies recently developed to overcome the traditional remelting routes' drawbacks, focusing on a specific family of processes named friction stir-based processes. In this regard, friction stir extrusion and friction stir consolidation were described.

Chapter 3, titled "Literature gap and aim of the research", describes the gap that drives the main research questions.

Chapter 4, titled "Answers to research questions", is the core of this thesis, where all the research questions are discussed, and the published works are presented along with the main findings.

Chapter 5, titled "Conclusions and future development", provides the summary of all the findings and the results of this dissertation. Additionally, a brief paragraph is dedicated to future work and perspectives.

1 Recycling of metal scraps: general overview

In this chapter, metal recycling is explored to provide a comprehensive view on the sustainable approaches that are rising nowadays for reducing the carbon footprint of traditional technologies. Firstly, the CO_2 global emissions and the material life cycle will be depicted; additionally, the fundamental concepts of the recycling methodology will be explained. Lastly, multiple recycling approaches already known in the literature and their efficiency will be discussed.

1.1 Introduction to sustainability

Global CO_2 concentrations in the atmosphere are the sum of two different contributions: anthropogenic emissions and natural processes (glacial age, volcanoes, etc..). As discussed by Seixas et al. [1], prior to 1750, the atmospheric CO_2 content had a slow increase (from 260 ppm to 280 ppm), which was the result of the carbon release during deforestation. Starting from 1990, namely the Industrial Era, the dominant source of anthropogenic emissions was the fossil fuels that set a record (41% increase) of Greenhouse Gasses (GHG) emissions without any signal of decreasing trend. In 2018, the GHG concentration reached a new maximum value of about 407.8 ppm, while a value of 413.03 ppm was observed in 2020.

The International Energy Agency (IEA) [2] and the International Resource Panel of UNEP [3], the main issues of fossil fuels (petrol, gas, coal, etc…) are the impossibility of being reused. During the use phase, these resources are consumed (most of the time are burnt) for producing energy, therefore this means that a continuous refill of fossil fuels is needed to keep the industrial machine always operative.

The fossil fuels are not the only responsible of GHG emissions. Hertwich [4] stated that the most important contribution to GHG emission (in 2011) belongs to Iron and steel production caused 3.6 $GtCO_2e$, cement, lime, and plaster production with 24%, and rubber and plastics, including basic plastics with 13%. Non-ferrous metals contributed 10% and non-metallic mineral products contributed 14%, with glass alone contributing 4%.

For limiting the GHG emissions, multiples strategies were adopted [1]. At the international level, an important framework was provided by the United Nations Framework Convention on Climate Change (UNFCCC), in force since 1994, aiming to stabilize GHG concentrations. The agreements included in this framework are:

- **Kyoto Protocol** (2005-2012), which established the emission reduction for all nations.
- **Paris Agreement** (2015), limited the increase of global temperature below 2°C by the end of the century, aiming for a "carbon neutrality" by 2025.

The policy instruments that have been adopted to achieve these goals are carbon pricing mechanisms, technological innovation, and action on carbon sinks.

Concerning the technological innovation approach, one of the rising methods to prevent the increase of GHG production is the recycling of materials, especially for metals. The recycling approach helps to reduce the burden on primary supply from new mining activities, required to meet the increase in mineral demand, mitigating the environmental and social impacts related to mining and refining (Figure 2).

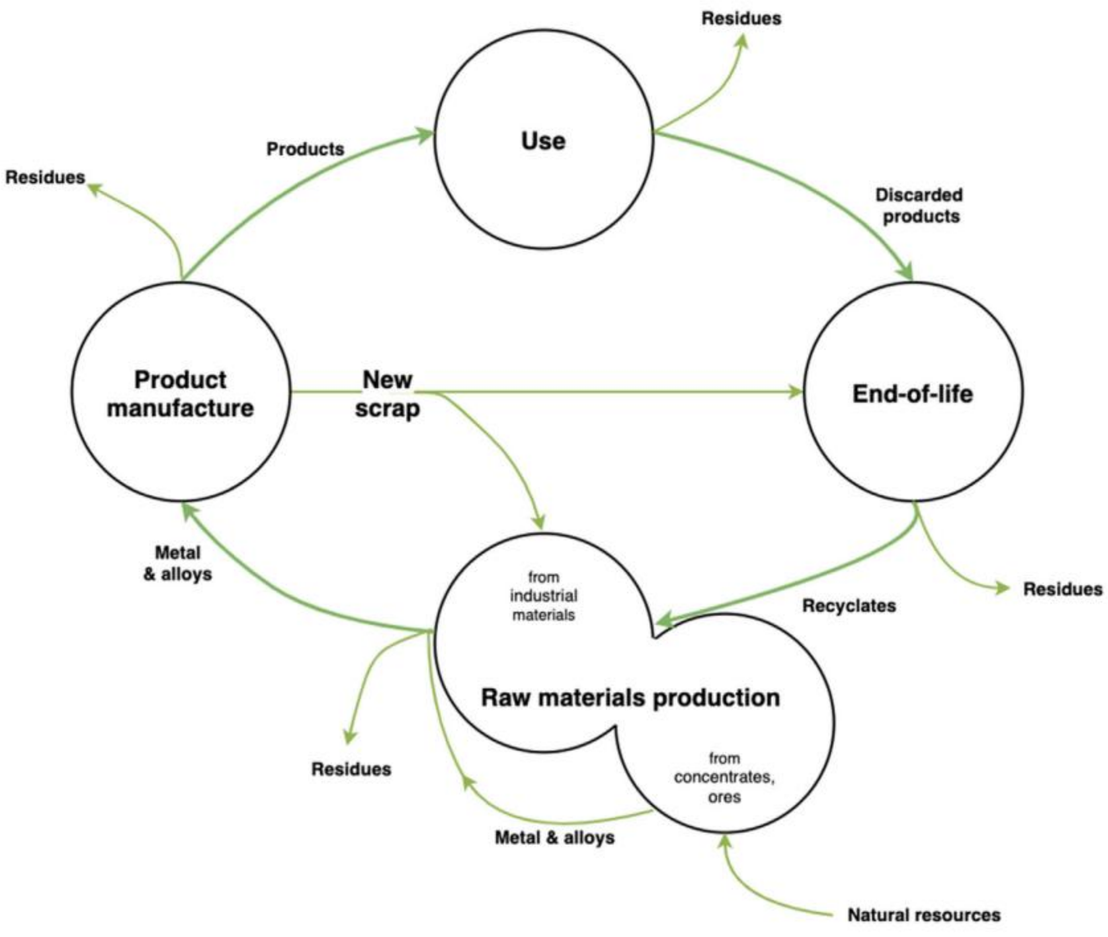

***Figure 2**. Life cycle of metal: production, product manufacture, use, and end of life [5].*

1.2 Classification of the circular economy methods

The traditional linear economy of a product is commonly represented by a horizontal line characterized by three main phases: production, use, and disposal (Figure 3). This means that when the end of life (EOL) is reached, it will be directly dispatched to a landfill without any kind of material recovery. To promote a more sustainable approach that limits the amount of waste, the Circular Economy method (CE) was developed. It aims to convert the traditional line (cradle to grave, C2G) into a circular loop where the product (or the components) is reintroduced again as a cycle (cradle to cradle, C2C) (Figure 4). Additionally, this reintegration of the product can be realized in two ways: closed loop or open loop [6]. The first one, the product is recycled or reused, keeping its function (e.g. a PET bottle can be recycled to produce another PET bottle), therefore, the loss of resources is minimal. On the other hand, in an open loop cycle, the product is recycled into a new product having a different function (e.g. a PET bottle is recycled into a polyester textile). In this last case, the material loss is higher than the closed loop.

Figure 3. *Traditional linear economy of a product [7].*

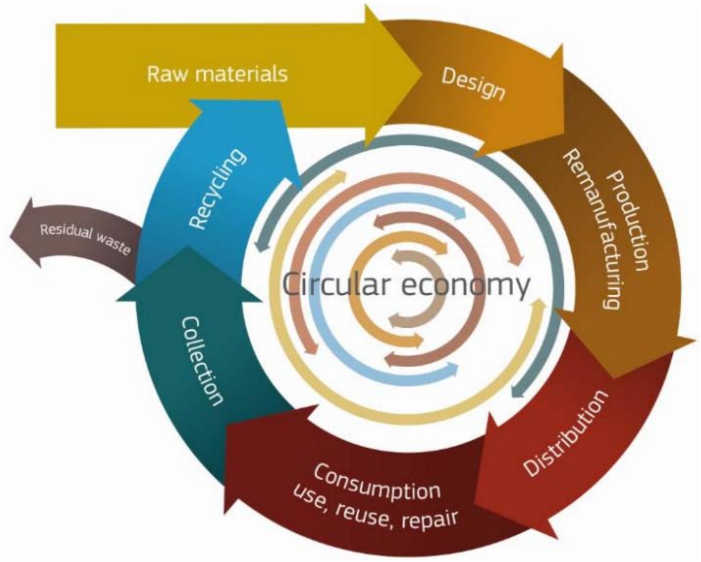

Figure 4. *Simplified conceptual diagram of the phases of circular economy [8].*

This topic has drawn the interest of many researchers over the last decades. Specifically, one of the fathers of this methodology was Kenneth E. Boulding who, in the 60s, published a paper named "The Economics of the Coming Spaceship Earth" that anticipated the concept of CE. Ten years later, Walter Stahel and Genevieve Reday highlighted the advantages of the CE in a report for the European Commission. At the beginning of the 21st century, William McDonough and Michael Braungart published a paper named "Cradle to Cradle" which introduced the necessity of the circular economy. Lately, the Ellen MacArthur foundation, born in 2010, has played an important role in promoting the circular economy as a reference model for companies. Nowadays, lots of researchers are still searching for a univocal definition of the circular economy [9].

Multiple solutions have been proposed for implementing circular economy strategies at the industrial level. Most of them can be summarized as the "*3R*". Concerning the "*3R*", this nomenclature is the result of three strategic actions, namely *Reduce*, *Reuse* and *Recycle*. The first one (Reduce) promotes the minimization of resources, preventing massive waste, by optimizing the productive process, proposing a product design (eco-design) focused on easy disassembling; the second one (Reuse) focuses on increasing the product's life by using them for the same scope they were built to or for a new scope. The way to reuse a product is by repairing, updating, sharing, or leasing the product. Lastly, the third R (recycling) aims to use part of a product or part of scraps as raw materials for new products.

Recently, new sustainable concepts were born, and new "*R*" were added to the list of the circular economy strategies (Figure 5). One of these was the "*Recovery"* that promotes energy recovery or material recovery from waste which cannot be reused or recycled, by means of incineration. This approach may be considered not so sustainable, but through this process, it is possible to produce thermoelectric energy, perform anaerobic digestion for recovering the energy and fertilizers, and recover metals from ashes. For the sake of clarity, all the other "*R*" developed during the last year will be directly listed in Table 1.

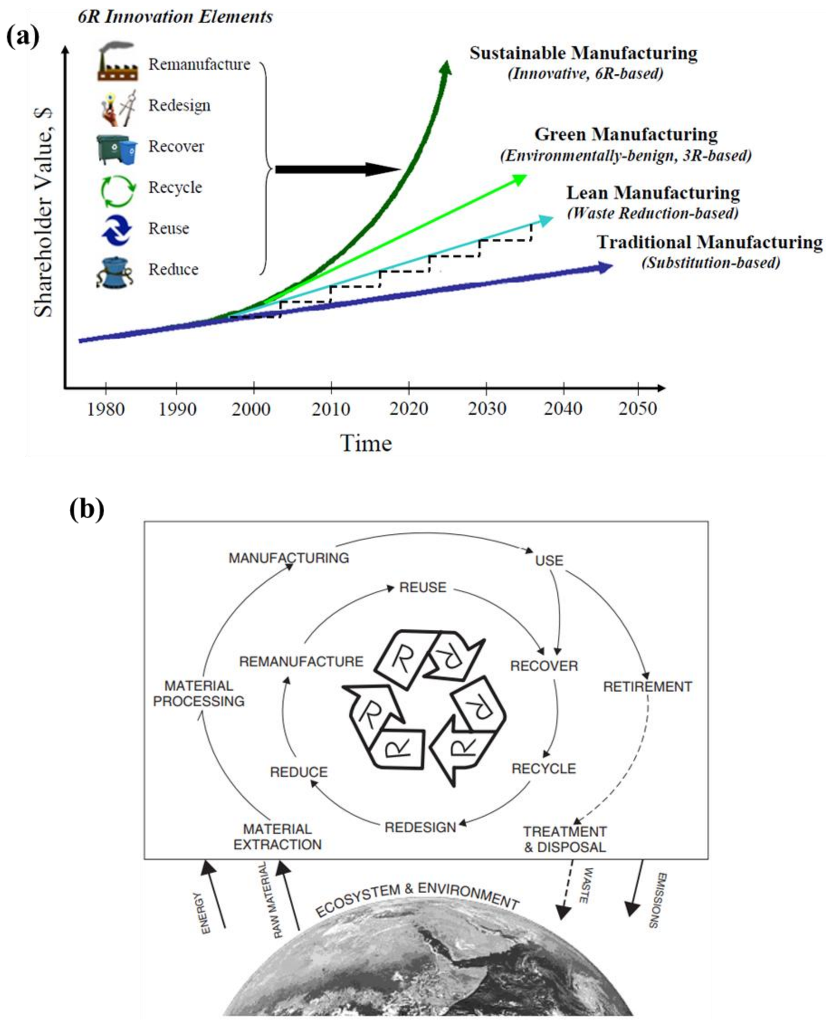

Figure 5. *(a) Evolution of sustainable manufacturing [10] and (b) closed-loop product life-cycle system in 6R approach [11].*

Table 1. *List of the "R" strategic approaches for applying the CE approaches.*

Level	R	Name	Main purpose
1	R0	*Refuse*	Avoid dangerous or useless products
2	R1	*Rethink*	Rethink the design and the use of the product
3	R2	*Reduce*	Reduce the material and the energy demand in the first stages
4	R3	*Reuse*	Use the product or its components more times
5	R4	*Repair*	Repair the product to extend its life
6	R5	*Refurbish*	Update and refresh the products
7	R6	*Remanufacturing*	Rebuild the product as new using waste parts
8	R7	*Recycle*	Convert components/material considered waste to new material or products
9	R8	*Recover*	Energy or material recovery from unrecyclable products

In this thesis, the sustainable approach that will be investigated is the recycling method. Specifically, aluminium scraps will be turned into consolidated products, such as billets, wires/rods or tubes, by using dedicated processes.

1.3 Efficiency and metrics of sustainable strategies

Nowadays, it is necessary to provide a better understanding of the current situation and monitor progress towards desired directions. The constant monitoring of the resources is ensured by different recycling metrics or indicators. [12, 13] that are listed in Table 2:

Table 2. *List of indicators used for estimating recycling efficiency.*

Name	Abbreviation	Description
End-of-life recycling input rate	EOL-RIR	Indicates the ratio of secondary raw materials obtained through the recycling of products divided by the overall quantity of raw materials fed into the economy.
End-of-life recycling rate	EOL-RR	Describes the share of a material in waste flows (output) that is actually recycled.
End-of-life collection rate	EOL-CR	Indicates the ratio between EOL products gathered for recycling and EOL available products
Recycled input rate	RIR	Ratio between metals produced from secondary production (including scraps and EOL products) and total metal production.
Recycling rate	RR	Ratio between metals recovered from secondary production and metals contained in the initial material (feedstock). It evaluates the efficiency of the entire chain (gathering, separation, metallurgy)

An example of EOL-RIR calculation is given in Figure 6. In this figure, the system boundaries defined for calculating this indicator include the processing and manufacturing stages for the European scenario. Specifically, the green flows refer to primary production, the yellow one represents an import of primary material, and the purple one illustrates secondary materials from old scrap. Equation 1 describes the mathematical ratio for quantifying the EOL-RIR value.

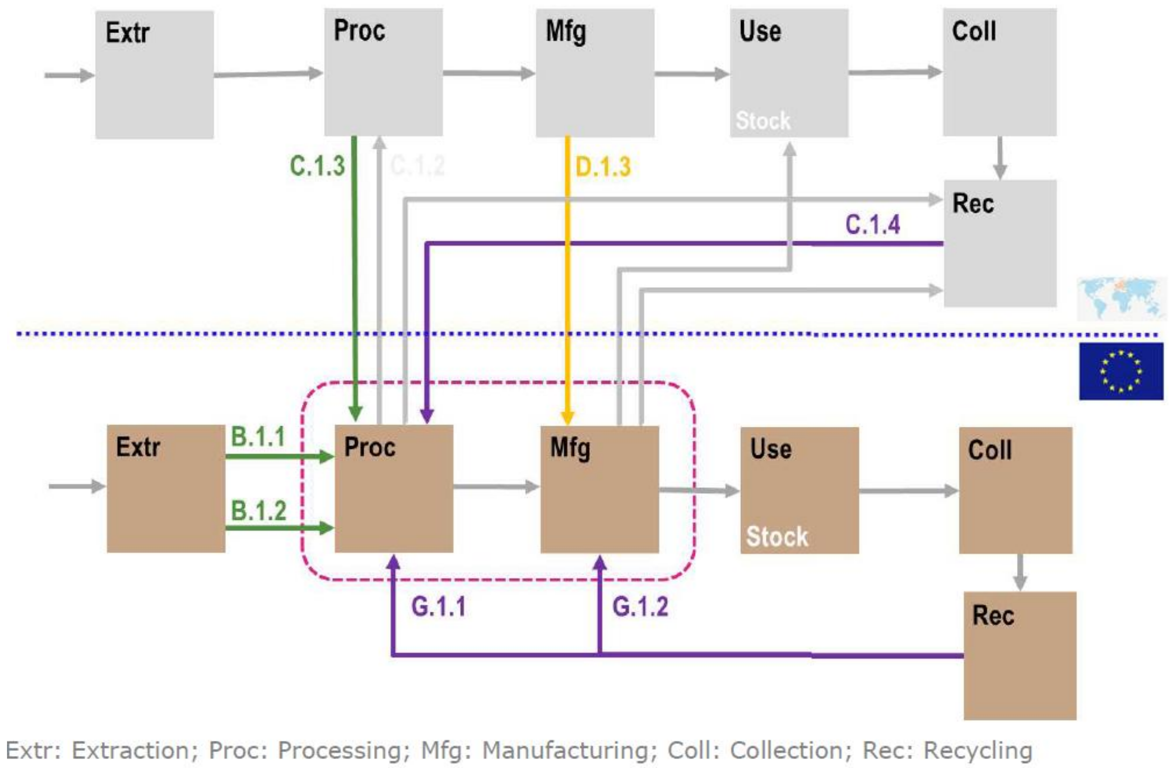

Figure 6. *System boundaries and material flows for the EOL-RIR calculation [13].*

$$EOL - RIR = \frac{G.1.1 + G.1.2}{B.1.1 + B.1.2 + C.1.3 + D.1.3 + C.1.4 + G.1.1 + G.1.2} \quad (1)$$

Where:

- EU secondary production (old scraps) flows
  - **G.1.1** Production of secondary material from post-consumer functional recycling in the EU sent to process in the EU
  - **G.1.2** Production of secondary material from post-consumer functional recycling in the EU sent to manufacture in the EU
- Primary production flows
  - **B.1.1** Production of primary material as the main product in the EU is sent to processing in the EU
  - **B.1.2** Production of primary materials as by product in the EU sent to manufacturing in the EU
- Import flows
  - **C.1.3** Imports to the EU of primary material
  - **C.1.4** Imports to the EU of secondary material
  - **D.1.3** Imports to the EU of processed material

The schematic life cycle of a generic product and the adoptable strategies are depicted in Figure 7. Considering three main phases, such as material production, product manufacturing, and product use, it is possible to qualitatively define the energy related to each phase. Specifically, it will be considered as "material energy" the energy required for producing the material after natural resources gathering, as "manufacturing energy" the energy required for building the product, and as "use energy" the one required during the usage of the product. The evaluation of the energy saving will be performed by comparing the recoverable energy calculated as the sum of material and manufacturing energy to the energy of the selected CE strategy (Figure 8).

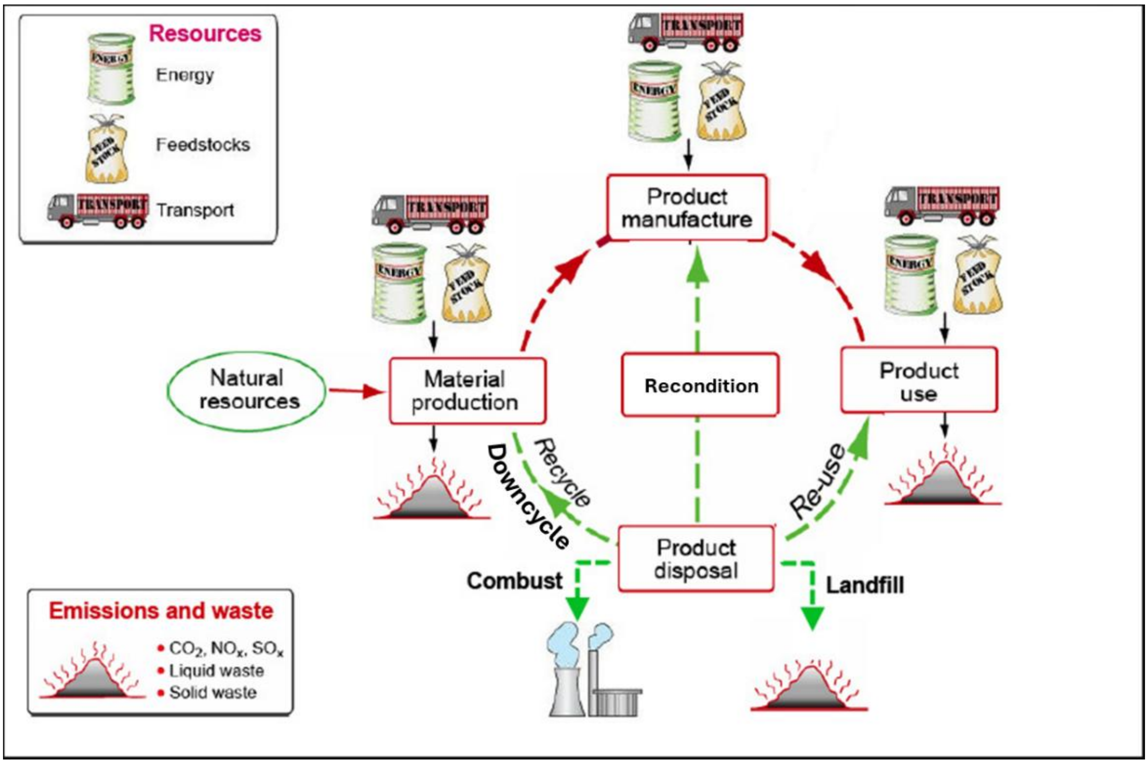

Figure 7. *Life cycle of a generic product and adoptable strategies [14].*

Starting with the reuse, it is clear that with this strategy, the entire material and manufacturing energy is saved because it won't be necessary to get new material or produce a new product, but a small amount of energy is still required to operate this strategy. Concerning the reconditioning, the aim is similar to the previous one; therefore, a large amount of recoverable energy will be saved, but this action requires spending more energy to restore the product.

On the other hand, the recycling approach does not save any manufacturing energy because this strategy is employed to avoid material production. Additionally, it requires energy therefore, the energy savings are way less than the previous ones. The combustion and the landfill are the lowest energy saving strategies because the product at its EOL is destroyed.

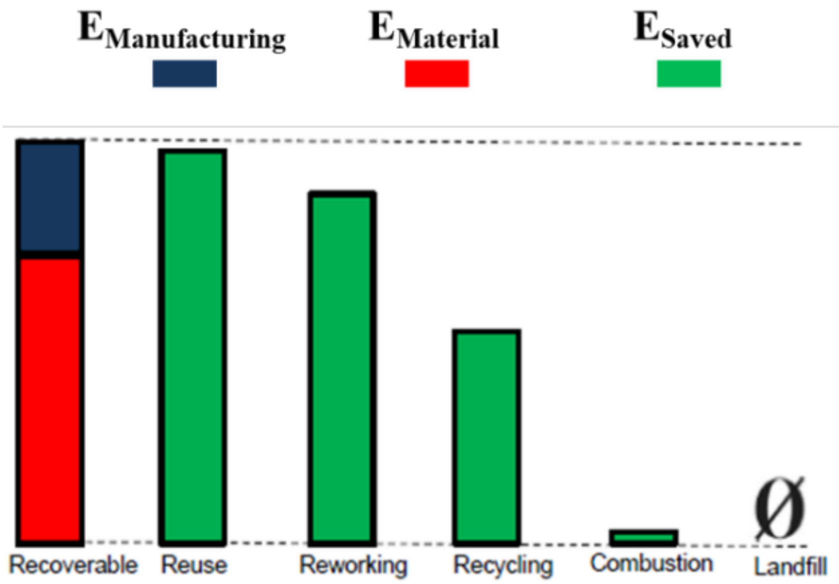

Figure 8. *Energy saving for each strategy of the generic product's life cycle.*

1.4 Aluminium in the recycling scenario

This chapter describes the role of aluminium in the industrial sectors and the environmental impact during the production phase. The traditional productive cycle of aluminium, from mining to casting, will be analyzed, highlighting the phases that aluminium goes through and the related environmental impact.

1.4.1 Properties and industrial applications

Aluminium is a non-ferrous metal which was widely employed in different sectors such as aerospace, automotive, energy, packaging, and construction. Since the 19^{th} century, this material has had huge issues due to its challenging obtainability until in 1886 Charles Hall and Paule Héroult discovered a way to obtain aluminium from alumina, by using electrolysis. A few years later, in 1888, Karl Bayer developed a chemical process for gathering alumina from bauxite, making the aluminium Hall-Héroult cycle economically affordable.

Aluminium is well known for its lightness and ductility (excellent weight/strength ratio), moreover, due to the slim natural oxide film made of alumina (Al_2O_3), it has high resistance to corrosion. The main thermos-mechanical properties are listed in Table 3. This metal has also been alloyed with different chemical elements such as manganese, magnesium, silicon, and copper to enhance different structural and corrosion properties (Table 4); most of these aluminium alloys (2xxx, 6xxx, and 7xxx) are heat treatable (quenching, aging, and annealing) to further improve the mechanical behavior.

Table 3. *Table of thermo-mechanical properties of pure aluminium [15].*

Mechanical		**Electrical**		**Thermal**	
Vickers hardness	15 HV	*Resistivity*	$2.7 \cdot 10^{-6}$ ohm-cm	*Thermal expansion coefficient*	24 µm/m °C
Elasticity modulus	68 GPa	*Magnetic susceptibility*	$6 \cdot 10^{-7}$	*Specific heat capacity*	0.9 J/g °C
Poissons ratio	0.36	*Oersted CMFS*	101.9-107.9	*Thermal conductivity*	210 W/m K
Shear modulus	25 GPa	*CST*	1.73-1.77 K	*Melting point*	660.37 °C

Note: CMFS = Critical Magnetic Field Strength, CST = Critical Superconducting Temperature

Table 4. *List of existing aluminium alloys with composition.*

Alloy	**Main alloying element**	**Main features**	**Heat treatment**
1xxx	Pure aluminium (≥99%)	Excellent conductivity, corrosion resistance, and low mechanical strength	O, H12, H14
2xxx	Copper	High mechanical strength, low corrosion resistance, and heat treatable	T3, T4, T6
3xxx	Manganese	Good corrosion resistance, good formability, not heat treatable	O, H14, H16
4xxx	Silicon	Wear resistance, good castability, used in welding and thermal applications	O, T5, T6
5xxx	Magnesium	Excellent corrosion resistance, good weldability, not always heat treatable	O, H32, H34
6xxx	Magnesium, Silicon	Good mechanical and corrosion resistance, heat treatable, and good weldability	T4, T5, T6
7xxx	Zinc, Magnesium	Very high mechanical strength, used in aerospace, low weldability, and corrosion resistance	T6, T73, T76
8xxx	Other elements (Li, Fe, Sn, etc…)	Specialty alloys for specific applications: sheets, packaging, batteries	O, H19, T6

1.4.2 Primary production: Bayer e Hall-Héroult cycle

The cycle for producing aluminium (Figure 9) involves four phases [16]:

1. Bauxite extraction,
2. Alumina production – Bayer process,
3. Aluminium production - Hall-Héroult process,
4. Refinement.

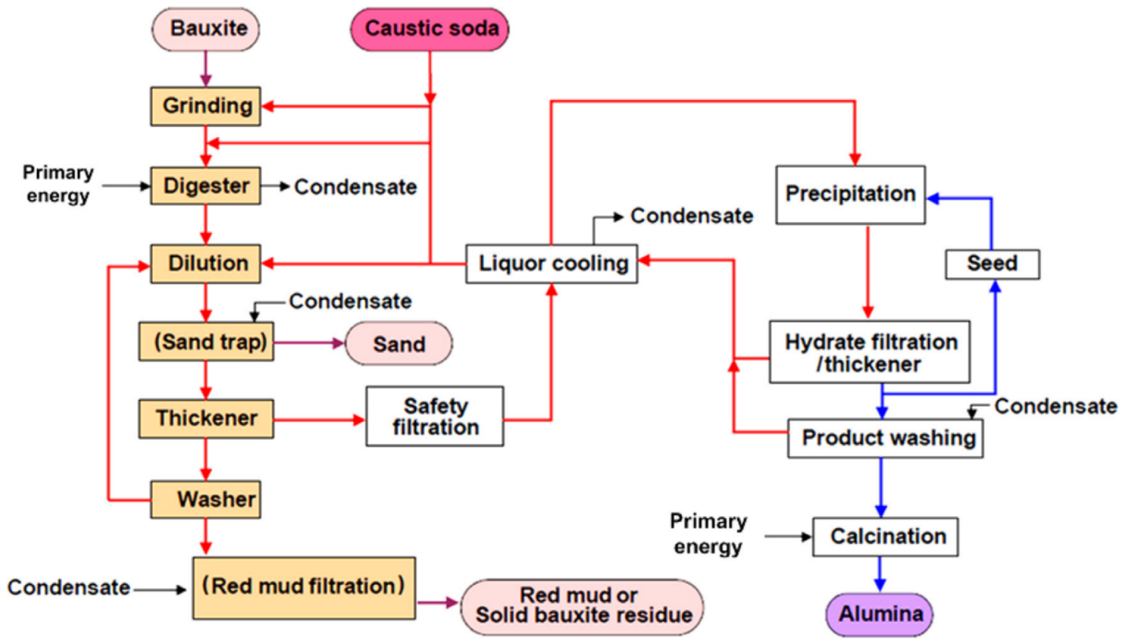

Figure 9. *Graphical overview of the alumina production workflow [17].*

Bauxite ($Al_2O_3 + nH_2O$), which is the most important mineral used for obtaining aluminium, is first mined from caves. This ore only contains 30-50 % of alumina, while the remaining part is made up of silica (SiO_2), iron oxides, and titanium dioxide. Before being transformed into aluminium, alumina requires purification (digestion phase) by cleaning with a sodium hydroxide solution (NaOH) at 175 °C. At this point, the alumina is converted into an aluminate ion $Al(OH)_4$, according to reaction (Eq. 2):

$$Al_2O_3 \cdot nH_2O + NaOH \rightarrow Na[Al(OH)_4](+Fe_2O_3 + TiO_2 + \cdots) \quad (2)$$

The other components are then filtered and discarded as a mixture of solid impurities called "*red mud*", which has many disposal problems. After the reaction, the hydroxyl bath is cooled, letting the aluminium hydroxide precipitate (precipitation phase) (see Eq. 3).

$$Na[Al(OH)_4] \rightarrow Al(OH)_3 + NaOH \quad (3)$$

Finally, the aluminium hydroxide is heated up to 1050 °C for chemical decomposition into alumina (calcination phase), releasing water (Eq. 4).

$$2\,Al(OH)_3 \rightarrow Al_2O_3 + 3\,H_2O \tag{4}$$

Once alumina was created, it was dissolved into a bath of molten cryolite, which generates a molten "salt", employed for obtaining aluminium through electrolysis.

Specifically, cryolite is first obtained by the reaction in Equation 5, while the aluminium production is carried out in an electrolytic cell with a cryolite/alumina mixture (80% / 10%) and fluxes (calcium fluoride, lithium carbonate) as electrolyte (Eq. 5,6, and 7).

$$Al_2O_3 + 12\,HF + 6\,NaOH \rightarrow 2\,Na_3AlF_6 + 9\,H_2O \tag{5}$$

This mixture helps to reduce the melting point of the alumina from 2000 °C to about 980 °C, which is easier to work with. During the electrolysis process (Figure 10), aluminium is spilled from the bottom of the bath because of its density. The electrolytic reactions are described in the following equations (Eq. 6-8)

$$Al^{3+} + 3\,e^- \rightarrow Al \tag{6}$$

$$2\,O^{2-} + C \rightarrow CO_2 + 4\,e^- \tag{7}$$

$$2\,Al_2O_3 + 3\,C \rightarrow 4\,Al + 3\,CO_2 \tag{8}$$

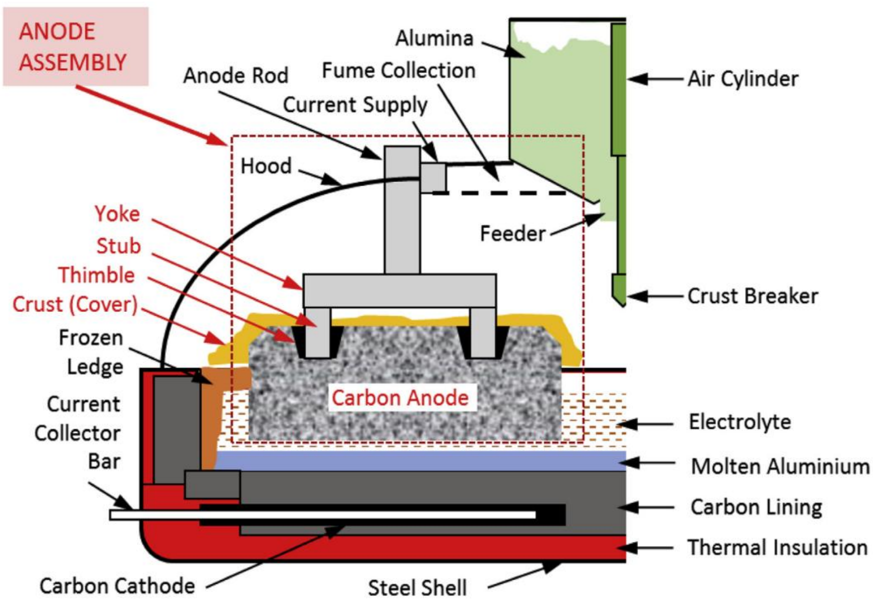

Figure 10. *Hall-Héroult electrolytic cell for aluminium production from alumina [18].*

1.4.3 Environmental impact of aluminium primary production

The Hall-Hèroult process is high-energy demanding, and for 1 ton of aluminium it can absorb up to 11500 ÷ 13500 kWh of electrical energy. In the report developed by Cusano et al. [19], emissions and the consumption levels of primary production of aluminium were studied. In particular, they found out that approximately two tons of bauxite are required for producing one ton of alumina, which in turn produces 0.53 tons of aluminium. During the electrolysis, the anodes are consumed, resulting in the use of 0.4-0.45 tons of carbon. Moreover, the energy required for alumina production during digestion and calcination is mainly influenced by the chemical composition of the bauxite. Other inputs considered during alumina production are listed in Table 5.

Table 5. *Main inputs for alumina production [19].*

Input	Typical range (kg/t of alumina)
Bauxite	2065 -2275
NaOH (50%)	30 -70
CaO	30 - 80
Water	1000 - 5000
Energy (GJ/t)	7.6 - 11.7

The energy used in anode production is 2000-2400 MJ per ton of anode (depending on the fuel used), and the packing coke is consumed at a rate of 12-18 Kg per ton of anode.

In Figure 11 the main inputs and outputs of aluminium primary production are shown. The aluminium electrolysis stage has a high energy use, ranging from 53 GJ per ton (prebaked cells) to 61 GJ per ton (Soderberg cells). The main output due to the electrolysis process is mainly emissions to air and can be distinguished into three main sources: process gases from cells, pot room ventilation, and decreasing/casting.

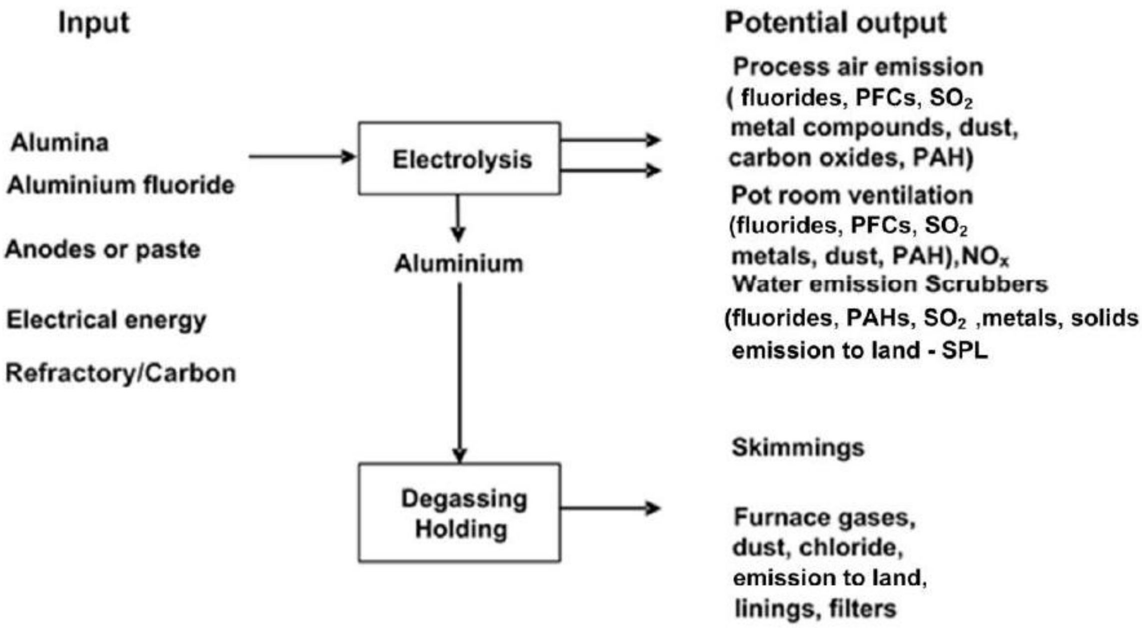

Figure 11. *Inputs and outputs during the production of aluminium [19].*

The potential emissions from the electrolysis stage [19] are listed as follows:

- carbon dioxide (CO_2) and carbon monoxide (CO),
- Polyfluorocarbons (PFCs) in connection with anode effects,
- Dust, mainly linked to alumina and fluorinated product handling, from around the pots or
- the handling systems,
- fluorides, both gaseous and as particulates, at the surface of the bath,
- Sulphur dioxide (SO_2) and other sulfur compounds, resulting mainly from anode,
- consumption, and due to the sulfur contained in coke and pitch,
- tars and polycyclic aromatic hydrocarbons (PAH) in the case of Søderberg electrodes,
- metal compounds,
- oxides of nitrogen (NO_X).

For the sake of simplicity, the data of the report [19] will be shown as figures below (Figure 12, Figure **13**, Figure **14** and Figure **15**).

Parameter	Prebake	Søderberg
Alumina (kg/t Al)	1910–1960	
Anodes net (kg/t Al)	410–450	NA
Anode paste (kg/t Al) (1)	NA	470–530
Al F_3 (kg/t Al)	13–30	18–25
Cathode life (years)	5–8	4–6
Amperage (kA)	90–360	
Power for alumina production (GJ/t Al)	< 10	< 10
Specific energy consumption for electrolysis (kWh/kg Al)	13.2–15.0	14.5–17.0 (2)
Total electrical power (kWh/kg Al) (3)	13.6–15.7	15.1–17.5

(1) Expressed as total Søderberg paste. In the case of Søderberg cells, the figures represent the gross carbon consumption as the baking losses happen during the electrolysis.
(2) In the Søderberg process, these figures account for all energy consumption, while in the Prebake process there is additional consumption in the baking furnace.
(3) Including rectifier loss, pollution control and auxiliary consumption.
NB: Energy data are produced based on the conventions used by Industry.
NA = Not applicable.

Figure 12. *Input ranges for the electrolysis process [19].*

Parameter	Range
Skimmings/dross produced (kg/t Al)	10–50
Fluxes (kg/t Al)	0–1.5
Gases (kg/t Al)	0–0.04
Swarf, etc. (kg/t Al)	0–3
Water (kg/t Al)	200–10 000
Homogenisation energy (MJ/t Al)	500–1200
Casthouse energy (MJ/t Al)	300–2500 (1)

(1) Excluding remelting of cold metal.

Figure 13. *Cast-house consumption ranges [19].*

Parameter	Emission (kg/t of aluminium)
Dust	0.01–0.1 (1)(2)
NO_X	< 0.1–0.4
SO_2	0–1.8 (2)

(1) Depending on filter system.
(2) Depending on fuel used.

Figure 14. *Primary aluminium cast-house emissions to air [19].*

Parameter	Søderberg
Fluorides (kg/t Al)	0.5–1.5
Suspended solids (kg/t Al)	0.5–2.0
PAH (Borneff 6) (g/t Al)	6–15

Figure 15. *Process emissions to water from the primary aluminium electrolysis plants using ventilation air wet scrubbers or SO2 wet scrubbers [19].*

1.5 Remelting route and challenges in aluminium recycling

Producing aluminium has turned out to be highly expensive in terms of energy and emissions. For this reason, the recycling strategy has been widely adopted for saving or reducing the primary production and the related consumption. One of the most well-known solutions for recycling aluminium is the remelting route, which allows metal scraps transformation into new products through melting and casting phases. This approach is characterized by an energy demand of about 95% less than the traditional one.

An example of this route is described in Figure 16, that shows the inputs and outputs for each phase. Despite the energy saving promoted by the material recycling, this procedure has different drawbacks, such as emissions (Figure 17), initial pre-treatment of the scraps, chemical contaminations, difficulty in separation of specific components, and losses due to oxidation.

This last issue is very important because the material loss can reach up to 16-25 % of the recycled material. This phenomenon happens when light metal particles, which are floating on the melting bath surface, start to react with oxygen contained in the air. Because of the high reactivity of the molten aluminium to the oxygen, the oxidized scraps are not recoverable anymore, being then discarded, resulting in a loss (Figure 18).

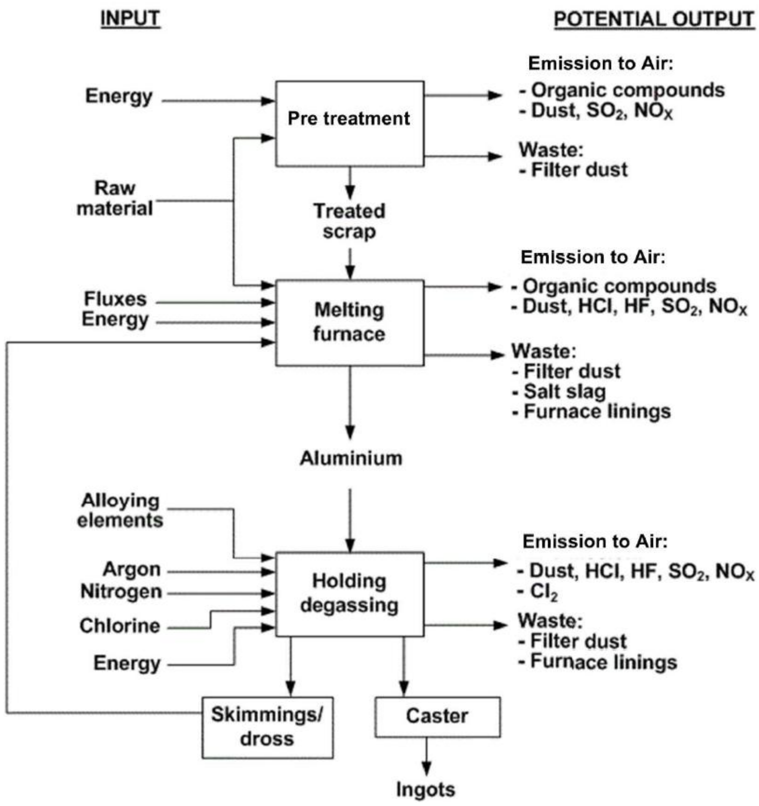

Figure 16. *Typical input and output of a secondary aluminium plant [19].*

Component	Pretreatment	Melting	Molten metal treatment and degassing
HCl, HF and Cl_2	••	••	•••
Metals and compounds	••	••	••
Oxides of nitrogen	•	••	• (combustion gases)
SO_2	• (with suitable fuel)	• (with suitable fuel)	• (combustion gases)
Organic compounds (CO, TOCs, PCDD/F)	•••	•••	NR
Dust	•••	•••	••
NB: ••• More significant – • Less significant. NR = Not relevant.			

Figure 17. *Significance of potential emissions to the air of a secondary aluminium plant [19].*

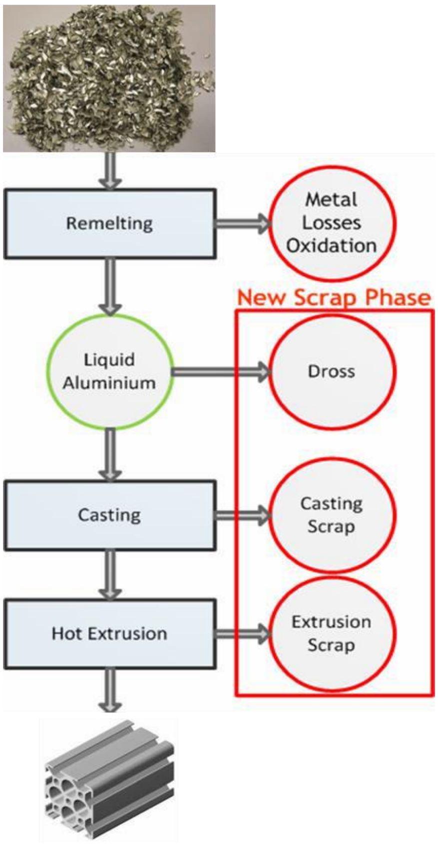

Figure 18. *Metal losses occur during the remelting route, from melting to the final product.*

The drawbacks of the remelting route have been addressed by shifting the focus to processes that do not involve the huge energy demand of the melting phase. These processes are commonly known as "*Solid State Recycling*" (SSR) processes. Their main innovation relies on the ability to recycle the metals by skipping the remelting phase. This approach is possible because during the solid state recycling process, metal chips/powder are directly transformed into semi-finished or final product by plastic deformation that operates at temperature levels which are below the melting temperature of the metals. The fact that the process does not involve any molten material is crucial because in this case the metal is less reactive to oxygen, and the oxidation is significantly reduced, leading to a recycled product with superior mechanical properties [20].

SSR techniques possess many advantages over the conventional remelting-based recycling methods, including lower energy consumption (no melting), lower metal loss (less oxidation), as well as almost no emissions of harmful gases and solid waste. The common steps associated with the SSR (Figure 19) include the material reduction into chips, cleaning and drying, and lately cold compaction to ensure an easier workability and to reduce oxygen in the cavities between chips. Finally, this batch is processed to get the final product.

Metals such as aluminum [21], magnesium [22], iron [23], copper [24], nickel [25], and titanium [26] have been successfully recycled through different SSR processes.

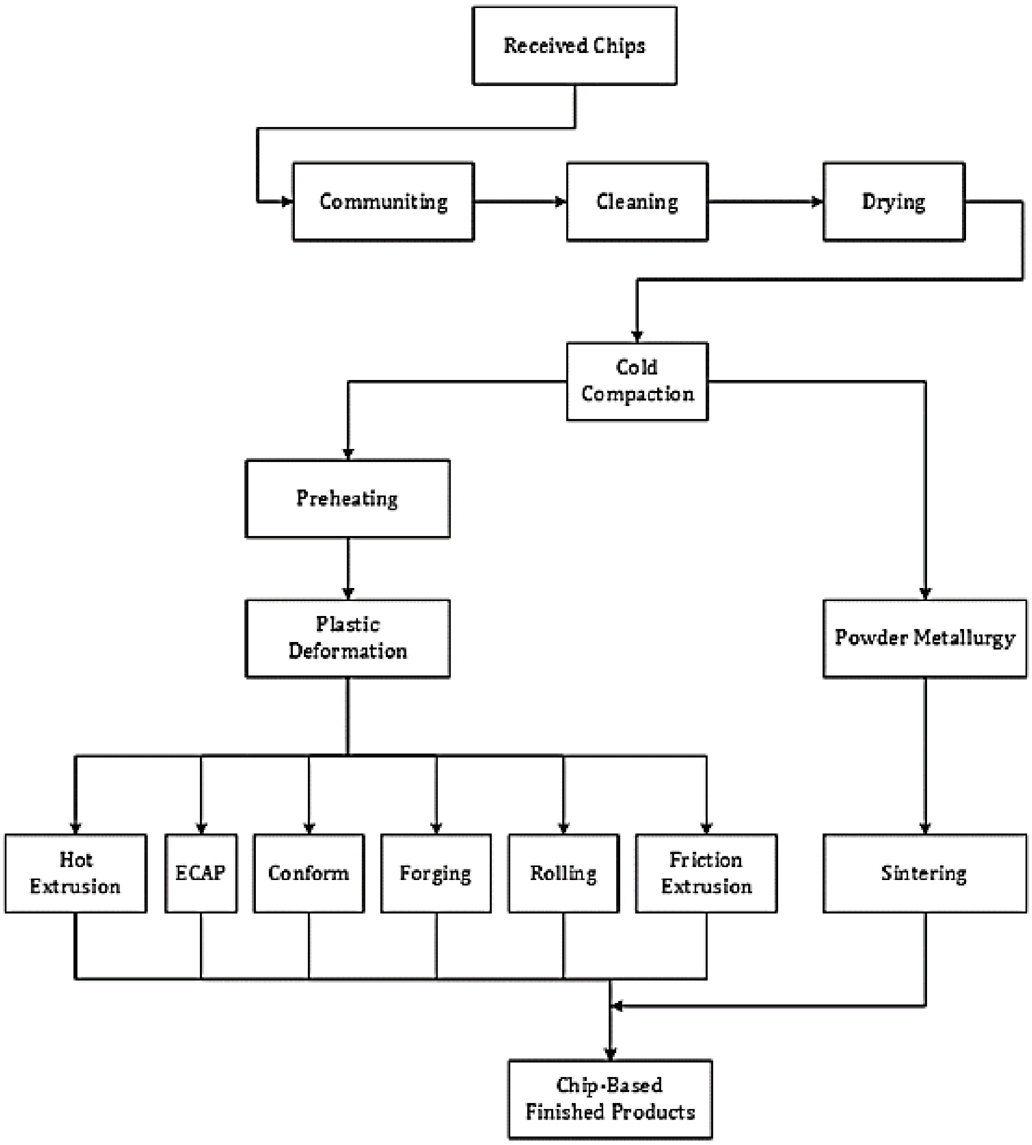

Figure 19. *Flow chart of chips pre-processing and different solid-state recycling methods by plastic deformation and powder metallurgy approach [27].*

2 Solid state recycling processes

2.1 Powder metallurgy

The powder metallurgy (PM) technique is a rapid, economical fabrication process for making near-net shape products from powders. The common practice of PM includes the compaction of powder into a desired shape, and then the shape is heated below the melting temperature, which enables the bonding of particles to join together. Upon compression and heating, the interparticle gaps diminish leading to a relative density close to100%, which approximates the properties of the main material. The process generally takes only seconds to complete. The post-form sintering step, however, can take several hours to complete.
Spark Plasma Sintering (SPS) is a widely used SSR method based on the sintering process for recycling metallic scraps. Ease of operation, high sintering speed, low sintering temperature, high reproducibility, and highly dense sintering samples of finer grain [28] are many of the advantages that characterize this process category over conventional sintering techniques, namely pressureless sintering (PLS), vacuum hot pressing (VHP) and hot isostatic pressing (HIP).

2.1.1 Spark Plasma Sintering (SPS) Process

Spark plasma sintering (SPS), as a rapid consolidation method, is widely used for the consolidation of metallic powders [29]. In this process, the high-energy pulsed Direct Current (DC) is applied to the powder particles, enabling the individual particles to uniformly generate Joule heat. The spark generated by the discharge of the pulsed DC current between the powders activates the surface of the particles, resulting in higher heating efficiency. The process schematic has been represented in Figure 20.
However, due to the lack of strain and strain rate occurrence, the consolidation level and final density provided by this process category could not be satisfying, consequentially some authors proposed to apply a further process step after the sintering step. Koch et al. [30] proposed a recycling process made of a field-assisted sintering (FAST) process to consolidate the aluminum alloy chips, and a forward rod extrusion process. Behrens et al. [31] recommended a hybrid approach made of compacting, sintering, and forming to consolidate aluminum chips. Other researchers [32] applied an isothermal sintering process with multiple ECAP passes to increase the mechanical properties of magnesium alloys.

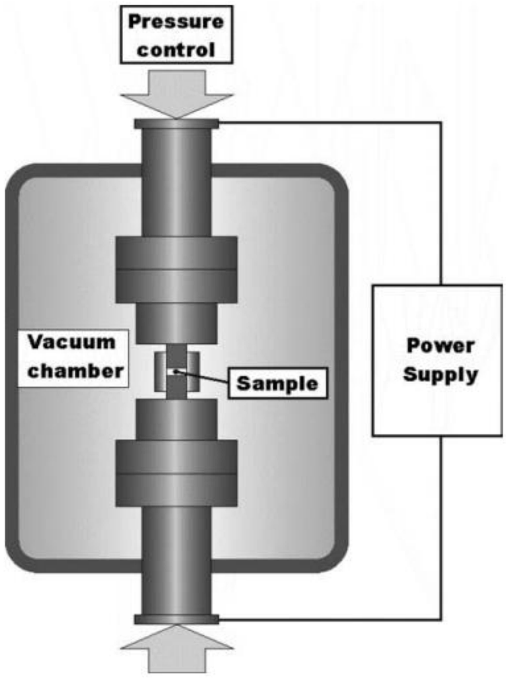

Figure 20. *The SPS process schematic diagram [28].*

2.2 Plastic deformation

This process category of SSR methods is based on the physical disruption and dispersion of oxide contaminants by imposing high temperatures, significant shear strains [33]. For promoting the aluminium surface bonding, the plastic deformation must be large enough to break the surface oxide layer of the metal in order to expose clean, non-oxidized metal surfaces. Some of the typical methods include Equal Channel Angular Pressing (ECAP), Hot Extrusion (HE), Screw Extrusion (SE), High Press Torsion (HPT), Cyclic Extrusion Compression, High Pressure Forging (HPF), and Friction Stir (FS) Based Techniques.

2.2.1 Equal Channel Angular Pressing (ECAP)

IECAP is used to fabricate bulk ultrafine-grained materials with high-angle grain boundaries via pure shear, and the main advantage of this process is that exceptionally large, unidirectional, uniform deformations can be brought to the bulk solids even under relatively low loads, as shown in Figure 21. The procedure is simple, and it involves samples passing through a designed channel, introducing simple shear for each pass. Despite a very intense shear strain produced within the sample, the cross-sectional dimensions of the sample remain unchanged, allowing for repetitive deformation [34].

Although ECAP is generally applied to the severe plastic deformation of the bulk material, it has also shown promising results to be a good candidate for solid-state recycling. For example, Matsuki et al. [21] applied the ECAP process for the consolidation of 2024Al-3Fe-5Ni alloy powder to obtain an almost fully dense compacted sample with a very fine microstructure. Moreover, other authors used well-mixed powders, i.e., carbon nanoparticles and pure Al particles, for fully densifying Al-C nanocomposites, showing significantly high mechanical properties, fine equiaxed grains, and uniform distribution of C particles into the Al matrix [35].

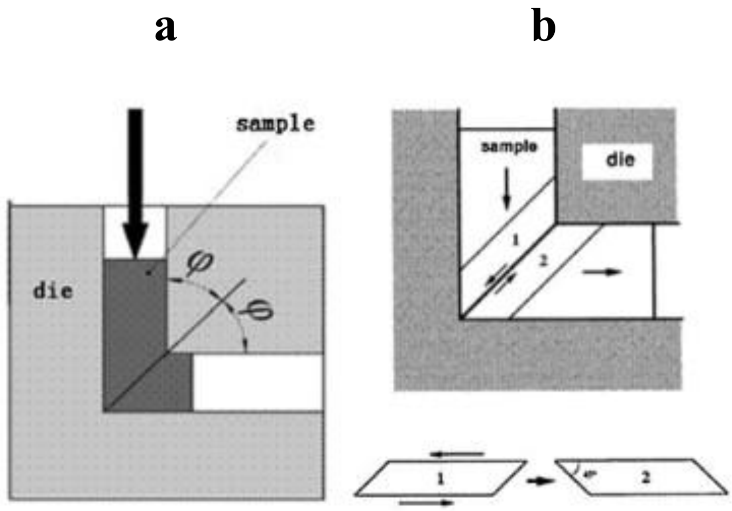

Figure 21. *The process of ECAP (a) schematic illustration of the typical two-dimensional ECAP set-up; (b) principle of shearing on passage within the die [20].*

2.2.2 Hot Extrusion (HE)

During the HE process, the machining chips are filled into a cylindrical container and pressed into billets with the desired pressure at room temperature. Then the billets are hot extruded into rods with a certain extrusion ratio and extrusion rate while maintaining the extrusion temperature below the melting temperature of the extruded material [36] as shown in Figure 22.

Some initial attempts were made to achieve better bonding of aluminum chips using cold compression only. Other authors found that high compressive forces with long pressing time were not enough for obtaining sound chip bonding [37]. Hence, an additional shear force, such as an extrusion process, was applied to the as-pressed billet to produce chip-consolidated products of high quality. However, considering relatively higher thermal energy requirements and processing costs during the hot working (such as hot extrusion), some researchers were devoted to recycling chips through cold working.

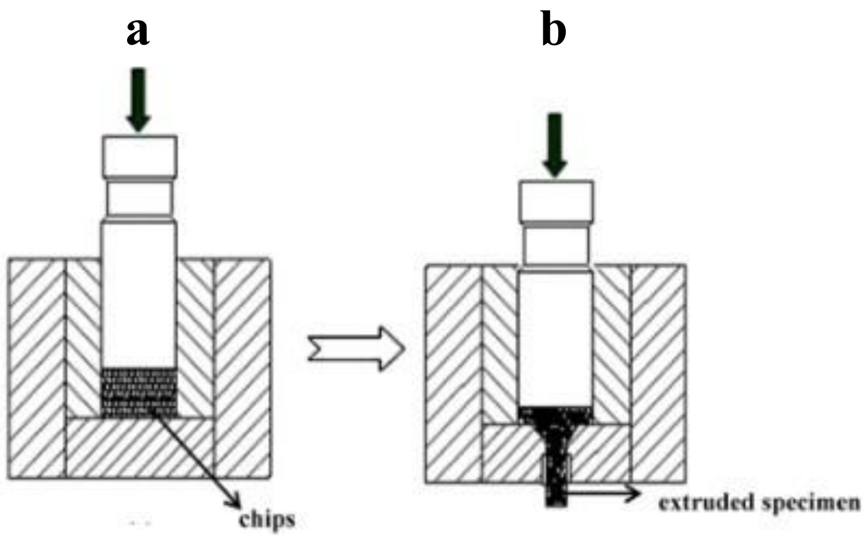

Figure 22. *Illustration of hot extrusion process (a) cold pre-compacting; (b) hot extrusion [20].*

2.2.3 Screw Extrusion (SE)

Werenskiold et al. [38] introduced the screw extruder for the continuous extrusion of materials with high viscosity, which is preferably applicable for the treatment of the granulated chips of aluminum and its alloys. Figure 23 shows the schematic illustration of the cross-sectional view of an extruder. Granules are fed to the screw through the inlet, which goes at the gap between the screw and the liner. The combination of high temperature and the screw's rotation leads to the material compaction and consolidation into the desired extruded product. It is worth noticing that the innovative point of the screw extrusion method was the rotating screw that could impose compression and rotation to the materials simultaneously in one single continuous operation. Later on, Widerøe et al. [39] applied the screw extrusion process to the welding of the aluminum AA6060 granulates, finding that the rotational movement obviously reduced the amount of axial compressing force necessary for the compaction of granulates.

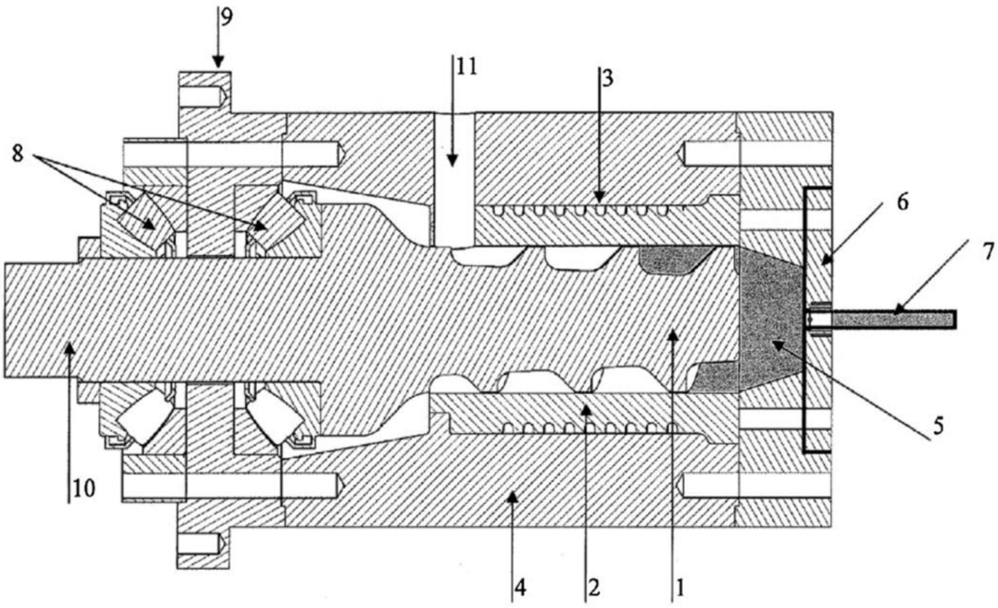

Figure 23. *Schematic illustration of the cross-sectional view of an extruder. (1) screw, (2) liner, (3) cooling channel, (4) screw housing, (5) extrusion chamber, (6) die, (7) extruded product, (8) thrust bearing, (9) support plate, (10) screw shaft, (11) inlet [20].*

2.3 Friction stir-based techniques

Recently, friction stir-based methods have drawn the attention of many researchers. These are process variants of friction stir welding (FSW) technology; the process mechanics are quite similar, but the purpose is strictly related to material recycling. In these processes, the material (chips) is simultaneously heated up and compressed thanks to the action of a rotating tool. The combination of friction and compression results in chips consolidation. Among the friction stir-based techniques, friction stir extrusion (FSE) and friction stir consolidation (FSC) are very popular. Basically, both FSE and FSC have the same process mechanics and can share a common experimental setup.

During FSE, a rotating die is plunged into a cylindrical chamber containing metal scraps. The stirring action of the tool plastically deformed the material and forced it into the extrusion chamber. Finally, after densifying and heating, fully consolidated rods are extruded. The detailed discussion of the FSE process has been presented in Chapter 2.3.2.

Similar to FSE, friction stir consolidation is a novel solid-state process. The only exception is that FSC lacks an extrusion channel within the tool. Therefore, the scrap metals are consolidated into a billet or disc shape rather than extruded into a wire shape. The FSC process has two main steps: compaction and consolidation. Compaction refers to the initial pressing of aluminum chips or powder in a hollow die chamber by applying a specific load. Then, materials are further pressed and stirred through the tool’s downward force and rotational speed, namely "consolidation phase". The detailed discussion of the FSC process has been reported in Chapter 2.3.1.

2.3.1 Friction Stir Consolidation (FSC)

Friction stir consolidation is a solid-state recycling process, which usually involves the use of a cylindrical tool, a die, and a backing plate (Figure 24), used to turn machining chips into a consolidated billet. In the FSC processes, there are three main factors: time, pressure and temperature. The last two parameters are related to the action of the tool; the heat input depends on the friction generated by the rotational speed between the tool's surface and the material's one, while the pressure is applied by imposing the vertical load on the tool. The die and the backing plate are utilized to contain the chips during the process.

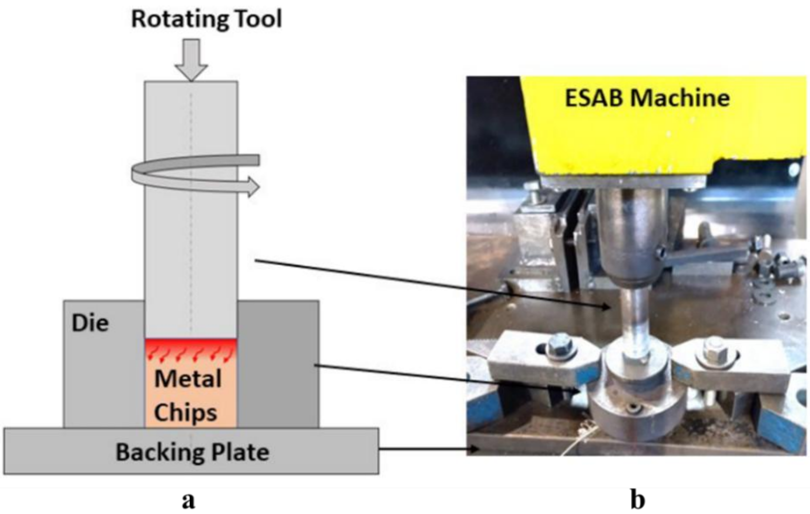

Figure 24. *(a) FSC process sketch and (b) ESAB machine setup [40].*

One of the first FSC processes was developed by Tang and Reynolds [41] which obtained solid disks starting from different aluminum alloy chips (2xxx, 5xxx, 6xxx, and 7xxx). Through the microstructure analysis, they found a ring zone at the bottom part of the disk where there was a localized lack of consolidation (Figure 25). Specifically, they assumed that these defects were due to the lower deformation and heat input generated during the process with respect to the upper part of the disk (where the material is directly in contact with the tool).

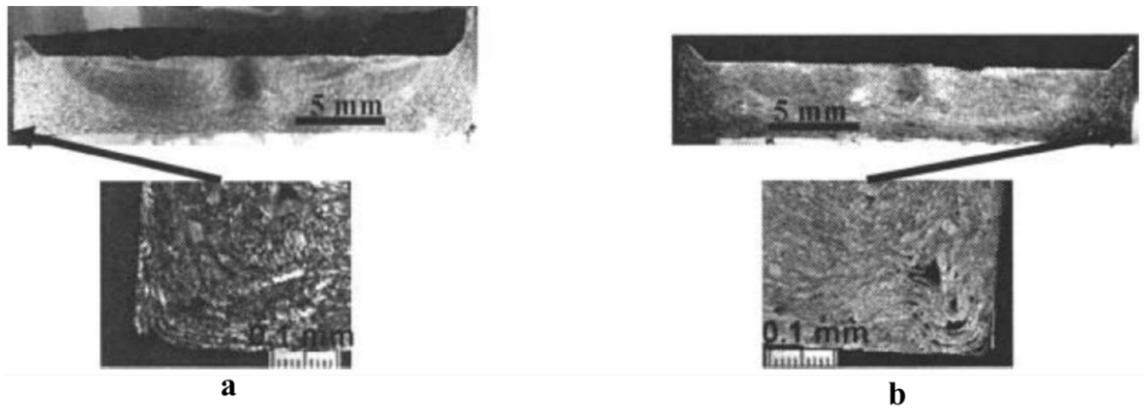

Figure 25. *Consolidated disks cross sections and lack of consolidation defects for the (a) AA2050 and (b) AA7075 [41].*

Li et al. [42] studied the effect of the different combinations of the three main parameters of the FSC processes (time, pressure, temperature). They carried out a set of nine experiments varying the rotational speed, the vertical load, and the processing time, obtaining AA6061 billets with different grades of consolidation (Figure 26), by performing a two-step process: first, they pre-compacted the chips using only the vertical load, then they created the consolidated billet through the FSC process.

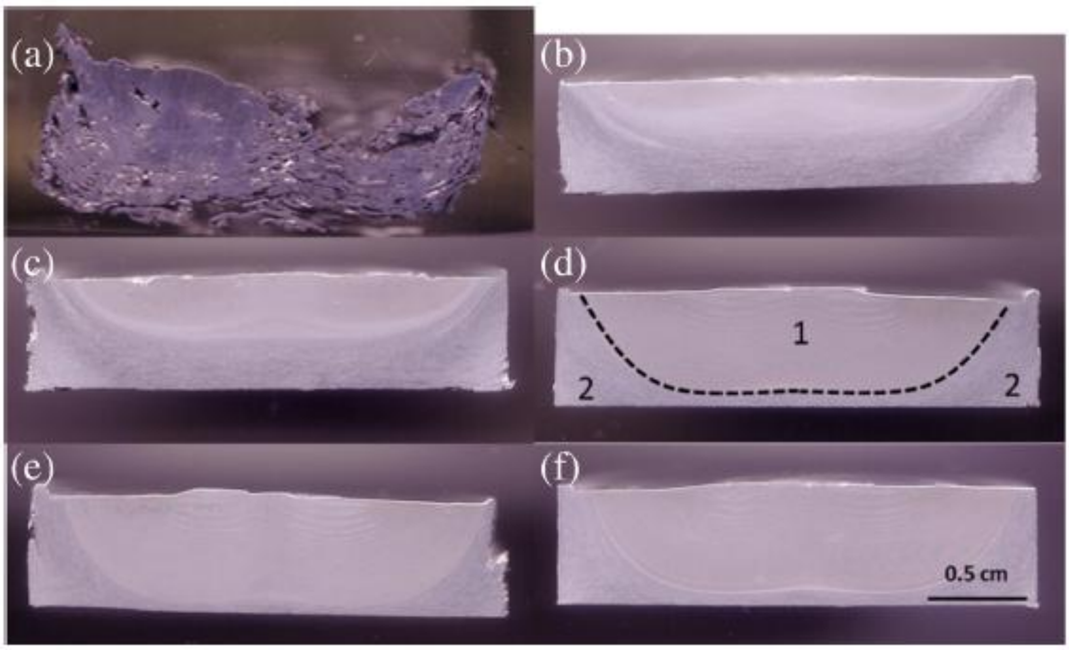

Figure 26. *Cross-sections of a series of partial consolidation discs, 300 rpm and 17.8 kN, from (a) to (f): 6.1, 12.5, 19.2, 30.9, 42.3, and 45.1 s processing time [42].*

Sectioning and analyzing the cross-sections of the sample, they noticed that the effect of the time is small when compared to high processing times because they assumed that the complete consolidation occurs at a finite processing time. Furthermore, they found that the recrystallization of the grains was in the upper part of the billet, near the contact with the tool. Moreover, they carried out a numerical analysis (Figure 27) modeling the chips as a porous billet, considering as yield surface formulation the Shima-Oyane one for porous material. Thanks to this analysis, it was possible to understand the evolution of different variables during the process.

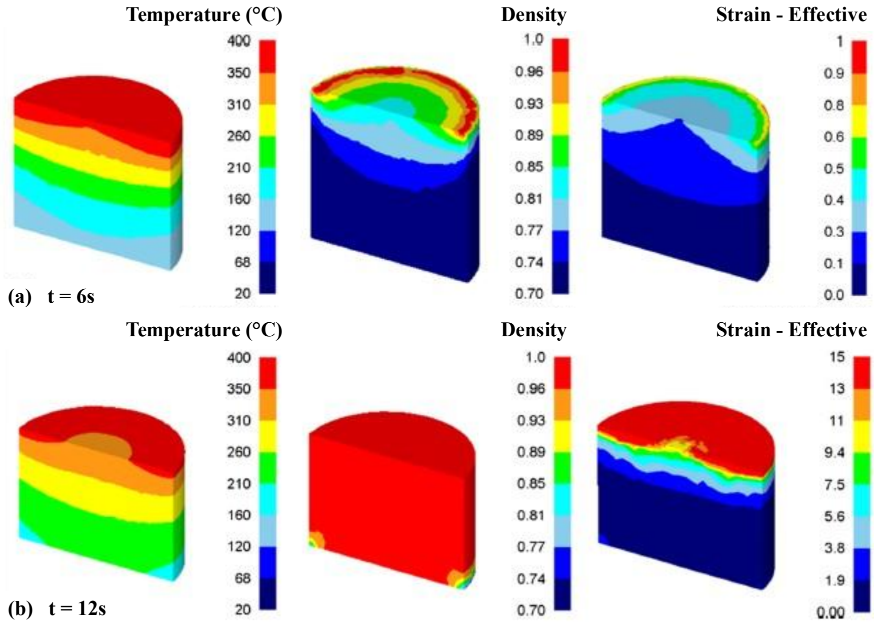

Figure 27. *Simulated temperature, density, and effective strain profile at processing time in (a) 6 s, (b) 12 s, 300 rpm, and 17.8 kN [42].*

The characterization of aluminum alloy consolidated billets through FSC processes sparked interest in much research. One of them [43] was focused on three main aspects in order to highlight products quality and the environmental impact of the process:

1. metallurgical and mechanical properties of the consolidated products.
2. primary energy demand, as compared to conventional processes.
3. forgeability of the consolidated products, as compared to the parent material.

Having a look at the first point, the authors showed that an inadequate combination of these parameters results in voids at the bottom of the billets, and finding the correct process parameters. The study of primary energy demand provided good energy consumption for the FSC process (Figure 28). In the last study (forgeability) authors found that FS consolidated parts can be directly used as input workpieces for net shape processes. In fact, they assumed that forged components were characterized by no material flow defects (Figure 29).

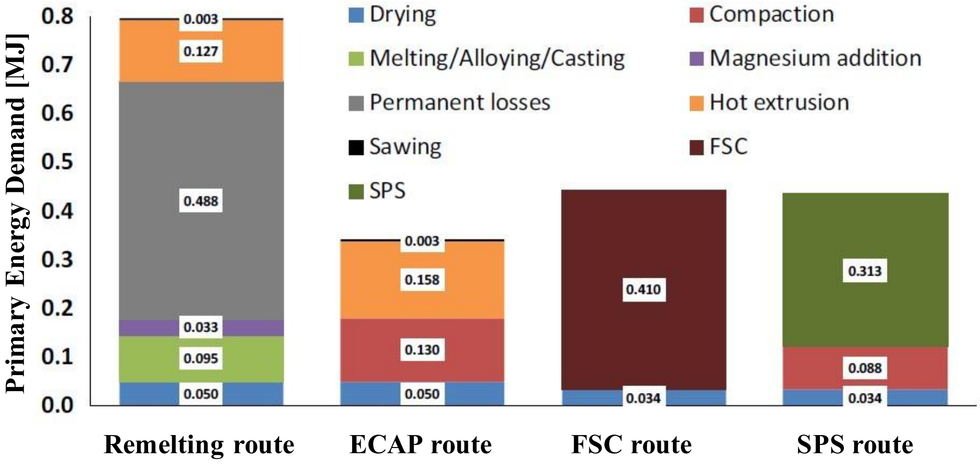

Figure 28. *Primary energy demand for different recycling routes [43].*

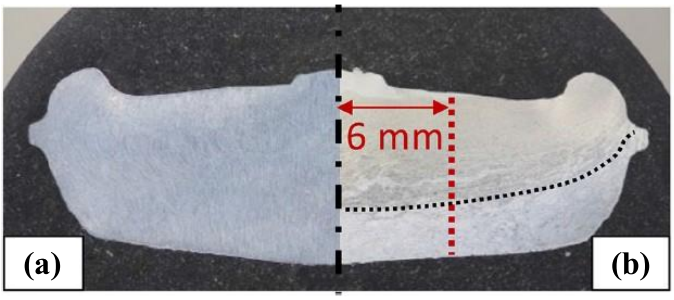

Figure 29. *Etched cross-section of forget parts: (a) parent material (PM-F) and (b) 1500-30 case study [43].*

Other authors analyzed the effects of the FSC recycling process applied to multi-material chips. Multi-material billets made of AA2011-T3 and AA7075 were realized by Latif et al. [44] varying the rotational speed and the percentage of aluminum alloy inside the billet (Figure 30). The results of this particular FSC process showed that the hardness value of the multi-material consolidated billet varied with the variation of the material position (Figure 31); there was an increasing or decreasing trend of the hardness value corresponding to the material boundary between the AA2011 and AA7075. For this reason, the authors deduced that the hardness distribution can be controlled by:

- the hardness of the starting materials.
- the material's position.
- mass fraction of each material.

Experiment ID	Rotational speed (rpm)	Process time (s)	Material on top, mass (g)	Material on bottom, mass (s)
Exp 1	1500	30	AA7075 , 5	AA2011 , 10
Exp 2	1500	30	AA7075 , 10	AA2011 , 5
Exp 3	1500	30	AA2011 , 5	AA7075 , 10
Exp 4	1500	30	AA2011 , 10	AA7075 , 5
Exp 5	1500	30	AA7075 , 15	N.A.
Exp 6	1500	30	AA2011 , 15	N.A.
Exp 7	1000	30	AA7075 , 5	AA2011 , 10
Exp 8	1500	60	AA7075 , 5	AA2011 , 10
Exp 9	1500	30	AA7075 , 7.5	AA2011 , 7.5

Figure 30. *Design of the experiments [44].*

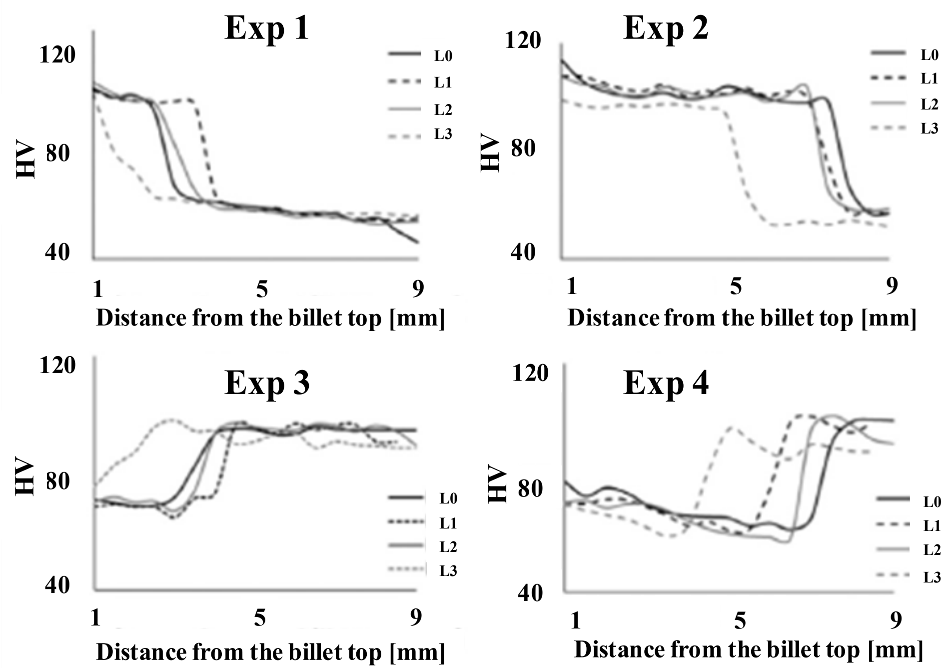

Figure 31. *Effect of material position and mass fraction on hardness value [44].*

Further analysis was carried out using the EDX mapping to highlight the material flow (Figure 32). Specifically, to map the distribution of main alloying elements across the billet section, zinc and copper were assumed to be representative for AA7075 and AA2011, respectively. In the EDX images, it was possible to notice that the upper layer of the billet was influenced by the back extrusion flow due to the small space (gap) existing between the die and tool. A numerical model was also developed to understand the effect of the gap previously announced.

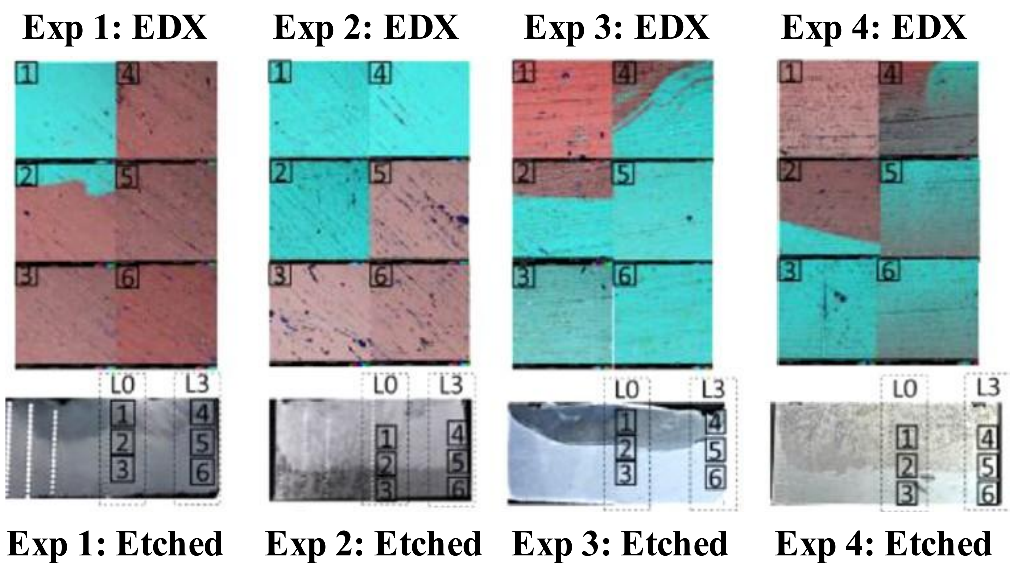

Figure 32. *EDX mapping analysis for Exp 1, Exp 2, Exp 3, and Exp 4 at the central line (L0) and near the external surface (L3) [44].*

To overcome the decreasing hardness properties, Latif et al. [45] performed a multi-step analysis creating three different methodologies: mass addiction, double-sided, and hybrid (Figure 33).

After the analysis of all the processes, the authors found that all two-step FSC methods except the hybrid method successfully led to a fully consolidated billet (Figure 34). In terms of homogeneous mechanical properties, a more uniform hardness profile was observed for mass addition that further improved with rising process parameters. A more uniform grain size distribution was noticed for the double-sided approach. Overall, the mass addition approach has the best mechanical properties and quality of billet among all FSC methods, including single-step and two-step. The mechanical properties of the hybrid approach were between those of mass addition and double-sided approaches. However, the two-step hybrid approach failed because the rough surface was a prerequisite for developing bonds between the billet of step 1 and the developing billet of step 2.

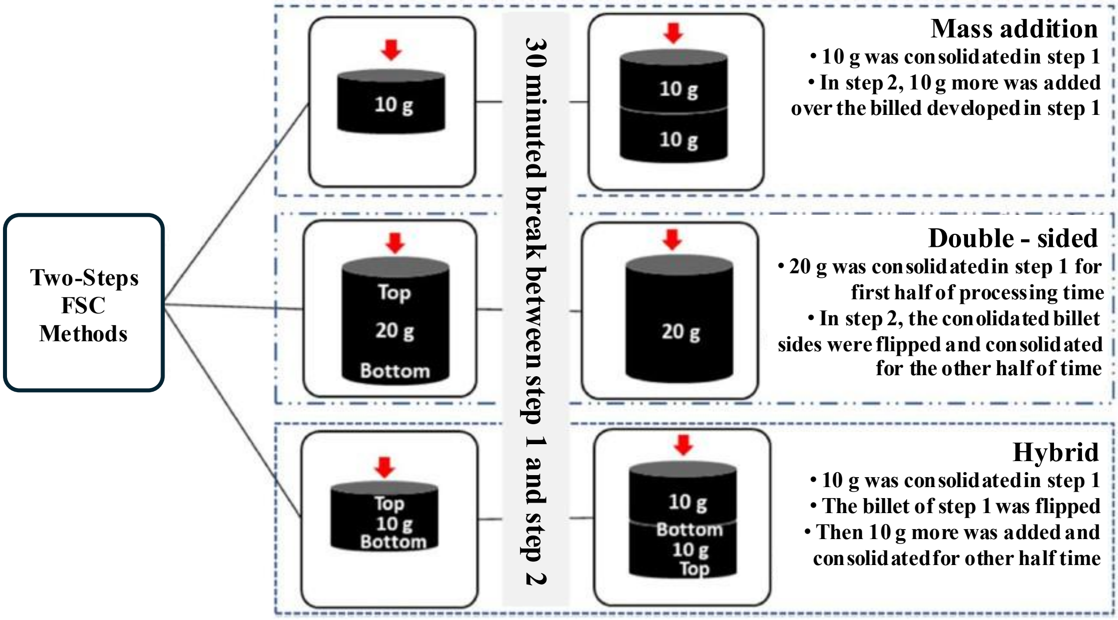

Figure 33. *Schematic of two-step FSC methods [45].*

Figure 34. *Schematic diagram for the hardness profile a) single-step, and b) two-step methods [45].*

On the other hand, this process was also used to recycle chips made of different materials. It's worth mentioning Behnagh et al. [46] who performed the FSC process using pure copper as chips material (Figure 35). Their study aimed to compare the microstructure and electrical conductivity properties of the consolidated billet with the as-received material (pure copper). Through this study, a decrease in hardness in the consolidated billet has been highlighted, while the electrical conductivity was not changed. Authors attributed the variation of the hardness value to the effect of two phenomena: the annealing softening and the grain refinement. Specifically, they assumed that the annealing softening is predominant over the grain refinement, and for this reason, the grains did not reach the size needed to increase the hardness.

Moreover, these authors developed a numerical simulation to understand FSC process details in terms of the temporal and spatial distribution of density, temperature, and strain (Figure 36).

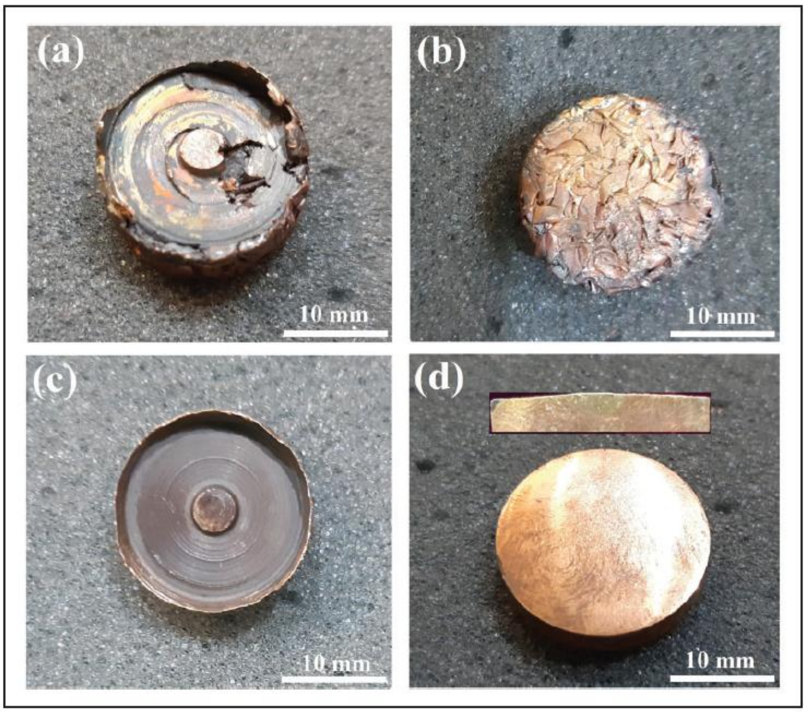

Figure 35. *Recycled sample's view: (a) top of 1200 r/min; (b) bottom of 1200 r/min; (c) top of 1600 r/min; (d) sectioned and top of 1600 r/min polished sample [46].*

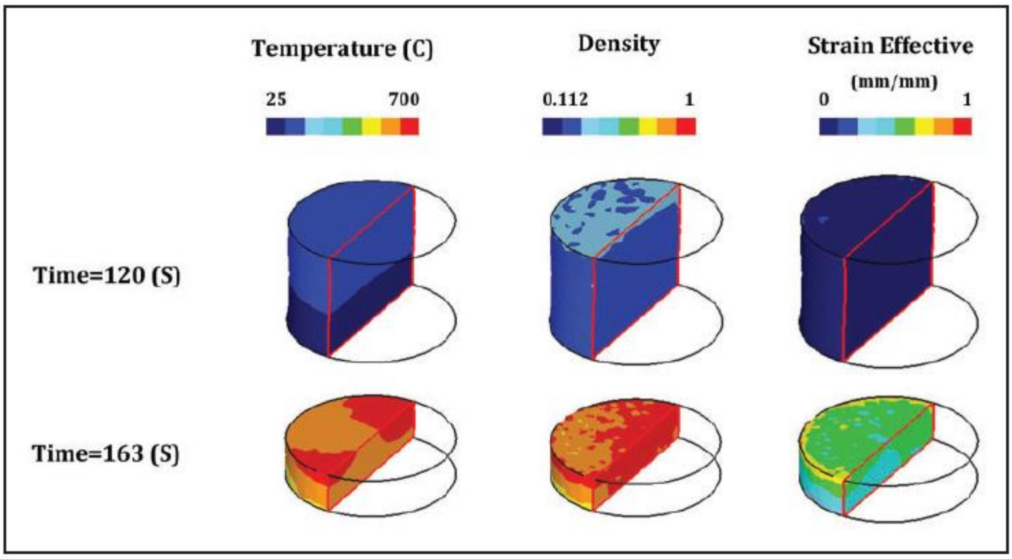

Figure 36. *Simulation results of temperature, density, and strain in different time steps [46].*

Although the friction stir consolidation technique was mainly used to consolidate metal chips and scraps, other authors focused their work on the use of different powders. It's worth mentioning Catalini et al. [47, 48] and their work on Fe-Cr-Al ferritic oxide dispersion-strengthened alloy by FSC processing. Starting with a defined set of parameters (Figure 37), they performed an analysis of the porous billet microstructure with the aim of describing the behavior of oxide dispersion and its similarities to the conventionally processed material.

Sample	Force (N)	Rotation Speed (rpm)	Die	Energy (kJ)
3371	22,240	500	flat	244
3417*	22,240	500	scroll, 4 mm/rev	837
3421	44,480	300	scroll, 7.6 mm/rev	611

*Double-sided consolidation: 392 kJ in the first processing and 445 kJ in the second processing.

Figure 37. *Processing condition for the FSC processing of Fe-Cr-Al [47, 48].*

As expected, the authors obtained an increase in grain size near the contact between the tool and the material due to the heat input (Figure 38). In contrast to the previous findings, low hardness values were observed in regions of high expected temperature and good consolidation, while high hardness values were observed in regions of low expected temperature and poor consolidation (Figure 39); they assumed this phenomenon was related to the fact that its microstructure did not completely recover from the mechanical alloying process, and for this reason, this not-processed zone has a hardness value similar to the as-received material.

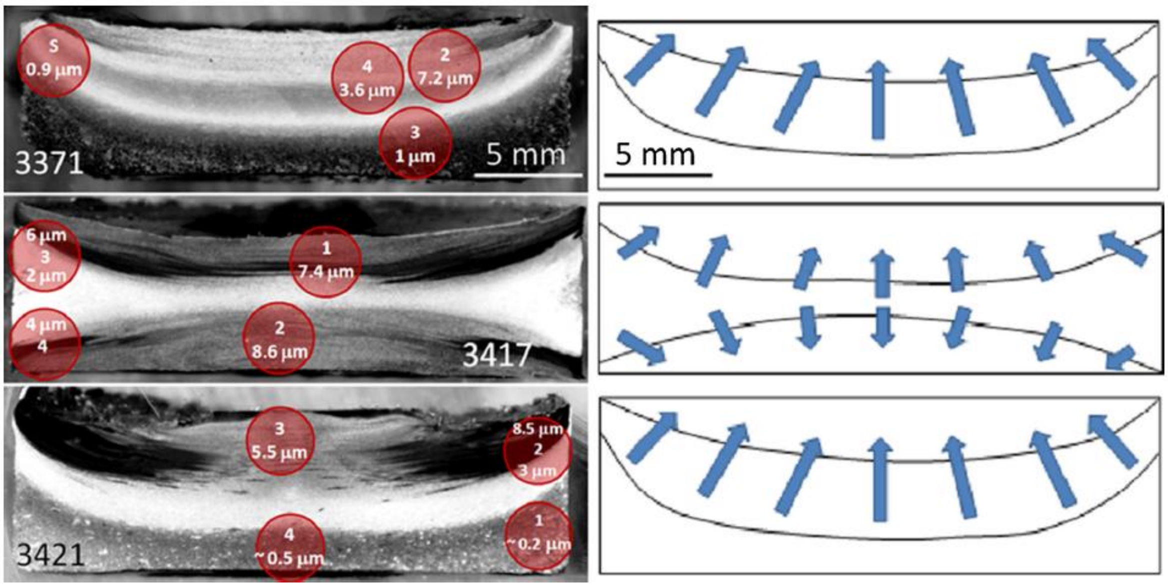

Figure 38. *Grain size measurement values at different locations in samples 3371, 3417, and 3421. Arrows indicate the directions in which grain size increased [47, 48].*

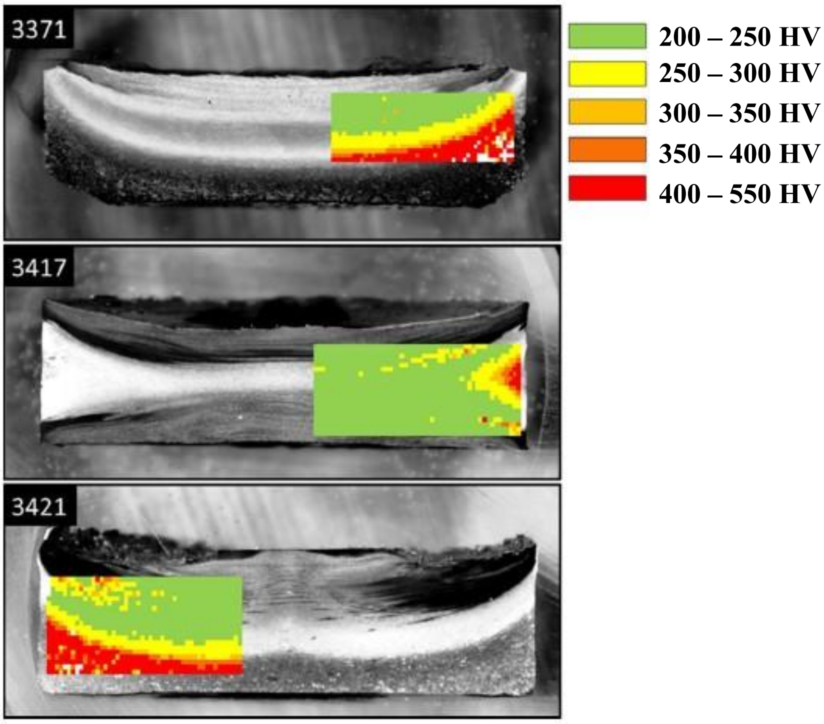

Figure 39. *Hardness maps for the three samples. Locations of higher hardness correlate to locations where lower temperatures were expected. In samples 3417 and 3421, where a scrolled tool was used, the maps show evidence of induced material flow from the walls (where the temperature was lower) to the center [47, 48].*

An analysis of the precipitate components was also carried finding that the grain size of the precipitate increased where high temperatures, material flow, and plastic deformation were expected (Figure 40); aluminum content increases as precipitates grow larger, and phase transformation tends toward $Y_3Al_5O_{12}$.

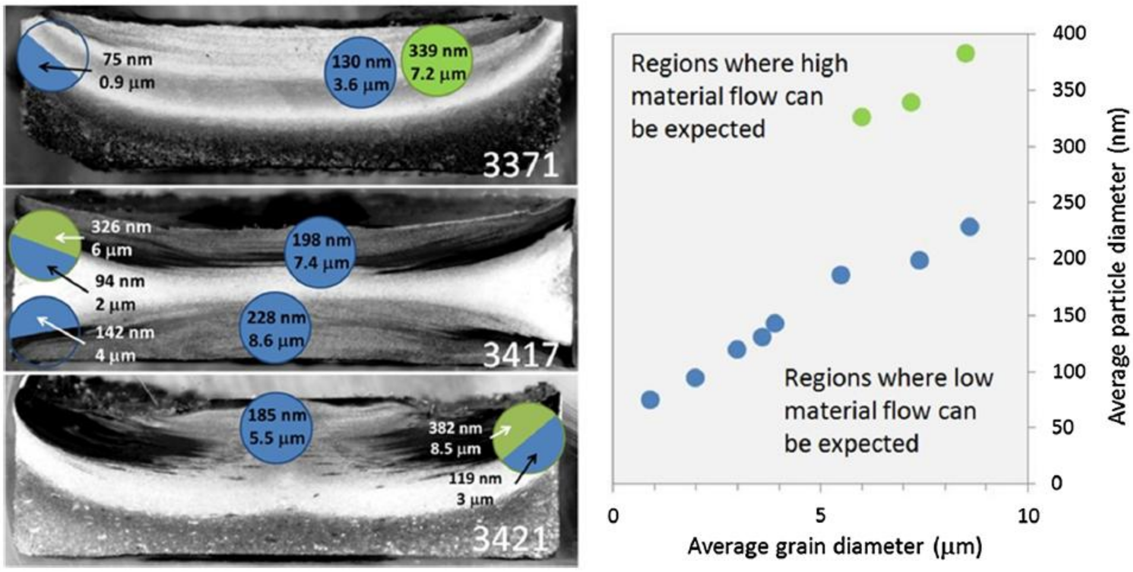

Figure 40. *Average grain diameter (lm) and average precipitate diameter (nm) in selected regions (shown at left) of the three specimens. The green dots represent locations in the disk where high material flow was expected, while the light blue dots represent locations where lower material flow was expected [47, 48].*

2.3.2 Friction Stir Extrusion (FSE)

In 1993, The Welding Institute (TWI) of Cambridge patented a new recycling process to be applied to metal chips, named Friction Stir Extrusion (FSE). This technique belongs to the Friction Stir Processing (FSP) technologies, developed following Friction Stir Welding (FSW). A rotating tool is used to produce heat and plastic deformation through friction between the tool itself and the recycling chips by compacting, stirring, and extruding the material [49]. Figure 41 shows the sketch of the friction stir extrusion process.

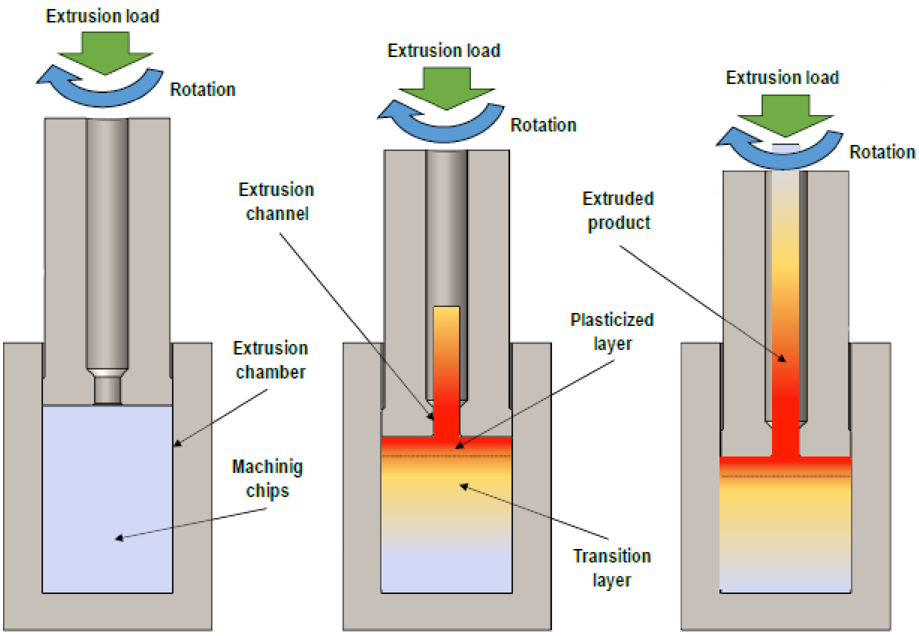

Figure 41. *Sketch of the Friction Stir Extrusion process [50].*

After the TWI patent expiration, one of the first attempts to use FSE as a recycling technique was made by Tang and Reynolds [41]. In their paper, the authors started with AA2050 and AA2195 machining chips to produce 2.5 mm wires. They found that sound wires can be produced, although higher extrusion rates must be used to increase the process's industrial appeal. Buffa et al. [51] carried out an experimental campaign on the FSE of AZ31 Mg alloy, imposing the extrusion speed through the control of the rotating tool vertical displacement. The results obtained show that the process is feasible, and mechanical resistance of about 80% of the base material can be reached. Tool rotation is a key process parameter for the effectiveness of the process. With low rotation values, corresponding to low heat input, no extrusion is obtained. On the contrary, the combination of large rotation values and high strain can result in swirl defects compromising the specimen's mechanical properties. Behnagh et al. [52] highlighted the wire defects due to both cold cracks and hot cracks occurring during FSE of AA7277 wires, 6 mm in diameter. The author also highlighted that, with proper process parameters, mechanical properties comparable to those of the parent material can be reached in the extruded wires. A scrolled face-inserted head for the extrusion of wire is shown in Figure 42.

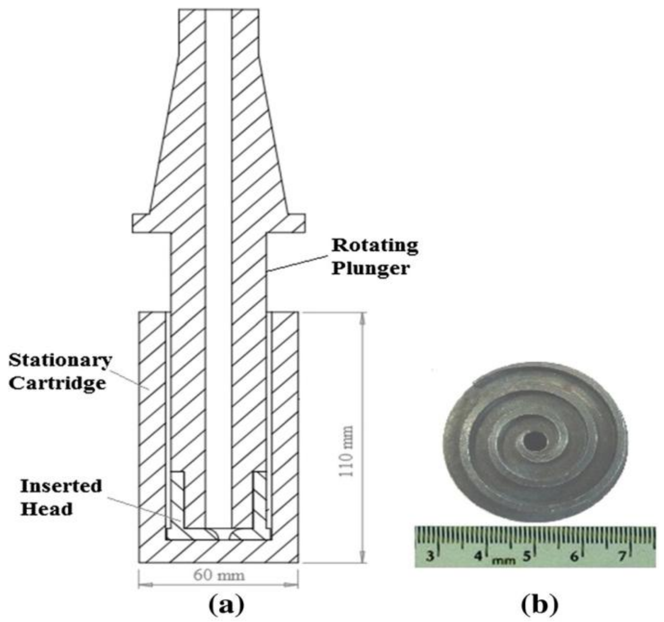

Figure 42. *(a) Schematic representation of process apparatus, (b) scrolled face inserted head [52].*

Tahmasbi et al. [53] focused on the corrosion resistance properties of AA7022 wires produced starting from machining chips. The authors found that corrosion resistance decreases as heat input, i.e., tool rotation, increases. Li et al. [54] highlighted the process mechanics of Friction stir extrusion by experimentally measuring strain and strain rate through the use of a proper marker. The results show how the process parameters influence the "deformation zone" and the "dead zone", also highlighting the complex material flow occurring during the process. Material flow and deformation zone are shown in Figure 43.

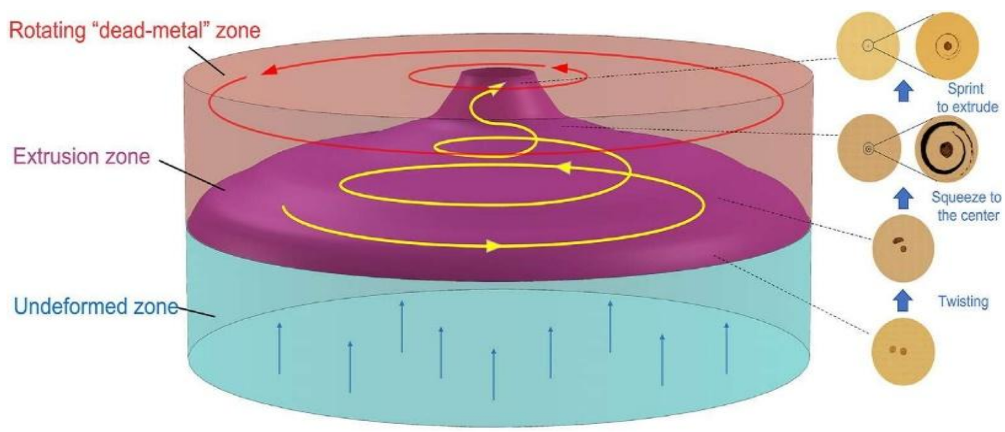

Figure 43. *(a) Material Flow and deformation in Friction Stir Extrusion. From bottom to top undeformed zone, extrusion zone, and dead-metal zone [54].*

Baffari et al. [55] have also investigated the influence of process parameters and the initial temper of the base material on the process variables and the extrudates' mechanical properties. The results show that at optimum process parameters, the produced wires have good quality and good mechanical characteristics**.** Figure 44 shows the schematic diagram of extrusion and the process parameters.

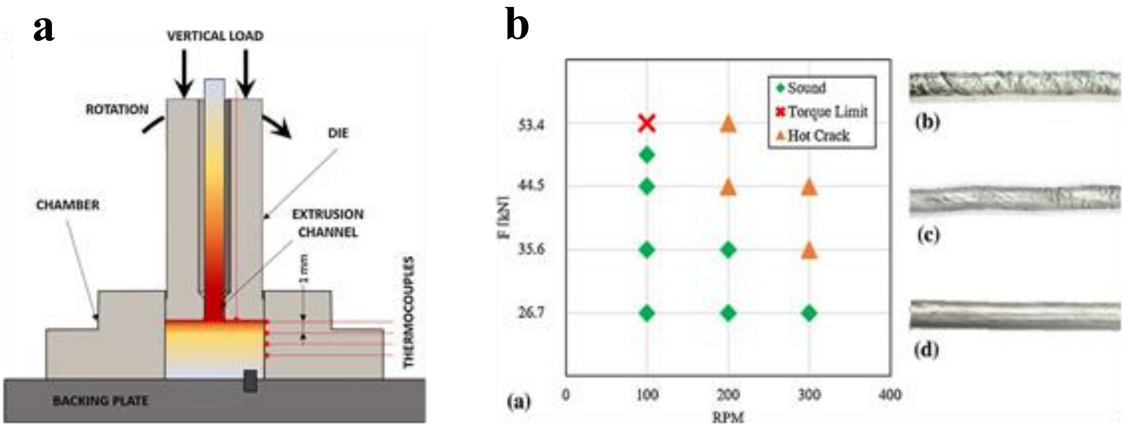

Figure 44. *(a) Sketch of the FSE setup. (b) Matrix of experiments for AA2050-T3, AA2050-T3 44.5 kN (b) 300 rpm, (c) 200 rpm, and (d) 100 rpm [55].*

Whalen et al. [56] produced aluminum rods from Al-12.4TM powder. The friction stir extrusion method was able to consolidate the power and extrude the rods all in one process. They were able to produce 5 mm diameter rods that had a higher elongation than rods of the same material that were conventionally extruded.

To measure the energy demand during the friction stir extrusion process (Figure 45), Baffari et al. [49] and Ingarao et al. [50] characterized the energy demands at various parameters. It was observed that energy demands vary with varying parameters, and specific energy consumption decreases with the increase in extrusion rate. It also revealed that FSE enables substantial energy savings, FSE allows a reduction in energy demand up to 74% and 63% concerning the conventional (remelting-based) and the ECAP routes, respectively shown in Figure 46.

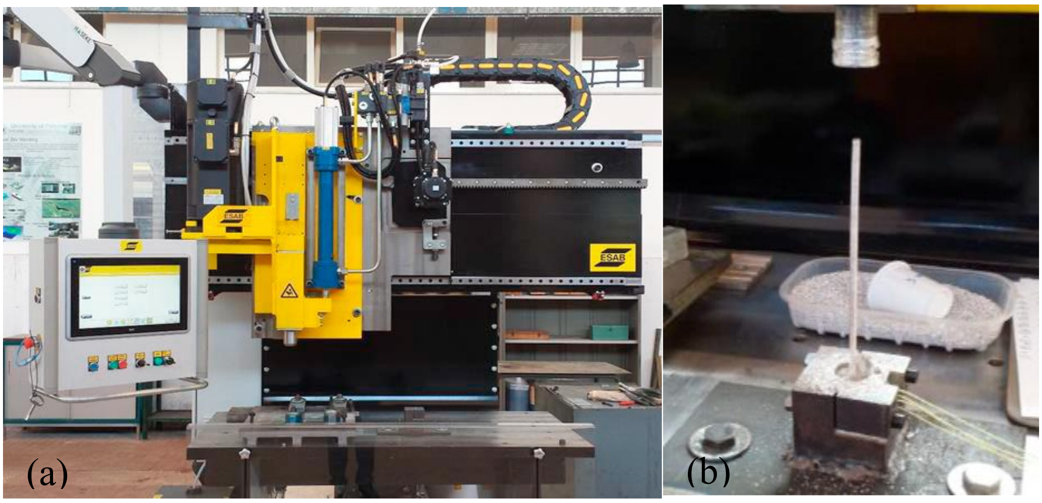

Figure 45. *(a) The used machine and (b) an example of the obtained wire [49].*

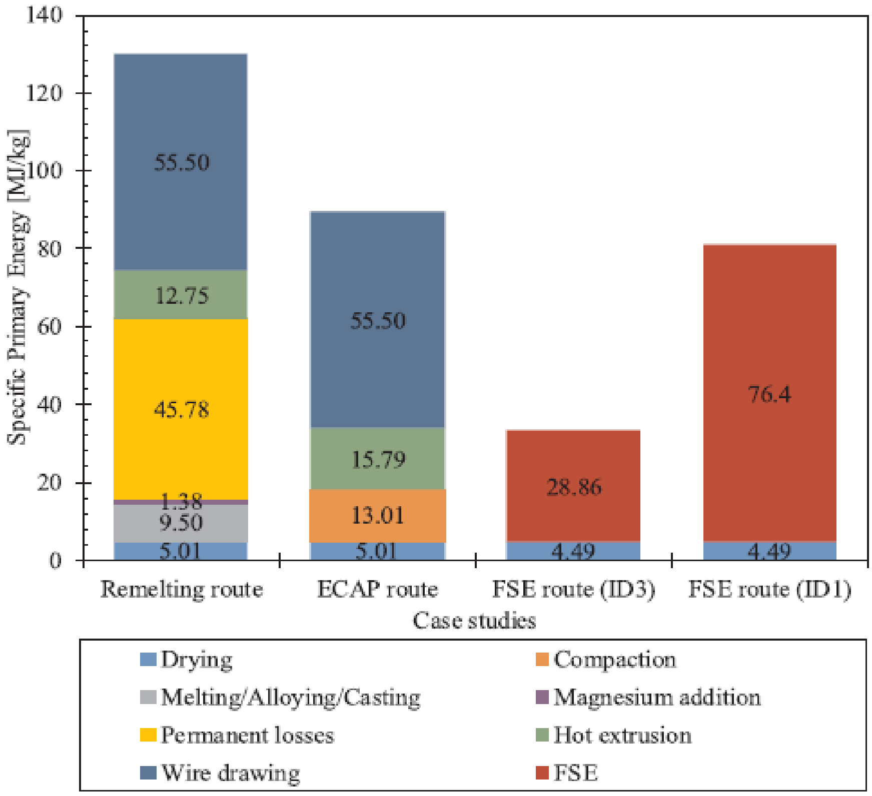

Figure 46. *Primary energy demand for different recycling routes (AA-2050 T3) [50].*

Ansari et al. [57] conducted process optimization studies using the Taguchi method on backward FSE using magnesium alloy chips. The analysis of variance shows that the RS of the plunging die is the most dominant factor in deciding the soundness of the joint, while PR also plays a significant role. The best wire can be produced by using a proper combination of process parameters. Figure 47 shows the percentage of contribution of process parameters.

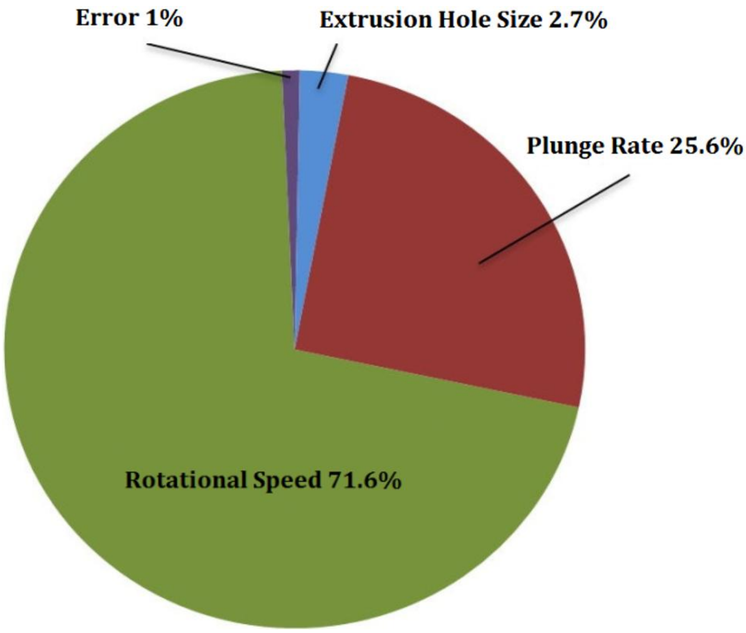

Figure 47. *Percentage of the contribution for process parameters [57].*

Behnagh et al. [58] observed dynamic recrystallized grain structure in friction-extruded wires produced from Mg chips. Compared with the plunge rate studied in this experimental analysis, rotational speed played a more significant role in heat generation and final wire properties. The microhardness of the extruded wires decreased at higher process temperatures with the increased recrystallized grain size**.** Figure 48 shows the microstructure of the wire.

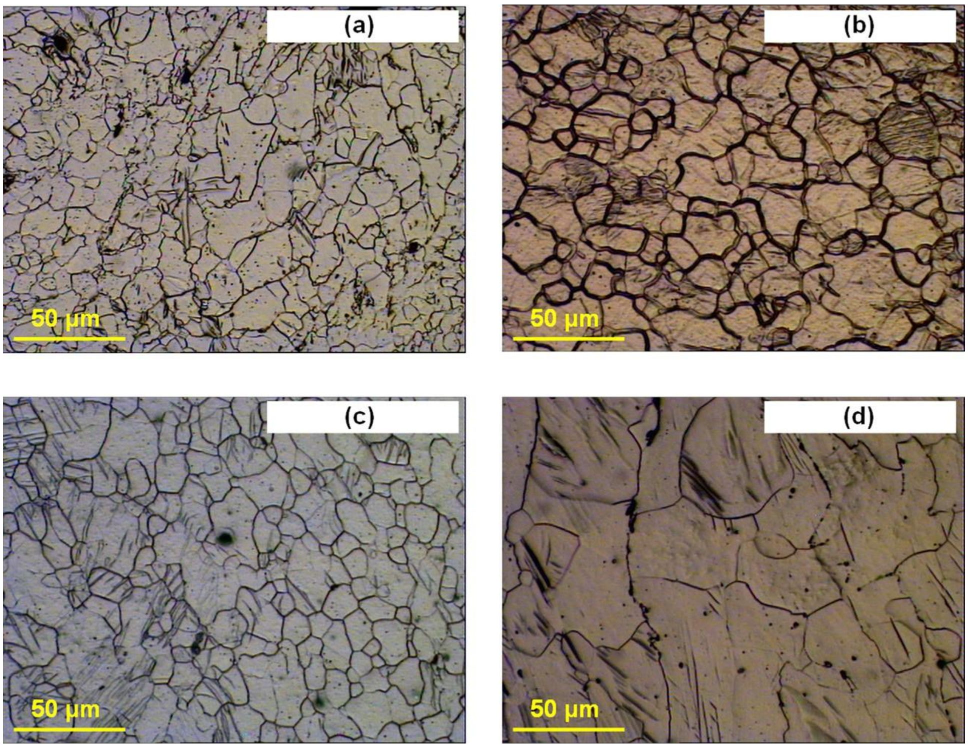

Figure 48. *Microstructures at the center of fabricated wires in different conditions: (a) F14-250 rpm; (b) F20-250 rpm; (c) F14-355 rpm; and (d) F20-355 rpm [57].*

In order to see the microstructure behavior of the friction stir extruded wire Behang et al. [59] have developed a three-dimensional finite element process model by using commercial software DEFORM 11 to predict the thermal field, mechanical deformation, and material flow during the FSE process. The author reported that the predicted grain size is in good agreement with the experimentally measured grain size. It is also worth mentioning here that grain size decreases from the center to the edge of the wire. Figure 49 shows the optical micrograph of the grain size at the center, middle, and edge of the wire.

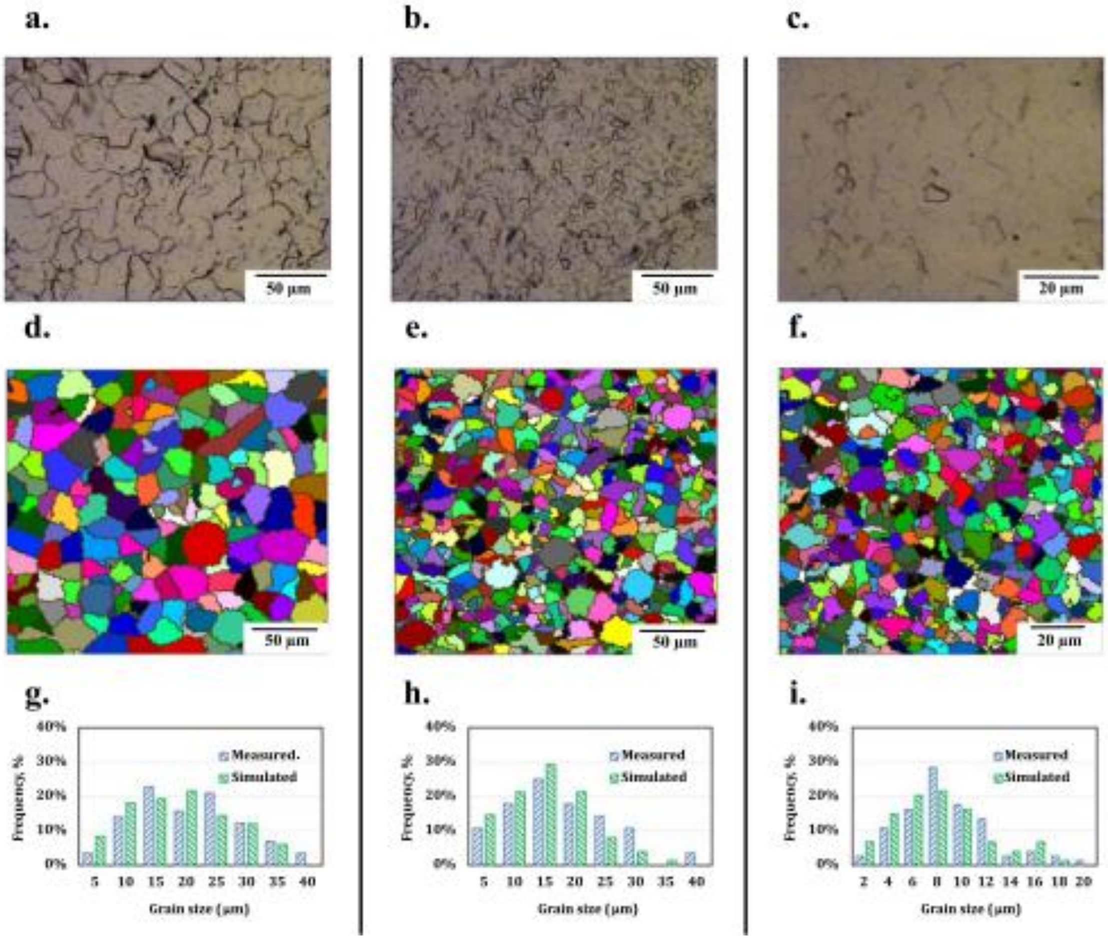

__Figure 49.__ Optical micrographs (a)–(c) and simulated microstructures (d)–(f), and comparison of histograms of experimentally measured and predicted grain size distribution for FSE process with tool rotation 250 rpm for three CA simulations (Sim. 1 at center of the extruded wire, Sim. 2 at mid region along radius of the extruded wire, and Sim. 3 at the edge area of the extruded wire) [59].

Darsell et al. [60] have studied the effect of instrument parameters and tool features on densification and microstructural evolution on ShAPE™ of AZ91E Flake. The design of the tool has been shown on Figure 50. The author reported that increasing the number of scrolls on the die face reduced the force required for extrusion, and increasing the tool rotational velocity resulted in small changes in both power and die temperature due to die and material interactions.

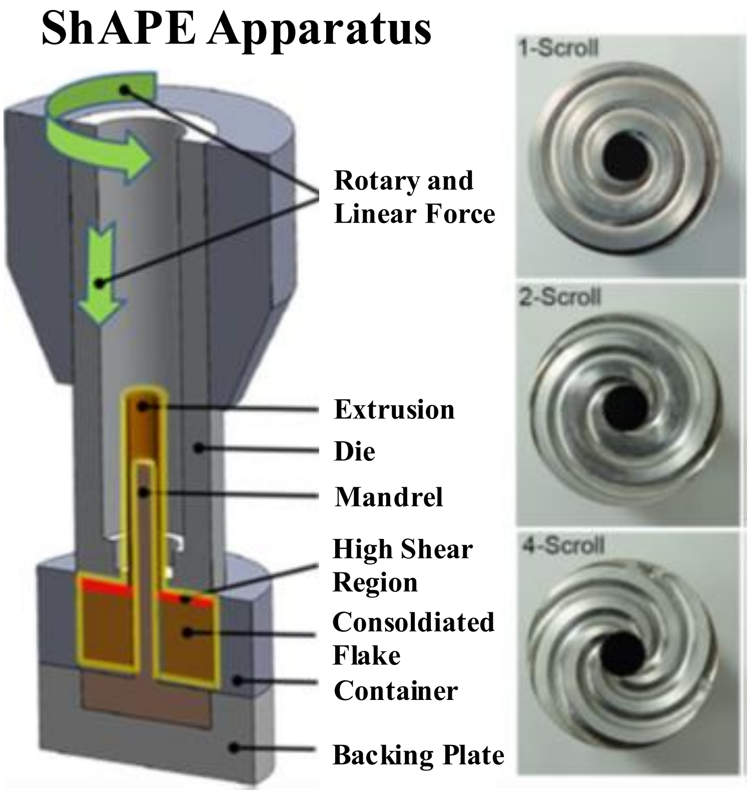

Figure 50. *Diagram of the ShAPE process and an image of the extrusion die faces used in this work. From top to bottom, the extrusion die with 1, 2, and 4-scroll patterns [60].*

As far as the numerical simulation of the FSE process is concerned, only a very limited number of papers can be found in the literature. As for Friction Stir Welding, two main approaches can be used: (i) CFD-based and (ii) solid mechanics-based. The research group guided by Prof. Reynolds at the University of South Carolina has been one of the most active in this field during the last few years. One of the first papers presenting a dedicated numerical model for FSE is the one by Zhang et al. [61]. A CFD model was proposed, able to provide insights into the complex material flow occurring during the process through the prediction of strain, strain rate, and particle path lines. Later, a thermal model was presented by the same research group to predict the evolution of temperature during the process [62] shown in Figure 51. and, finally, a comprehensive model able to consider both the evolution of temperatures and the material flow was proposed [63]. Recently, Li et al. [64] presented a smoothed particle hydrodynamics (SPH) based numerical model. The mesh-free approach, after proper validation, was used to successfully predict material flow, temperature, and extrusion forces. Figure 52 shows the point tracking of material flow.

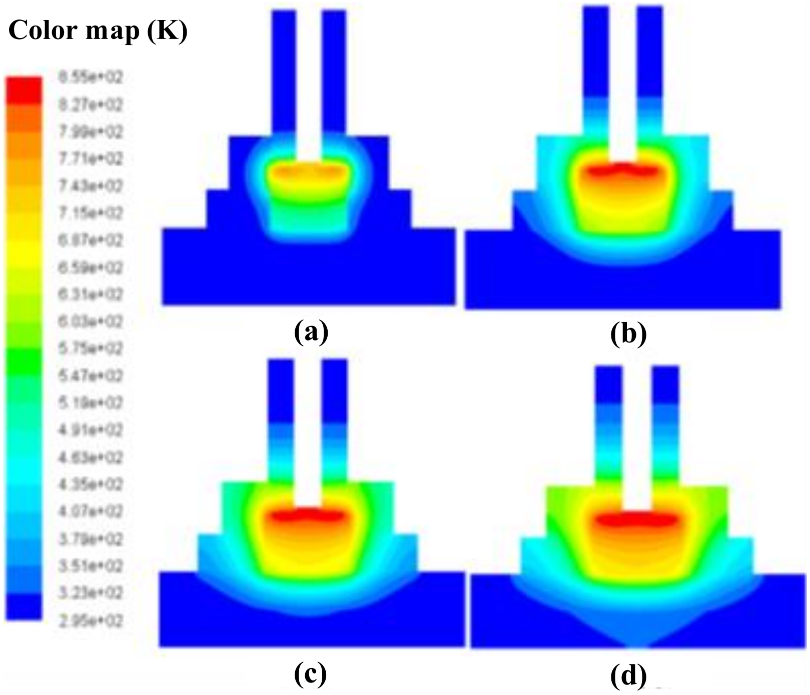

Figure 51. *Predicted temperature contours at (a) t = 7 s, (b) t = 14 s, (c) t = 21 s, and (d) t = 27.7 s [62].*

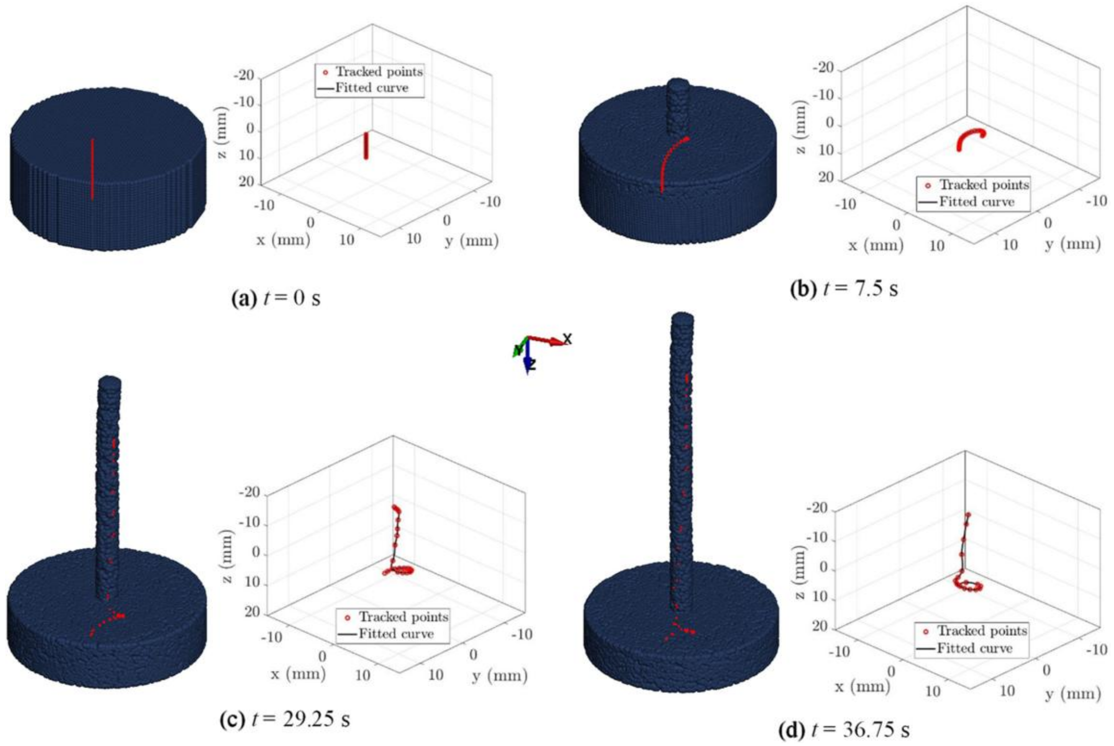

Figure 52. *Vertical point position tracking in the case of 300 rpm die rotational speed and 8 mm/min die advance speed, isometric view at a t= 0 s; b t= 7.5 s; c t= 29.25 s; d t= 36.75 s [64].*

Baffari et al. [65, 66] developed a dedicated model for FSE of Mg alloys able to predict the occurring material flow, the distribution of the main field variables, i.e., temperature, strain, and strain rate, as well as the occurrence of solid bonding as a function of the main process parameters, i.e., tool rotation and extrusion force on the tool. The author also compares the experimental results with the simulation shown in Figure 53.

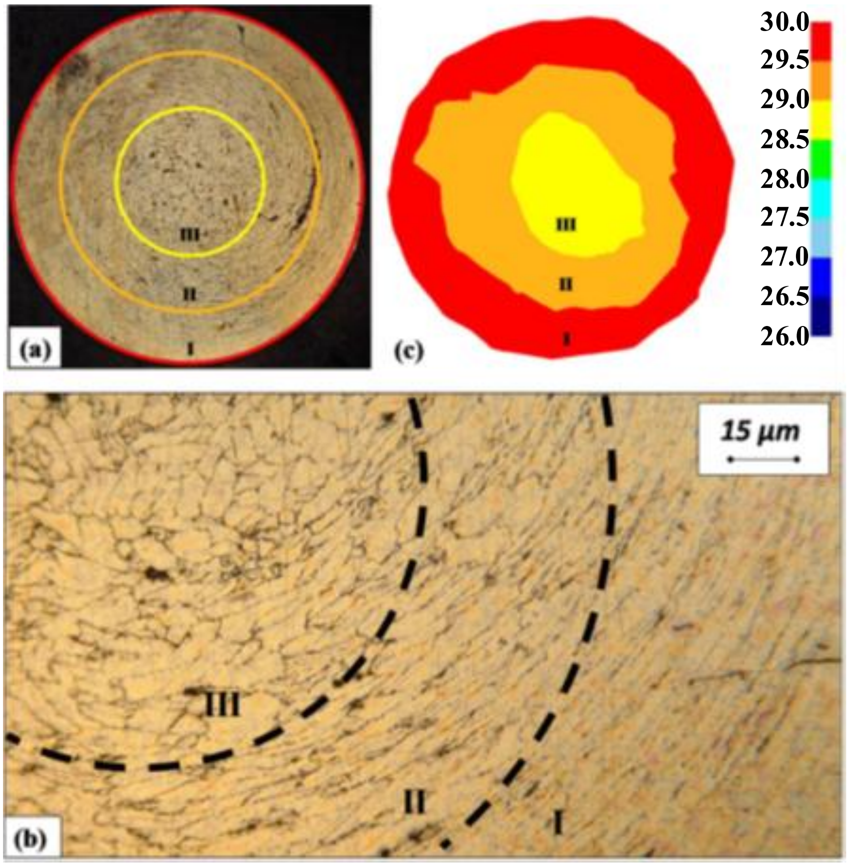

Figure 53. *Comparison between (a) and (b) experimental micrograph and (c) Zener-Hollomon parameter (ln(Z)) − R = 900 rpm, F = 14 kN, d = 5 mm [65, 66].*

Karwa [67] developed a finite element method (FEM) model in FORGENxT® for FSE, and comprehensive studies were carried out on the simulation results to analyze all aspects of the FSE process. Bocchi et al. [68] developed a numerical model for the friction stir extrusion of aluminum alloy to study the bonding condition, considering both the heat and the stresses generated at different process parameters. A combined approach involving the Finite Element Analysis (FEM) and the Piwnik and Plata criterion was used to analyze the bonding condition. The author concluded that it is possible to achieve bonding conditions that depend on both the temperature and stress conditions experienced by the scraps during the FSE process (Figure 54).

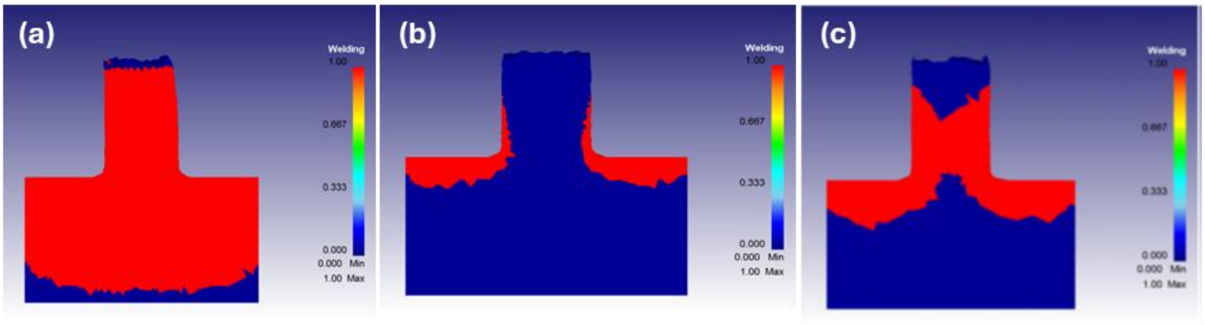

Figure 54. *Different bonding conditions: (a) Completely bonded (b) Completely not bonded (c) Limit condition [68].*

Asadi and Akbari [69] have done numerical modelling of FSBE to produce brass wire based on the Coupled Eulerian - Lagrangian technique (CEL) and verified by experiments. The effects of FSBE parameters such as tool rotational and plunging speed on the strain and temperature distributions, microstructure, and patterns of material flow have been studied. The author reported that the highest temperature and strain occur near the tool/workpiece interface, and the material flow pattern during the process is a conical helix and does not change meaningfully by the process parameters shown in Figure 55. It was also observed that at high rotational speed and low tool plunge speed result in a coarser microstructure.

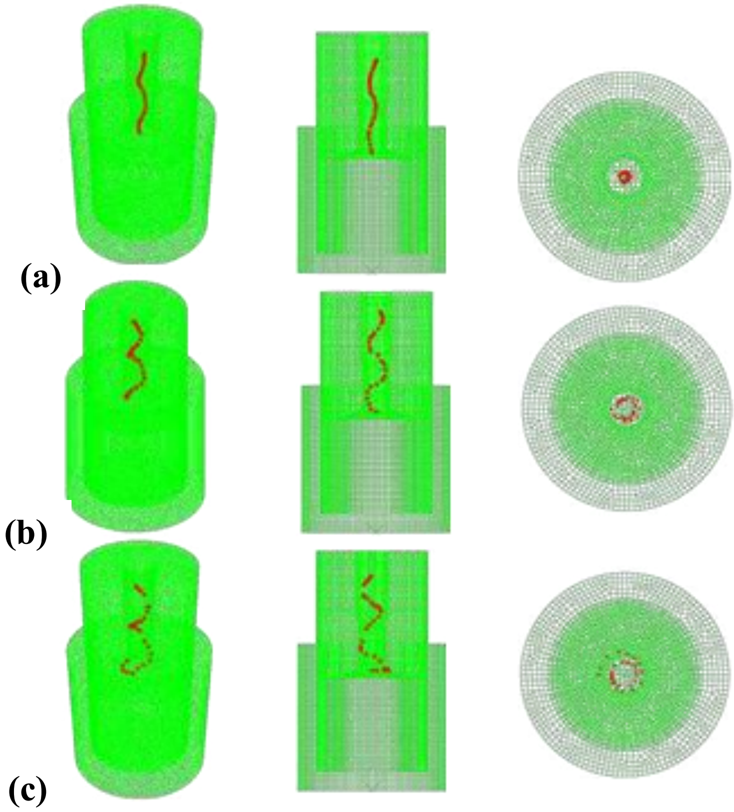

Figure 55. *The moving path during the FSBE of brass for the points at (a) 1 mm, (b) 3 mm, and (c) 5 mm distance from the central axis [69].*

2.3.3 Continuous Friction stir Extrusion (CFSE)

Friction stir extrusion is an innovative direct recycling technology developed for metal recycling chips, but presents a limitation due to the discontinuity of the process caused by the limited extrudate volume of the chamber. The first attempt to propose a continuous solid-state extrusion process concept is reported by Widerøe et al. [70] but this machine was used for the extrusion of the polymer. To overcome these limitations of discontinuity in FSE and to recycle the light metal, continuous friction stir extrusion machines have been designed by Baffari et al. [71]. The design of the continuous friction stir extrusion machine has been shown in Figure 56. The author has described and analyzed the design challenges for continuous friction stir extrusion machines by using both experimental and simulation analysis. Through this process, the wire produced from the recycled scrap will be used as filler wire for the additive manufacturing process, which can lead to obtaining 100% of the material used within the same production plant.

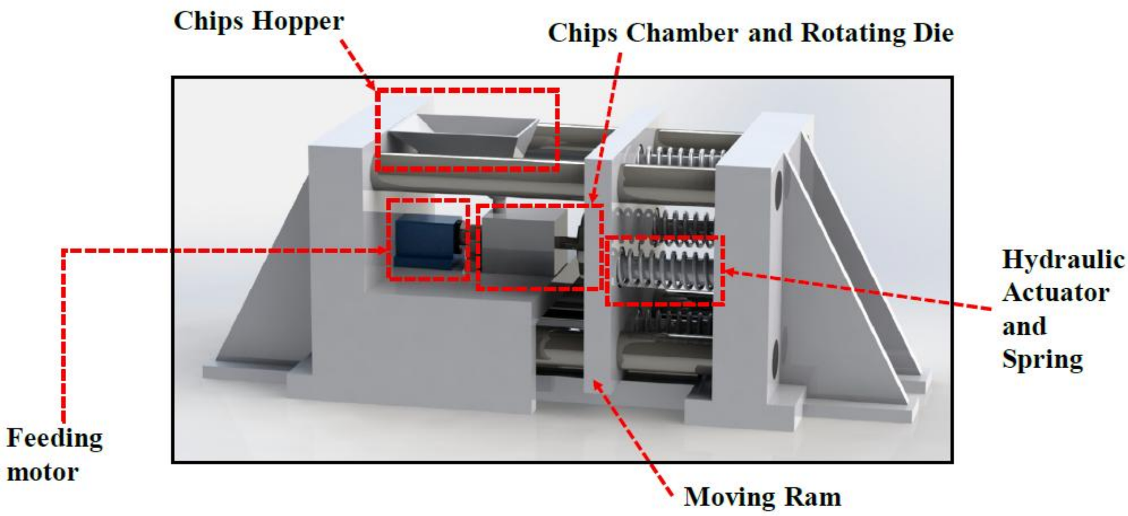

Figure 56. *CAD of the proposed CFSE Machine Design [71].*

For the continuous extrusion process, the optimum design of the extrusion tool is a key factor. Buffa et al. [72] have designed and developed a new machine tool for the continuous extrusion process. Lagrangian implicit thermomechanical numerical model has been used to determine the proper ranges of the most relevant process parameters. Figure 57 shows the physical and numerical model of the CFSE Machine.

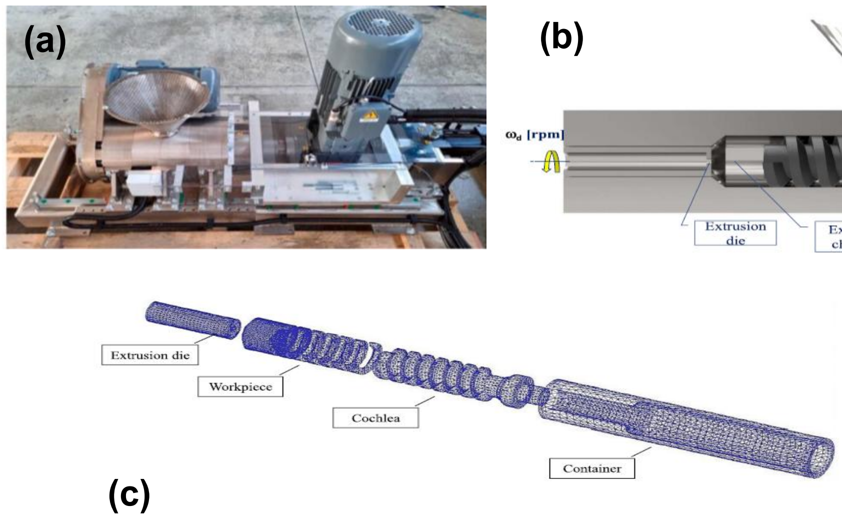

Figure 57. *(a) CFSE physical machine (b) The CFSE process (c) The CFSE numerical model [72].*

In another publication Buffa et al. [73] have created the numerical model of continuous friction stir extrusion based on the experimental results obtained. The author presented the setup of machine tools and the experimental findings of case studies. The author also reported the flow of the material using point tracking, shown in Figure 58.

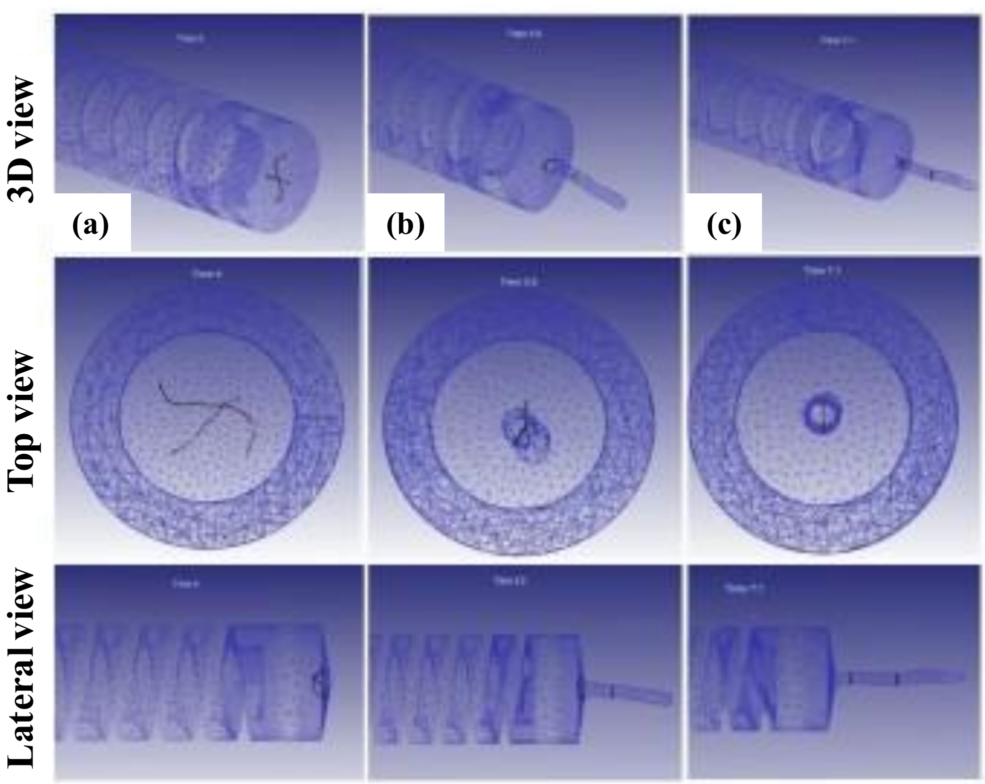

Figure 58. *Point tracking positions in three different steps: (a) initial, b)-c) out of the extrusion channel at different times – R = 900 rpm, F = 22 kN [73].*

Recently, Gumaste et al. [74] introduced innovative continuous friction stir technology named solid stir extrusion, where wire has been used as a raw material instead of chips used in the conventional FSE process. In this process, the die has an opening on the top through which a retractable tool rotating at a specific rotation rate is inserted. The feedstock pushed from either side engages with the rotating tool. The contact between the feedstock and tool generates heat and softens the material. By leveraging frictional heat produced with the rotating tool, the feedstock material is sheared, which undergoes severe plastic deformation. The spiral features on the tool exert a downward force on the soft deformed material, which gets extruded downwards. The author reported that in this process, continuous extrudates of the desired diameter can be obtained, and the quality of the extrudates has been improved. The conceptual model of the solid stir extrusion is depicted in Figure 59.

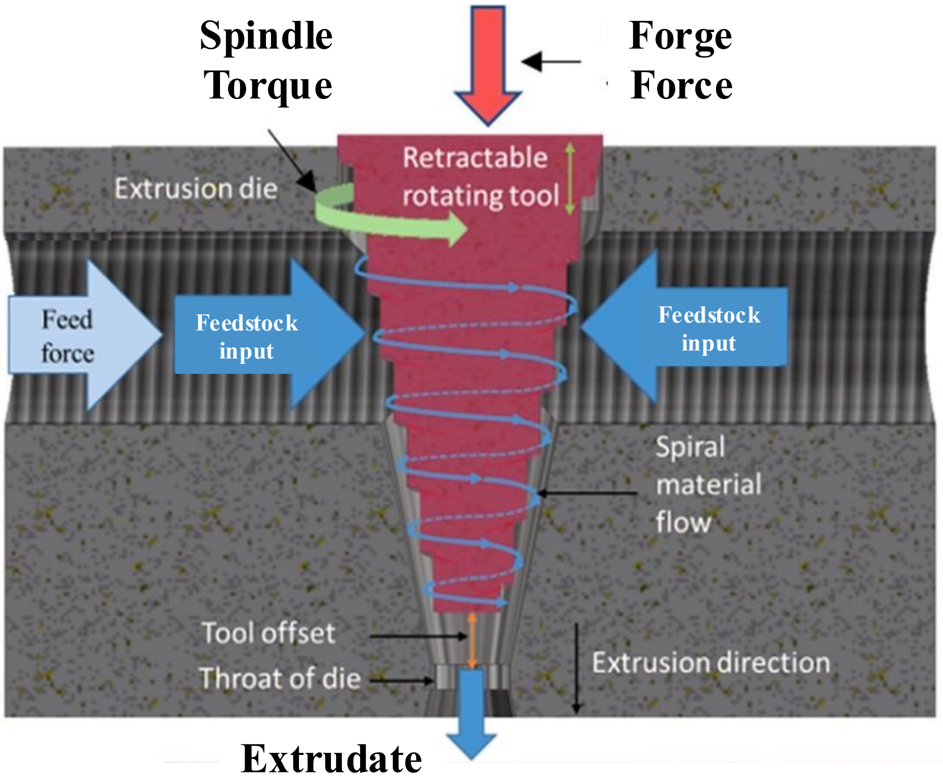

Figure 59. *Schematic of Solid Stir Extrusion process [74].*

3 Literature gap and aim of the research

In this chapter, the aim of the research will be discussed, addressing four research gaps identified in solid state recycling via friction stir-based technologies:

1. Ineffective solid bonding prediction in FSC processes.
2. Characterization of mechanics in FSC processes.
3. Suitability and sustainability of FSE in tube manufacturing.
4. Discontinuous behavior of FSE processes.

Concerning the solid bonding criteria, basically, two kinds of solid bonding modelling exist: the energy barrier and the film theory formulation. The first approach proposes a threshold value as a measure of bonding occurrence; the threshold is calculated by analytical formulations of stresses and/or strain cumulative values. One of the first implementations of the energy barrier modelling was presented by Akeret [75], who defined the critical value as the ratio between the normal pressure and the flow stress of the material evaluated during the process. The first modification of this approach was proposed by Plata and Piwnik [76], who proposed to integrate over time the Akeret model. These first formulations were applied to model the solid bonding occurring in the porthole die extrusion process. A further modification of this criterion was proposed by Donati and Tomesani [77]; they included in the formulation the local velocity to improve the bonding prediction in the dead zones of an extrusion process. Ceretti et al. [78] proved that the Plata and Piwnik criterion threshold value decreases with increasing temperature. Guley et al. [79] improved the Donati and Tomesani formulation by considering the effect of the shear stress as a trigger for the bonding occurrence. The authors identify a shear stress threshold ensuring the oxide layers between chips are broken. The authors implemented this new approach to the porthole die recycling of aluminum alloy chips. Baffari et al. [80] applied the conventional Plata and Piwnik criterion to model the bonding of AZ31 magnesium alloy chips when they are processed by FSE. On the other hand, the film theory proposes the concept of oxide film breakage to motivate the solid bonding. In other words, the bonding occurs when the oxide layer covering the material is broken, allowing the metal-to-metal surface contact. The first investigation in this concern was carried out by Bay [81] who outlined the main aspect characterizing the solid bonding occurrence: local oxide layers breakage enabling metal micro extrusion that activates material solid bonding. Cooper et al. [82] improved the formulation considering the oxygen captured in the material cavities and applied this approach. Kolpak et al. [83] adapted the Cooper and Allwood model [82] to the case of aluminum alloy chip recycling by porthole extrusion process. The model they proposed allowed the quality of the chips' bonding to be evaluated with varying geometrical and process parameters. Recently, Cooper and Oberhausen [84] have extended the film theory of solid-state welding to consider non-plane strain deformations at the billet-billet interface for modelling the transverse welding in aluminum extrusion.

All the criteria mentioned here were primarily developed for traditional manufacturing processes, and only a few of them address recycling-oriented applications. In addition, the literature review reveals that their formulation depends on specific process mechanics and therefore they are normally adapted only to the analyzed process.

For this reason, the present research aims to propose a new solid bonding criterion capable of modeling and predicting bonding occurrence in solid-state recycling processes, such as friction stir consolidation and friction stir extrusion. Furthermore, the development of this tool was extended to different aluminium alloys to demonstrate the versatility of the criterion.

The investigation of FSC also highlighted another gap in the literature: insufficient process investigations. Specifically, only a limited number of papers deal with FSC processes and with process dynamics, and additionally, the key factors governing sound bonding are still insufficiently investigated. An example is the study performed by Tang and Reynold [85] where a lack of consolidation was found in the bottom corner of the billet (far from the tool action) due to high heat conduction.

In this context, the second goal of this research was to identify the main variables responsible for proper bonding occurrence and to design a new setup capable of overcoming the common issues observed in FSC processes.

Among the friction stir-based technologies, FSE has been commonly applied for wire extrusion from recycled chips, but its potential for tube manufacturing remains poorly explored. Lots of papers propose two-step approaches or produce tubes from bulk materials, limiting the sustainability of the process. Therefore, as a third objective, this study also aims to demonstrate that FSE can be effectively employed for tube production from machining chips by a single direct step, highlighting its environmentally sustainable characteristics compared to conventional extrusion routes.

Finally, the literature review revealed a common drawback among most papers dealing with scrap recycling via friction stir-based techniques, namely, discontinuity of the process. In this regard, the last goal of the research was to develop a dedicated machine for continuous/endless wire production through chip recycling, identifying the optimal process parameters for manufacturing sound consolidated wires.

3.1 Overview of experimental and numerical campaigns

The research gaps identified in the previous sections were addressed through a combination of experimental and numerical investigations. Regarding the experimental campaigns, the FSC process was studied using an ESAB LEGIO machine, while the FSE process was analyzed employing both an ESAB machine and a prototypal continuous machine.
Although FSE and FSC share the same process setup (Figure 60), the tool geometry differs. In the FSC process, the tool is a solid cylinder with a diameter equal to the die hole. On the other hand, in FSE, the tool either includes a central hole serving as the extrusion channel for wire production or has a diameter quite smaller than the die one, so the tool–die clearance acts as the extrusion channel during wire or tube manufacturing.

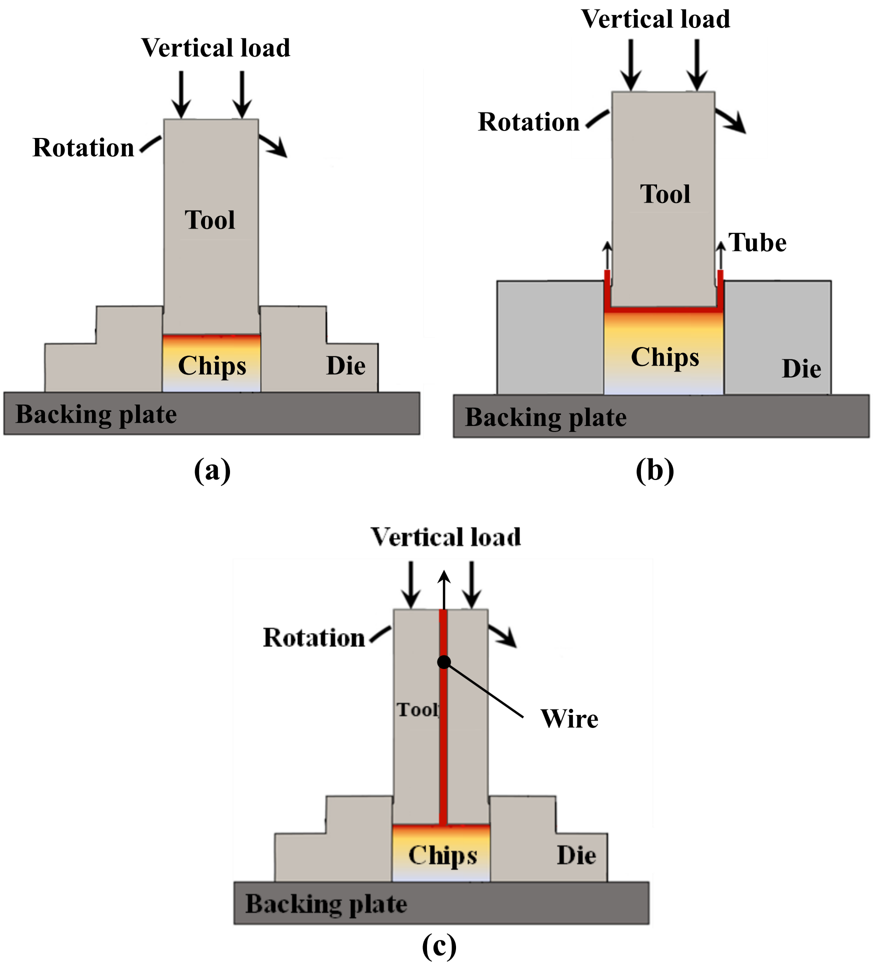

Figure 60. *Schematic setup for (a) FSC, (b) FSE of tube, and (c) FSE of wire.*

The workflow for both processes follows the same main step:

1. Die filling with aluminium chips, which are pressed with a specific load (ensure the complete filling).
2. Process starting (activating tool rotation and vertical load).
3. Material consolidation (billet for FSC) or extrusion (wire or tube for FSE).
4. Process ending (consolidated product removal).

Depending on the case study, the pressing load (Step 1) and the process starting conditions (Step 2) were subjected to slight variations. In general, at the beginning of Step 2, the process starts with a 5 kN vertical load and the selected rotational speed. After a few seconds, the vertical load is increased at a rate of 0.5 kN/s until the target value is reached. A detailed description of the experimental campaigns for each research topic is provided in Chapter 4.

It is worth remarking that there is an important issue in these techniques due to the discontinuity of the processes. In fact, once the die is filled with a certain amount of aluminium chips, and the consolidated product is formed and removed, the die must be refilled before restarting the process. This discontinuous behavior affects the overall productivity, especially when considering industrial applications. To overcome this limitation, a continuous machine (Figure 61) was developed. This machine takes advantage of an endless screw (cochlea), which continuously feeds the die. Specifically, the scraps are introduced through the hopper and pushed forward thanks to the rotational speed of the cochlea. The material dragged by each filet of the cochlea pushes the material in the extrusion chamber in contact with the tool, giving the proper pressure for extrusion.

Thanks to this design, the main limitations of conventional FSE processes were effectively solved (for more details, see Chapter 4.8).

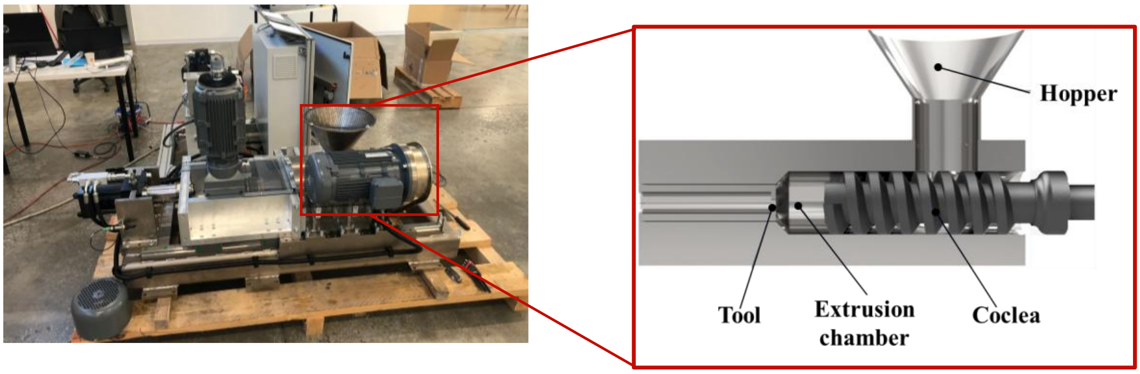

Figure 61*.Continuum friction stir extrusion machine and 3D CAD of the machine [72] .*

In this thesis, numerical simulations were adopted for studying the FSC and FSE processes, giving an insight into the variable evolutions and material flows. Moreover, numerical simulations were used to justify major assumptions that arose during the interpretation of experimental results.

The software used in this thesis was mainly the commercial software named SFTC DEFORM 3DTM. The numerical simulation of the friction-based processes consisted of three components for FSE, namely tool, die, and chips (Figure 62a, c), while four components for FSC, namely tool, die, backing plate, and chips (Figure 62b). Because modelling every single metal scrap results in computationally heavy and complicated, the chips batch inside the die was usually modeled as a porous cylinder using the Shima and Oyane [86] formulation. The relative density of the porous billet was calculated experimentally and used in numerical analysis.

The number of nodes (or the mesh size) used for the characterization of the porous billet, as well as for the other component, was selected based on the recycling process. Lastly, the tool, as well as the die and the backing plate, was considered a H-13 steel rigid component. It is worth remarking that, for characterizing the material, the stress formulations were directly selected from the DEFORM library, after double-checking and comparing them to the ASM books. The thermal coefficients, such as specific heat capacity and conductivity, were instead selected from online databases. Proper material characterization is essential for solid bonding studies because they mainly rely on material flow and effective stress. Inaccurate material behavior modeling can compromise the effectiveness of the bonding calculation. A selected friction shear factor was used to model the contact between rigid bodies and aluminium material, along with the heat transfer coefficient. The thermal coefficients employed in numerical simulations were given by tuning works between numerical and experimental data. To be more specific, a thermocouple was located close to the material, aiming to acquire the evolution of the temperature during the process. This temperature profile was then used as a benchmark for the numerical temperature profile.

In this tuning process, the interface heat transfer coefficient (IHTC) and the shear value were varied, aiming to match the numerical temperature profile with the experimental one. Once the two profiles were correctly overlapping, the shear and heat coefficients were noted and used for running the final simulations. Although two or more thermocouples may increase the accuracy of the results, only one thermocouple was adopted for the validation of the models presented in this dissertation, mainly because the symmetry and simplicity of these processes made this method (single thermocouple) highly representative of the experimental results. Results of these validations will also be presented in Chapter 4.

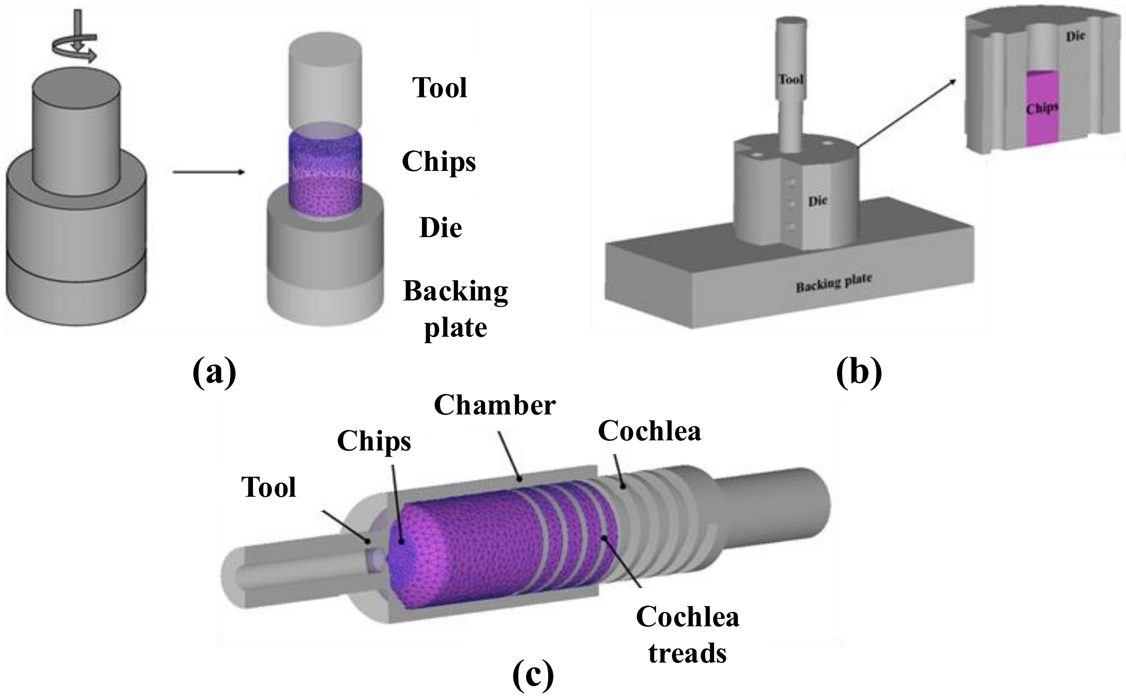

Figure 62. *(a) Numerical simulation setup for (a) FSC process, (b) FSE of tubes process, and (c) CFSE process [87].*

4 Answers to research questions

In this chapter, the published and ongoing research will be presented, and the research questions addressed by a concise description of both experimental and numerical results.

4.1 Design of a numerical solution for solid bonding occurrence prediction in FSC processes

In this chapter, different research questions such as "*What are the limitations of the existing criteria?*", "*Are they suitable for friction stir consolidation (FSC) processes?*" were addressed to demonstrate the effectiveness of a new solid bonding criterion here proposed, and the lack of effective criteria designed for the FSC process. Specifically, selected solid bonding criteria, available in literature, were tested in FSC processes along with two new criterion formulations. All the criteria selected are listed in (Table 6).
In this research, the first approach to research questions regarded the FSC of AA7075 aluminium alloy, then the developed model was tested and validated on three other aluminium alloys, namely AA2024, AA6082, and AA5083 (Chapter 4.2).
Note: the images reported in this chapter are taken from the following published work [88].

Table 6. *Bonding criteria equations and ID reference.*

ID	Criterion	Literature equation	Adopted equation
C1	*Akeret (1992)*	$W_{C1} = \frac{p}{\sigma_f}$	$\frac{\lvert\sigma_{mean}\rvert}{\sigma_f}$
C2	*Plata and Piwnik (2000)*	$W_{C2} = \int \frac{p}{\sigma_f} dt$	$W_{C2} = \int \frac{\lvert\sigma_{mean}\rvert}{\sigma_f} dt$
C3	*Donati and Tomesani (2004)*	$W_{C3} = \int \frac{p}{\sigma_f} dt \cdot v$	$W_{C3} = \int \frac{\lvert\sigma_{mean}\rvert}{\sigma_f} dt \cdot v$
C4	*Kolpak et al. (2019)*	$W_{C5} = \frac{\sigma_{b.n}}{\sigma_f, n} = max\left(\frac{\sigma_{b,i}}{f, i}\right)$	$W_{C4} = \frac{\lvert\sigma_{mean.n}\rvert}{\sigma_f, n} = max\left(\frac{\lvert\sigma_{mean,i}\rvert}{\sigma_{f,i}}\right)$
C5	*Plata - Piwnik – Weighted*	Here proposed formulation	$W_{C5} = w_t \cdot w_s \cdot \int \frac{\lvert\sigma_{mean}\rvert}{\sigma_f} dt$
C6	*Plata - Piwnik – Zener*	Here proposed formulation	$W_{C6} = \begin{cases} 0 \quad , & T < 480 \\ \int \frac{\lvert\sigma_{mean}\rvert}{\sigma_f} \cdot \frac{1}{z} dt, & T \geq 480 \end{cases}$

Note: Plata – Piwnik [s], Donati - Tomesani [mm], Plata – Piwnik – Weighted [s], Plata - Piwnik – Zener [s^2].

4.1.1 Experimental methodology

A friction stir welding (FSW) dedicated machine (ESAB LEGIO 3ST, Figure 63) was adapted for performing friction stir consolidation. The starting material was an aluminum alloy AA7075 sheet with a thickness of 3 mm. The aluminum sheet was reduced into chips through a milling operation (Figure 64) with details listed in Table 7.

Table 7. *Details of the milling process for chips preparation.*

Process	Tool	Number of teeth	Rotational speed [RPM]	Feed rate [mm/min]	Depth of cut [mm]
Milling	BDMT11T308ER-JT PR1225	3	1250	280	1

For effective cleaning, chips were submerged for 30 minutes in acetone, which is a commonly used washing solvent for cleaning metal scraps, and it is equally applicable both at laboratory and industrial scales. First, 15g chips were loaded in a cylindrical die with a nominal diameter of 25.4 mm and then compacted at a 5 kN force by an H13 cylindrical steel tool with a 25 mm diameter. After the pre-compaction, tool rotation was activated with vertical load starting from 5kN. The load gradually increased from 5kN to 20 kN with a step increment of 0.5 kN/s in 30 seconds. This step was referred to as a transition phase. Due to machine limitations, an instant load increment from 5 kN to 20 kN was not possible. In this way, a transition period of 30 seconds was a prerequisite before the consolidation step. Productive time was measured once the force reached 20 kN; the time period after 20 kN achievement was referred to as consolidation time. Overall, chips welding was performed at different rotational tool speeds and various laps of consolidation time according to the experimental plan shown in Table 8. Each experiment was repeated three times. The selection of these parameters was driven by previous research in this field. In this regard, Latif et al. [44, 89, 90] have already explored the FSC process, identifying the best process parameters (rotational speed and vertical load), and demonstrating that the increase in rotational speed over 1500 slightly affected the consolidation behavior.

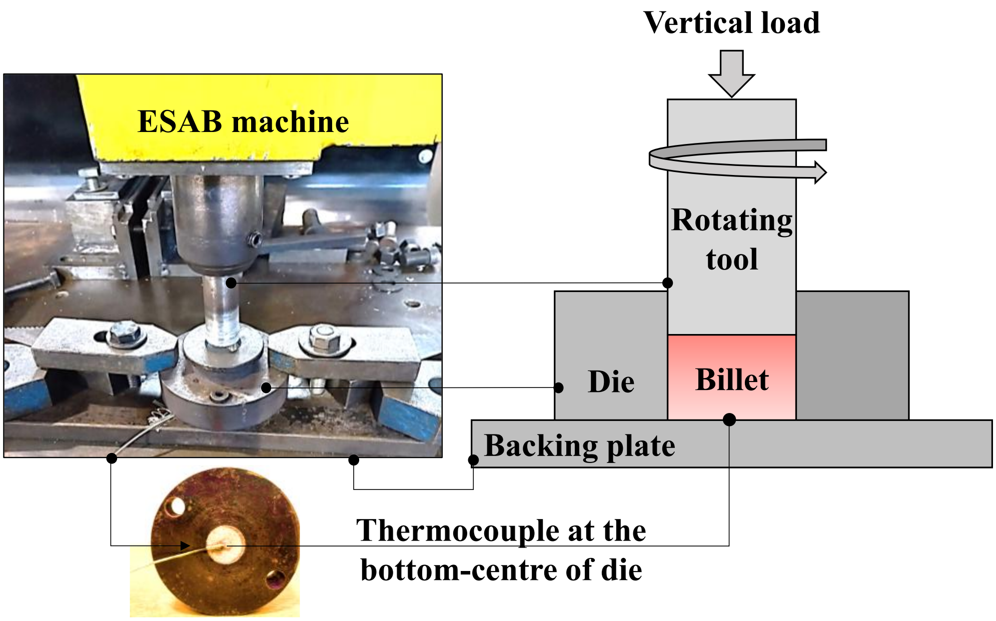

Figure 63. *Friction stir consolidation experimental setup and process sketch.*

Table 8. *The developed experimental campaign.*

Exp ID	Rotational speed [RPM]	Mass [g]	Transition time [s]	Consolidation time [s]
Exp 1	1500	15	30	0
Exp 2	1500	15	30	10
Exp 3	1500	15	30	20
Exp 4	1500	15	30	30
Exp 5	1000	15	30	20
Exp 6	1000	15	30	30

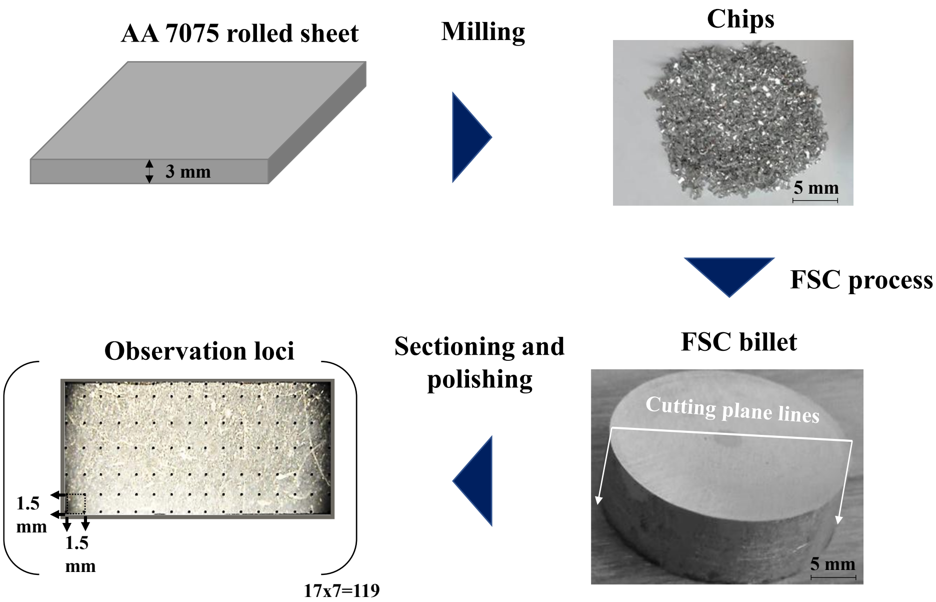

Figure 64. *Different process stages to transform the as-received material AA7075 sheet into FSC solid billet.*

4.1.2 Numerical methodology

The simulation of the FSC process was carried out using the commercial software DEFORM 3D^{TM}. The chips inside the die were considered as a single block chip-based billet, and it was modelled as a porous cylinder, considering the Shima and Oyane [86] formulation for porous materials. The porous billet was characterized by a relative density equal to 0.44, the heat transfer coefficient equal to 11 N/sec/mm/C, and a mesh of 60000 elements with a refinement in the upper surface where the tool contact takes place. The other objects involved in the process were the tool, the die, and the backing plate (Figure 65) that were modelled as rigid parts with a mesh of 15000, 15000, and 35000 elements, respectively. The contacts between the billet and rigid parts were modelled through a friction shear model with a constant shear factor of 0.25. The temperature, strain, and strain rate dependent material flow of the considered AA7075 alloy was obtained by both the material database JMatPro (higher temperature stress-strain-strain rate curves) and in-house experiments (room temperature stress-strain-strain rate curves). The data obtained have been used to perform a numerical regression and determine the constants shown in the material model (Eq. 9).

$$\sigma_f = 129 \cdot (\dot{\varepsilon}_0 - \bar{\varepsilon}^{\,0.201}) \cdot \dot{\varepsilon}^{\,0.002} \cdot exp^{441/T} \tag{9}$$

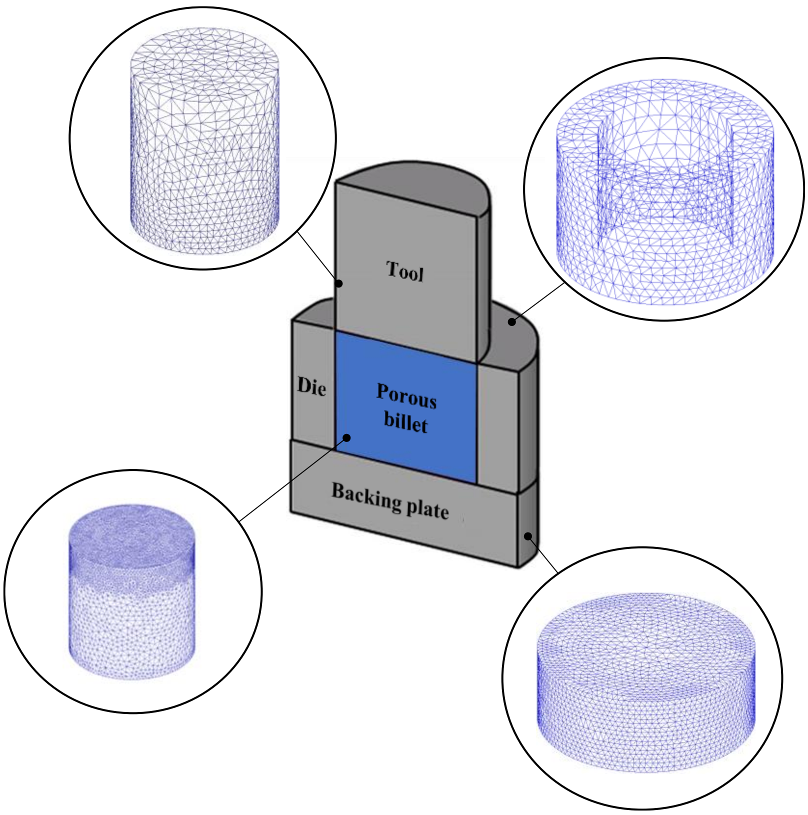

Figure 65. *Numerical model for tool, die, backing plate and porous billet.*

The numerical simulation was carried out using a force-controlled tool characterized by a vertical load obtained from the experimental tests and a rotational speed equal to 1500 rpm. The duration of this process was set to 60s. To ensure the reliability of the numerical results, the experimental velocity and the displacement of the tool were compared to the numerical ones; the results are shown in Figure 66 prove a good match between the experimental measurement and the numerical prediction. To further test the reliability of the numerical model, a thermocouple was used to record the temperature at the bottom-center of the chips-based billet; also in this case, the numerical tool provided a successful prediction (see Figure 67).

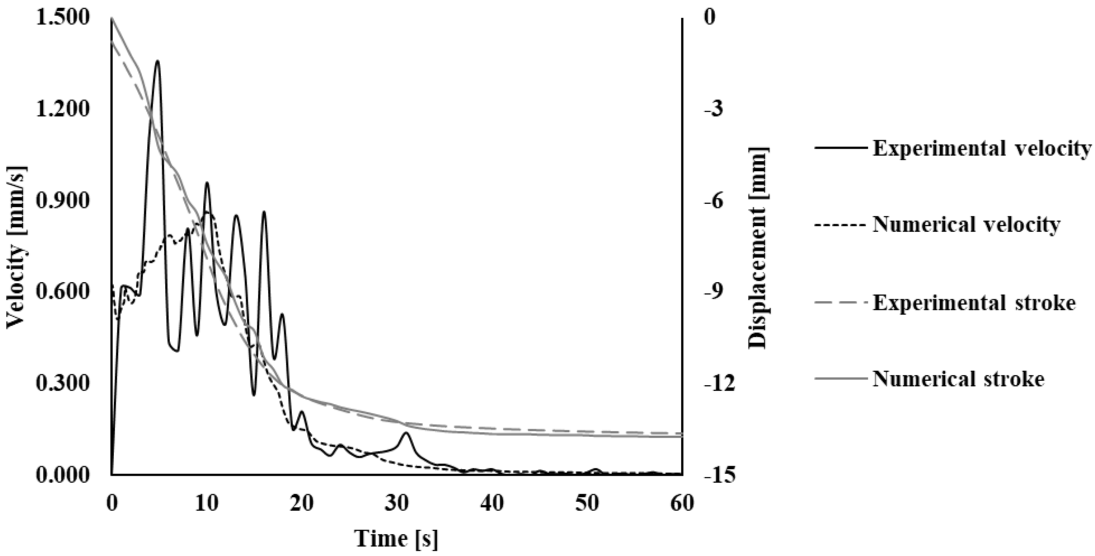

Figure 66. *Experimental and numerical velocity and displacement comparison for numerical-simulation tuning.*

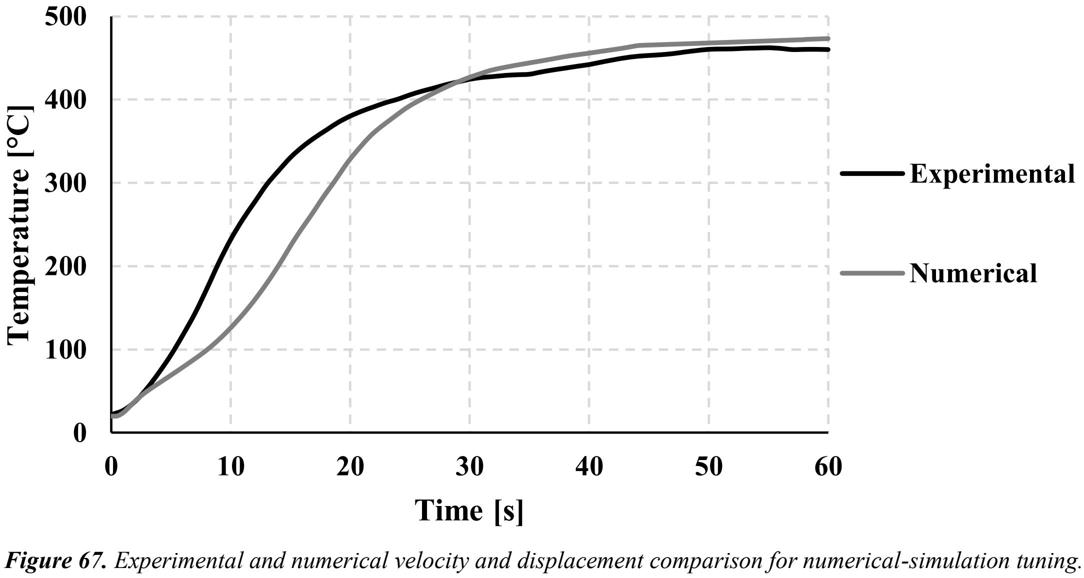

Figure 67. *Experimental and numerical velocity and displacement comparison for numerical-simulation tuning.*

4.1.3 Sample preparation methods after processing

For the microstructural analysis and hardness measurement of the FSCed specimens, the samples were first sectioned using a grinding wheel with a low cutting speed. Then the cut samples were mounted by using the compression mounting method. After that, the sectional surface was polished with a series of abrasive papers with grit numbers: P80, P180, P320, P600, P1000, and P12000 by using water to obtain a smooth surface with uniform surface roughness. In the final stage, a polishing cloth of Reflex PAD-MAG, ⌀ 300 mm, NT was applied, assisted by silicon carbide as a lubricant. Then, the samples were etched using Keller's reagent (0.5 ml HF, 1.5 ml HCl, 2.5 ml HNO3, and 95.5 ml H2O). GX51 Olympus optical microscope was utilized to analyze the microstructure by using 5x, 50x and 100x lenses. evaluated following the ASTM E112–96 by the ImageJ software. For microstructural analysis, an SEM equipped with EDS was also employed to investigate defects within the samples, surface characteristics, and material composition.

For Mechanical analysis, Vickers microhardness testing was conducted along the surface of the samples, in compliance with ISO 6507 standards. This procedure provided insights into the material's localized hardness gradients.

4.1.4 Experimental and numerical bonding criteria definition

In order to test various numerical models predicting the quality of chips welding during FSC, it is important to quantitatively evaluate the bonding prediction performance of each numerical model with respect to an experimental reference. For this reason, a reference experimental benchmark was developed based on two measured outputs: hardness value and average grain size. From now on, the identified reference will be referred to as the experimental bonding criterion. This criterion was framed out after a detailed investigation of three different objects: as-received material, compacted chips obtained from a milling operation, and manufactured FSCed solid billet.

First, the starting material (as-received material) AA7075 sheet was fully analyzed. Average values of 150 HV and 155 µm were noticed for hardness and grain size, respectively.

In the next step, the AA7075 sheet was reduced into chips, and the microstructure of chips was investigated in order to know the changes caused by the milling process. Due to the process mechanics of the milling operation, the average grain size was significantly reduced to a range of 0.5-2 µm. However, the hardness value was not measured because pre-processed compacted chips were in the form of a porous material with a relative density equal to 0.44. However, for each individual chip, a relatively higher hardness value is expected due to the milling operation as reported by Rofman et al [91].

Finally, chips were consolidated into a solid cylindrical billet during the FSC process. A detailed investigation was carried out on 119 different observation loci to analyze the microstructure and hardness distributions obtained after the FSC step. Based on the values measured in such loci, hardness values, and grain size distributions were interpolated to obtain the consolidated/non-consolidated areas as reported in (Figure 68, step 2).

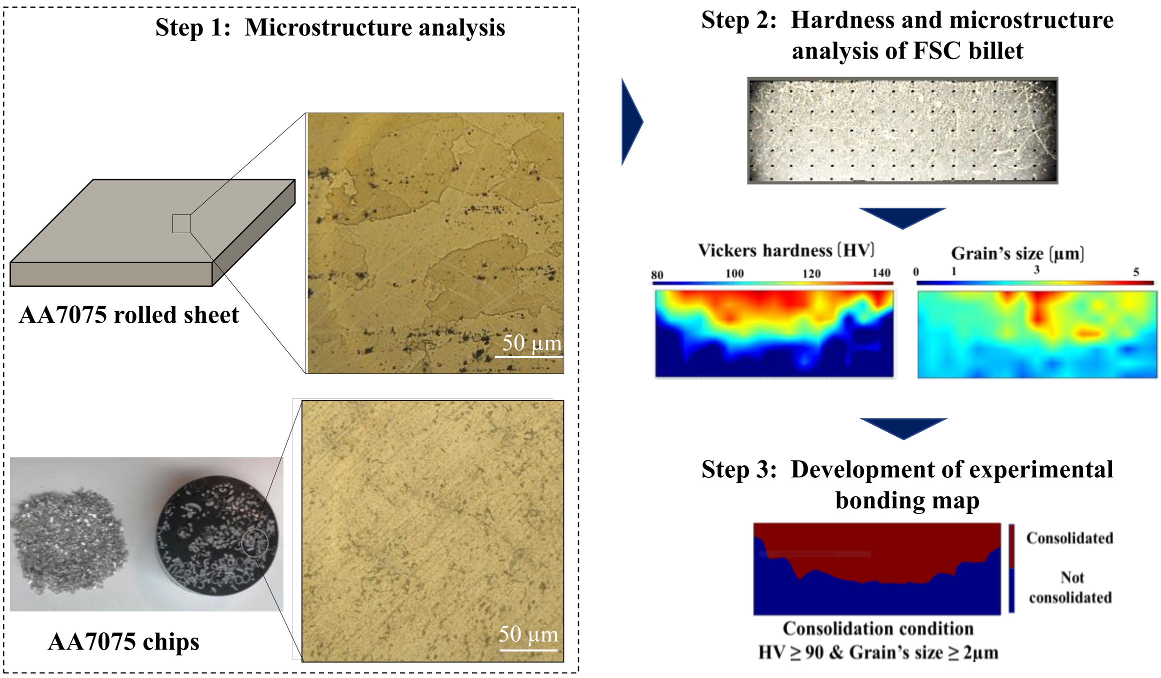

Figure 68. *Steps for experimental bonding criteria development.*

In the bottom section of the billet, the microstructure was found similar to the pre-processed chips with several defects such as visible chips boundaries, voids, cavities, cracks, etc. (Figure 69); the average grain size fell within the range of 0.5-2 µm. This indicates that the microstructure of the bottom part remained unaltered during the FSC process. Moving toward the top part of the billet, changes in microstructure (grain growth) and the improvement in billet quality (disappearance of defects) were noticed. It was quite evident that these changes occur specifically at grain sizes exceeding 2 µm. To ensure the achievement of the full consolidation condition, a minimum hardness value of HV 90 (60% of as-received material) was also considered based on experimental evidence. At this hardness value, the billet showed good consolidation without any defects like visible chips boundaries, voids, cavities, cracks, etc. In this way, an idea of experimental bonding condition evolved by taking into account the combined effect of microstructure and hardness values.

The definition of experimental criteria for the AA7075 alloy is, therefore, formulated as follows:

"Any zone on the FSC billet section that has an average grain size at least equal to the maximum average grain size of the unprocessed chip (2 μm) AND the hardness value of at least 60% of the as-received material hardness (HV 90) is labeled as fully consolidated".

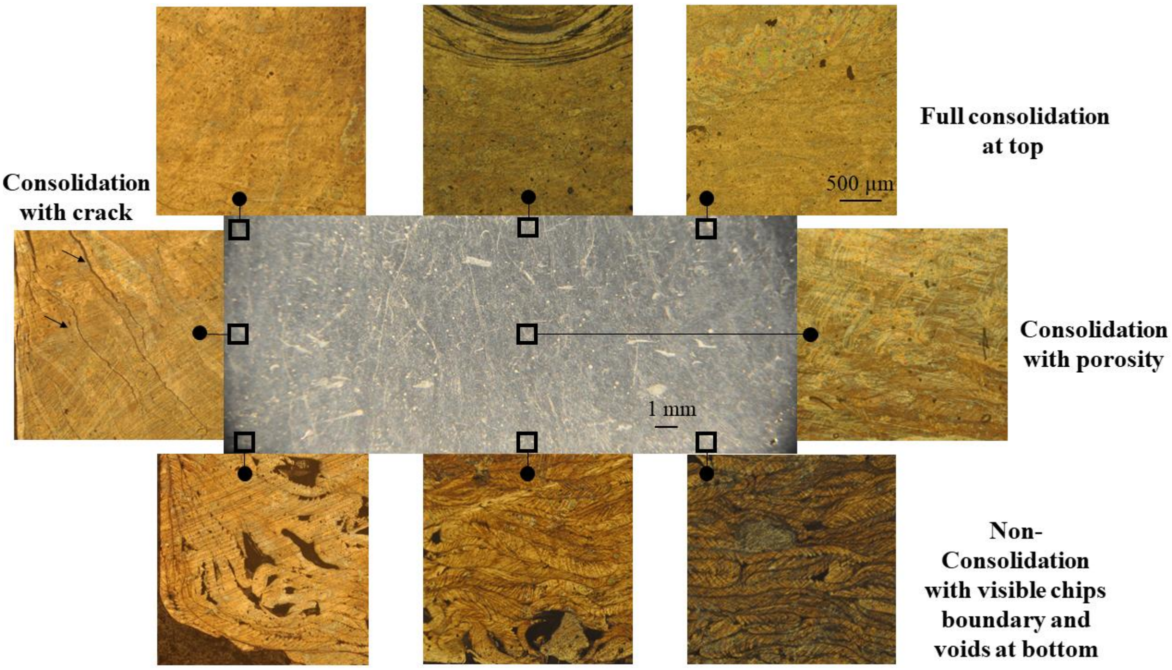

Figure 69. *Detailed microstructure analysis for Exp 1.*

4.1.5 Numerical bonding criteria

Together with the bonding criteria already available in literature, two more bonding criteria are proposed and analyzed (see Table 6). The first new criterion is reported in Eq. (10), where the Zener–Hollomon parameter (Eq. 11) was included in the Plata–Piwnik criterion. The Zener–Hollomon parameter is related to the recrystallization of the material, and it takes into account the effect of the temperature-compensated strain rate in the consolidation process. Overall, the aim was to analyze whether the inclusion of a factor related to grain size and recrystallization would improve the solid bonding occurrence prediction during FSC.

$$W_{C6} = \int_{t_i}^{t_f} \frac{|\sigma_{mean}|}{\sigma_f} \cdot \frac{1}{Z} dt \tag{10}$$

$$Z = \dot{\varepsilon}\, exp^{\left(Q/_{R \cdot T}\right)} \tag{11}$$

Where R is the gas constant (8.314 J/mol K), T is the temperature (K) of the point, and Q (J/mol) is the activation energy (AA2024 [92], AA6082 [93] and AA5083 [94]).

This criterion was tested considering a temperature activation threshold (480 °C), which is higher than the aluminum recrystallization temperature, usually on the range of 300 °C. In other words, as the temperature of the tracked point is below this threshold, the bonding value (W_{C6}) was considered equal to zero (see Eq. 12). This assumption was defined in order to avoid the excessive growth of the W value because of the "stationarity" of the FSC process as further explained in Chapter 4.2.6.

$$\begin{cases} W_{C6} = \int_{t_i}^{t_f} \frac{|\sigma_{mean}|}{\sigma_f} \cdot \frac{1}{Z} dt & T \geq 480\,°C \\ W_{C6} = 0 & T < 480\,°C \end{cases} \tag{12}$$

The used threshold was also chosen on the basis of the optimization procedure that aimed to maximize the overlap between the experimental results and the numerical predictions. In these cases, the best overlapping performance was obtained at about 480 °C.

The second developed criterion (see Eq. 13) involves the use of two parameters, which can be defined as "weights" of the bonding criterion. The main aspect of these parameters is the ability to emphasize the bonding in those material zones where temperature and strain changes occur synergistically. These parameters are expressed as the ratio between the variation of the variable over a given time span (equal to the simulation time step) and the value of the same variable at simulation step *i*. In this research, the time span was considered equal to 0.05 s.

$$W_{C5} = w_s \cdot w_T \cdot \int_{t_i}^{t_f} \frac{|\sigma_{mean}|}{\sigma_f} dt \tag{13}$$

where w_T and w_s (see Eq. 14) are the weights of the temperature and of the strain, respectively; *i* is the considered simulation step and σ_f is the material flow stress.

$$w_T = \frac{T_i - T_{i-1}}{T_i} = \frac{\Delta T}{T_i} \qquad w_s = \frac{\varepsilon_i - \varepsilon_{i-1}}{\varepsilon_i} = \frac{\Delta \varepsilon}{\varepsilon_i} \tag{14}$$

All the criteria analyzed in the present research are listed in Table 6, both the original equations (named in Table 6 “Literature Equation”) and the adopted equations are reported. Specifically, the mean stress absolute value and effective stress were used in place of the contact pressure and the flow stress, respectively. In order to calculate the different criteria in the 119 observation loci of the cross-section, the track point procedure was used. This procedure highlighted the evolution of the considered field variables and of the material flow stress for each of the 119 observation loci. The different integrals reported in Table 6 were, therefore, numerically calculated using the trapezoidal

4.1.6 Numerical bonding threshold values calculation procedure

For each criterion, a threshold value (W_{Ci}^{lim}, where i = 1, 2, …, 6) for predicting the bonding condition was calculated. The W_{Ci}^{lim} was calculated with the iterative model depicted in Figure 70. For each criterion and for each analyzed consolidation time (Exp 1 to 4 of Table 8), the W_{Ci}^{lim} was identified. In this respect, an automatic procedure able to calculate the W_{Ci}^{lim} providing the best fit with experimental results was designed and implemented. This procedure integrates experimental data with numerical results through a minimization algorithm implemented in the MATLAB environment. The purpose of this model is to create an automatic and more accurate calculation process for the identification of the bonding criterion threshold (W_{Ci}^{lim}). The steps of the developed procedure are reported in the flow chart depicted in Figure 70.

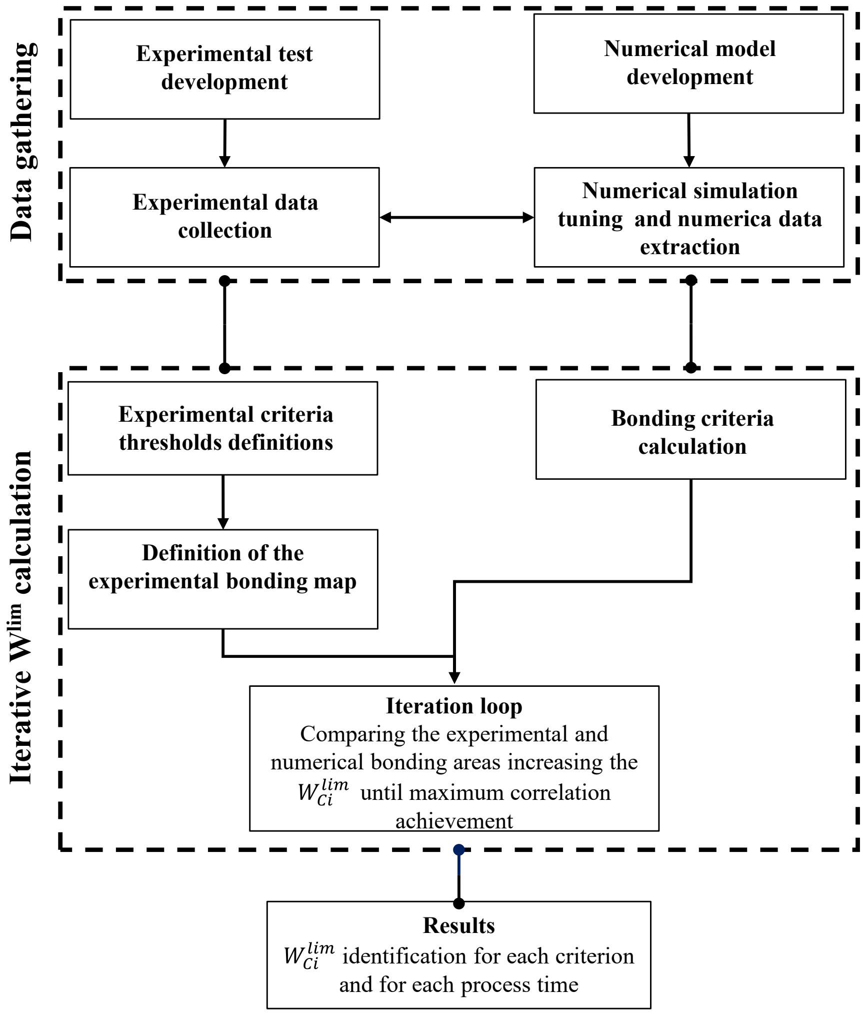

Figure 70. *Implemented workflow for automatic* W_{Ci}^{lim} *calculation.*

The iteration cycle starts with the data gathering phase. In this step hardness and grain size of the four samples (see Table 8, Exp 1 to 4), as described in Chapter 4.2.3, were collected. In the meantime, the values of the main variables related to bonding occurrence were extracted from the numerical results. Specifically, the variables were extracted for the 119 loci (see Figure 64) to have an effective matching between experimental and numerical observations. In this respect, the matrix of numerical points (observation loci), used for developing the points tracking and following the evolution of the field variables, was the same for both experimental and numerical cross sections.

Once the experimental data were acquired, two different matrices containing the hardness and the grain size values for the 119 analyzed observation loci were created for the Exp 1-4. These matrices allow maps of hardness (Figure 71a) and grain size (Figure 71b) of the cross sections of the analyzed samples to be obtained.

As explained in Chapter 4.2.3, for the analyzed aluminium alloys, specific hardness and grain size thresholds were identified. According to this criterion, two specific regions can be identified in the sample's cross sections:

- Consolidated area: the area where the combined value of hardness and grain size exceeds both the hardness and the grain size thresholds previously identified.
- Not Consolidated area: the area where neither the hardness nor grain size values reach the value of the thresholds previously identified.

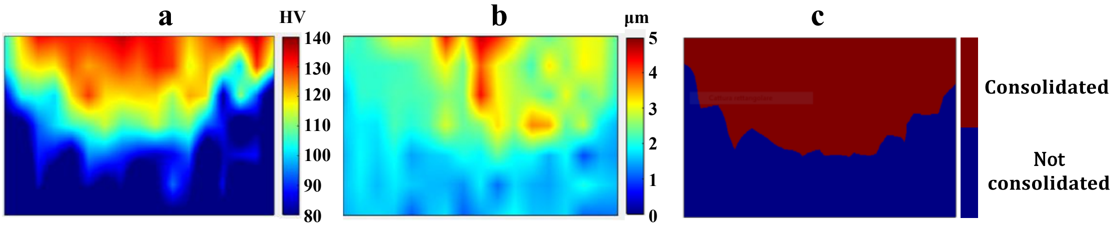

Figure 71. *Example of colored map for (a) hardness, (b) grain size, and (c) derived experimental bonding map for Exp 1.*

The next step concerns the bonding criteria calculation, using all the field variables extracted from the simulation, the bonding criterion value has been calculated for each of 119 loci, for each Exp 1-4. Once the values of the numerical criteria are available, the iteration procedure can be initialized according to the following steps.

1. Setting the scale limit of the numerical bonding map equal to a bonding limit value (W_{Ci}^{lim}). For the first step of the iteration, the W_{Ci}^{lim} value was set equal to zero.
2. Incrementally increasing the W_{Ci}^{lim} value and check the area similarity between the experimental bonding map and the numerical bonding map using an image comparison approach available on MATLAB. The similarity has the meaning of the correlation coefficient (r) calculated in the following way (Eq. 15):

$$r = \frac{\sum_m \sum_n (A_{mn} - \bar{A})(B_{mn} - \bar{B})}{\sqrt{(\sum_m \sum_n (A_{mn} - \bar{A})^2)(\sum_m \sum_n (B_{mn} - \bar{B})^2)}} \tag{15}$$

   Where A and B are the logical array representing the two maps, m and n are the elements of the array, $\bar{A}$ and $\bar{B}$ are respectively the mean values of A and B.
   The procedure is stopped when the maximum correlation, i.e., when the best overlapping between experimental and numerical bonding areas is reached.
3. Obtainment of the optimal W_{Ci}^{lim} values and of the corresponding correlation coefficients.

The procedure was implemented for the six criteria reported in Table 6 and for all the case studies reported in Table 8.

4.1.7 Results and discussion

In this Chapter, the obtained results of both the experimental procedure and the numerical bonding criteria calculation are discussed for the process conditions Exp 1, Exp 2, Exp 3, and Exp 4 of Table 8. In Figure 72 the observed hardness and grain size distributions, along with the derived experimental bonding maps, are reported.

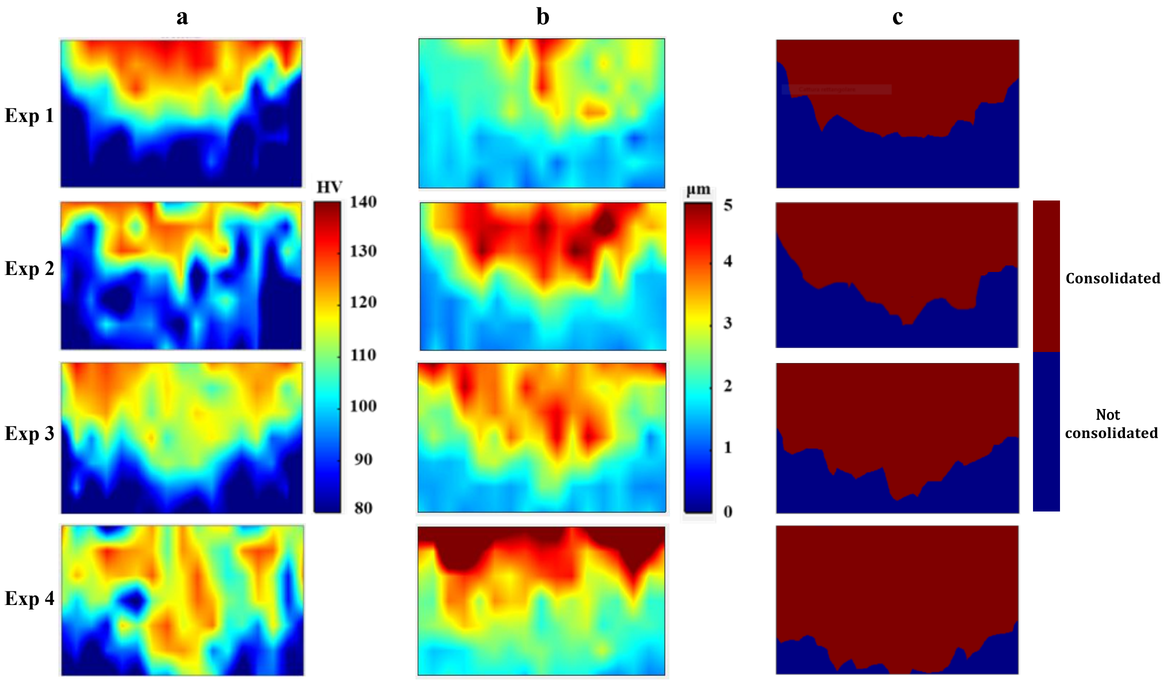

Figure 72. *(a) Hardness, (b) grain size distributions and (c) experimental bonding maps for Exp 1, Exp 2, Exp 3 and Exp 4.*

Since moving from Exp 1 to 4, the consolidation time increases from 0s to 30s, it is possible to notice that increasing the processing time the bonding area significantly increases. Specifically, the consolidation front moves downwards according to the heat and strain evolution over time [42]. In fact, an axisymmetric heat flow moving from the top toward the bottom occurs, moreover, the die and the backing plate serve as a heat sink, reducing the temperature and constraining the deformation of nearby aluminum alloy chips [85]. In conclusion, the further the chips are from the top (rotating tool), the more difficult it is to achieve the solid bonding conditions.

In the analyzed case studies, it is possible to notice that even with the maximum consolidation time, a fully consolidated billet was not obtained. Actually, a non-consolidated region is still visible at the bottom of the Exp 4 experimental bonding map of Figure 72.

The numerical bonding map obtained by means of the optimization procedure described in Chapter 4.2.5 is shown in Figure 73 and Figure 74. The different maps represent the material bonding criteria distribution for different consolidation times: 0, 10, 20, and 30 seconds. To better highlight the bonding zone and to provide a better comparison between the numerical and the experimental bonding maps, the maximum value of the numerical bonding maps scale was set equal to the W_{Ci}^{lim} found. This particular setting allows the creation of a dark red zone characterized by values that are greater than or equal to the W_{Ci}^{lim}, thus representing a fully consolidated region. The different calculated W_{Ci}^{lim} for each criterion and for each consolidation time are reported in Table 9. In this table, the correlation coefficient values as described in Chapter 4.2.3 are also listed. It is possible to notice that C1, C2, and C4 are characterized by bad values of the correlation coefficient, and this results in an unreliable bonding map evolution as visible in Figure 73 and Figure 74. On the other hand, C3, C5, and C6 maps, although characterized by different bonding region shapes, provide a good match between the experimental bonding criterion and the numerically predicted one. Nevertheless, as it is possible to notice from Figure 73 and Figure 74, the W_{Ci}^{lim} is not a constant value but varies with varying the considered consolidation time, and this happens for each analyzed criterion. In other words, it is not possible to find a unique W_{Ci}^{lim} value with varying process conditions (temperature, strains, stress status, etc.). To further highlight such an assumption, the test provided in Figure 75 was developed. Specifically, in Figure 75a, the bonding map (for the Plata–Piwnik–Zener criterion) is reported for the 0 second consolidation time (Exp 1) using the calculated 30 seconds consolidation time (Exp 4) W_{Ci}^{lim}. It is possible to notice that the obtained map does not predict at all the bonding occurrences; in fact, the identified W_{Ci}^{lim} underestimates the bonding occurrence significantly. On the other hand, in Figure 75b the bonding map for Exp 4 using the calculated Exp 1 W_{Ci}^{lim} is reported, and also in this case, the prediction is not reliable as the W_{Ci}^{lim} overestimates the bonding occurrence. This misleading result was observed for all of the criteria analyzed.

In conclusion, the use of a single value for different process times does not provide a reliable bonding occurrence prediction, as a matter of fact, either over-estimation or under-estimation of the bonding occurrence was observed. What was described for the Plata–Piwnik–Zener was observed all the same for the six criteria here analyzed. This result was somehow expected, indeed, in the literature it has already been proved the dependence of the W_{Ci}^{lim} on the temperature, to be more specific, Ceretti et al. [78] proved, for instance, that W_{C2}^{lim} decreases with increasing the processing temperature in a port hole extrusion process. This result can be easily explained as with increasing temperature, the required activation energy for bonding decreases and, thus, the value W_{Ci}^{lim} decreases as well.

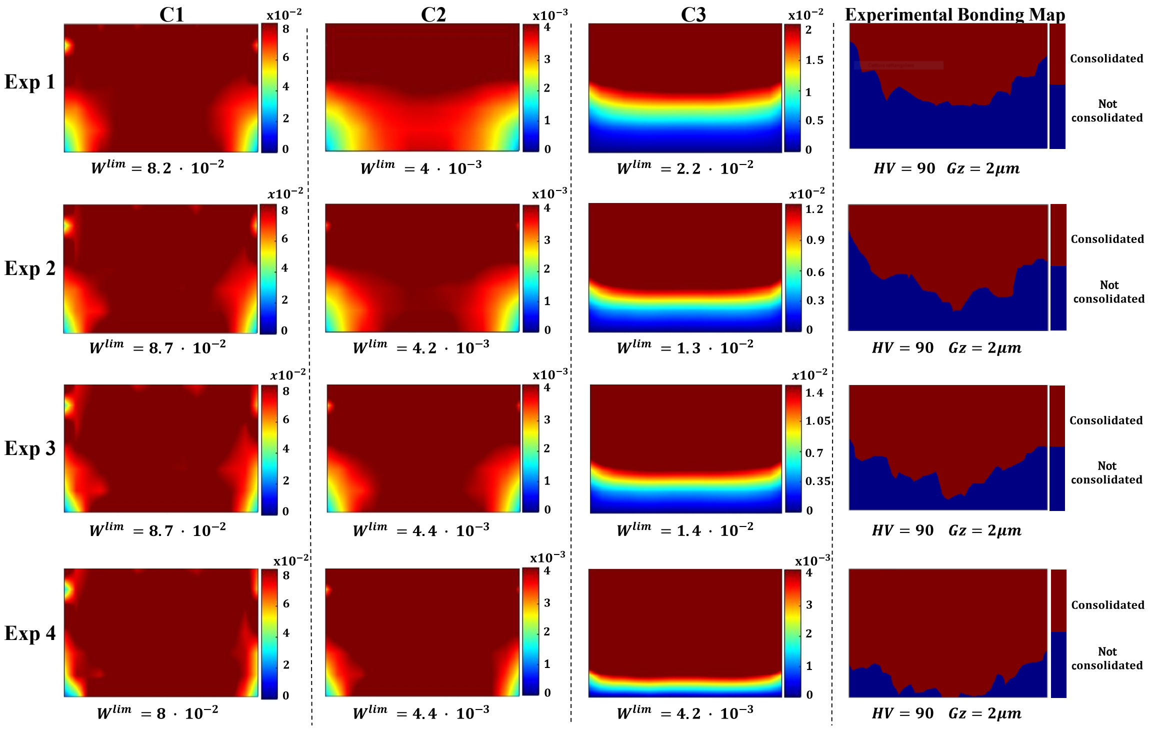

Figure 73. *Numerical bonding maps for Akeret (C1), Plata – Piwnik (C2), Donati and Tomesani (C4) criteria and Experimental bonding maps.*

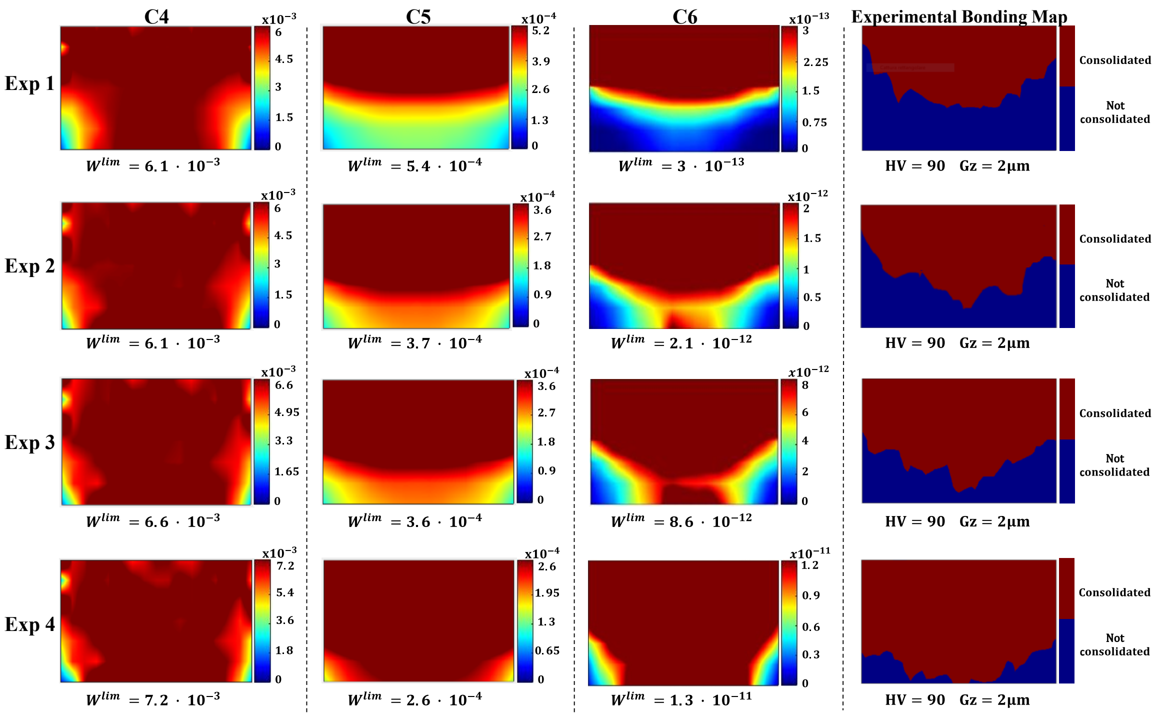

Figure 74. *Numerical Bonding map for Kolpak et al. (C4), Plata – Piwnik weighted (C5) Plata – Piwnik - Zener (C6) criteria and the experimental bonding maps.*

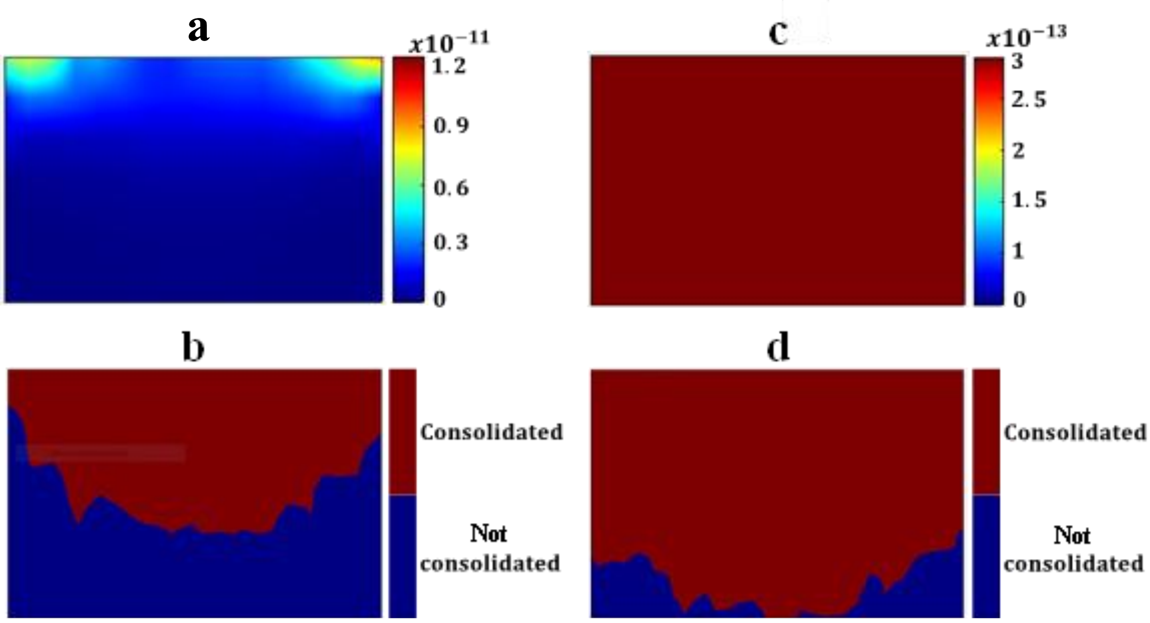

Figure 75. *(a) Exp 1 numerical bonding map based on* W_{C6}^{lim} *calculated for Exp 4, (b) Exp 1 experimental bonding map, (c) Exp 4 numerical bonding map based on* W_{C6}^{lim} *calculated for Exp 1 and (d) Exp 4 experimental bonding map.*

A better overview of these trends is provided by the graphs reported Figure 76. In these graphs, the value of the bonding limit W_{Ci}^{lim} versus the mean temperature values of the bonding line are reported. It is possible to notice that the bonding limit value W_{Ci}^{lim} for most of the criteria increases with temperature, this trend is quite unrealistic considering the solid bonding physics, questioning the effectiveness of some of the tested criteria. Looking at the results of Figure 76, the only criteria characterized by a decreasing trend with increasing temperatures are C3 and C5. These criteria, in fact, can better take into account the peculiar solid bonding mechanics of FSC.

Table 9. *Values of maximum correlation coefficients and the corresponding W_{Ci}^{lim} for Exp 1, Exp 2, Exp 3 and Exp 4.*

Criterion	**Exp ID**	**Correlation coefficient [%]**	$\mathbf{W_{Ci}^{lim}}$
	Exp 1	51	$8.2 \cdot 10^{-2}$
Akeret	Exp 2	64	$8.7 \cdot 10^{-2}$
(C1)	Exp 3	51	$8.7 \cdot 10^{-2}$
	Exp 4	40	$8.0 \cdot 10^{-2}$
	Exp 1	49	$4.0 \cdot 10^{-3}$
Plata – Piwnik	Exp 2	58	$4.2 \cdot 10^{-3}$
(C2)	Exp 3	51	$4.4 \cdot 10^{-3}$
	Exp 4	39	$4.4 \cdot 10^{-3}$
	Exp 1	95	$2.2 \cdot 10^{-2}$
Donati – Tomesani	Exp 2	77	$1.3 \cdot 10^{-2}$
(C3)	Exp 3	89	$1.4 \cdot 10^{-2}$
	Exp 4	87	$4.2 \cdot 10^{-3}$
	Exp 1	57	$6.1 \cdot 10^{-3}$
Kolpak et al.	Exp 2	65	$6.1 \cdot 10^{-3}$
(C4)	Exp 3	60	$6.6 \cdot 10^{-3}$
	Exp 4	48	$7.2 \cdot 10^{-3}$
	Exp 1	96	$5.4 \cdot 10^{-4}$
Plata – Piwnik – Weighted	Exp 2	82	$3.7 \cdot 10^{-4}$
(C5)	Exp 3	88	$3.6 \cdot 10^{-4}$
	Exp 4	98	$2.6 \cdot 10^{-4}$
	Exp 1	94	$3.0 \cdot 10^{-13}$
Plata - Piwnik – Zener	Exp 2	84	$2.1 \cdot 10^{-12}$
(C6)	Exp 3	87	$8.6 \cdot 10^{-12}$
	Exp 4	84	$1.3 \cdot 10^{-11}$

Note: Akeret W_{C1}^{lim} [Mpa/MPa], Plata - Piwnik W_{C2}^{lim} [s], Donati - Tomesani W_{C3}^{lim} [mm], Kolpak et al. W_{C4}^{lim} [Mpa/MPa], Plata – Piwnik – Weighted W_{C5}^{lim} [s], Plata - Piwnik – Zener W_{C6}^{lim} [s^2].

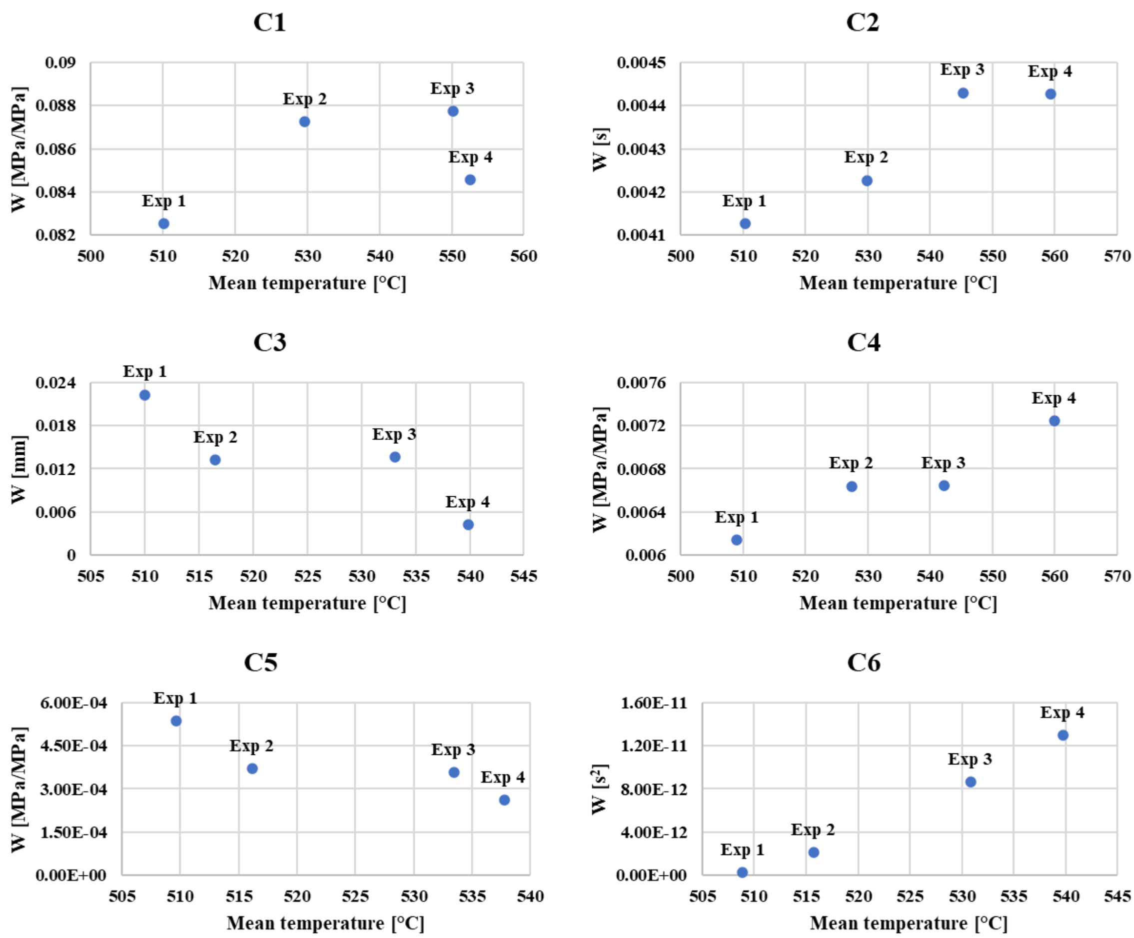

Figure 76. *Calculated* W_{Ci}^{lim} *values versus temperature trends for each analysed criterion.*

As a matter of fact, the chip-based billet remains inside the die for the entire process duration, consequently, the value of a given bonding criterion (W) steadily increases throughout the FSC process. This causes the W_{Ci}^{lim} threshold to be reached also for regions of the billet that could never reach actual solid bonding conditions. This phenomenon is similar to what was analyzed in the dead material zone by Donati and Tomesani (2004), for the case of port hole die extrusion. Moreover, from the results of the numerical simulation, it is possible to notice that the effective strain and nodal velocity values are characterized by limited values and variation, especially during the consolidation phase (from 30 to 60 second processing time) (Figure 77). It is worth remarking that in Figure 77 the nodal local velocity is reported, and a clear decreasing trend is visible (the maximum values of the colored scale were changed accordingly). These results support the assumption that the FSC process somehow resembles the dead zone analyzed by Donati and Tomesani (2004), hence changes in the classical bonding criteria are needed. To be more specific, the criteria that provide the best performance (C3 and C5) have been thought up with the idea to limit the constant summation of the solid bonding criterion where temperature, strain, and strain rate gradient values are low. This is obtained by the introduction of factors v, w_s and w_t for the C3 and the C5 criterion, respectively.

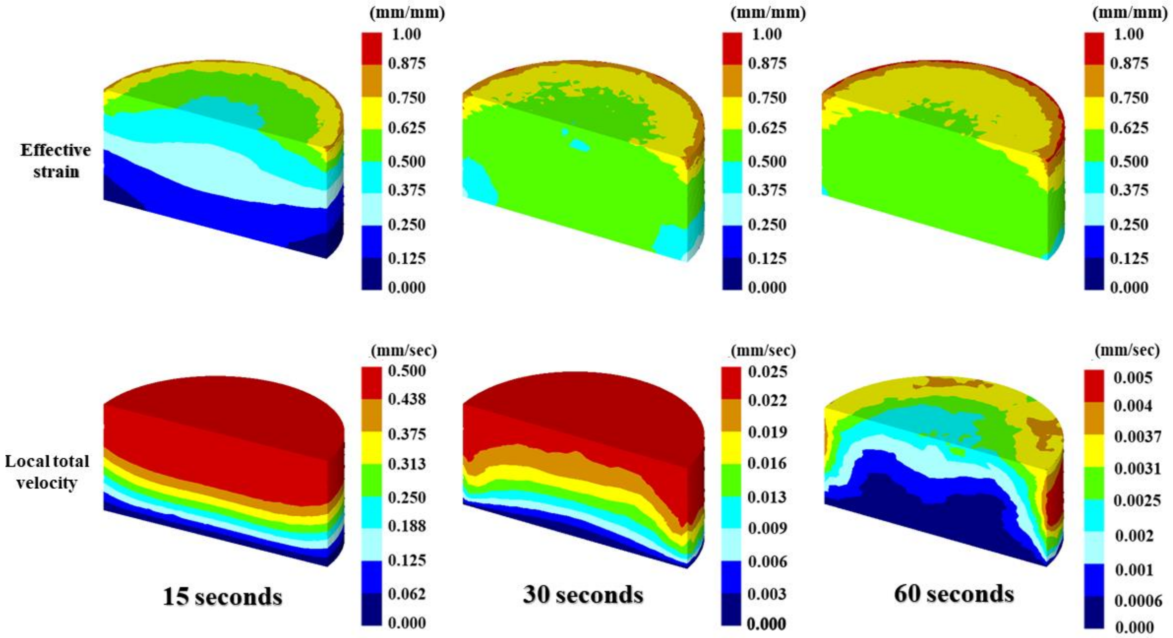

Figure 77. *Effective strain and local velocity for 15, 30 and 60 seconds process time (total time transition plus consolidation).*

4.1.8 Validation of the new solid bonding model for FSC

In order to test the solid bonding occurrence prediction performance during FSC of the different analyzed criteria, two more FSC tests (Exp 5 and 6) have been performed. Specifically, the new tests were performed by using 1000 rpm, 20 kN, and 20 and 30 seconds of consolidation time (see again Table 8). With these process parameters set, the heat generated by friction is slightly reduced, leading to a reduction in maximum temperature achievement. Therefore, a smaller consolidation area is obtained for a given consolidation time compared to the experiments developed with 1500 rpm. This choice was driven by the will to test the model on different conditions with respect to the ones the model was built. The difference in the experimental bonding criterion of the 20 seconds consolidation time obtained with different RPMs is reported in Figure 78; also, the difference in temperature distribution is reported in the numerical temperature map of Figure 79.

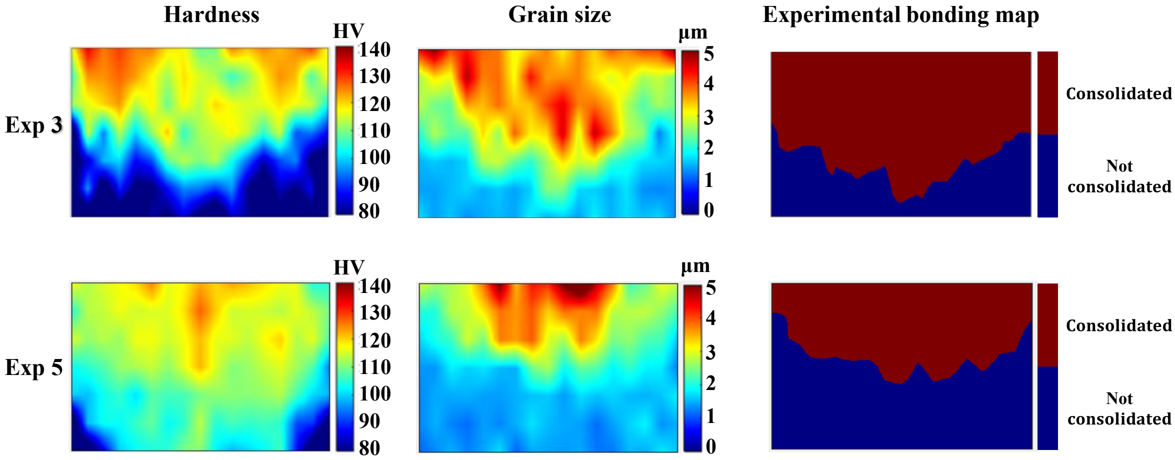

Figure 78. *Hardness, grain size, and experimental bonding map for the cases Exp 3 and Exp 5.*

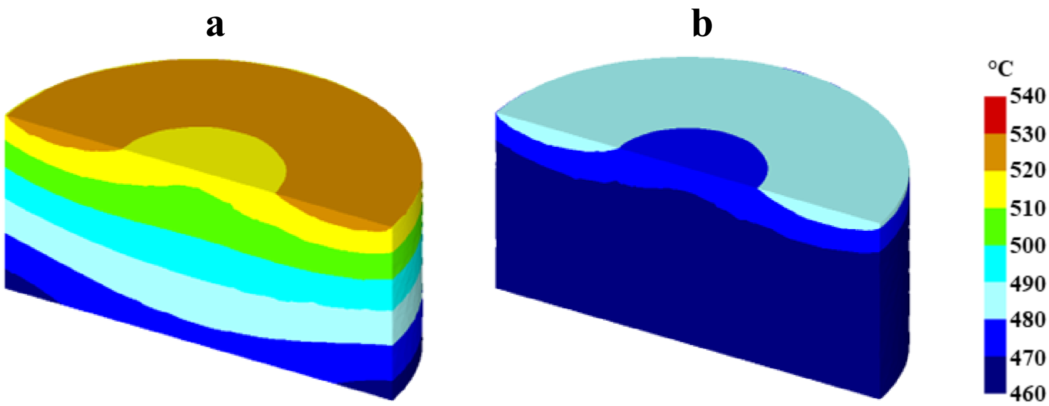

Figure 79. *Hardness, grain size, and experimental bonding map for the cases Exp 3 and Exp 5.*

The effects of different process parameters on the solid bonding phenomenon are also visible in the microstructure analysis reported in Figure 80. The different process parameters lead to different defect occurrences, Exp 3 is characterized by better solid bonding consolidation and grain size refinement, especially in the middle-side part of the billet, moreover in Exp 5 more evident defects are visible in the bottom region of the billet.

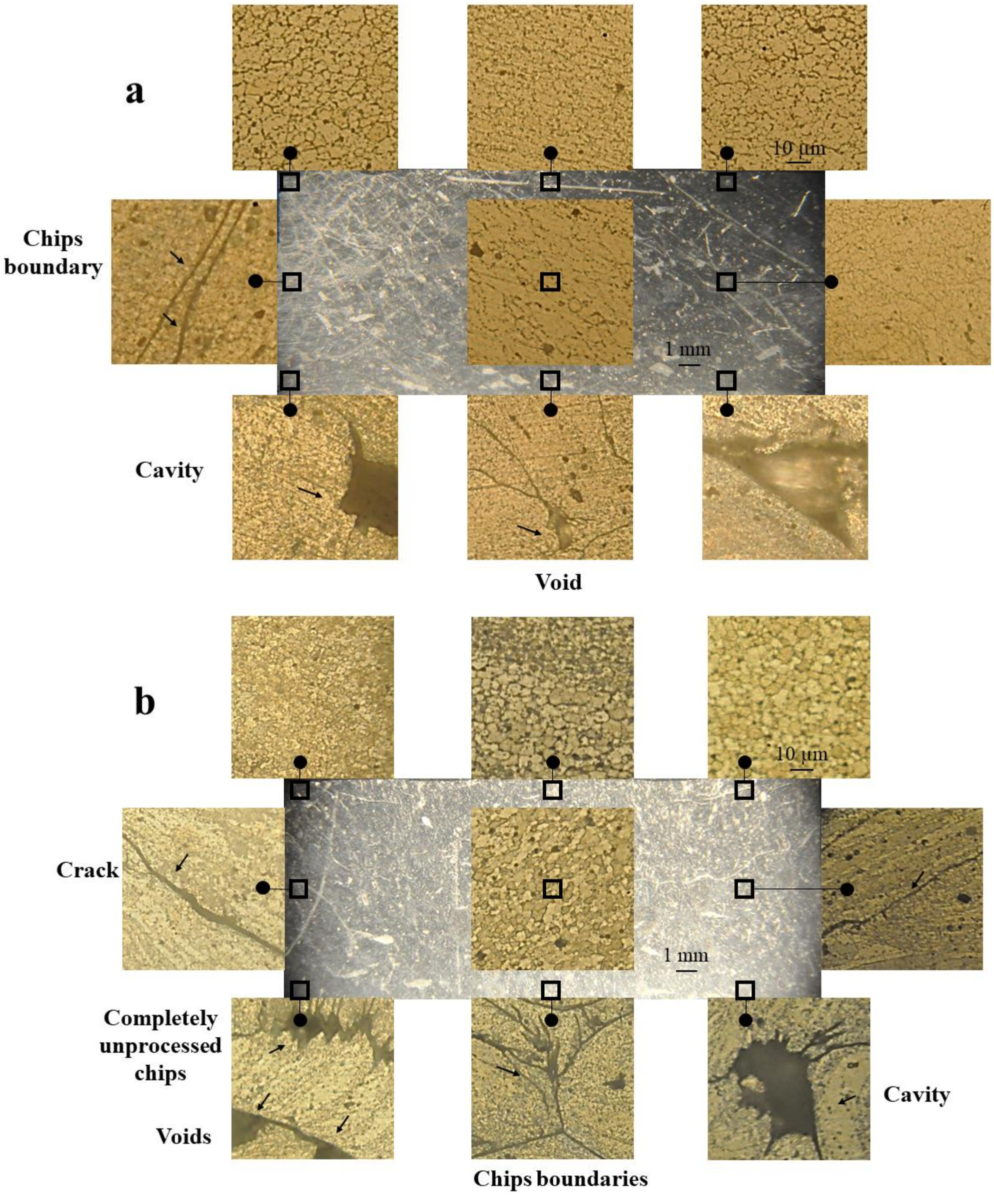

Figure 80. *Microstructure of AA70775 FSC billet section for (a) Exp 3 and (b) Exp 5.*

Overall, the aim is to turn all the experimental and numerical knowledge acquired by developing experiments from Exp 1 to 4 into a model able to predict the solid bonding occurrence of friction stir consolidation of AA7075 alloy. For a correct model implementation, a validation procedure is needed; in the present research, the testing procedure for each criterion was implemented by the following workflow.

1. Interpolating by a third-order polynomial fitting curve, the W_{Ci}^{lim} reported in Figure 76.
2. Formulating analytical expressions able to link the W_{Ci}^{lim} with temperature.
3. Performing the FSC for Exp 5 and 6 of Table 8.
4. Measuring the hardness and the grain size of Exp 5 and 6 (for the 119 loci).

5. Performing the numerical simulation and extracting temperature, strain, and stress variables.
6. Calculating the different Wi (i = 1 to 119) values for the 119 loci.
7. Calculating for each point the W_{Ci}^{lim} (i = 1 to 119) with the model developed in step 2.
8. Predicting for each point the bonding/non-bonding occurrence (if Wi ≥ $W_{Ci}^{lim}$the point is labelled as fully consolidated, elsewhere it is considered non-consolidated).
9. Comparing the predicted values with the experimental results.
10. Quantifying the prediction accuracy of each analyzed criterion.

The results of the testing procedure are reported in Table 10 and Table 11 for Exp 5 and 6, respectively. It is possible to see that the best performance in predicting the bonding occurrence in FSC is provided by C5. In fact, a prediction error, the number of loci mistakenly predicted divided by the total number of tested loci, equal to 6 % for Exp 5 and 10 % for Exp 6, was observed. Good performance is also provided by the C3 criterion, although the error for Exp 6 rises up to 21%. All the other criteria are not eligible as the prediction error performances are not satisfactory in both of the analyzed experiments.

Table 10. *Bonding criteria prediction performance for Exp 5.*

Criterion	N° loci correctly predicted	N° total loci	Prediction error [%]
C1 - Akeret	70		42
C2 - Plata - Piwnik	79		34
C3 - Donati and Tomesani	108		10
C4 - Kolpak et al.	66	119	45
C5 - Plata – Piwnik - weighted	112		6
C6 - Plata - Piwnik - Zener	73		39

Table 11. *Bonding criteria prediction performance for Exp 6.*

Criterion	N° loci correctly predicted	N° total loci	Prediction error [%]
C1 - Akeret	60		50
C2 - Plata - Piwnik	53		56
C3 - Donati and Tomesani	95		21
C4 - Kolpak et al.	65	119	46
C5 - Plata – Piwnik - weighted	108		10
C6 - Plata - Piwnik - Zener	54		55

Figure 81 provides a specific visualization of the experimental bonding map (Figure 81a) for Exp 5 and the related predicted consolidated zone obtained using the C5 criterion (Figure 81b). In this visualization, each analyzed point is modelled as a rectangle; in Figure 81b, the loci not correctly predicted are also highlighted. Overall, it is possible to notice that the predicted shape is very close to the experimental bonding area, and the prediction errors occur in the transition zone between the consolidated and non-consolidated area. In this area, the hardness and grain size values are close to the threshold values. Also, it may occur that either the hardness or the grain size values exceed the value of the thresholds previously identified. This area is very close to the bonding conditions, making the prediction very challenging to implement.

In order to highlight the improvement obtained with the here proposed Plata–Piwnik–weighted (C5) criterion, a comparison with a standard one is reported. Specifically, the predicted bonding map for Exp 5 using the Plata–Piwnik criterion (C2) is reported in Figure 81c. As it is possible to notice, the bonding area is significantly different from the experimental one; in particular, an overestimation of the bonding occurrence is predicted.

It is worth remarking that the same trends were observed when also analyzing the prediction of the criteria for Exp 6.

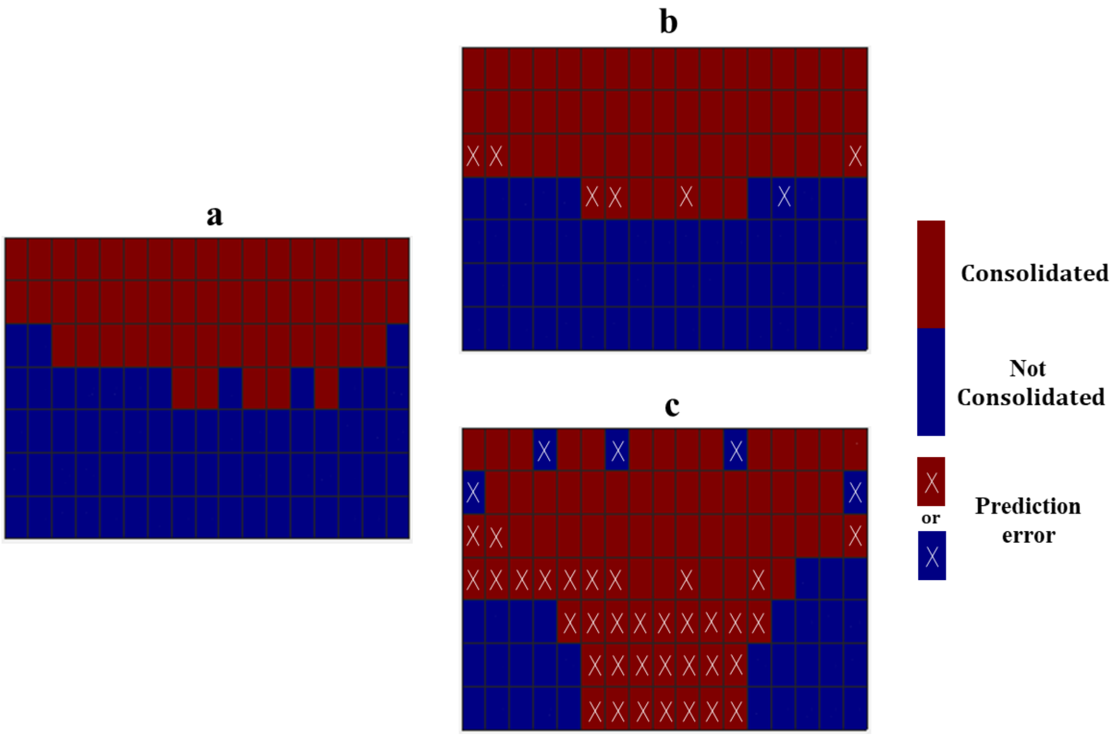

Figure 81. *(a) Experimental bonding map for Exp 5, (b) predicted boning area of Plata – Piwnik - weighted (C5) criterion prediction and (c) Plata – Piwnik (C2) criterion prediction.*

4.1.9 Summary of the results

In this research, different solid bonding criteria have been tested for the modelling of chips recycling by Friction Stir Consolidation. The performances of conventional criteria have been compared with that of a new, here proposed, bonding criterion. The analyses were performed by setting up a procedure for the automatic evaluation of the threshold values of the different analyzed bonding criteria. The developed procedure can be considered as a flexible and adaptable approach for the evaluation of the solid bonding criteria in different solid bonding-based processes.

Specifically, the developed analyses allow for drawing some main findings.

- Conventional bonding criteria already available in the literature fail to predict the solid bonding occurrence for FSC recycling.
- The failure is mainly due to the peculiar nature of the FSC process: strain and strain rate values are limited (especially during the consolidation time) with no material flow within the die. This makes the criteria already tested for extrusion-based approaches ineffective.
- For all the analyzed criteria, it was not possible to identify a unique W_{Ci}^{lim} value with varying process conditions, and a model depending on temperature was identified for each criterion.
- A new and accurate analytical solid bonding criterion specifically designed for the FSC recycling process is proposed. The presented criterion allows a correct prediction of bonding occurrence in FSC.
- The new Plata–Piwnik-Weighted criterion presented here is characterized by three strengths: its trend decreases with increasing temperature (and this is in line with what is expected considering the physics of the process), provides a better prediction occurrence accuracy for a given processing time, and is characterized by the best performances in the developed validation test. Concerning the latter aspect, two validation tests were performed, varying the process parameters. Actually, a maximum prediction error equal to 10 % was observed; this score is significantly lower than those observed for the other criteria, for instance, the conventional Plata–Piwnik criterion is characterized by an average Prediction error equal to 45 % (almost half of the observation loci are incorrectly predicted).

4.2 Applicability of the new bonding predicting tool to other aluminium alloys

The tool developed in the previous study demonstrated higher effectiveness and accuracy than the traditional FSE-based criteria. A new research question arose from the results obtained in Chapter 4.1: "*Can a versatile tool be developed for different materials?*".
As a consequence, this chapter is a direct application of the PPW criterion to two more aluminum alloys. Specifically, AA2024 and AA6082 recycling chips were considered for investigating the solid bonding phenomena in FSC processes. Consequently, a dataset containing the details of solid bonding mechanics for the three aluminium alloys was built, and a generalized parametric model was developed, aiming to create a general prediction tool that can be used for predicting the bonding occurrence for all the aluminium alloys' recycling chips. The validation of this generalized model was also investigated by implementing a fourth aluminium alloy, namely AA5083.

Note: the images reported in this chapter are taken from the following published work [95].

4.2.1 Experimental methodology

In this case, chips of three different aluminum alloys, AA2024-T4, AA6082-T6, and AA5083-H111, were utilized (Figure 82). These chips were obtained from the as-received materials, with details listed in Table 12 by using the milling operation previously described in Table 7. The choice of these materials was driven by the difference in their thermo-mechanical properties, aiming to gain deeper insights into the FSC. Further, AA2xxx, AA5xxx, and AA6xxx alloys are popular materials in aerospace, marine, and automotive applications, respectively [36]. The experimental plan shown in Table 13 was executed for AA2024-T4 and AA6082-T6 using ESAB machine (Figure 83). For these materials, four experiments (Exp 1 to Exp 4 of Table 13) were performed to analyze and model the bonding occurrence; one experiment, with different process parameters settings (Exp 5), was used to validate the results. The indicated procedure was consistent with the approach proposed and described in Chapter 4.1 for AA7075.

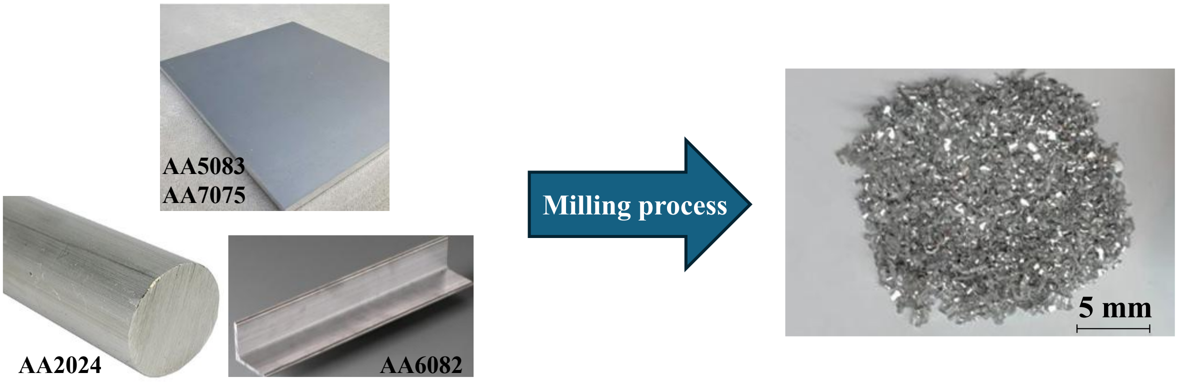

Figure 82. Schematic view of the milling process for obtaining aluminium chips from as-received material.

To verify the newly introduced formulation based on the proposed linear parametric model (described in Chapter 4.2.6), FSC recycled billets were manufactured from a fourth, new material (AA5083-H111); for this material, only Exp 1 and Exp 4 were developed, as it was used for validation purposes.

Table 12. Details of as-received materials.

S#	As-material	As-shape	Vickers hardness [Hv]	Grain size [µm]	TC [W/mm K]	SHC [J/g °C]
1	AA2024-T4	Extruded round bar	100	52.2	0.13	0.96
2	AA6082-T6	Extruded angle bar	98.7	8.6	0.17	0.9
3	AA5083-H111	Rolled sheet	70	75	0.12	0.87

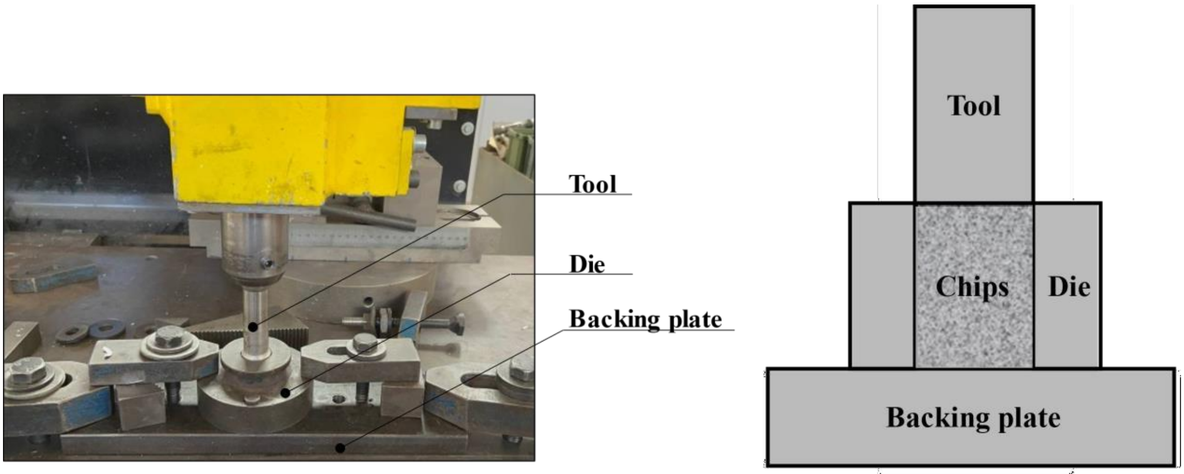

Figure 83. Friction stir consolidation experimental setup and process sketch.

Table 13. Process parameters setting of the developed FSC tests.

Exp ID	Rotational speed [RPM]	Mass [g]	Transition period [s]	Consolidation time [s]
Exp 1	1500	15	30	0
Exp 2	1500	15	30	10
Exp 3	1500	15	30	20
Exp 4	1500	15	30	30
Exp 5	1000	15	30	20

For each sample, hardness and microstructure characterization were developed; these analyses are needed for the definition of the experimental bonding criterion (see chapter 4.1.4). This criterion allows the bonding occurrence in the FSCed billet to be described, and it is based on hardness and grain size values.

4.2.2 Numerical methodology

The FSC process simulation was performed using the commercial software SFTC DEFORM 3DTM. Specifically, the model consists of four components: tool, die, backing plate, and chips (Figure 84). The tool, as well as the die and the backing plate, was considered a H-13 steel rigid component characterized by a mesh size of 30000 elements. Friction shear factors equal to 0.2, 0.25, and 0.28 were used to model the tool-chip contact for AA2024, AA6082, and AA5083, respectively. On the other hand, the chips were considered as a porous billet, using the Shima and Oyane [37] formulation to model the discrete nature of the starting billet. An initial relative density value of 0.44 was used to model the starting billet porosity; this value was experimentally quantified. The heat transfer coefficient was considered equal to 11 N/sec/mm/C, and a mesh of 30000 elements was used for the billet; a refining mesh window was also located in the tool-billet contact surface. The material mechanical behavior was evaluated through the study of the ASM compendium and the database JMatPro, for each material. The temperature stress-strain-strain rate curves obtained for AA2024, AA6082, and AA5083 are shown in Eq. 16, Eq. 17, and Eq. 18, respectively.

$$\sigma_f = 8.958 \cdot (18486.1 + \bar{\varepsilon})^{0.1729} \cdot \dot{\varepsilon}^{\,0.0485} \cdot exp^{549.865/T} \quad (16)$$

$$\sigma_f = 0.563 \cdot (34.819 + \bar{\varepsilon})^{1.49} \cdot \dot{\varepsilon}^{\,0.405} \cdot exp^{916.48/T} \quad (17)$$

$$\sigma_f = 6.4963 \cdot (18.546 + \bar{\varepsilon})^{0.1030} \cdot \dot{\varepsilon}^{\,0.00404} \cdot exp^{1090.52/_T} \quad (18)$$

The numerical simulation was tuned and validated through experimental temperature measurement at the center bottom of the billet by using a K-thermocouple. In Figure 85 temperature trends obtained from experimental and numerical measurements for each material are reported; a good overlap can be observed.

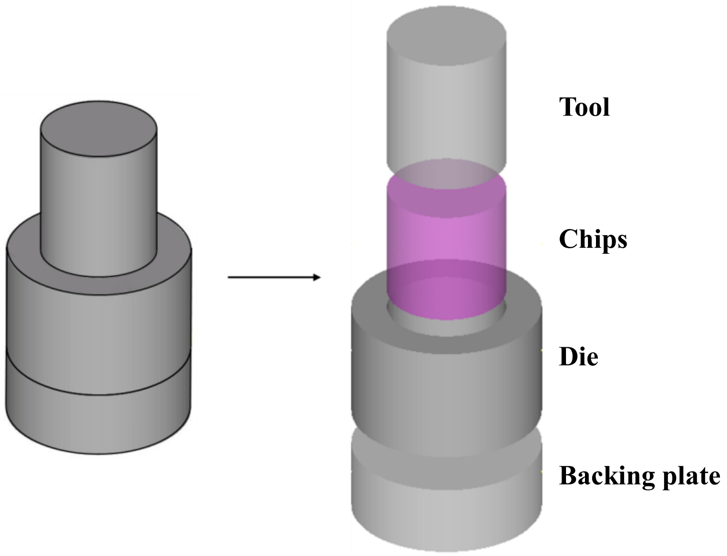

Figure 84. *Numerical model for tool, die, backing plate and porous billet.*

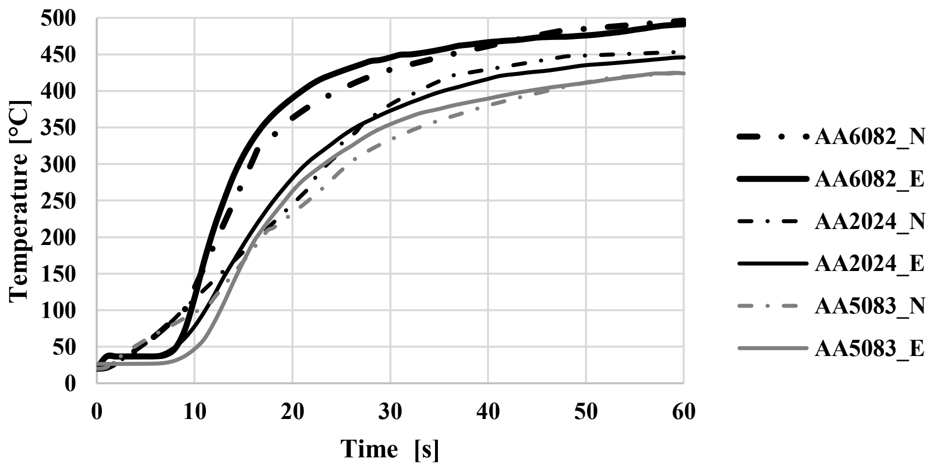

Figure 85. *Comparison between experimental and numerical temperature profiles during FSC, at the center bottom of the billet (N = numerical, E = experimental).*

The aim of these simulations was the acquisition of all the stress and strain values characterizing the FSC over the processing time (transition and consolidation). The trends of such a variable allow different bonding approaches to be analyzed and the bonding occurrence in FSC to be better investigated.

4.2.3 Analyzed bonding criteria

It has been proven that the available film theory model [32] fails in modelling the bonding occurrence in the FSC process and, moreover, they are very complex to implement as they require several assumptions to be made and coefficient values to be identified. For these reasons, only the energy barrier bonding criteria are analyzed, specifically the formulations reported in Table 6 will be taken into account.

The first three criteria (Akeret, Plata-Piwnik, Donati and Tomesani) were already available in literature and were used to predict the bonding occurrence in extrusion processes. The last two criteria of Table 6 (Weighted and Zener), were instead proposed here for the FSC process. All the criteria here reported were tested for each analyzed material by identifying the thresholds with an iterative procedure reported in Chapter 4.3.5.

4.2.4 Results and discussion

The aim of the experimental campaign is the definition of the experimental bonding map for each Exp I.D. (1 to 4) reported in Table 13 and for each of the analyzed materials. The experimental bonding map derives from the definition of an experimental bonding criterion defined in Chapter 4.2.3.

For the experimental bonding map implementation, it is necessary to develop thorough microstructural and hardness analyses of the FSCed samples. The grain size was measured throughout the billet section at 119 observation loci equally spaced at a distance of 1.5 mm (Figure 86).

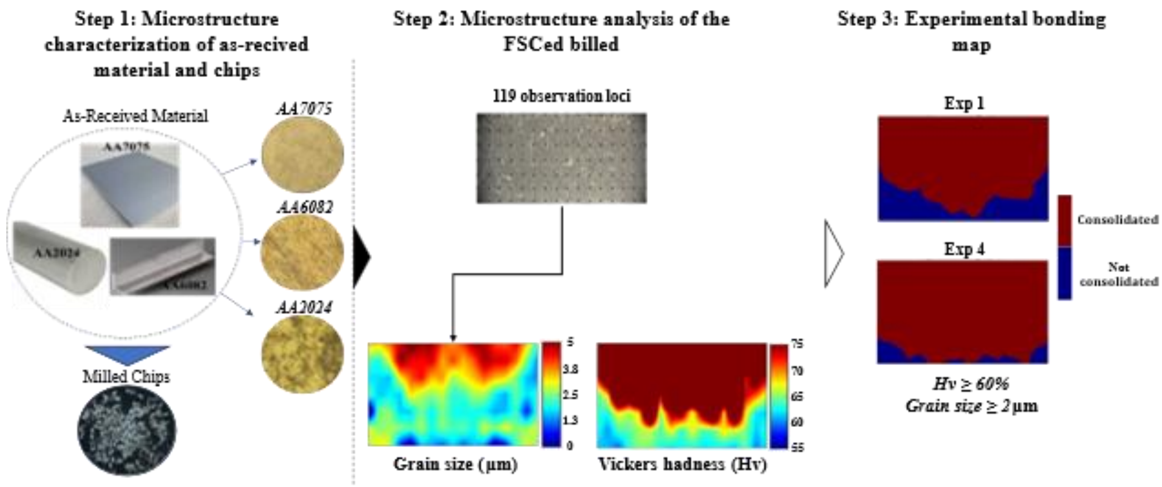

Figure 86. *Procedure adopted for the experimental campaign.*

The microstructural view of Exp 1 and Exp 4 for the AA2024 can be seen in Figure 87 and Figure 88 while those of AA6082 are reported in Figure 89 and Figure 90. To better highlight the grain size evolution, only Exp 1 and Exp 4 are shown as representing the first and the last time of acquisition.
It is clearly visible from Figure 87, Figure 88, Figure 89 and Figure 90 a direct correlation between processing time and the consolidation effect. The increasing processing time leads to an increase in the consolidation effect throughout the observed section of the specimen. In particular, for Exp 1 of AA2024 material (Figure 87) the upper section of the billet was fully recrystallized, but an unconsolidated zone with loose bonding chips was noticed at the bottom section of it. Further, the microstructure of the bottom zone was not much altered compared to the starting input material (chips). It indicates that processing time was not enough processing time to achieve full consolidation. As the processing time increased to 60s in the case of Exp 4 (see Figure 88), the consolidated zone expanded toward the bottom, resulting in a more consolidated area with good bonding conditions among the chips except near the external surface at the bottom. This zone, which can be compared to the dead zone of the extrusion process, can never reach the consolidation conditions, irrespective of the processing conditions [22].
Increasing processing time led to a larger consolidated area with improved billet quality in the case of the AA6082 (comparing Figure 89 and Figure 90). Concerning the influence of material, thermophysical characteristics such as the thermal conductivity of the input material could also play an important role. A material with a higher thermal conductivity proves conducive in transferring heat from the contact section towards the bottom section. Therefore, a higher heat transfer rate leads to a change in the microstructure of the bottom more rapidly compared to a material characterized by a lower value of thermal conductivity, as can be seen in the case of AA6082 compared to AA2024 (comparing Figure 87 and Figure 90). On the other hand, the AA6082 micrography shows that the grain growth is limited to the upper half of the billet's cross-section.

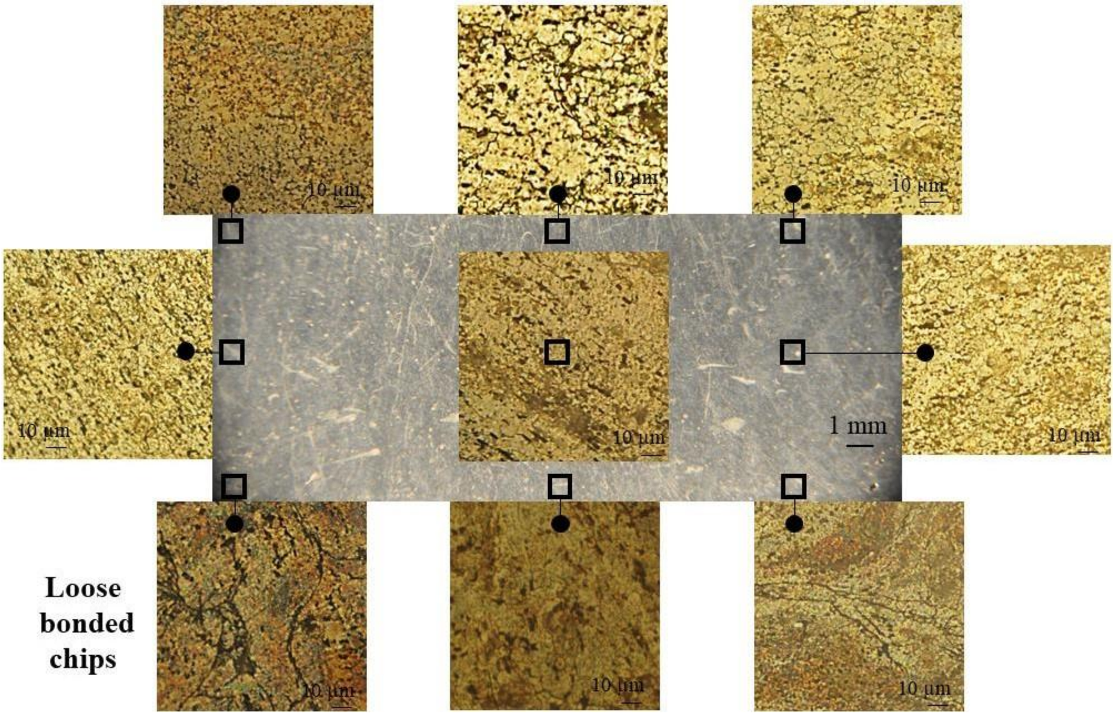

Figure 87. *Microstructural view of the grains for AA2024, Exp. 1.*

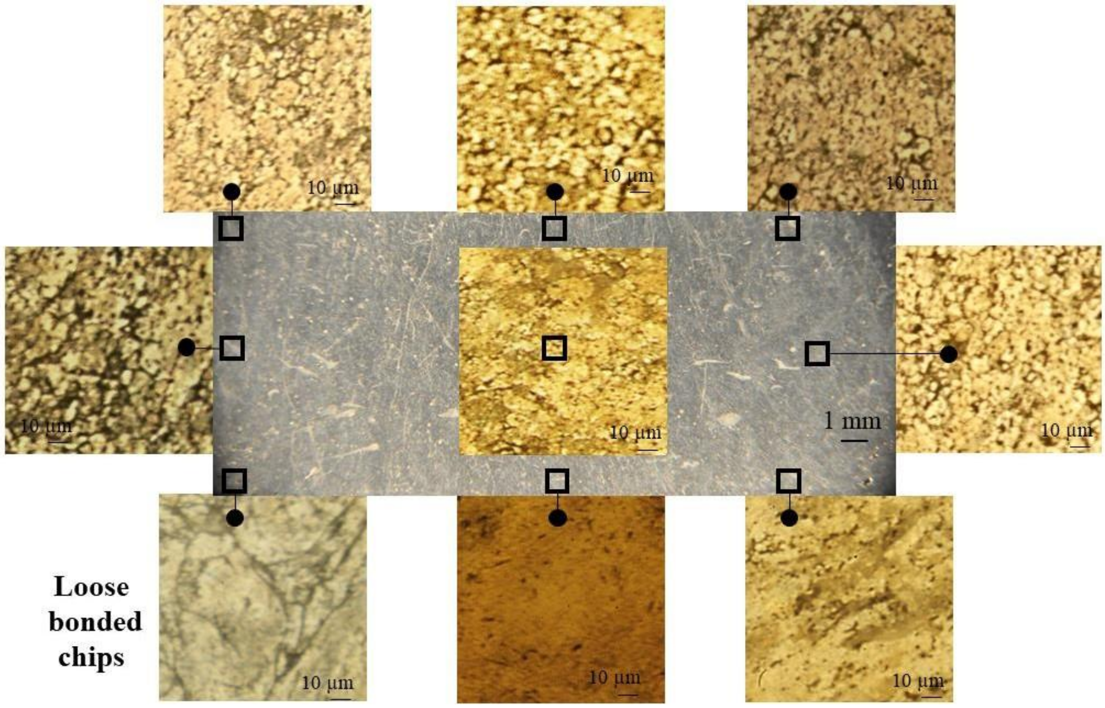

Figure 88. *Microstructural view of the grains for AA2024, Exp. 4.*

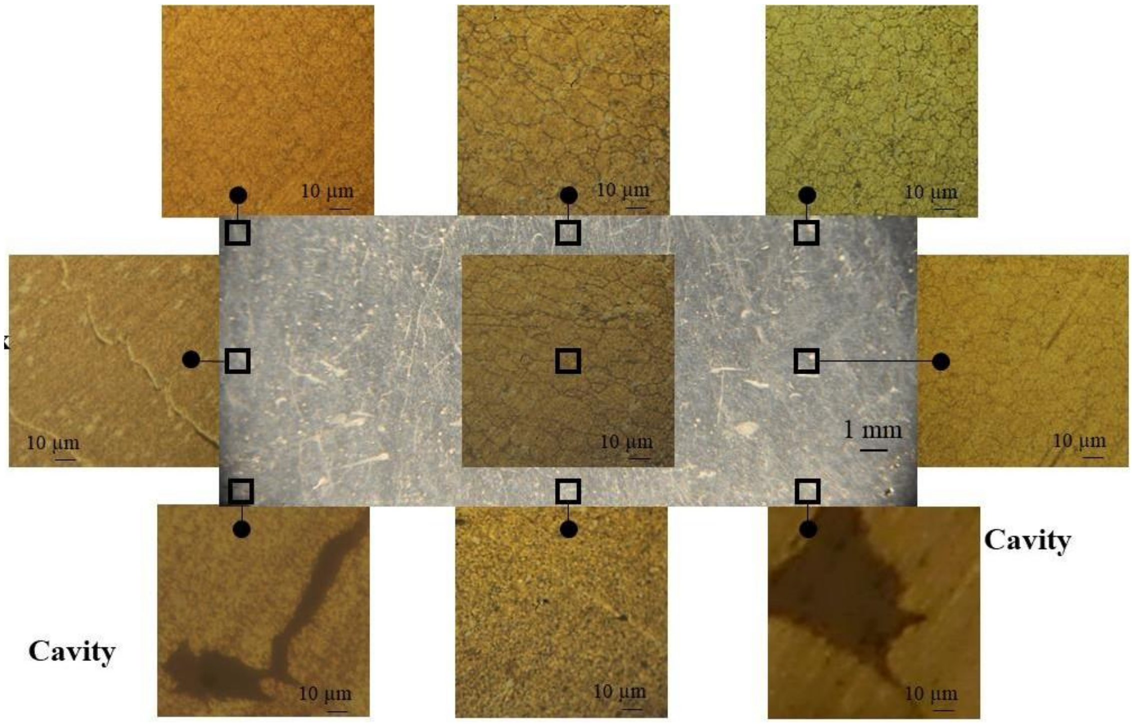

Figure 89. Microstructural view of the grains for AA6082, Exp. 1.

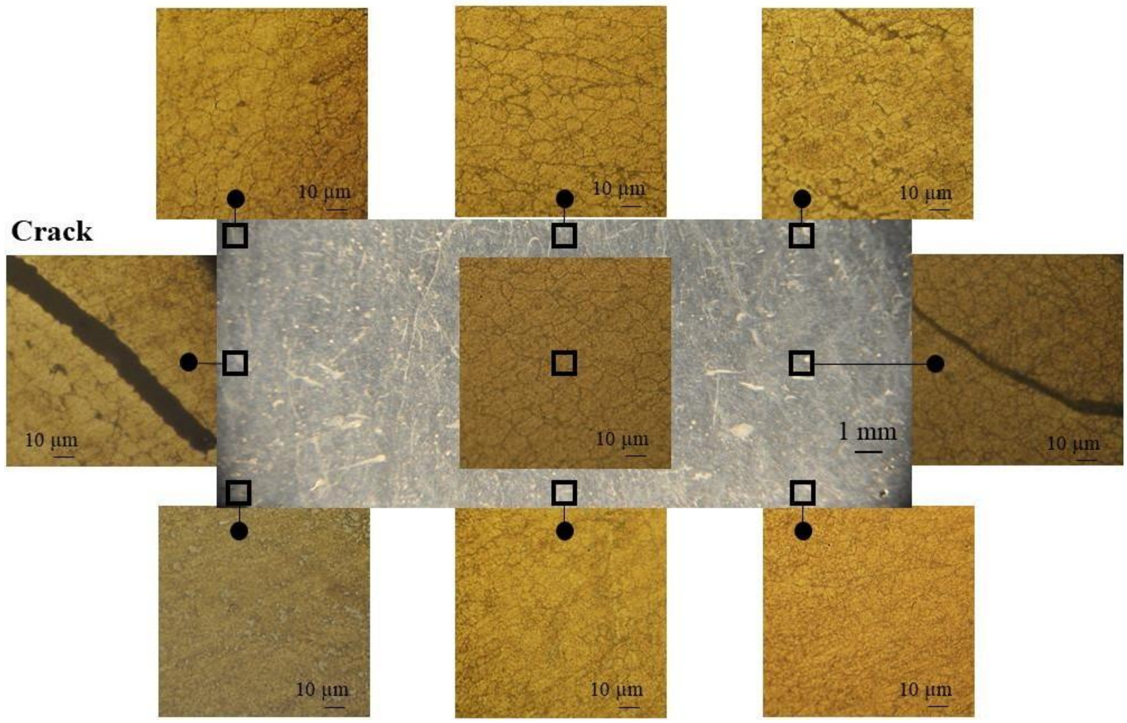

Figure 90. Microstructural view of the grains for AA6082, Exp. 4.

However, a clearer visualization of the bonding map can be obtained by analyzing the hardness and grain size values and combining them by the defined experimental bonding criterion. The grain size and hardness distributions for AA2024 and AA6082, along with the derived experimental bonding map, are reported in Figure 91 and Figure 92, respectively. The evolution of the consolidated area is clearly visible as it expands downward from Exp 1 to 4. With the selected process parameters, an almost fully consolidated billet can be obtained for the AA2024, whereas for the AA6082, a large part of the billet is still not consolidated, even in Exp 4. Overall, it is possible to notice that the consolidation region increases with increasing processing time; this phenomenon is due to the non-symmetric nature of the process, as the strain and heat flow start from the top region and move downwards. This finding has already been discussed by Xi et al. [42] Latif et al. [45].

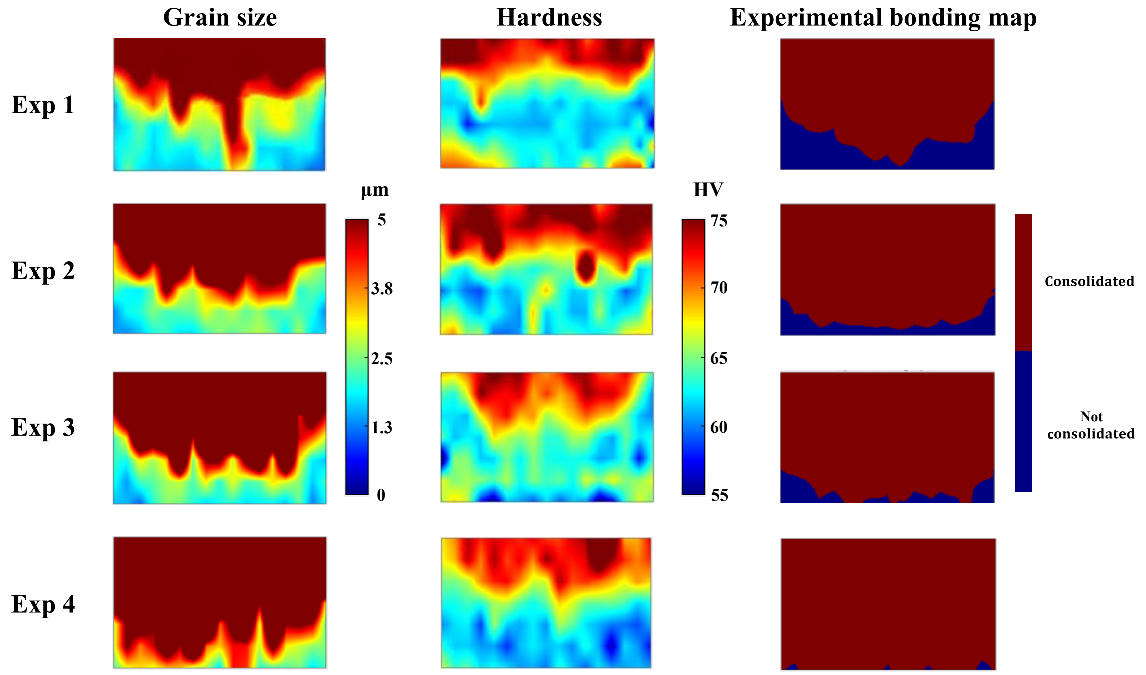

Figure 91. *Grain size and hardness distributions and experimental bonding map for Exp 1 to Exp 4 (AA2024).*

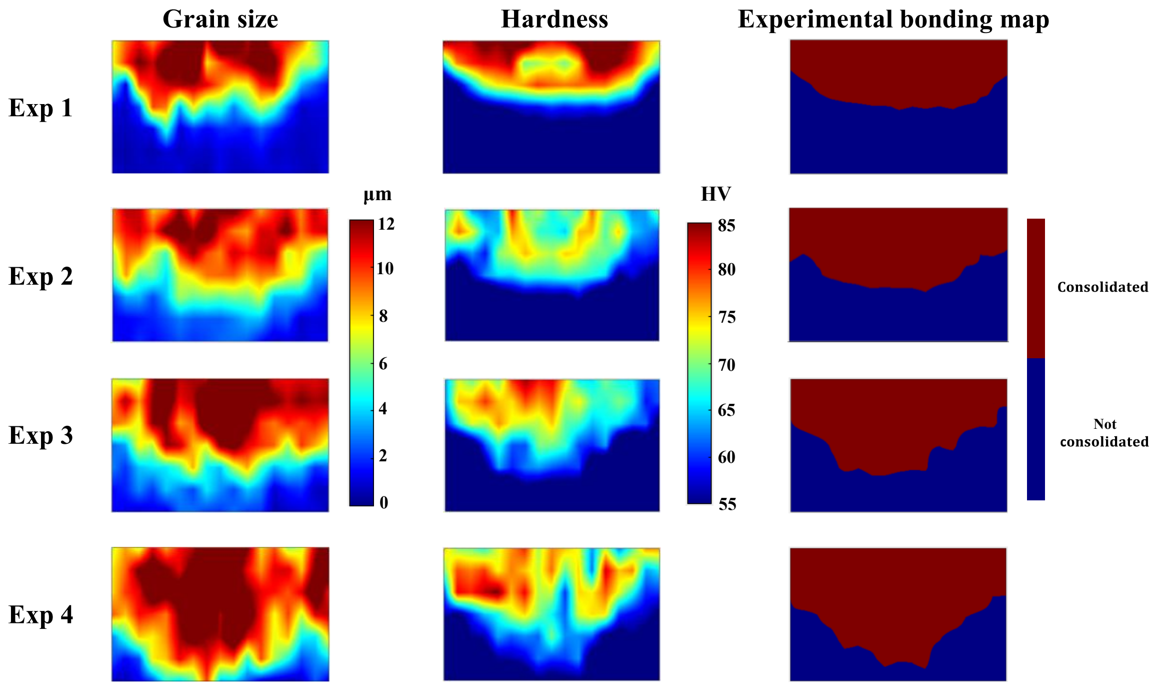

Figure 92. *Grain size and hardness distributions and experimental bonding map for Exp 1 to Exp 4 (AA6082).*

4.2.4.1 Numerical bonding maps

The mathematical iterative analysis for determining the solid bonding maps discussed in Chapter 4.1.6 was also applied in this study. The numerical and experimental bonding maps for AA2024 and AA6082 are reported in Figure 93 and Figure 95, respectively.

Correlation coefficients obtained for all the tested criteria, together with the identified threshold values, are reported in Table 14. It is possible to notice that Donati–Tomesani [77] and PPW [88] criteria provide the best performance and, overall, with increasing the processing time, the prediction performance of each criterion improves. The results are satisfactory as the numerical bonding maps perfectly mimic the experimental ones, as it is possible to notice in Figure 93.

Actually, for the AA2024 alloy case, both the PP and PPW criteria have good performance, as proved by the correlation coefficient values of Table 14 and the maps of Figure 93. Despite that, it is worth mentioning that the W^{lim} values increase moving from Exp 1 to Exp 4 for most of the criteria reported in Table 14; it means that W^{lim} increases with increasing the processing temperature. Specifically, this trend can be seen in Figure 94 where PP and PPW W^{lim} values obtained for each EXP I.D. are plotted.

This trend cannot be considered a reliable result if the solid bonding mechanics is considered: as a matter of fact, higher temperature increases the material softening effect, making it easier to achieve the solid bonding condition; the bonding limit must, therefore, decrease with increasing temperature [78]. Actually, the only criterion showing a clear decreasing trend with increasing temperature is the PPW, developed in Chapter 4.1.

Table 14. *W^{lim} and correlation coefficient for both criteria, case study AA2024.*

Criterion	Exp ID	Correlation coefficient	W^{lim}
Akeret (1992)	Exp 1	71%	$1.7 \cdot 10^{-1}$
	Exp 2	81%	$1.9 \cdot 10^{-1}$
	Exp 3	92%	$2.1 \cdot 10^{-1}$
	Exp 4	90%	$2.0 \cdot 10^{-1}$
Plata – Piwnik (2000)	Exp 1	78%	$2.6 \cdot 10^{-1}$
	Exp 2	82%	$4.2 \cdot 10^{-1}$
	Exp 3	92%	$5.8 \cdot 10^{-1}$
	Exp 4	91%	$7.1 \cdot 10^{-1}$
Donati – Tomesani (2004)	Exp 1	87%	$2.3 \cdot 10^{-2}$
	Exp 2	87%	$2.6 \cdot 10^{-2}$
	Exp 3	96%	$2.6 \cdot 10^{-2}$
	Exp 4	97%	$1.0 \cdot 10^{-3}$
Plata – Piwnik – Weighted (2023)	Exp 1	88%	$7.7 \cdot 10^{-4}$
	Exp 2	95%	$7.1 \cdot 10^{-4}$
	Exp 3	93%	$7.0 \cdot 10^{-4}$
	Exp 4	97%	$5.8 \cdot 10^{-4}$
Plata - Piwnik – Zener (2023)	Exp 1	45%	$1.0 \cdot 10^{-11}$
	Exp 2	81%	$5.0 \cdot 10^{-11}$
	Exp 3	92%	$6.0 \cdot 10^{-10}$
	Exp 4	94%	$1.6 \cdot 10^{-9}$

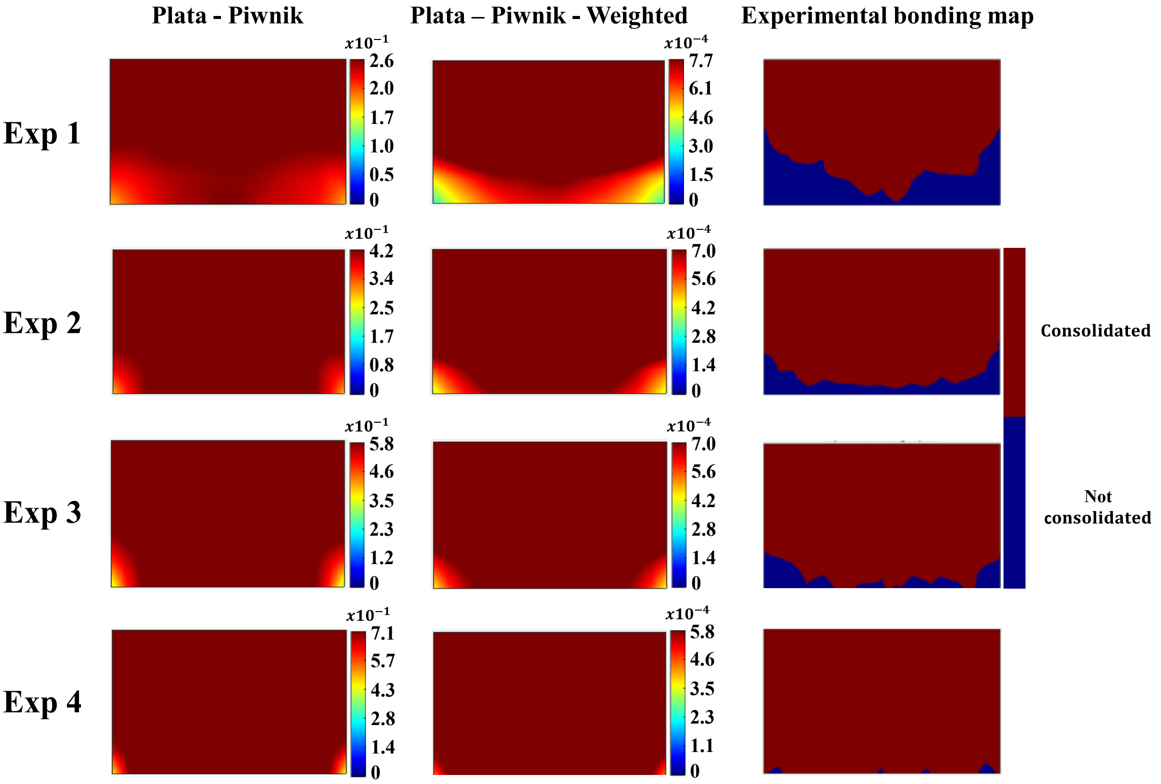

Figure 93. *Calculated solid bonding maps and experimental bonding maps (AA2024).*

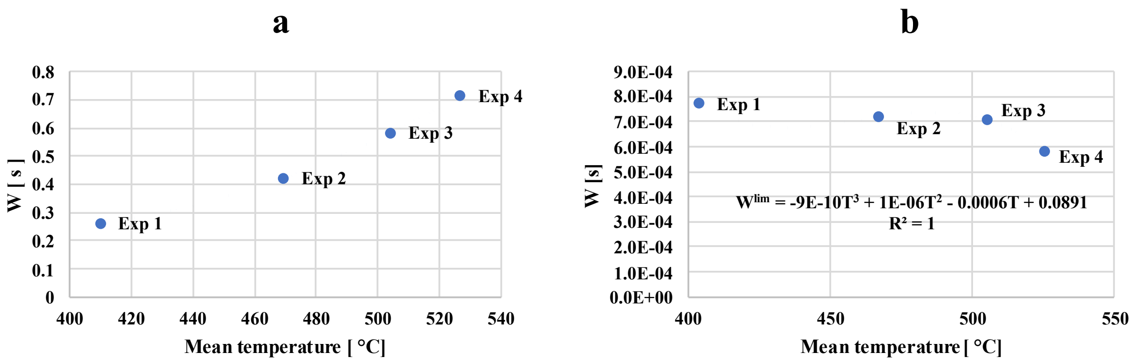

Figure 94. *Example of W^{lim} (threshold) temperature trends for the PP (a) criterion and for the PPW (b) AA2024.*

The same analyses were developed for the AA6082, and the results are reported in Table 15 and Figure 95. The Akeret and PP criteria provide poor results in terms of correlation coefficient; this bad performance is reflected in Figure 95. In this figure, it is possible to see that the PPW criterion again predicts the bonding map evolution perfectly, whilst PP criterion fails in predicting the bonding occurrence. Also, for the AA6082, the only criterion providing a clear decreasing W^{lim} trend with increasing temperature is the PPW.

Table 15. *W^{lim} and correlation coefficient for both criteria, case study AA6082.*

Criterion	Exp ID	Correlation coefficient	W^{lim}
Akeret (1992)	Exp 1	67%	$3.4 \cdot 10^{-1}$
	Exp 2	65%	$6.4 \cdot 10^{-1}$
	Exp 3	60%	$6.7 \cdot 10^{-1}$
	Exp 4	71%	$7.4 \cdot 10^{-1}$
Plata – Piwnik (2000)	Exp 1	91%	$3.7 \cdot 10^{-1}$
	Exp 2	67%	$8.6 \cdot 10^{-1}$
	Exp 3	61%	$1.5 \cdot 10^{-0}$
	Exp 4	75%	$2.2 \cdot 10^{-0}$
Donati – Tomesani (2004)	Exp 1	95%	$5.7 \cdot 10^{-2}$
	Exp 2	97%	$6.0 \cdot 10^{-2}$
	Exp 3	82%	$4.3 \cdot 10^{-2}$
	Exp 4	74%	$4.4 \cdot 10^{-2}$
Plata – Piwnik – Weighted (2023)	Exp 1	94%	$6.8 \cdot 10^{-4}$
	Exp 2	98%	$6.5 \cdot 10^{-4}$
	Exp 3	88%	$6.3 \cdot 10^{-4}$
	Exp 4	80%	$6.2 \cdot 10^{-4}$
Plata - Piwnik – Zener (2023)	Exp 1	86%	$1.0 \cdot 10^{-15}$
	Exp 2	97%	$1.5 \cdot 10^{-14}$
	Exp 3	85%	$5.1 \cdot 10^{-14}$
	Exp 4	84%	$1.8 \cdot 10^{-13}$

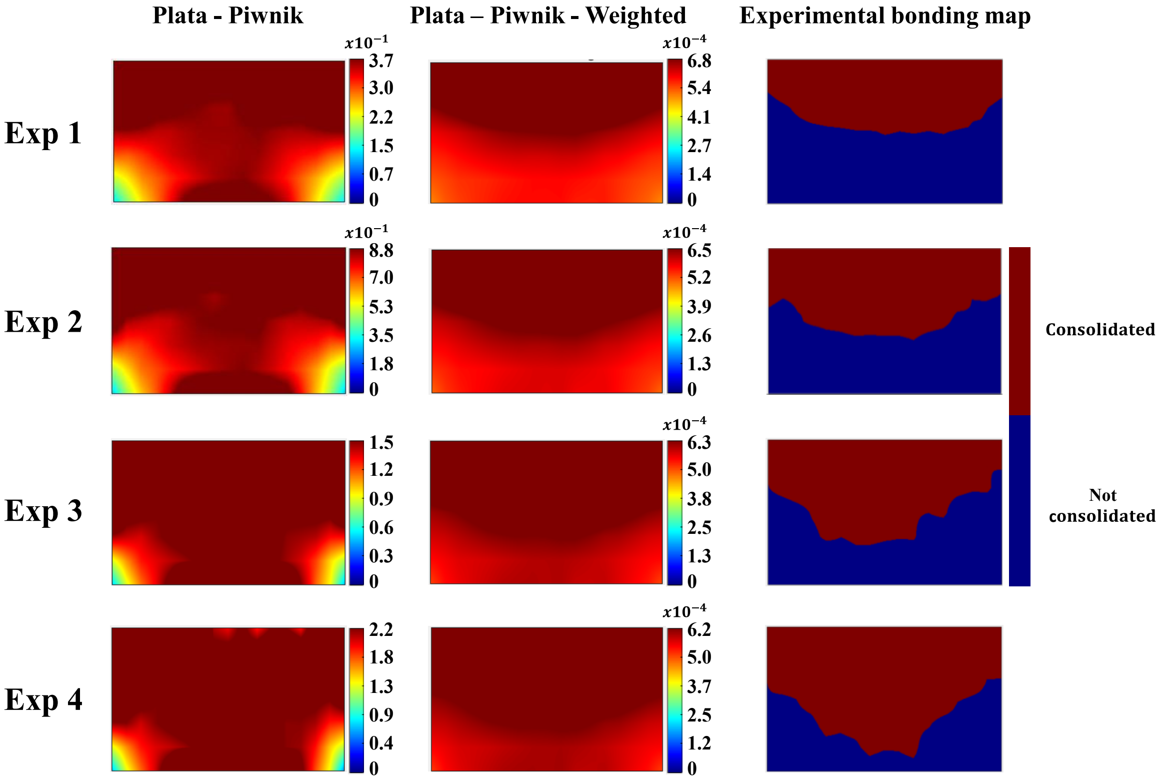

Figure 95. *Calculated solid bonding maps and experimental bonding maps (AA6082).*

In order to validate the performance of the proposed criterion on these two new aluminum alloys here tested, one more experiment for each alloy was performed. The process parameters used are the Exp 5 configuration reported in Table 13. The validation procedure is based on the comparison between the predicted bonding map, generated with the W^{lim} values reported in Table 14 and Table 15, with the experimental bonding map. For each criterion, the Wlim values vs temperature values were interpolated by a third order model (see Figure 94b) allowing to identify the Wlim for a given processing temperature. The numerical bonding map was actually derived from local calculation of the bonding criteria values on 119 observation loci as described in Chapter 4.3.4. If this value is higher than the W^{lim} calculated by the third order model, that point was labeled as consolidated, vice versa it was labeled as not consolidated.

The validation results for the AA2024 are reported in Figure 96, where the predicted numerical bonding map by the PPW and the PP criteria are reported along with the experimental bonding map. In order to improve the results visualization, each observation loci are represented by a small rectangle (red = consolidated; blue = not consolidated). It is possible to note that the PPW criterion has excellent prediction performance, as it mistakenly predicts the bonding occurrence only in 4 loci. Whereas the PP provides poor performance, overestimating the bonding map extension. This means that although the PP criterion has good correlation coefficients (at least for the AA2024), it cannot predict the bonding occurrence for conditions different from those the cubic model was built; in other words, it cannot be used as a predictive criterion.

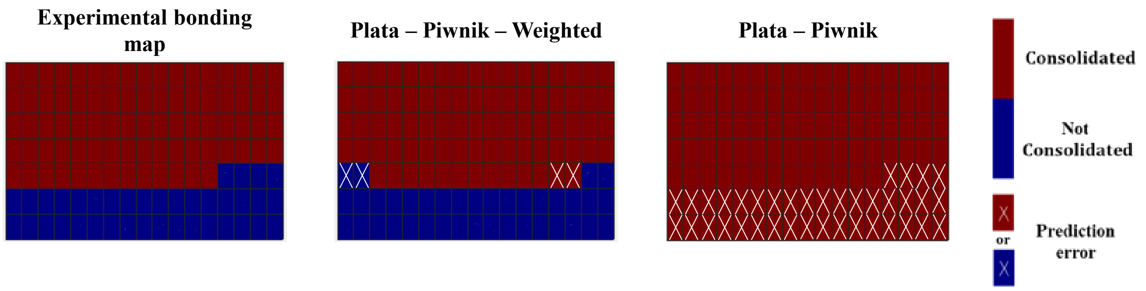

Figure 96. *Graphical analysis of the error's prediction for the validation test, case study AA2024.*

The results of the validation procedure for each criterion are reported in Table 16 and Table 17 for AA2024 and AA6082, respectively. It is possible to see that the best performance in predicting the bonding occurrence in FSC is provided by the PPW. In fact, an error prediction, the percentage of loci mistakenly predicted is equal to 6% for AA2024 and 11% for AA6082. Good performance is also provided by the Donati and Tomesani criterion.

These results allow to positively answer the first question of the present research. Actually, it has been proven that the PPW criterion is effective on different aluminum alloys. Specifically, it predicts and models the bonding occurrence in FSC processes correctly; the performance provided is better than that provided by the other criteria. This criterion particularly outperforms the other criteria in generalization capability, in fact providing the best performance in the validation test.

Table 16. *Prediction of the bonding occurrence for each observation loci, AA2024.*

Criterion	N° loci well predicted	N° total loci	Error
Akeret	89		26%
Plata - Piwnik	81		32%
Donati - Tomesani	113	119	6%
Plata - Piwnik - Weighted	115		4%
Plata - Piwnik - Zener	65		46%

Table 17. *Prediction of the bonding occurrence for each observation loci, AA6082.*

Criterion	N° loci well predicted	N° total loci	Error
Akeret	55		54%
Plata - Piwnik	55		54%
Donati - Tomesani	105	119	12%
Plata - Piwnik - Weighted	108		9%
Plata - Piwnik - Zener	86		28%

4.2.5 Model generalization - linear parametric model development

In this Chapter, a parametric model is presented with the purpose of generalizing the bonding limit curve by means of a predictive parametric linear model based on the thermo-mechanical material properties. The choice of shifting towards a linear model was driven by the will to simplify the modelling effort, still keeping up the bonding prediction performance of the model itself. The parametric model was developed following the workflow reported in Figure 97.

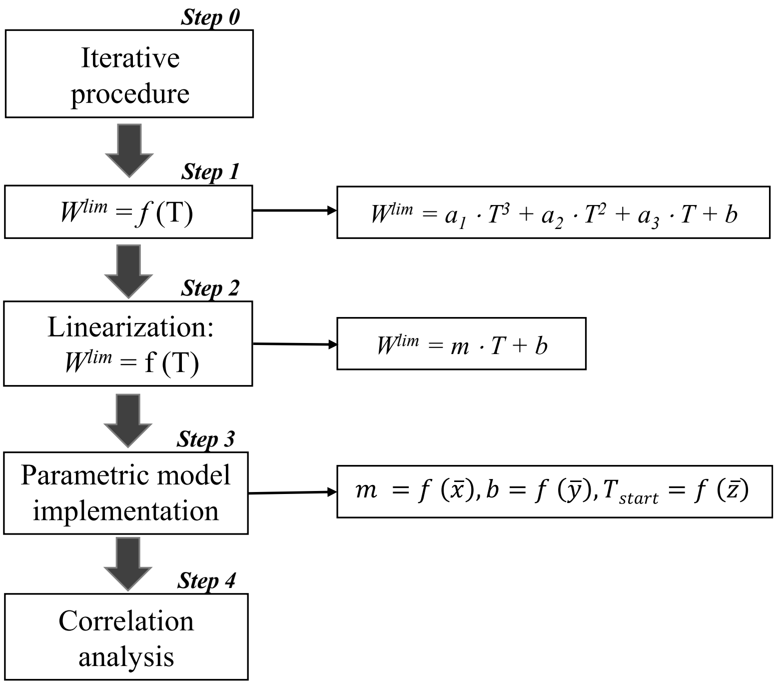

Figure 97. *Workflow for the parametrization of the bonding limit curve, where a is the constant values (third-order curve), m and b are the slope and the y-intercept of the straight line, respectively.*

In the modelling, the results obtained with the PPW criterion were used for the three different materials. The trends of W^{lim} values vs temperature, instead of being interpolated by a third-order polynomial curve, were approximated by linear models. The cubic and linear curves for all the analyzed materials are reported in Figure 98. The linear models obtained for the three different aluminum alloys are reported in Eq. (19), Eq. (20), and Eq. (21).

In order to test the prediction performance of the linear model with respect to that of the cubic model, a performance check step was executed. The performance check was developed by comparing the bonding prediction accuracy provided by either the cubic or the linear models with the experimental bonding map. Results in terms of correctly predicted loci are reported in Table 18. As it is possible to note, by using the linear model, only a slight worsening in prediction accuracy occurs; this result makes the linear models reliable tools for the modeling of solid bonding occurrence in FSC.

It should be observed that in Figure 98 for each material, a T_{start} temperature is indicated, namely a temperature threshold at which the bonding phenomenon is first recognized.

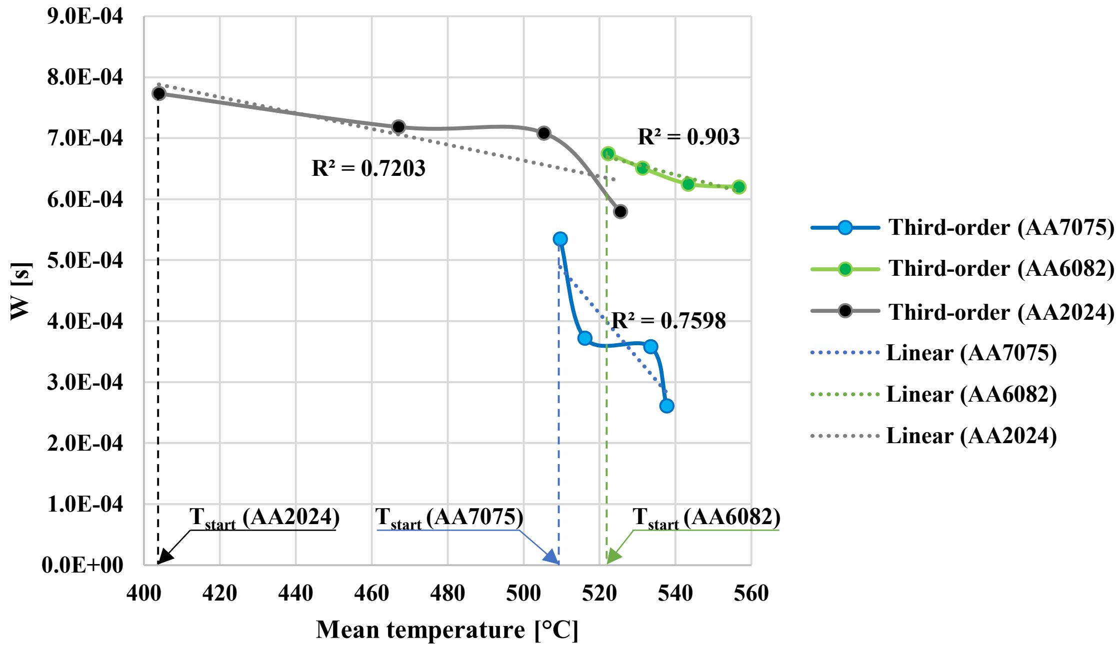

Figure 98. *W^{lim} vs mean temperature curve evaluated in four observation windows (points) for three materials. Exp 1 up to Exp 4 from left to right (for all the three curves).*

AA7075: $$W^{lim} = -7.35 \cdot 10^{-6} T + 0.0042, R^2 = 0.76 \quad (19)$$

AA6082: $$W^{lim} = -1.62 \cdot 10^{-6} T + 0.0015, R^2 = 0.90 \quad (20)$$

AA2024: $$W^{lim} = -1.3 \cdot 10^{-6} T + 0.0013, R^2 = 0.72 \quad (21)$$

Table 18. *Comparison of the validation results between third-degree and linear interpolation curves, for the Plata – Piwnik – Weighted criterion.*

Interpolation curve	Material	N° loci well predicted	Total observation loci	Error
Third order	AA2024	115	119	4%
	AA7075	112	119	6%
	AA6082	108	119	11%
Linear	AA2024	109	119	9%
	AA7075	113	119	6%
	AA6082	100	119	16%

Once the linear models were obtained, it was possible to focus on the parametric model development. Specifically, the idea was to express the slope (m), the y-intercept (b) and the starting temperature (T_{start}) as a function of the thermo-mechanical properties of the analyzed material (Table 19). In this regard, the properties reported in Table 20 were taken into account. In this table, the identified m, b, and T_{start} values for the three different materials are also reported. Tensile tests were developed on the base materials to obtain UTS, TYS, and EB values; thermal properties have been identified on dedicated databases [92, 93].
With the data reported in Table 20, a simple correlation analysis was performed in an Excel environment, and the related correlation coefficients are reported in Table 21. It is worth remembering that the closer to either -1 or 1 the coefficient values are, the stronger the relationship between the analyzed couple of items is. A coefficient value close to 1 means a strong positive relationship (one variable increases, the other increases almost proportionally). A coefficient of -1 means a strong negative relationship (one variable increases, the other decreases more or less proportionally).
For the slope (m) and y-intercept (b) models, TYS and SHC were selected as independent variables to build the linear model on. Actually, the correlation coefficient values were high, with an absolute value very close to one. As far as the T_{start} is concerned, only EB was selected instead. The identified linear model equations, with the related R-squared values, are reported in Eqs 22, 23, and 24.

__Table 19.__ Thermo-mechanical properties for the four aluminium alloys studied.

	Tensile yield stress [MPa]	Ultimate Tensile Strength [MPa]	Elongation at break [%]	Hardness [HV]	Thermal conductivity [W/mm °C]	Specific heat capacity [J/g °C]
AA7075	503	572	11	175	0.14	0.96
AA6082	250	290	9	95	0.17	0.9
AA2024	324	469	20	137	0.12	0.875
AA5083	193	300	16	91	0.12	0.9

__Table 20.__ List of angular coefficients (m), y-intercept (b), experimental starting temperature and thermo-mechanical properties.

	m (slope)	b (y-intercept)	T_{start} [°C]	TYS [MPa]	UTS [MPa]	EB [%]	Hv [HV]	TC [W/mm K]	SHC [J/g °C]
AA7075	-7.35E-06	0.004233	510	503	572	11	175	0.13	0.96
AA6082	-1.62E-06	0.001517	520	250	290	9	95	0.17	0.9
AA2024	-1.30E-06	0.001313	400	324	469	20	137	0.12	0.87

__Table 21.__ Correlation values of m, b and starting temperature with the thermo-mechanical properties.

	TYS [MPa]	UTS [MPa]	EB [%]	Hv [HV]	TC [W/mm K]	SHC [J/g °C]
m (slope)	-0.944	-0.748	0.389	-0.825	0.298	-0.971
y-(intercept)	0.939	0.738	-0.403	0.817	-0.284	0.974
T_{start}	0.159	-0.228	-0.995	-0.104	0.698	0.673

As is possible to notice in Table 21, the slope (m) has a negative correlation with the tensile yield strength (TYS) and the specific heat capacity (SHC), whilst a positive correlation was observed for the y-intercept (b). On the other hand, the starting temperature has a negative correlation with the elongation to break (EB).

It is possible to define a generalized parametric function involving the values of the angular coefficient, constant term, and starting temperature. To be more specific, for each of the considered materials, it was evaluated the equation of a straight line was evaluated using the value of m, b, and T_{start} calculated using the obtained correlation with TYS, SHC, and EB (Eq. 22, Eq. 23, Eq. 24).

$$m = 4.361 \cdot 10^{-5} - 1.148 \cdot 10^{-8} \cdot TYS - 4.696 \cdot 10^{-5} \cdot SHC,\ R^2 = 1 \quad (22)$$

$$b = -2.089 \cdot 10^{-2} + 5 \cdot 10^{-6} \cdot TY + 2.346 \cdot 10^{-5} \cdot SHC,\ R^2 = 1 \quad (23)$$

$$T_{start} = -11.311 \cdot EB + 627.48,\ R^2 = 0.99 \quad (24)$$

4.2.6 Model validation

In order to test the designed parametric model, a fourth material was selected. Specifically, the AA5083 aluminum alloy was used. For this fourth material, two process parameter configurations were investigated, namely Exp 1 and Exp 4 parameter settings of Table 13. The validation phase consisted of the following steps.

Step 1: Identifying the solid bonding map.

Step 2: Applying the iterative procedure for W^{lim} (PPW criterion) calculation in Exp 1 and Exp 4 conditions (A and B in Figure 99).

Step 3: Collecting TYS, UTS, and EB values for the new material (AA5083).

Step 4: Building the W^{lim} linear model by applying Eq. 22-24.

Step 5: Comparing the obtained prediction with that obtained with the conventional procedure (step 3).

By implementing this procedure, the obtained W^{lim} linear equation for the AA5083 material is reported in Eq. 25.

$$W^{lim} = -8.69 \cdot 10^{-7}\, T + 0.0012 \quad (25)$$

with a T_{start} equal to 426 °C.

In Figure 99 the predicted linear model for the AA5083 material is reported together with the linear models discussed in Chapter 4.2.5 (Figure 98). The W^{lim} values for the two process parameter settings are also reported (Exp 1 and Exp 4). It is worth mentioning that these values have been calculated with the automatic procedure discussed in Chapter 4.3.5. These values, therefore, serve as a benchmark for assessing the accuracy of the bonding map predicted on the basis of the W^{lim} values predicted by Eq. 25.

It is possible to see that the predicted linear curve for the AA5083 is very close to the W^{lim} calculated in Exp 1 and Exp 4 conditions. To further explore the effectiveness of the predicted W^{lim} values, the bonding map obtained by using the W^{lim} values calculated by the iterative procedure of Chapter 4.1.4 and the W^{lim} predicted by the predicted linear model of Eq. 25 are plotted in Figure 100 along with the experimental bonding map. It can be seen that the predicted and calculated bonding maps are very close to each other and, more importantly, mimic the experimental map perfectly.

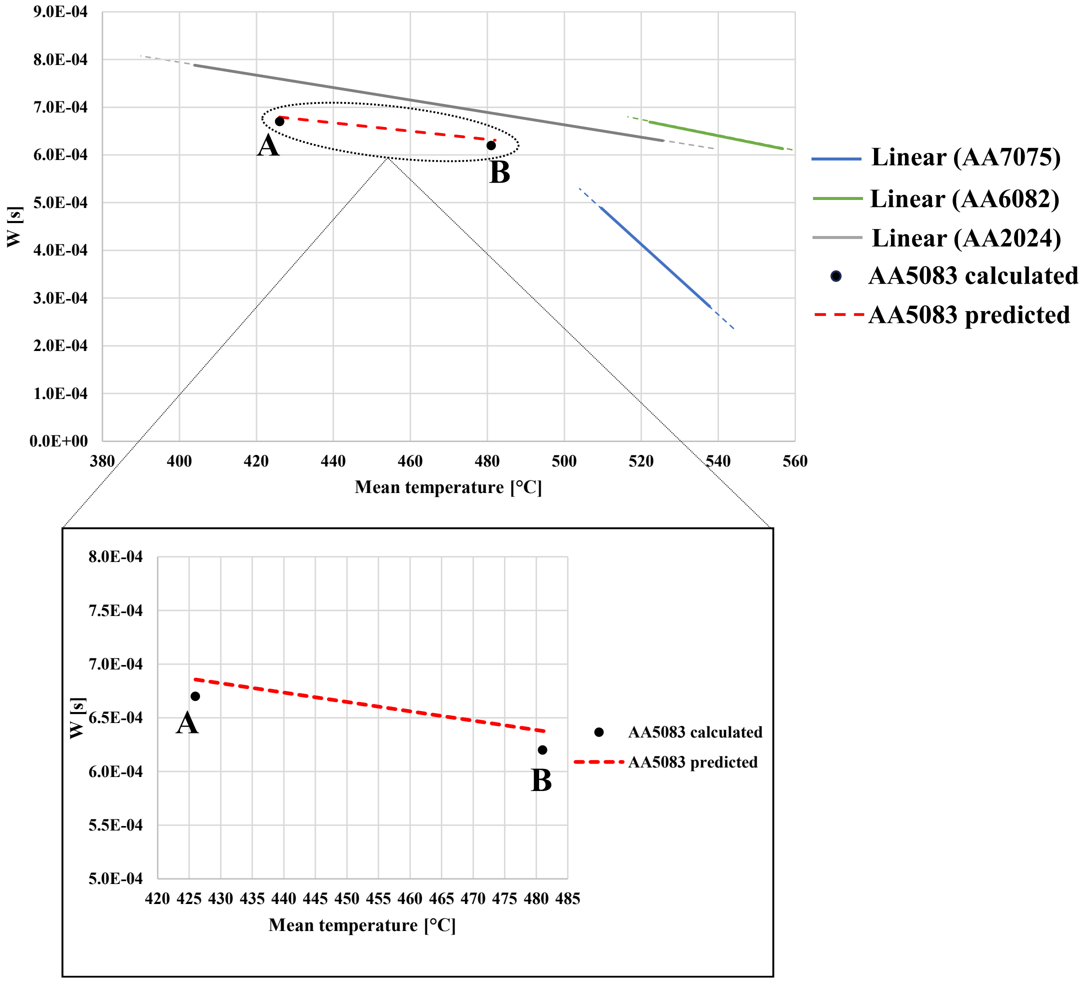

Figure 99. *W^{lim} linear models.*

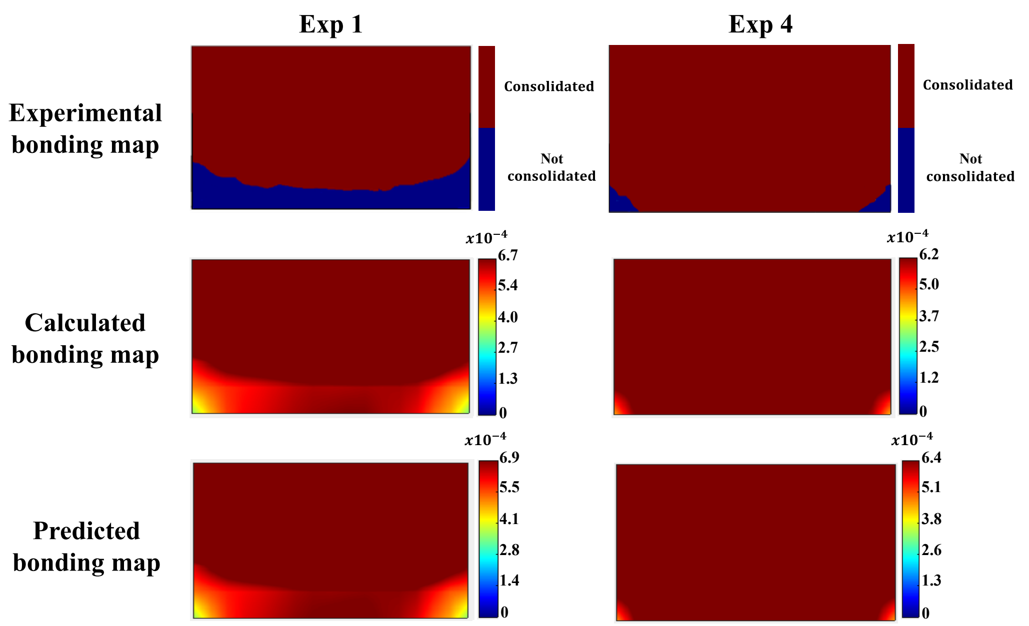

Figure 100. *Experimental, calculated and predicted bonding maps for AA5083 in EXP 1 and EXP 4 conditions.*

In this way, also the second research question of the study was effectively addressed: a parametric model was set up able to describe, with a single analytical expression, the bonding occurrence of different materials at the variation of properly selected thermo-physical characteristics.

4.2.7 Summary of the results

The overall aim of this research was to provide knowledge and tools for analyzing and predicting the bonding occurrence in FSC of aluminum alloy chips. Starting from the Plata–Piwnik–Weighted (PPW) solid bonding criterion already presented and tested for the FSC of AA7075 chips, here, two more pieces of knowledge have been added.

- The effectiveness of the PPW criterion has been proven on two more aluminum alloys, namely AA2024 and AA6082. Specifically, the performance provided is better than that of the other solid bonding criteria presented in the literature. This criterion particularly outperforms the other criteria in generalization capability. In fact, it provides the best performance also on the validation test, providing for both the proposed materials a very low error prediction (percentage of loci mistakenly predicted): namely, 6% for AA2024 and 11% for AA6082. These results strengthen the findings concerning the FSC criterion presented here, making it usable for a wide range of materials (at least for the aluminum alloys materials family).
- On the basis of the knowledge acquired to meet the first research objective, a further generalization effort was developed. In particular, a linear parametric model was designed to predict the W^{lim} vs Temperature curves with varying material properties. The W^{lim} vs Temperature was reduced to a linear model, so that it could be modeled by knowing the slope (m), the y-intercept (b), and the activation temperature (T_{start}). A correlation analysis was carried out to identify three different linear analytical expressions able to link m, b, and T_{start} with some of the thermo-mechanical material properties. Results of this approach showed that to identify the W^{lim} curve vs temperature curve for the PPW criterion, it is enough to know just the Specific Heat Capacity, the Tensile Yield Strength, and the Elongation at Break of a given material.
- The model was successfully tested for predicting the bonding occurrence of FSC of a further material, namely the AA5083; the predicted bonding map matched the experimental bonding map perfectly.

4.3 Friction stir consolidation applicability to magnesium alloys

This research framework extends the methodology applied to aluminium recycling chips to AZ31B magnesium alloy. In addition to the mechanical properties of the FSC magnesium billet, a brief power consumption analysis was carried out to measure the energy demand of the process, compared to the aluminium one.

Note: the images reported in this chapter are taken from the following published work [96].

4.3.1 Experimental methodology

In this research, a (30 x 80 mm) AZ31B bar, 76 HV of microhardness value, was used to obtain magnesium chips through a milling operation performed at 1250 rpm, a feed rate of 28 mm/min, and a cutting depth of 1 mm. Figure 101 shows a sketch of the process setup.

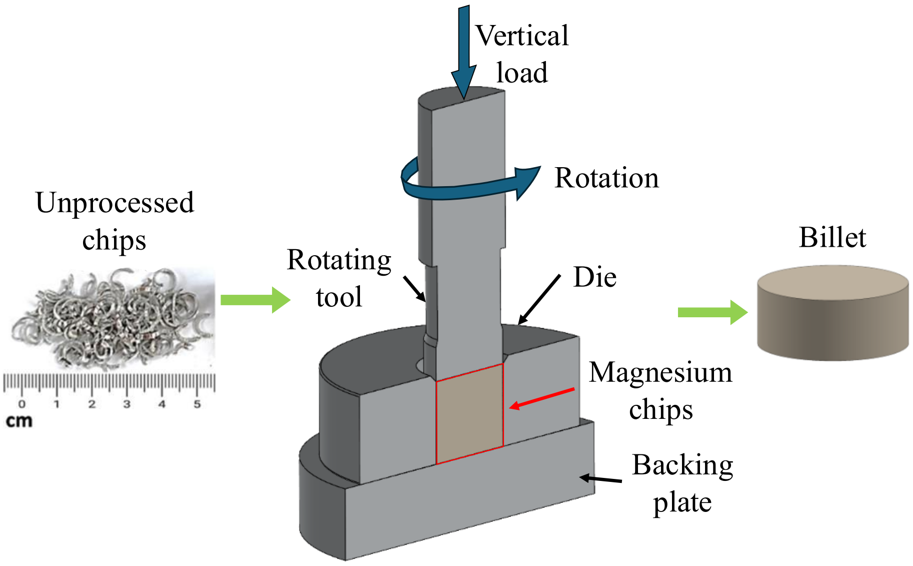

Figure 101. *Chips, experimental setup, and consolidated billet, for the FSC process.*

The process parameters and the process times are listed in Table 22. Overall, four tests were carried out to investigate the AZ31B magnesium alloy consolidation during the FSC process. After producing the samples, in order to prepare the specimens for hardness measurement, they were cut into two halves and the cross-sections were mechanically ground using abrasive papers of different grit sizes and polished with a diamond suspension (see Chapter 4.1.3). Details about harness measurements are provided in the discussion of the results section.

Table 22. *Process parameters and time, for the FSC of AZ31B magnesium alloy.*

Exp ID	Rotational speed [RPM]	Mass [g]	Transition period [s]	Consolidation time [s]
Exp 1	1500	15	30	0
Exp 2	1500	15	30	10
Exp 3	1500	15	30	20
Exp 4	1500	15	30	30

For each test, the power-time data was collected by connecting the power meter CHAUVIN ARNOUX C.A. 8331 to the electrical connection to the Esab machine. The recording started at the first compaction, until the end of the process.

4.3.2 Numerical methodology

The numerical simulation of the process was performed by using the commercial software SFTC DEFORM 3D^{TM}. As for the experimental campaign, this model involves four different parts: a die, a tool, a backing plate, and chips (Figure 102a). The first three parts were considered as H-13 steel rigid bodies with a mesh size of 30000 elements. On the other hand, the chips were modelled as porous-billet, characterized by a Shime-Oyane formulation [86] for porous material, initial relative density equal to 0.44, meshed by 20000 elements, with a refining mesh window located near the tool-billet contact. By a temperature tuning sing a K-thermocouple at the bottom center of the billet (Figure 102b), the shear factor was found equal to 0.3, and the heat transfer coefficient was found equal to 11 W/mm^2/K.

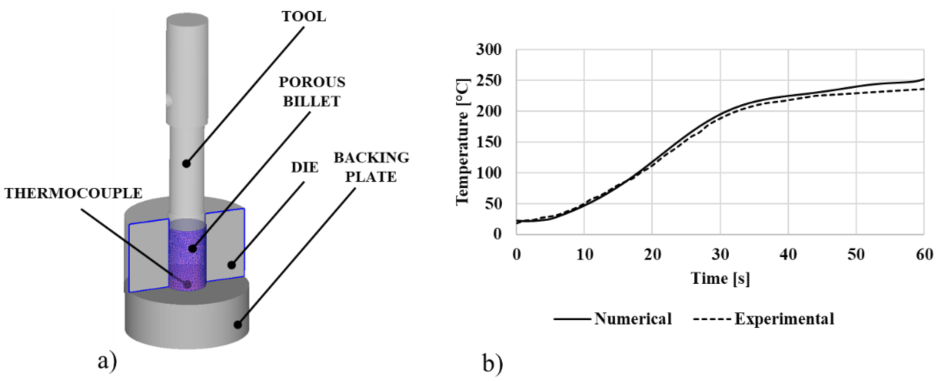

Figure 102. *a) FSC numerical setup and b) temperature tuning.*

4.3.3 Results and discussion

The variation in consolidation time was performed to assess the effect of the parameters on the chips' consolidation. The experimental campaign resulted in four billets having different levels of consolidation. The samples were cut, mounted, and the cross-section was analyzed. From the cross-section, it is clear to notice that the main issue of the FSC process, namely the low-tier consolidation at the bottom, was still visible, and the portion of the billet that was not consolidated decreases with the increase in the consolidation time (Figure 103c).

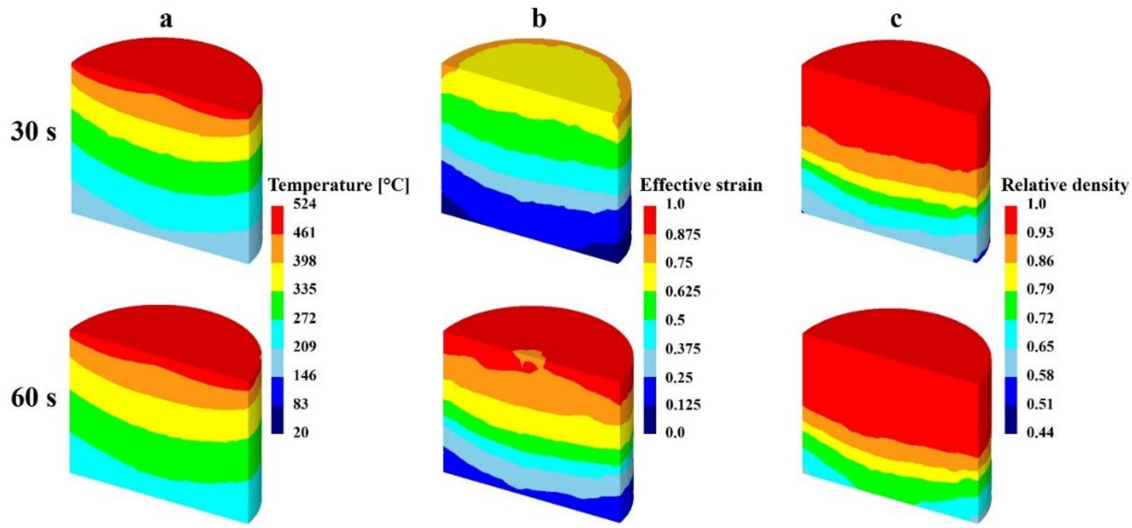

Figure 103. *Cross section of the billets at 30 and 60 seconds of consolidation time; a) temperature, b) strain and c) density plot.*

For verifying the chips' consolidation, a hardness analysis was conducted. The evolution of the hardness values was evaluated by means of a vertical set of 15 points, starting from the top of the billet, tool action zone, to the bottom. Figure 104 shows the HV measured in a cross-section along 3 vertical lines equally spaced with a horizontal pitch of 5 mm with respect to the center of the specimen (0, +5, +10 on x-axis) and with a vertical pitch of 1mm.

The study of the hardness for an FSCed billet was already presented, and a decreasing trend was expected from the top to the bottom of the billet. This effect is mainly due to the inhomogeneity of heat transfer during the process and the localized stirring action of the tool; the heat generation belongs to the friction between the tool and the metal material, and for this reason, it starts from the top of the billet. Consequently, the bottom corner of the billet is the part that has the biggest heat exchange, so it will be the least consolidated part (Figure 103a). On the other hand, the material is stirred mostly near the tool-material contact zone (Figure 103b), therefore, the tool is less likely to affect the oxide breakage at the bottom part of the billet, leading to a lower mechanical property in these zones.

The hardness results for the magnesium case study are visible in Figure 104 going into detail for 30s (Figure 104c) and 60s (Figure 104d) trends.

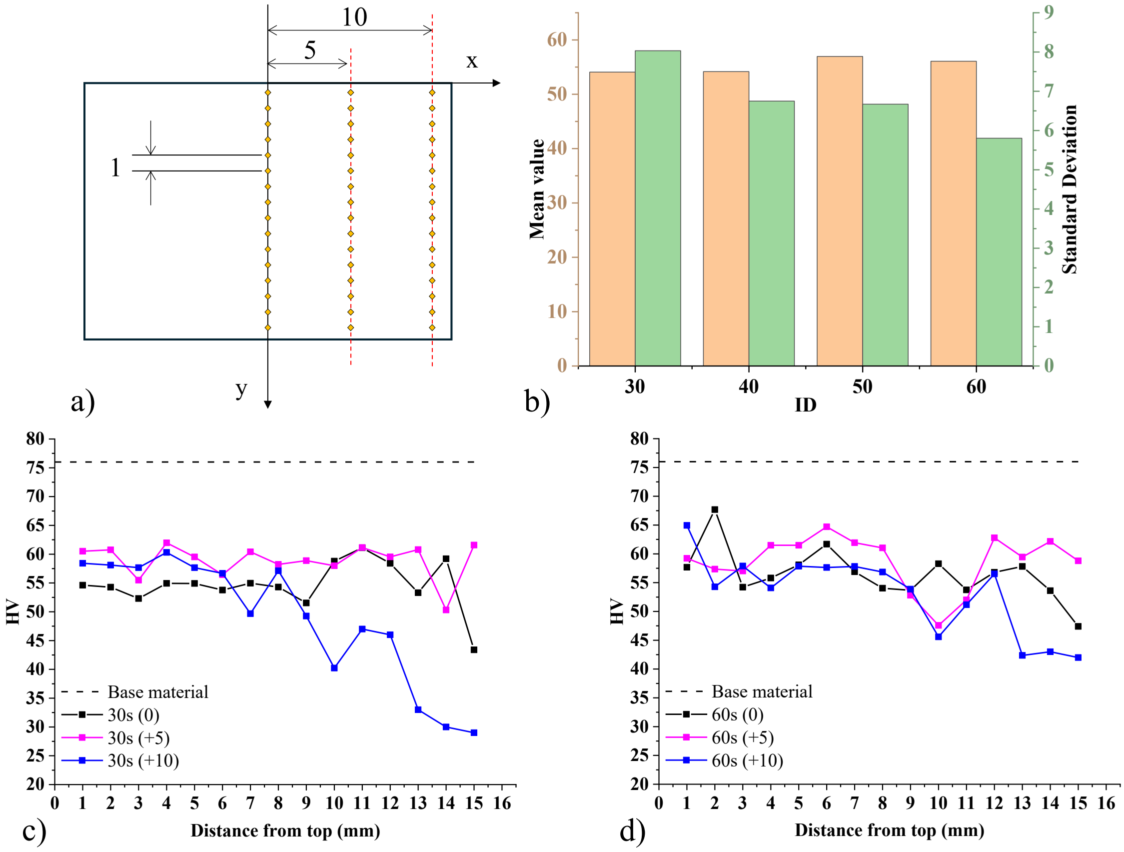

Figure 104. *a) Schematic representation of hardness indentation; b) Mean values and standard deviation of the billets' cross section, from the top (0mm) to the bottom (15mm) for 30s, 40s, 50s, and 60s; Hardness trends compared to base material for c) 30s, and d) 60 specimens.*

From the results reported in Figure 104 it is possible to state that the processing time does not affect the hardness average, but it is possible to observe that the standard deviation decreases with increasing processing time. The better standard deviation value for EXP 4 is due to the better consolidation at the bottom region of the billet, close to the bottom corner.

This is also highlighted in Figure 104c, d, where it is clear that the outer region of the billet of EXP 1 (30s) is less consolidated at the bottom as a drop in hardness occurs. Such a drop is instead much more limited when Figure 104d is analyzed. This detail is shown in Figure 105, where a macroscopic analysis of the surface of the billets is presented in order to investigate the consolidation occurrence for the case study 30s and 60s. In this figure, the unconsolidated areas are highlighted, in these regions porosity and unconsolidated chips are clearly visible, such a region is limited in the 60s case.

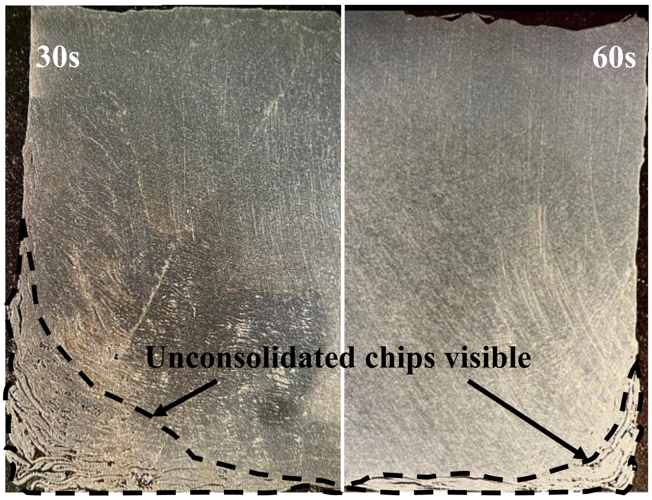

Figure 105. *Macroscopic analysis of cross sections for the 30s (left) and 60s (right).*

Lastly, the consolidated billet production was coupled with electrical energy consumption recording for each case study. A typical Power trend for the consolidation of a 60s billet is reported in Figure 106, where the six main phases are highlighted in different colors.

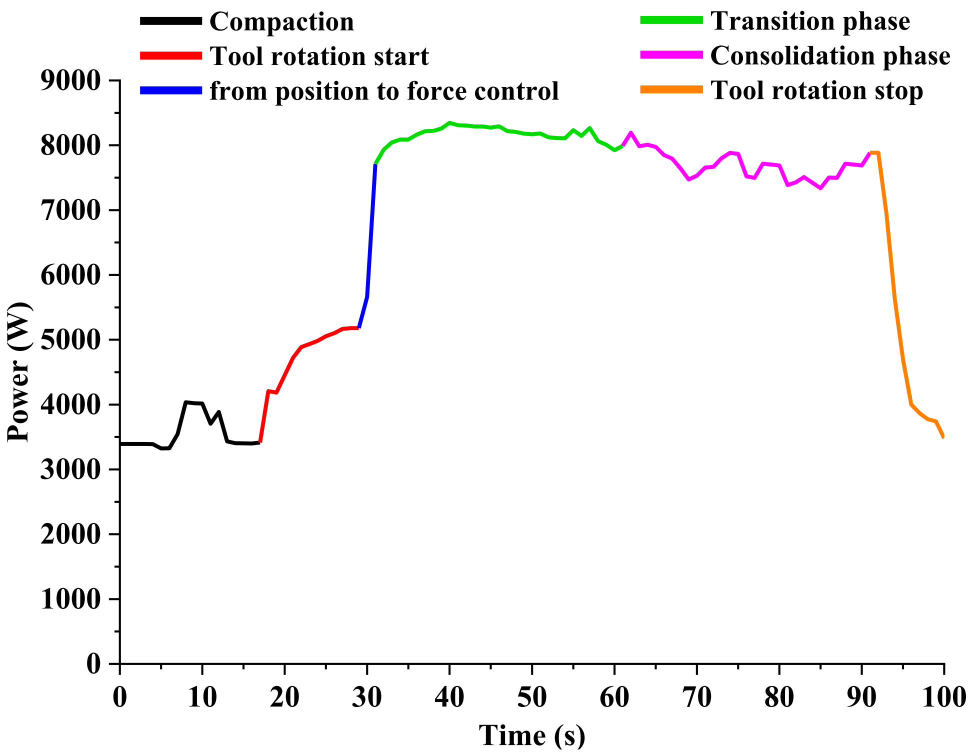

Figure 106. *Electric power trend of the FSC process for the 60s case study.*

To determine the energy required by the process, the compaction phase was disregarded, as it is a non-productive stage. However, this phase should be taken into account when considering an industrial case. The results are listed in Table 23.

Table 23. Energy data for the FSC of AZ31B magnesium alloy.

Exp ID	Transition phase [kWh]	Consolidation phase [kWh]	Total energy demand of FSC process [kWh]
Exp 1	0.065	-	0.065
Exp 2	0.065	0.025	0.090
Exp 3	0.065	0.045	0.110
Exp 4	0.065	0.066	0.131

Considering the case study Exp 4, the embodied energy of the FSC process is 73.1 MJ/kg, 27% higher than the embodied energy associated with the conventional recycling process (57.7 MJ/kg). To determine the Primary Energy Demand of the FSC process, the energy recorded during the process is divided by an average efficiency factor of 0.43, considering the energy mix of Italy. This value was obtained from the EcoInvent database. To assess the sustainability of the FSC process, a comparison in terms of Primary Energy Demand was conducted with the traditional recycling process (remelting). The data required for comparative analysis were obtained from a literature review (Table 24).

Hot extrusion material yield, oil removal, drying, and compaction were found in the DLR report [97, 98], and paper from Cooper [99]. Remelting and primary production demand of AZ31B were found by CES Edupack [100].

Table 24. Main Life Cycle Inventory data.

	Primary specific energy [MJ/kg]	Reference
Oil removal & drying	8.1	[24, 26]
FSC	73.1	Experimentally measured
Compaction	0.792	[25]
Remelting	57.7	[27]
Primary production AZ31B	393	[27]
Hot extrusion	2.16	[24, 25]

In Figure 107, the analyzed recycling routes highlight the contribution of each process step/factor to the total demand, as reported by the developed comparative analysis for a functional unit of 15g of magnesium billet.

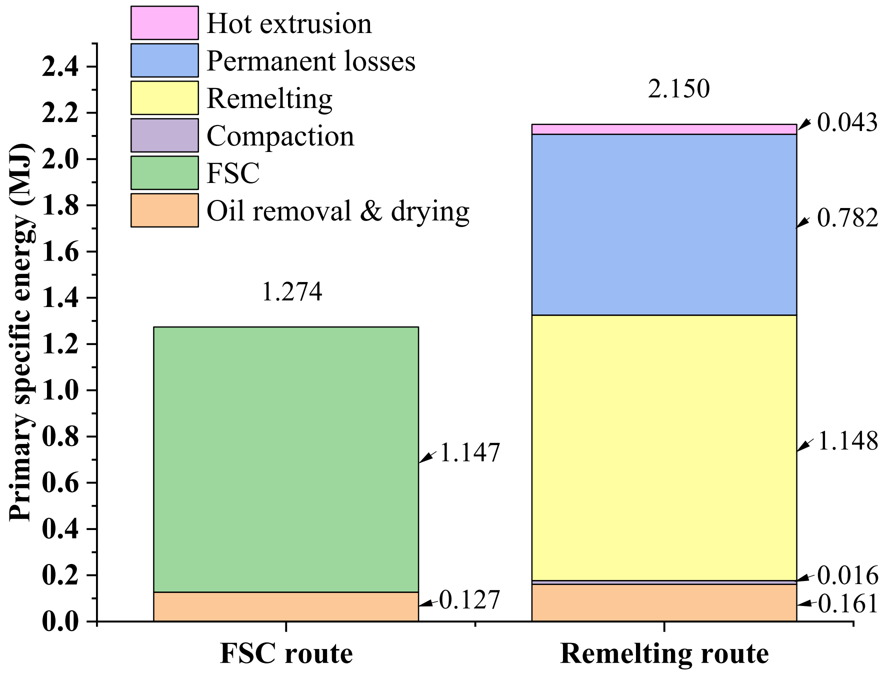

Figure 107. *Primary specific energy demands of the analyzed recycling routes.*

The FSC process outperforms the traditional process. This significant difference is primarily attributed to permanent losses, which account for 36.4% of the process's impact.

Additionally, the FSC process is more advantageous as it enables the production of a final product in a single step, whereas the traditional process would require additional intermediate steps to achieve the same result.

4.3.4 Summary of the results

The Friction Stir Consolidation process was performed to explore the capability of the friction stir consolidation technique to turn magnesium chips into consolidated billets. Four samples were well produced considering four different consolidation times, to assess the effect of the time process on the magnesium billets, and the following conclusions were drawn:

- The friction stir consolidation process successfully produced a consolidated billet. The billet obtained at 60 seconds process time is the one having the highest consolidation level.

- The hardness of the consolidated billet for each process window decreases from the top to the bottom of the cross-section, especially in the outer regions. Despite the hardness having a decreasing trend, the maximum value is less than the base material.
- The numerical simulation has successfully represented the FSC process for the AZ31B and helps to motivate the hardness evolution along the billet cross-section.
- The energy consumption analysis shows that the transition phase has a high impact compared to the consolidation phase. A primary energy demand comparative analysis proved that FSC can enable significant environmental impact reduction with respect to remelting-based routes.

4.4 Material flow dynamics in FSC processes

In all of the presented results, the best bonding condition was obtained after 60 seconds of FSC processing. Despite the high level of consolidation, the bottom-edge part has always shown a lack of consolidation. In literature, this phenomenon was ascribed to a lack of stain and a high thermal exchange [41]. This study aimed to use numerical simulation and experimental campaigns for exploring the material flow dynamics occurring in the FSC process, addressing the raised research question: "*How can the mechanical properties of consolidated billets be improved?*", "*Which variables are primarily responsible for sound bonding?*", and "*How can the bonding mechanism itself be enhanced in FSC?*".

Note: the images reported in this chapter are taken from the following published work [101].

4.4.1 Experimental methodology

In this study, a 3 mm thick rolled sheet of AA7075 with average values of 150 HV and 155 μm for hardness and grain size, respectively, was turned into machining scraps. The FSC process was performed using ESAB LEGIO (Figure 108a). The chips were loaded inside the die chamber of H13 steel with a nominal diameter of 25 mm, and an H13 steel tool was employed to compact the chips. A preliminary consolidation step was applied by activating the tool rotation at 1500 rpm with a pressing force starting from 5 kN to 20 kN with a 0.5 kN/s increment. Then, a hole with a nominal diameter of 1 mm was drilled inside the partially consolidated billet, and a copper wire of 1 mm diameter with a height equal to the height of the billet (10 mm) was inserted inside the hole as a marker (Figure 108b,c, and d). Copper has good ductility with good sensitivity to external deformation, and therefore it has been utilized for material flow in friction stir processing [7]. In order to ensure the precise location of the hole, the drill bit was guided by an auxiliary billet with a hole at a distance of 6.5 mm (1/2r) as shown in Figure 108d. Then the billet was fully consolidated by applying a rotational speed of 1500 rpm and a 20 kN pressing load of the tool for a processing time of 60s.

After cooling the equipment, the billet was detached from the die, and its surface was grind stepwise at a regular pitch distance of 0.5mm to reveal the marker across the billet height (Figure 108d). The geometry change of the markers was used as an index to quantify the strain distribution. The area lengths and average thickness of the markers in different layers were measured using ImageJ image processing software. Based on the geometry change, the true strain of the markers in the remnant billet was calculated according to the Eq. 26 to 30 specified by Li et al. [102]. By using the following equations, longitudinal strain, circumferential strain, radial strain, total strain, and effective strain were calculated at different depths of the billet.

$$\varepsilon_l = \ln\left(\frac{A_o}{A_n}\right) \tag{26}$$

$$\varepsilon_\theta = \ln\left(\frac{l_n}{d_o}\right) \tag{27}$$

$$\varepsilon_r = \ln\left(\frac{t}{d_o}\right) \tag{28}$$

$$\varepsilon_t = \varepsilon_l + \varepsilon_\theta + \varepsilon_r \tag{29}$$

$$\varepsilon_{eff} = \sqrt{}(\varepsilon_l{}^2 + \varepsilon_\theta{}^2 + \varepsilon_r{}^2) \tag{30}$$

Here $\varepsilon_l, \varepsilon_\theta,\ \varepsilon_r, \varepsilon_t$ and ε_{eff} are the longitudinal strain, circumferential strain, radial strain, total, and effective strain, respectively. A_0 is the original cross-sectional area of the marker, A_n is the area of the marker on a transverse cross-section. ln is the length of the marker in the circumferential (theta) direction, and d_0 is the original marker-wire diameter. t is the average thickness of the marker in the radial direction, and d_0 is the average chord of the original marker-wire diameter. By the definition of constant volume in continuum mechanics, the total strain ε_t, which is the sum of three mutually orthogonal strain components, the longitudinal strain, radial strain, and circumferential strain, should be zero. By plotting the strain values from the bottom to the top of the deformation zone, the strain evolution is revealed.

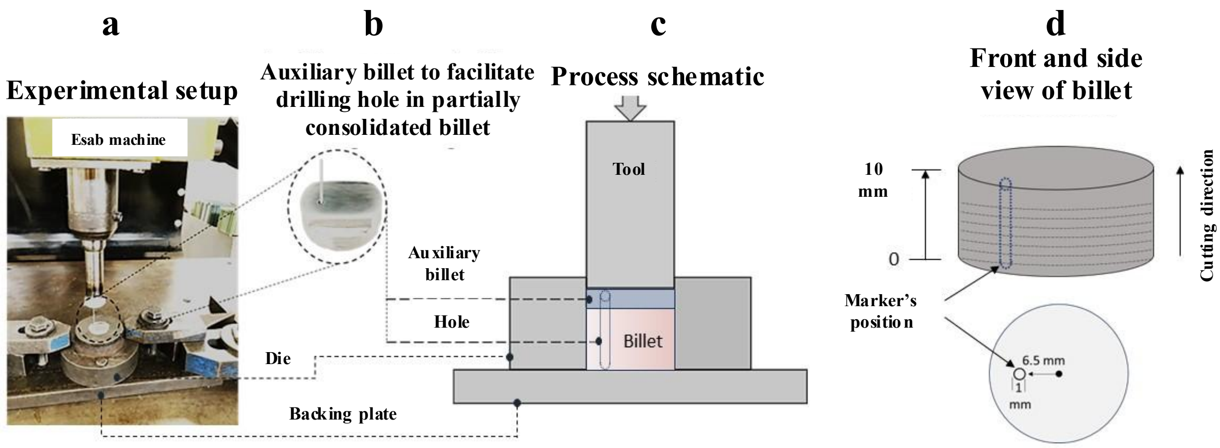

Figure 108. *Experimental setup and its schematic to analyze material flow during FSC process.*

4.4.2 Numerical Methodology

In order to further support the experimental results and get more insights into material flow during the FSC process, the numerical simulation was performed by using FEA commercial software DEFORM 3D. The tool, die, and backing plate were modelled as rigid bodies with a mesh size of 30000 elements, while the billet of compacted chips was considered a porous object (25000 elements), with an embedded copper wire, by implementing the Shima and Oyane [13] formulation on the mechanical properties definition of the material, as depicted in Figure 109. The inverse approach was adopted by setting suitable boundary conditions, in particular, constant friction equal to 0.4, and the heat transfer coefficient of 11 N/sec/mm/°C was considered.

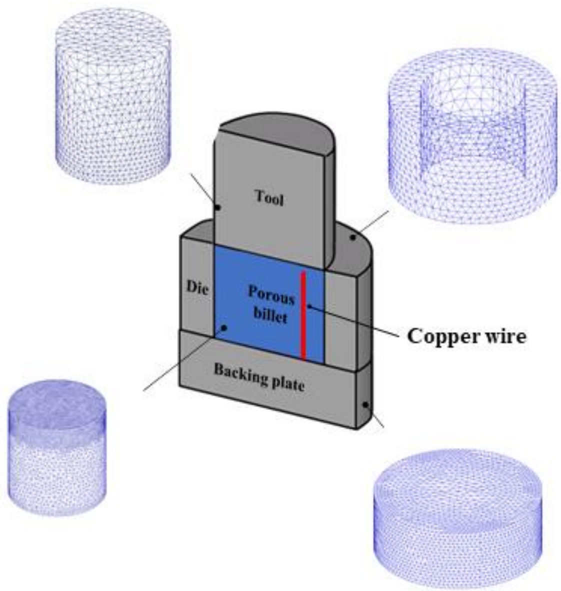

Figure 109. *Model for numerical simulation for material flow analysis.*

4.4.3 Results and discussion

To visualize the deformation evolution and calculate the strain distribution during the deforming volume of FSC, the cross-sectional images of the AA7075 billet at different layers are presented in Figure 110. Here, the bottom of the billet (contacting surface of billet and backing plate) was considered the zero position Figure 110. Each picture was labelled with the distance from the bottom of the billet. For example, 1 mm means the picture is taken from a cross-section that is 1 mm above the bottom of the billet, in other words, 1 mm from the backing plate.

From the series of images, it is evident that no deformation was noticed at the bottom of the billet. However, the deformation can be seen that occurred toward the top zone, almost 3 mm below the top surface, or in other words, the deforming zone is situated at a height between 7 mm and 10 mm from the bottom surface. As it moves from the bottom surface towards the top, the marker starts to deform along the circumferential direction at a 7 mm distance to the top surface. At the very top, from 9 mm to 10 mm, the marker exhibited the highest deformation, splitting, and dispersing across the surface of the billet. It represents that this zone undergoes the highest strain during the FSC process.

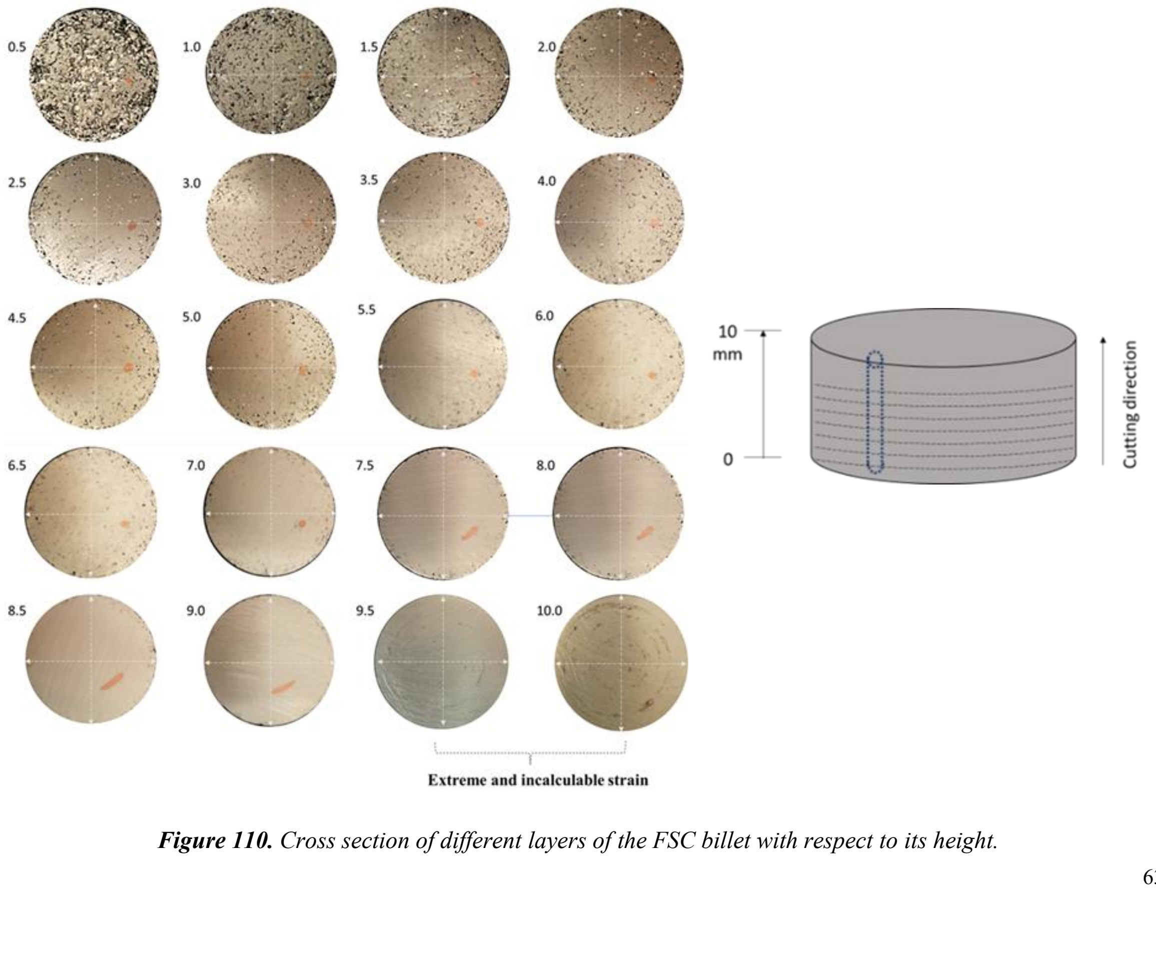

Figure 110. *Cross section of different layers of the FSC billet with respect to its height.*

The longitudinal strain (ε_l), circumferential strain (ε_θ), radial strain (ε_r), total strain (($\varepsilon_{t)}$), and effective strain (ε_{eff}), at different depths in the deformation zone, are presented in Figure 111. The circumferential strain increases from the position of 7 to 10 mm from the top of the FSC billet and then decreases. The longitudinal strain is negative, and the absolute value continues to increase from the bottom to the top. It is important to note that the total strain is always close to zero, given the measurement errors, which indicate the obtained results are reliable. Based on the definition of the Von Mises effective strain in plasticity theory, see Eq. 30, effective strain (ε_{eff}) was calculated from three orthogonal strain components. That is, three mutually orthogonal strain components are not the principal strains. Plots of the calculated strain values were plotted with respect to their depths in the deformation zone, shown in Figure 111. As the topmost part (9-10 mm) underwent the highest strain, causing the marker to disperse across the billet section, the strain in this zone was incalculable.

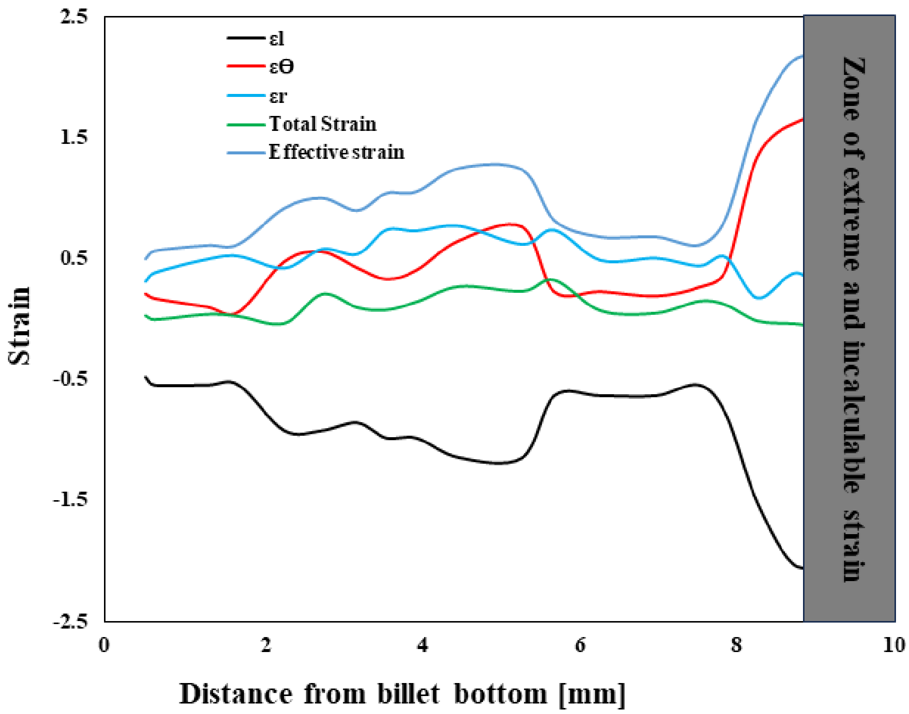

Figure 111. *Evolution of different strain across the FSC billet.*

The simulation provides a qualitative overview of the material flow that characterizes the FSC process. At the end of the process, a point tracking and a flow net analysis were performed to emphasize the flow inside the porous billet. The flownet analysis has shown the flow in the entire cross-section of the billet, while the horizontal point tracking was mainly added on the top surface of the billet to highlight how this surface moves during the FSC process (Figure 112).

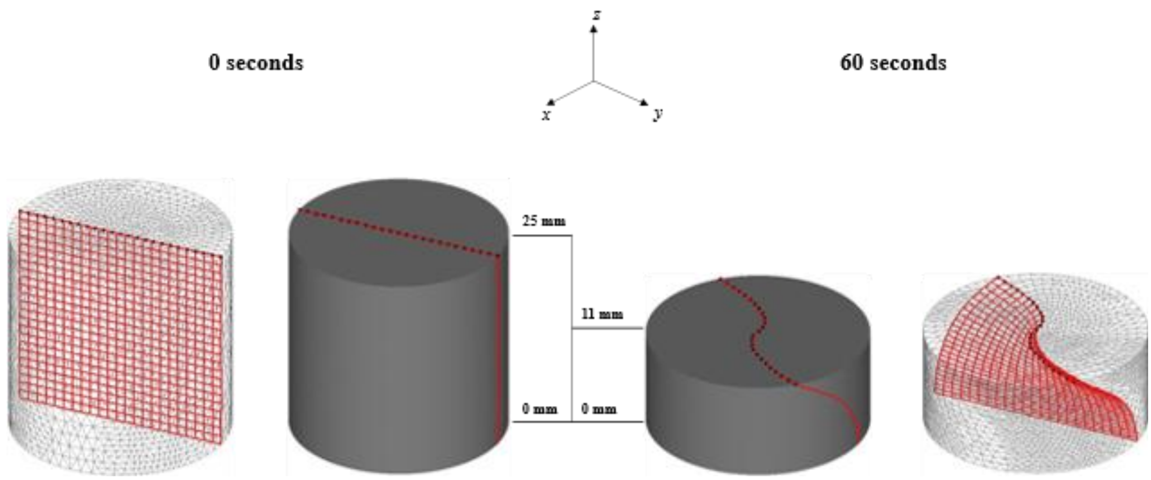

Figure 112. *Graphical visualization of the flownet (red grid) and the point tracking (black points) at the start (0 s) and the end of the process (60 s).*

Additional results of the first flow analysis are presented in Figure 113 where the rotation of the top surface is described by means of the displacement of a straight line of points. It is clearly visible that starting from the initial height of the billet, the surface has rotated by an angle of about 45°. Figure 113 also shows that, due to the process configuration, the material close to the rotational center of the tool is characterized by a simple upsetting condition, whilst the material close to the die-billet contact surface is characterized by the highest rotation. In the same way, it is possible to distinguish and divide the 3D consolidated billet into two main zones: high strain level zone and low strain level zone (Figure 114 and Figure 115).

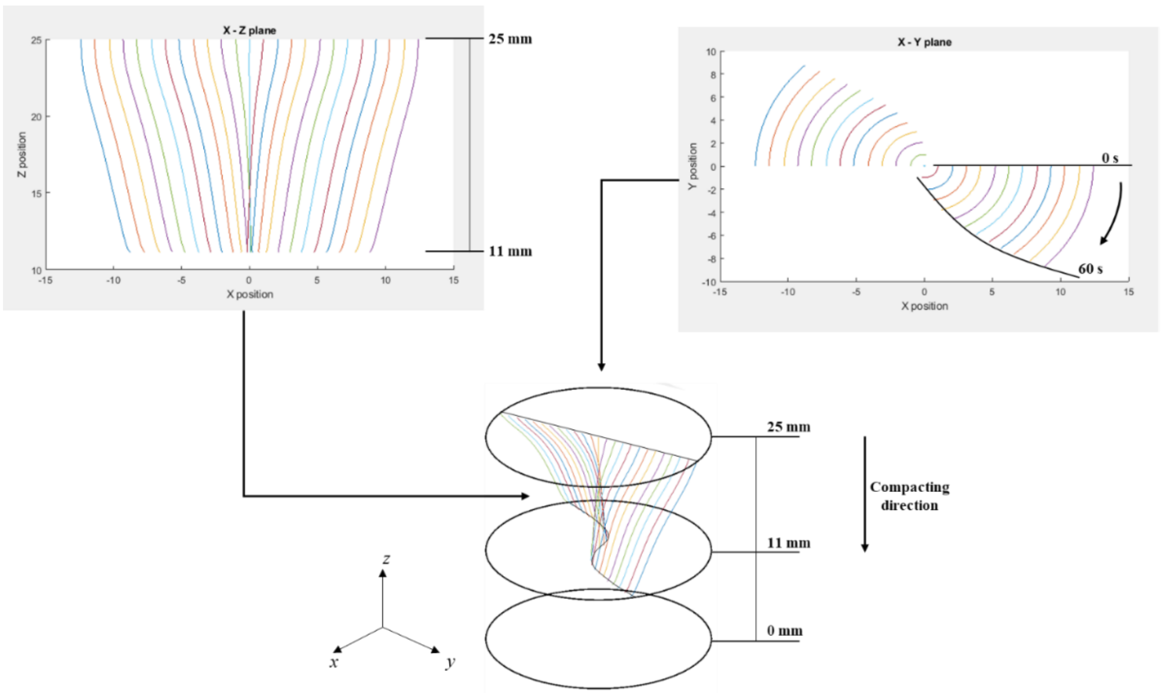

Figure 113. *Point tacking visualization on MATLAB environment.*

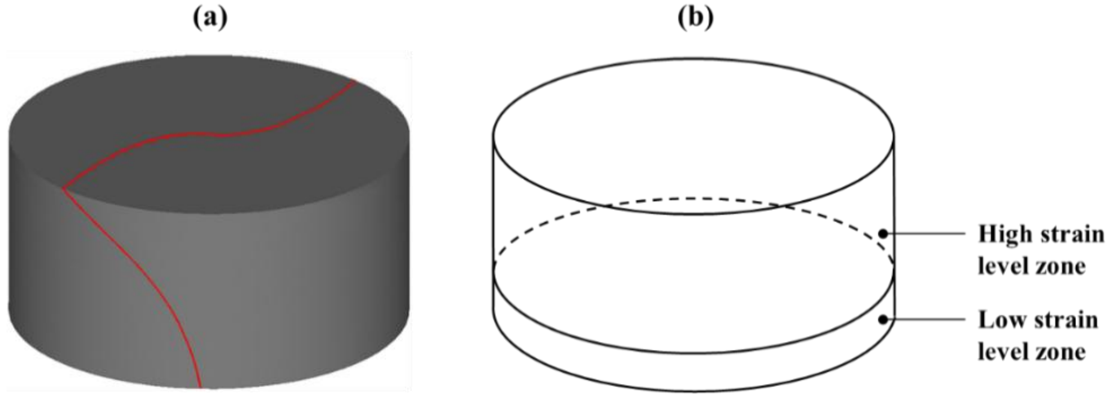

Figure 114. *(a) 3D view of the material flow and (b) two strain level zone divisions.*

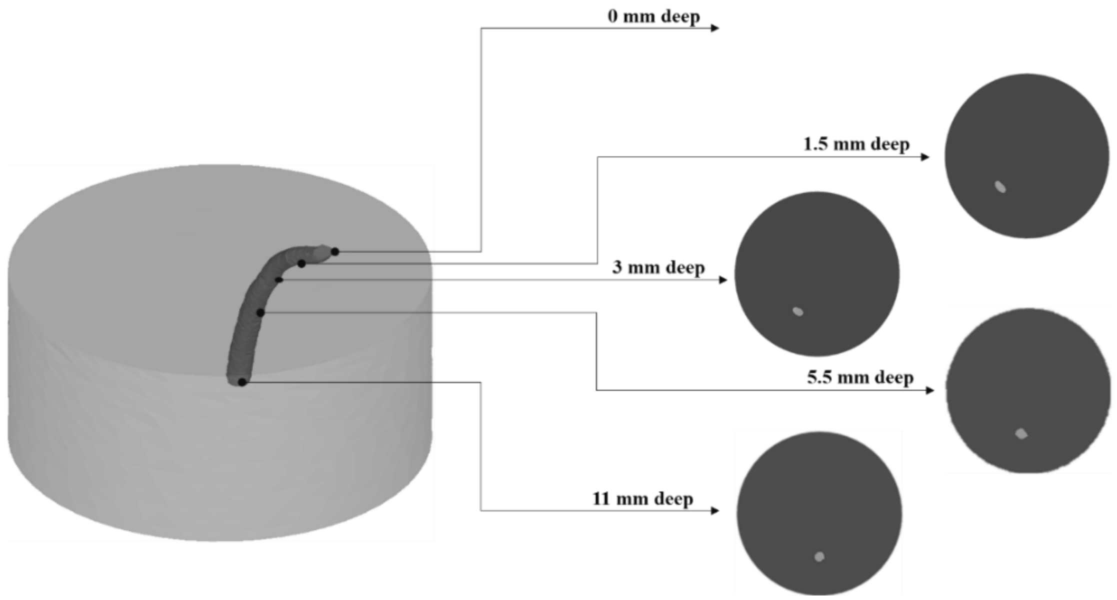

Figure 115. *Numerical acquisition of the wire surfaces at the end of the process, for different layers.*

In order to further strengthen the arguments of the material flow occurrence at the top part and the absence of material flow at the bottom, the microstructure of the AA7075 consolidated billet was analyzed along its height at a radial distance of 6.5 mm, as shown in Figure 116. At the bottom of the FSC billet, no significant change in the microstructure of the chips and the bottom of the billet occurred. On the other hand, the formation of the new grain can be clearly seen at the top of the billet. These results depict that the bottom region is not affected by the strain and strain rate, while it is expected that the top region is influenced by the combined effect of temperature, strain, and strain rate.

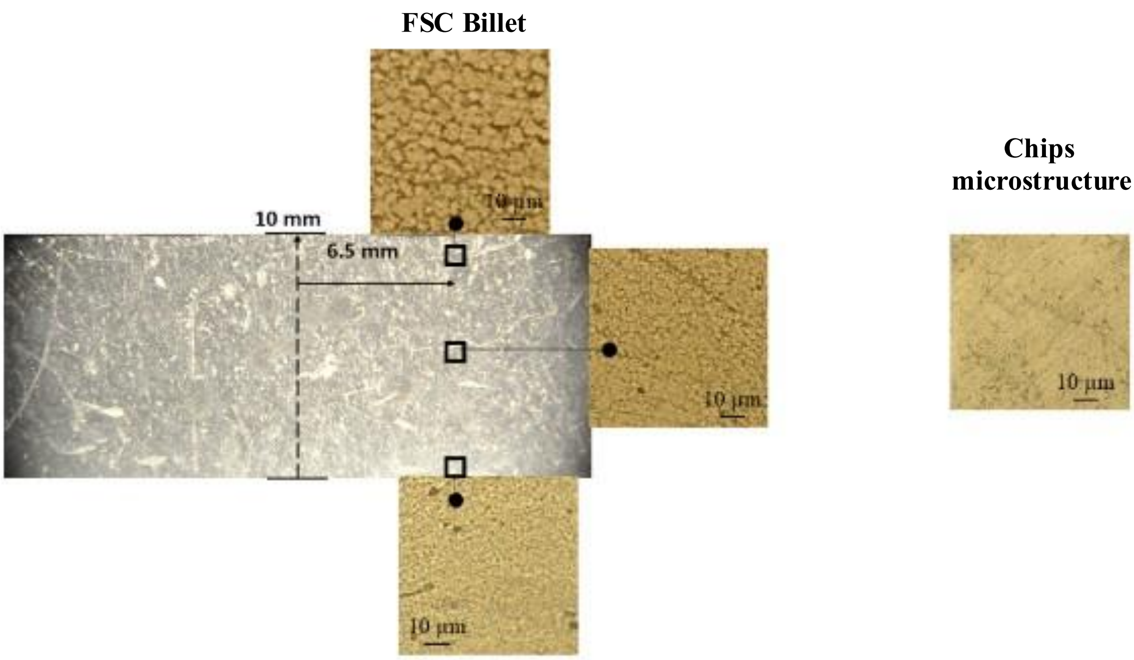

Figure 116. *Microstructure changes with respect to the height of the FSC billet.*

4.4.4 Summary of the results

Although this study provides only a preliminary insight into the material flow during the FSC process, this approach demonstrated to be enough representative of the FSC flow dynamics. In this regard, a few conclusions can be drawn from the results obtained.

- An experimental approach was successfully established to visualize and characterize the material flow during the FSC of AA7075 machining chips.
- The findings also offer a valuable basis for determining the strain distribution required to develop theoretical and numerical models of the FSC process.
- The material flow was found to occur predominantly in the upper region of the billet, particularly within the layer extending from the top surface down to approximately 3 mm in depth.

4.5 Improvement of friction stir consolidation process through numerical simulation

The research presented in Chapter 4.4 highlighted the main issue of the FSC process. Different approaches have been tested to improve the billet consolidation at the bottom-edge part; an example is the research developed by Latif et al. [103] who investigated two new approaches: double-sided and mass addition. In this research, the billet was processed from both sides (double-sided) and layer by layer (mass addition). A question still arises: "*What can we do to improve the stirring action (bonding) at the bottom of the FSCed billet?*".

In this regard, this research aims to propose an innovative method, which uses a heated backing plate, to overcome the issue of the lack of consolidation. The proposed approach was mainly studied through a numerical campaign using the experimental data from the previous publication. Firstly, a numerical simulation was performed to understand the effect of a heated backing plate on the temperature and strain of the billet. Secondly, the solid bonding approach (FSC-designed solid bonding criterion) was applied to study the actual bonding occurrence derived from the new setup.

Note: the images reported in this chapter are taken from the following published work [104].

4.5.1 Numerical methodology

In this study, the heated backing plate configuration was investigated by means of a numerical approach (Figure 117). The data used for the bonding evaluation between the new configuration proposed here and the previous one were based on previous experimental research (Chapter 4.1). The result of this campaign was multiple consolidated billets characterized by a total process time of 30, 40, 50, and 60 seconds (Table 25).

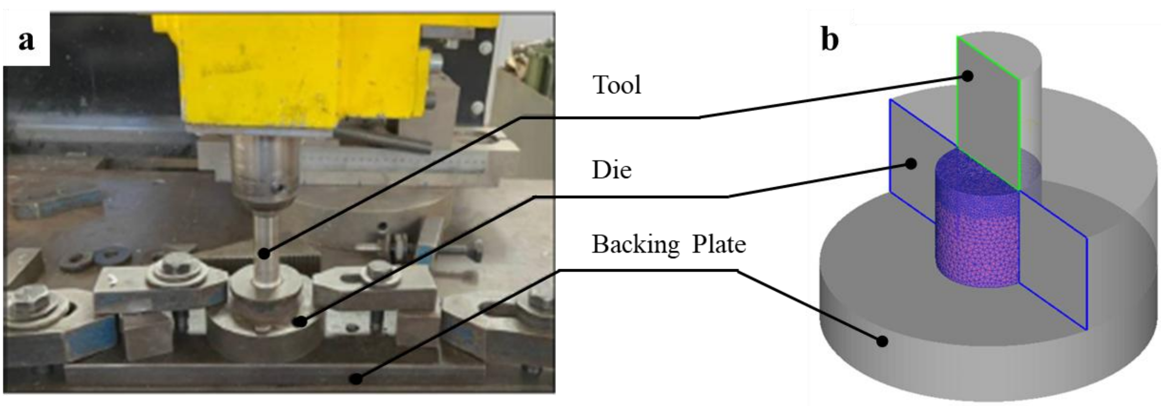

Figure 117. *a) Experimental [88] and b) numerical setup.*

Table 25. Process parameters and time process of each FSC test [88].

Exp ID	Rotational speed [RPM]	Mass [g]	Transition period [s]	Consolidation time [s]
Exp 1	1500	15	30	0
Exp 2	1500	15	30	10
Exp 3	1500	15	30	20
Exp 4	1500	15	30	30

The numerical model, on the basis of the previous campaign, was developed using SFTC DEFORM 3D™. The numerical model involves a tool, a die, and a backing plate modelled as rigid bodies, whilst the chips were modelled as a compressible rigid-viscoplastic porous billet characterized by an initial relative density equal to 0.44. For the aluminium material characterization, the material data were referred to previous research [95]. The rigid bodies were defined by a mesh size of 30000 elements, H-13 material, a shear factor equal to 0.3, and a heat transfer coefficient equal to 11 W/mm^2/K. On the other hand, the porous billet was defined by a mesh size of 20000 elements, with a refining mesh window close to the tool-billet contact (Figure 117b). To simulate the heating from the bottom, two different initial temperatures of the backing plate were selected: 300 °C and 400 °C. In Figure 118 the effect of the different backing plate temperature is reported for the case study of AA7075. This figure proves that the configuration at 400 °C does not bring any appreciable improvement in terms of strain and density, compared to the configuration at 300 °C. For this reason, and for the sake of the reduction of energy consumption, the analysis was performed considering an initial temperature equal to 300 °C.

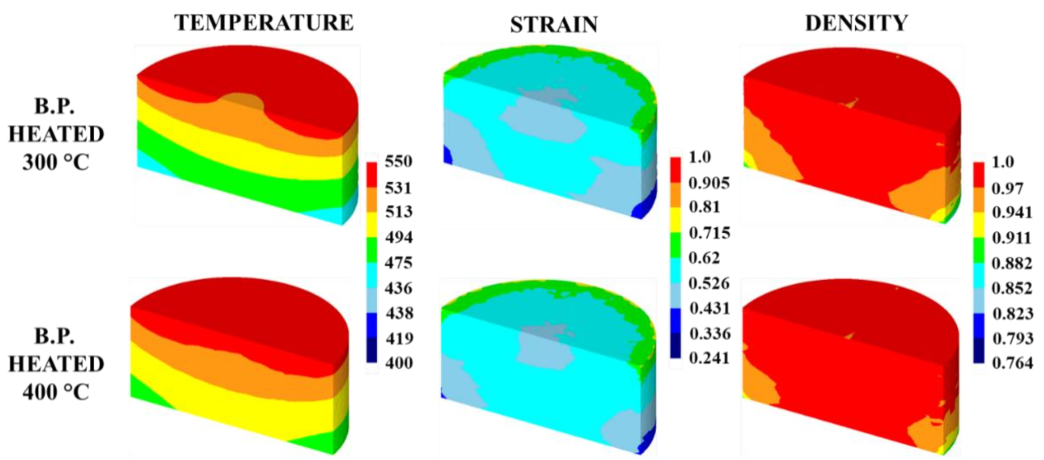

Figure 118. *Temperature, strain, and density comparison for the case of the backing plate heated at 300 and 400 °C, at 30 seconds process time.*

For both the campaigns, the middle cross-section of the consolidated billet was analyzed using a matrix of 17x7 loci. In these 119 loci the bonding occurrence was evaluated by two different methods: from the numerical side, the temperature and stress values were acquired, and the solid bonding value (W) was calculated (Eq. 13) as well as the solid bonding limit value for the three material AA2024 (Eq. 19), AA6082 (Eq. 20) and AA7075 (Eq. 21) [95]. In the experimental campaign, from the same matrix of points, the hardness and the grain size were obtained in order to identify the consolidation occurrence according to the experimental criterion in Chapter 4.2.3.

For each point of the 119 matrix, the W^{Lim} value was compared to the W value. When the bonding value calculated using Eq. 13 was higher than the W^{Lim} calculated using Eq. 19-21, the point was considered consolidated.

4.5.2 Results and discussion

For each material, a numerical simulation was performed, and the cross-section was studied. It can be assumed that the bonding quality is related to the oxide breakage during the consolidation process, and the main factors that help this phenomenon are the temperature and strain condition [101]. To clearly show the effect of the heated backing plate, the data related to 60 seconds of the FSC process, for both heated and cold baking plates, have been plotted in Figure 119, Figure 120, and Figure 121. The comparison between the cold backing plate and the new strategy of the heated backing plate shows that the temperature has obviously increased, slightly affecting the strain for the cases AA7075 and AA6082. On the other hand, AA2024 showed the biggest strain improvement, as well as for the temperature and density; this could be related to the higher ductility of this aluminium alloy. This combined effect led to a better consolidation (in terms of material density) along the cross-section. The bottom edge of the billet is still the coldest point of the material since this zone has the highest thermal exchange surface with the rigid bodies.

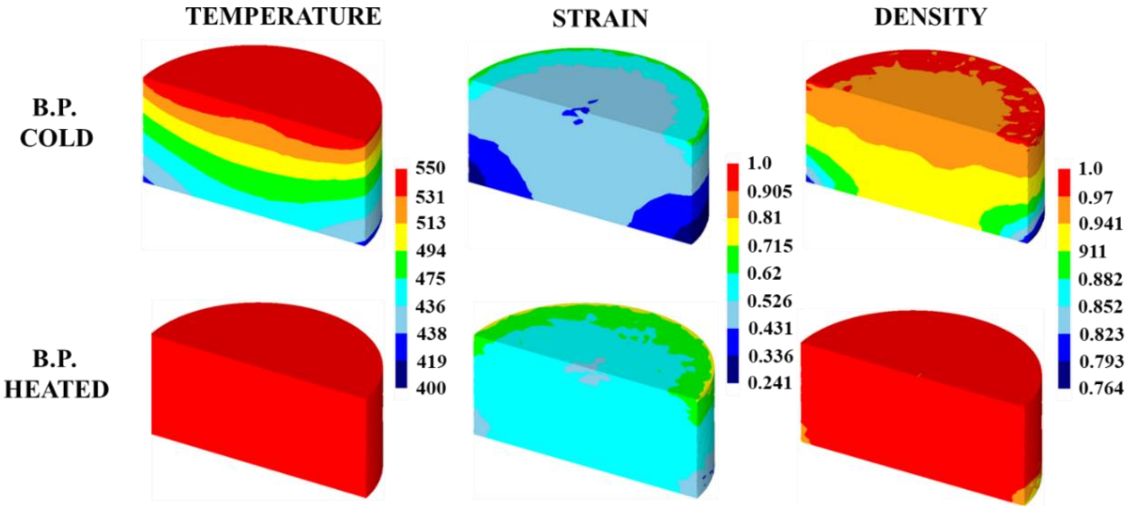

Figure 119. *AA2024 numerical results at 60s time process.*

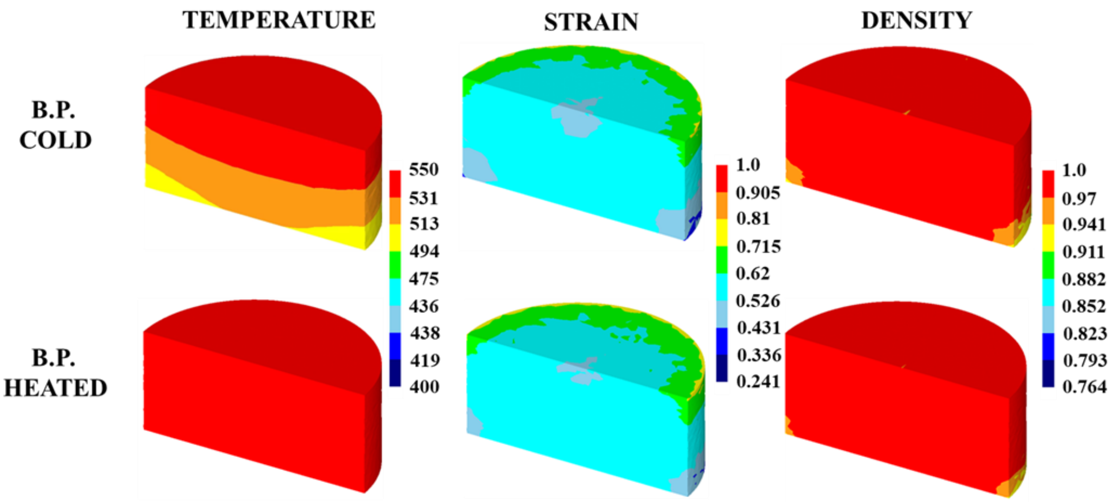

Figure 120. *AA6082 numerical results at 60s time process.*

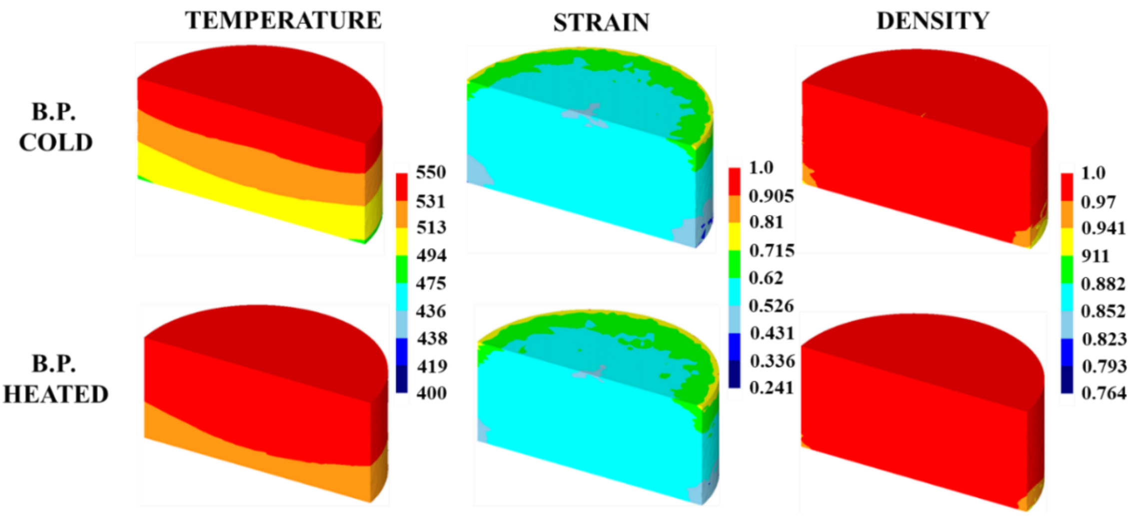

Figure 121. *AA7075 numerical results at 60s time process.*

Concerning the solid bonding phenomenon, it is worth mentioning that the bonding was also investigated using the PPW criterion developed, as it was clearly demonstrated that this criterion has the best prediction performances, specifically for the FSC process, compared to those already existing in the literature. The study of solid bonding is shown in Figure 122a, b, and c, and was performed for the case study 30 seconds, to guarantee a better visualization of the difference in terms of consolidation. In these images, the previously predicted bonding maps and the new ones were compared. As is possible to notice, for all the materials investigated, the effect of the new setup is reflected in a larger consolidated area. This difference is more visible when looking at case AA6082 (Figure 122b) than the other case study, because the bonding condition of all loci for this material was close to the consolidation threshold value [95]. Therefore, a slight increase in temperature resulted in bonding values over the limit. The results in Figure 122 were summarized in Table 26.

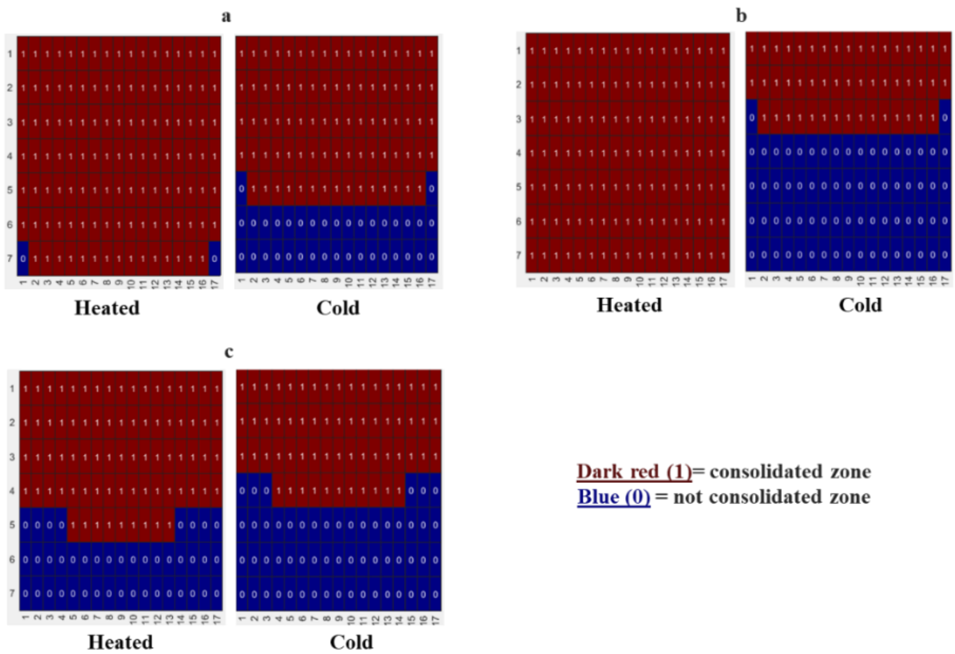

Figure 122. *Bonding occurrence maps of the 30s cross section of the billet. Cold-Heated comparison for a) AA2024, b) AAA6082 and c) AA7075.*

Table 26. *Comparison of the consolidated number of loci for the three materials, at 30 seconds time process.*

	N° CONSOLIDATED LOCI		**PERCENTAGE OF CONSOLIDATED LOCI**	
	Heated	*Cold*	*Heated*	*Cold*
AA2024	117	83	98%	70%
AA6082	119	49	100%	41%
AA7075	77	62	65%	52%

4.5.3 Summary of the results

A numerical approach for improving the friction stir consolidation process was performed by means of backing plate heating. Three materials were tested, and the following conclusions were drawn:

- The heated backing plate has increased the average temperature of the porous billet during the process, although strain has been slightly increased.
- The combined effect of the new level of temperature and strain has increased the relative density of the porous billet in the first 30 seconds.
- The W^{Lim} curve prediction already presented is consistent and allows for evaluating the bonding occurrence with the new setup proposed here.
- Looking at the prediction of the bonding occurrence, the heated backing plate is a solution for increasing the consolidated zone/surface, especially for the AA6082.

4.6 Tube manufacturing via friction stir extrusion

Once the friction stir consolidation was widely explored, another friction stir-based technique was studied, namely friction stir extrusion. This recycling process is commonly adopted for extruding wires; therefore, a research question arose: "*Is FSE a viable method for tube extrusion?*" and "*Is it more sustainable compared to conventional techniques?*".
In the literature, a few papers deal with tube production from metal swarf, and most of them require sub-steps [46] (homogenizing, pre-consolidation….) or use bulk material as a starting material,[105–107] but in this work, a single-step process is presented to directly turn machining aluminium chips into consolidated tubes. In particular, a matrix of process parameter combinations was explored to assess the feasibility of this technique to produce a consolidated tube. Moreover, complete mechanical characterization along with energy consumption and solid bonding analysis was carried out to enrich the study of this recycling process.

4.6.1 Experimental methodology

The starting point was the aluminium chips milling process performed on an AA2024-O aluminium bar. A fixed mass of 40 g of chips was loaded into the die chamber, which had an inner diameter of 25 mm and a height of 76 mm. Two H-13 steel tools were employed for the operation: one with a diameter of 25 mm for compacting the material and another with a diameter of 22 mm for extrusion. The complete experimental setup is shown in Figure 123.

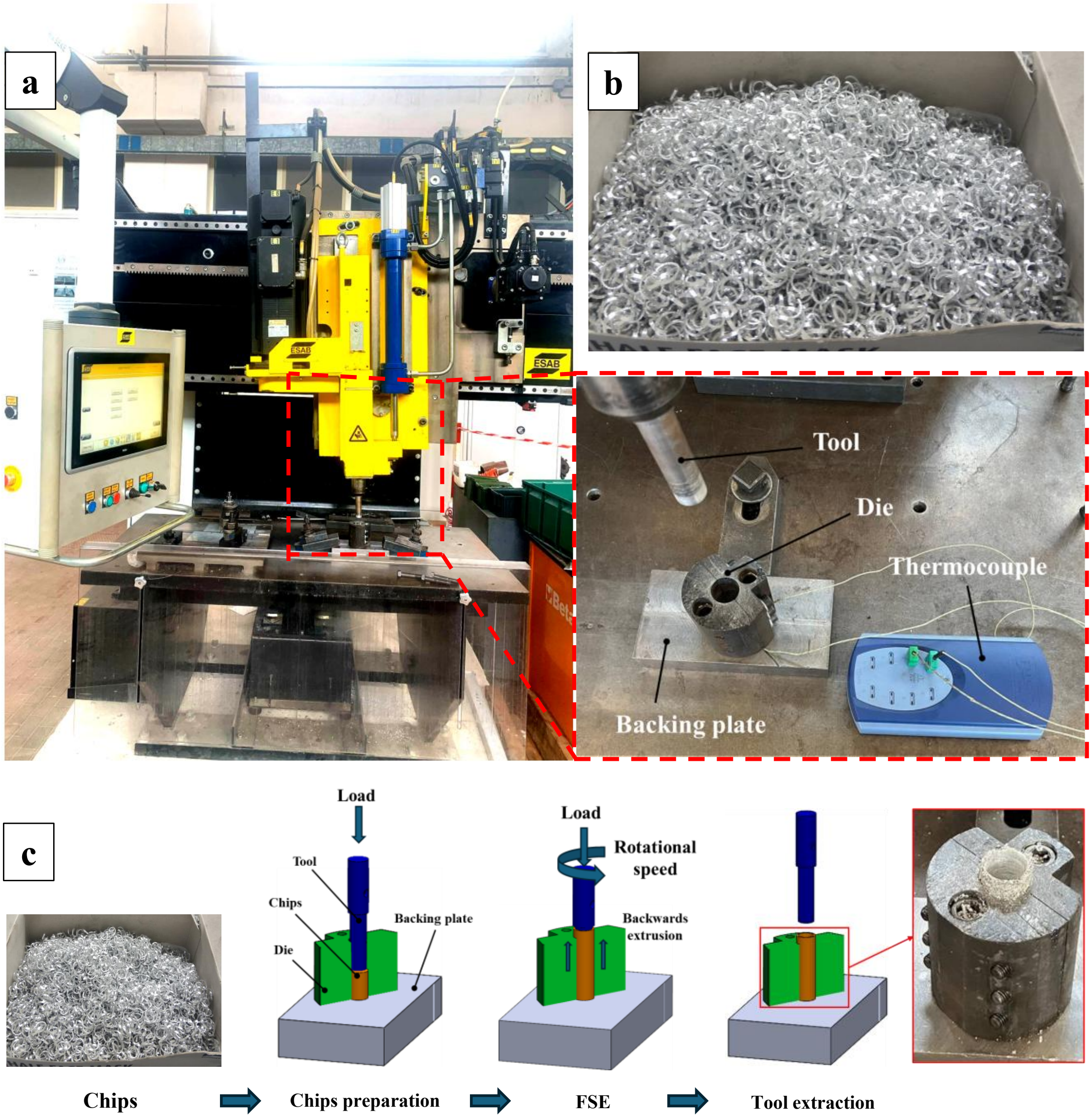

Figure 123. *a) ESAB LEGIO for FSE tube extrusion b) aluminium chips used for the experimental campaign c) schematic diagram of the process.*

The friction stir extrusion process for tube extrusion consists of two stages: chips preparation and the extrusion process. At the first stage, the chips were pre-compacted up to 35 kN force by using a compacting tool in order to adequately fill the die and avoid the dispersion of chips during the extrusion process. Moreover, the 35 kN compaction does not affect the extrusion process or the produced tube, but it is required to prepare the material for the extrusion stage. After this compaction phase, the compaction tool was replaced by the extrusion tool. In the second stage, the extrusion process is run by varying the process parameters as shown in Table 27. At the beginning of the extrusion process, the vertical force gradually increases by 0.5 kN/s from 5 kN to reach the maximum required force for the assigned processing conditions. At the end of the extrusion process, the tool automatically reached its initial position, and the tube was extracted. It is worth remarking that a similar setup has been adopted by Behnagh et al. [46] and Whalen et al. [108] for extruding tubes (from machining chips) via double-step friction stir consolidation and ShAPE process, respectively. In both cases, a rotating tool and a designed die were employed in the process setup.

In order to observe the variation in temperature at various processing conditions, a K-type thermocouple was placed into a hole drilled at 1/3 of the height of the die (from the bottom), 1 mm before the inner die wall. As reported in Table 27, the experimental plan included three different values of tool force (12, 15, and 18 kN) and rotational speed (1000, 1500, and 2000 rpm). Each test combination ("Ci") was run three times to ensure the reliability and consistency of the results.

Temperature monitoring is crucial to prevent the tube tool from sticking, which could result in damaging the machine and the tube itself; therefore the process was stopped when the tool displacement reached almost 35 mm, which, from the experimental campaign, corresponds to a measured temperature in the range of 370 - 380 °C. This range of the die's temperature can be assumed as the limit temperature of the setup proposed.

Table 27. *Set of process parameter combinations and ID name.*

ID	Rotational speed [rpm]	Vertical load [kN]
C1	1000	12
C2	1000	15
C3	1000	18
C4	1500	12
C5	1500	15
C6	1500	18
C7	2000	12
C8	2000	15
C9	2000	18

4.6.2 Numerical methodology

The numerical investigation of the tube production process was conducted using the commercial finite element software SFTC DEFORM 3D. Mirroring the experimental approach, the numerical model incorporated four key components, as illustrated in Figure 124a. Three of these components, namely tool, die, and backing plate, were modeled as rigid bodies made of H-13 steel, with mesh resolutions of 60,000, 60,000, and 30,000 elements, respectively. The aluminium chips were represented as a compressible rigid - viscoplastic porous billet. The initial relative density of the billet was analytically determined to be 0.7 based on the die chamber volume (25 mm diameter × 76 mm height) and the mass of the loaded chips (40 g). Additionally, a mesh window (reduction of 30%) was employed close to the bottom of the tool to better investigate the field variable in this critical zone.

A calibration procedure was performed for the 1500 rpm and 15 kN case to identify the optimal shear factor by comparing numerical and experimental temperature profiles (Figure 124b). This tuning approach, already validated in literature [88, 95], aims to vary the thermal coefficient until adequate matching is observed. As a result of the temperature tuning procedure, a shear factor of 0.2 and interface heat transfer coefficients (IHTC) of 11, 45, and 45 W/mm²/K for the billet-tool, billet-die, and billet-backing plate interfaces were selected. The process parameters applied during the experimental campaign served as input variables for numerical characterization.

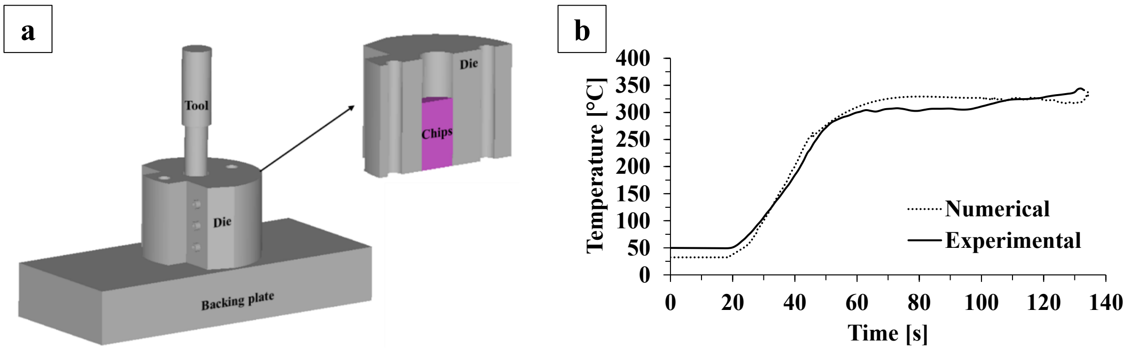

Figure 124. *a) Numerical setup of the FSE of tubes and b) temperature tuning of numerical and experimental tests.*

4.6.3 Results and discussion

For evaluating the mechanical properties of the extruded tubes, microhardness tests were conducted along the longitudinal section with equally spaced indentations (Figure 125). The resulting average hardness values are plotted in Figure 126. The hardness value increases with the increase in processing parameters, and a maximum hardness value of 147 HV was observed for the sample C8, resulting in a 140 % increase (from 61.5 HV to 147 HV) compared to the AA2024-O base material.

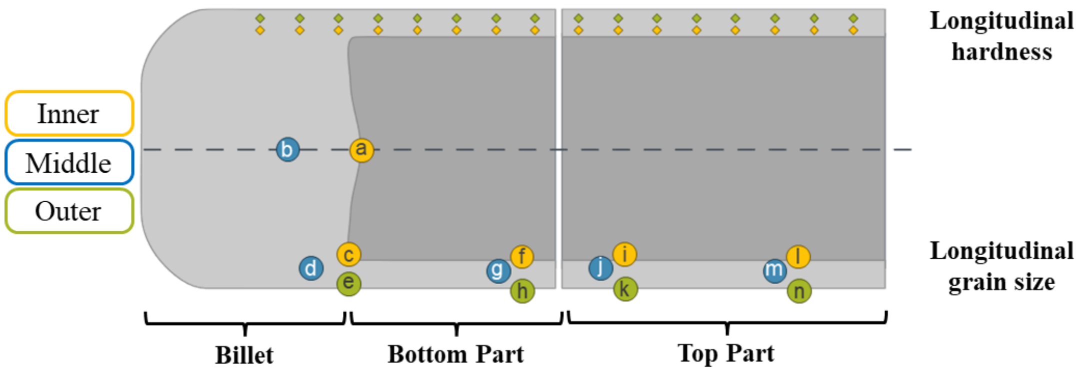

Figure 125. *Experimental observation loci for (a) FSC and (b) FSE of tubes.*

This huge improvement in hardness is in accordance with what was revealed by Baffari et al. [55] on AA2050 aluminium friction stir extruded wires. In this respect, Baffari observed that the hardness of the produced AA2050 wire via friction stir extrusion was close to the hardness of the AA2050 at the T3 condition.

The same phenomenon happened here, evidence of that, the hardness of AA2024-T3 is about 137 HV, which is very close to the hardness acquired and shown in Figure 126. Overall, the hardness increases with increasing vertical force. Such an effect is more visible when passing from 12 to 15 kN. The impact of the force increase on hardness is less visible when moving from 15 kN to 18 kN. For the ID C9, even a slight decreasing trend is visible. This phenomenon is related to excessive heat, i.e., high force and rpm, which results in hot crack formation and surface melting. On the other hand, the lowest hardness was observed at ID C1, which, in this case, is due to low heat input resulting in weak consolidation and porosity formation phenomena. Regardless of the processing parameters, the overall hardness value increased with respect to the base material.

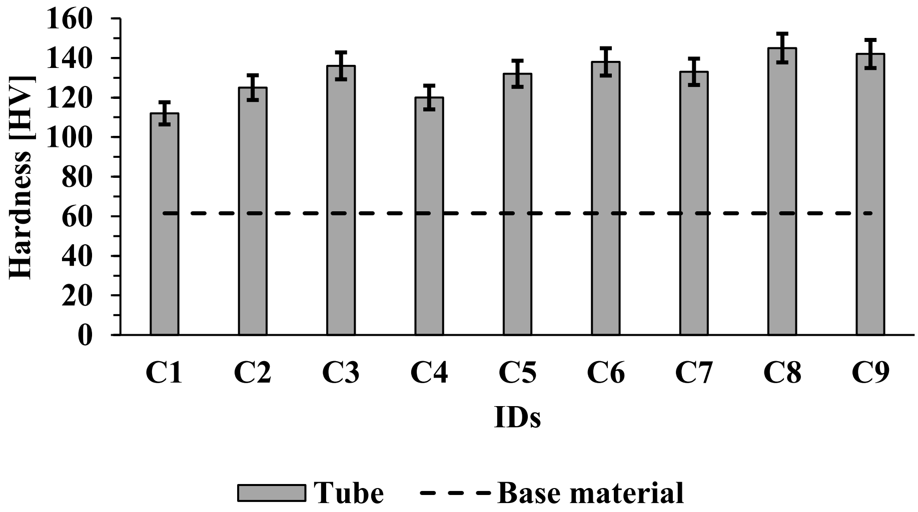

Figure 126. *Hardness results of the extruded tube for the 9 case study (longitudinal section).*

To evaluate the deformation behavior of the produced aluminium tubes, compression tests were conducted. In these tests, the cross-section of the tube was compressed between two flat, parallel, and rigid plates. As the top platen descended, initial contact with the tube occurred at discrete points, as illustrated in Figure 127a. With the increase of the load, the contact regions began to flatten against the plates, causing the tube to deform, showing barreling phenomena until reaching its elastic limit. Upon exceeding the elastic limit, two plastic hinges formed (Figure 127b), until fracture occurrence (causing a load drop). The load–load-displacement curves for the three case studies at various rotational speeds (1000, 1500, 2000 rpm) and under a constant extrusion force of 15 kN, are shown in Figure 127c. From the graph, it shows that the specimen ID C5 represents the maximum compression stress compared to IDs C2 and C8 rpm specimens. The good compression stress in sample ID C5 represents successful chips bonding and fewer cracks or porosity formation. Interestingly, similar average hardness values were reported in tube manufacturing via FSE of aluminium powders by Li et al. [109]. In particular, they observed an increase in hardness with increasing feed rate, with values in the range of 130–140 HV, consistent with the results shown in Figure 126.

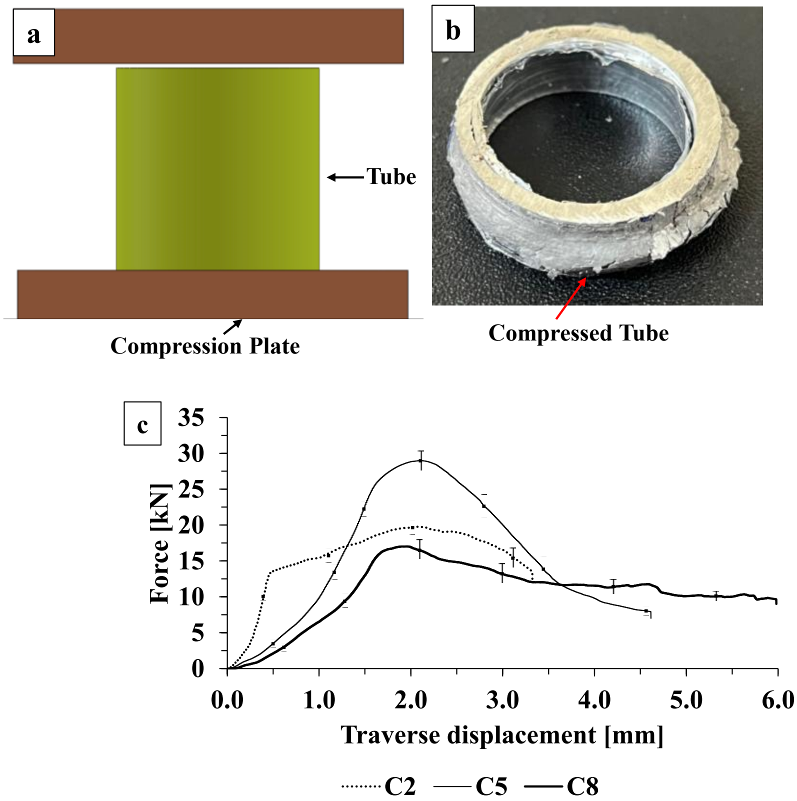

Figure 127. *a) Schematic fixture used for compression test of tubes, b) compressed tube for the case study ID C5. c) Compression test results at three case study IDs C2, C5, and C8.*

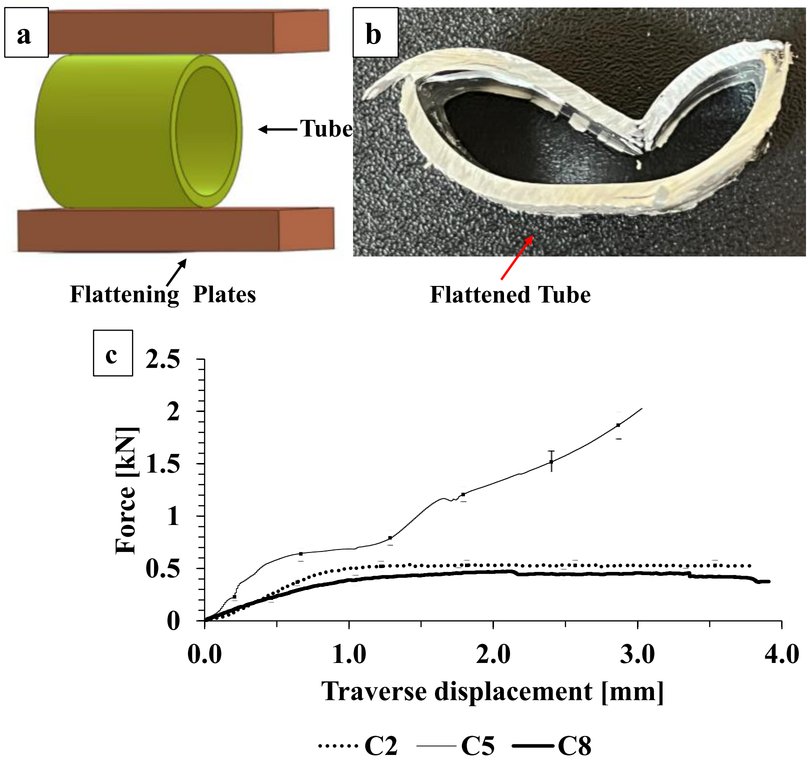

Figure 128. *a) Schematic fixture used for flattening test of tubes, b) flattened tube for ID C5. c) flattening test results in three case studies (IDs C2, C5, and C8).*

Flattening tests were also performed, and force-displacement curves (Figure 128c) for tube samples were plotted. As well as for the compression test, the case study ID C5 showed the highest mechanical properties, reflecting high flattening stress and effective bonding between chips. On the other hand, IDs C2 and C8, which observed porosity and hot cracks, showed lower mechanical behavior, as it will be better explained in the microstructural analysis part.

The results on global mechanical properties derived from compression and flattening tests can be explained by looking at local defects that will also be discussed in the next Chapters. Overall, it is possible to state that:

- The increase of the tool's rotational speed, i.e., C9, resulted in the formation of hot cracks and increased surface roughness.
- Insufficient heat generation at low rotational speed, i.e., C1, might result in a lack of consolidation and porosity occurrence.

4.6.3.1 Microstructural analysis

In the cross-section, different acquisitions were performed to characterize the evolution of the grain size along the radial direction (Figure 129). Results showed that the outer and inner regions of the tube are characterized by a smaller grain size compared to the grain size of the middle region. This phenomenon is due to the tool stirring action creating severe plastic deformation and frictional heat, therefore the dynamic recrystallization occurs and produces a fine-grained structure, especially in the inner surface. Concerning the outer region, the limited grain size is due to the external roughness that inhibits the grain growth [55, 80]. In this regard, the average grain size measured for the case study ID C5 (Figure 129) were 3.5 µm, 4.4 µm, and 3.4 µm for the outer, middle, and inner regions, respectively.

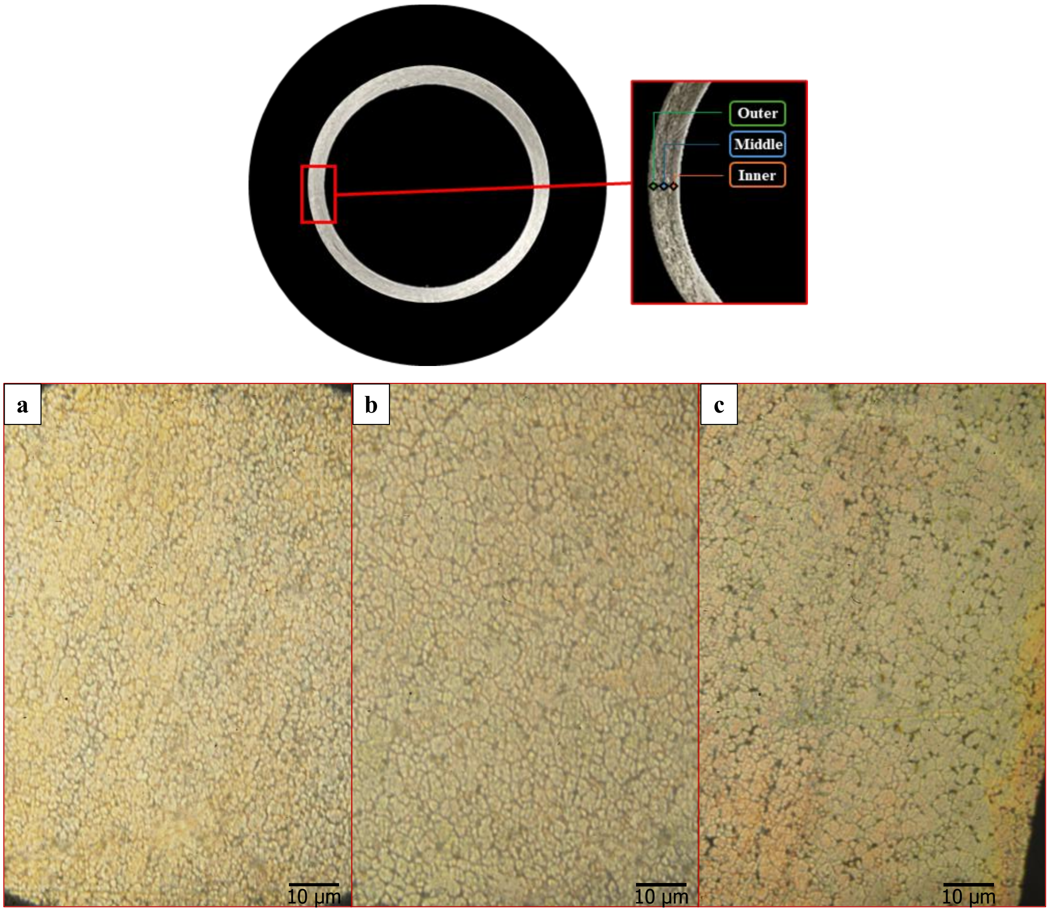

Figure 129. *Microstructure analysis of the cross section of the case study ID C5 tube: a) external, b) middle, and c) internal surface.*

An overview of the longitudinal grain size evolution was performed by considering the observation loci reported in Figure 125b. The selected observation loci provide a complete view of the grain evolution moving from the billet to the wall thickness, therefore it is possible to describe the "story" (evolution of the grains) of the material, from the unextruded chips to the extruded tube's wall. Results for case study IDs C2 and C5 are reported in Figure 130. The grains acquired just under the tool (position A and B) were subjected to a thermal coarsening due to the heat and a low level of strain (around 6 μm); close to the extrusion channel (C and D), the material flow had the effect of elongating the grain (around 8-10 μm) along the longitudinal direction. Before extruding, the material undergoes a consolidation mechanism similar to the friction stir consolidation (FSC); in fact, the range of grain size values is in accordance with what was found by Puleo et al. [95]. On the other hand, the material within the extrusion channel underwent high pressure and deformation, showing refined grain size (around 4 μm). After passing through the reduction zone, the grain size remains essentially unchanged along the tube walls (from zone E to zone H).

It is worth mentioning that points C and D show a bigger grain size for case study ID C5 than C2, mainly because of the different heat conditions. Specifically, the increase in rotational speed led to an increase in temperature [89] which promoted grain growth. When the material reaches the extrusion channel, a refining process starts (as mentioned before), but the effect of increased grain size remains visible along the longitudinal section of the tube. By comparing the microscopic and macroscopic analyses, it is clear that the hardness results (Figure 126) are consistent with the microstructural evolution shown in Figure 130. In particular, the fine and equiaxed grains observed for the C5 condition are correlated with the increased hardness values measured at the same process parameter. In Figure 130c, the porosity analysis of the extruded tubes for case study C5 was conducted using optical microscopy. The results indicate a porosity of 1.94 %, which is relatively low under appropriate rotational speed and extrusion force conditions. This reduction in porosity can be attributed to effective material plasticization achieved at the optimized process parameters, resulting in improved mechanical performance and enhanced microstructural integrity.

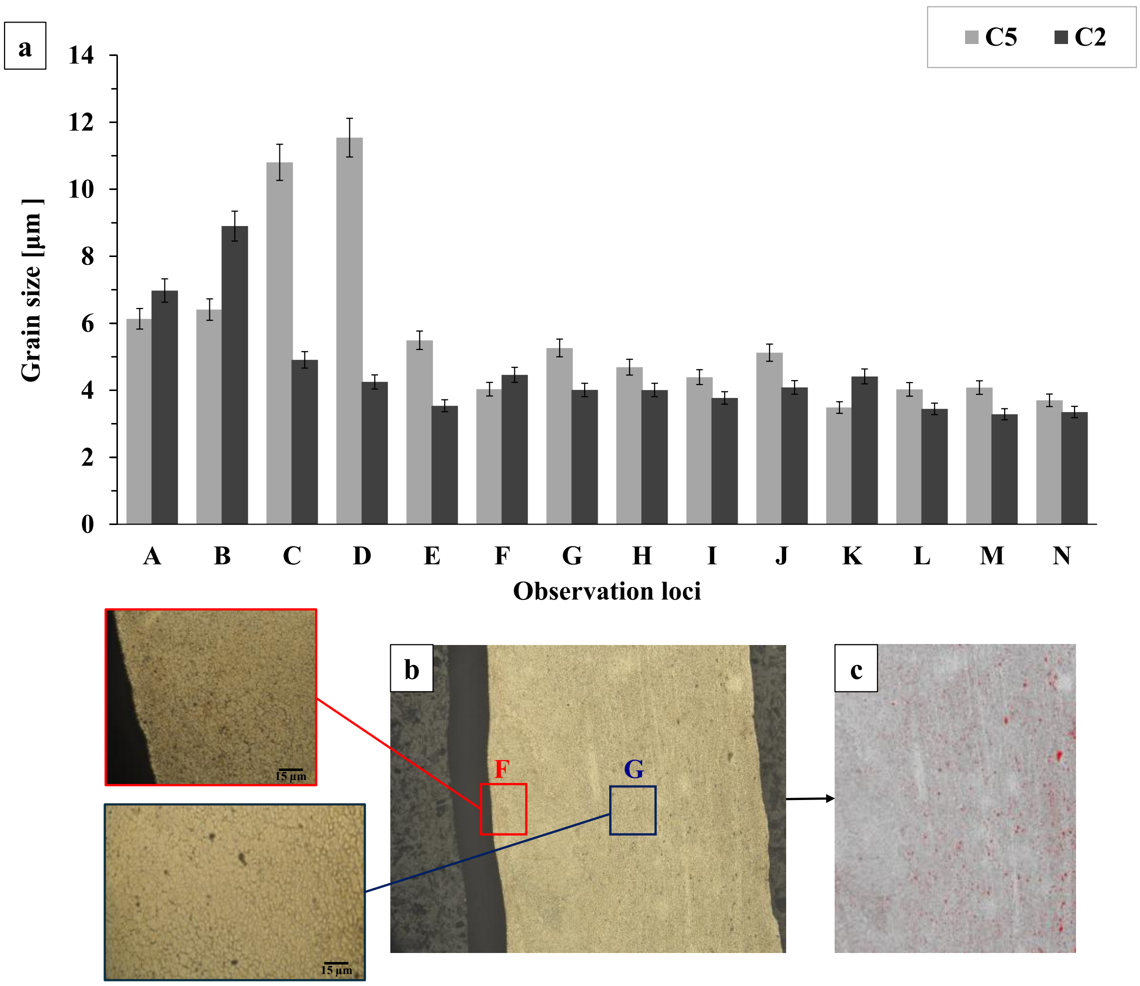

Figure 130. *a) Grain size distribution along the longitudinal section for C5 and C2, b) tube longitudinal section of C5, and c) porosity evaluation image.*

Lastly, the AA2024 tubes were sectioned in the longitudinal direction for microstructural evaluation by SEM. Micrographs of the tube wall are shown in Figure 131. For the case study C1, at low heat input, i.e., low tool force and rotation, (Figure 131a, and Figure 131b). This is due to insufficient heat for the chips to plasticize and bond. While at optimum rotational speed and force for the case study C5, the SEM image of the cross-section of the AA2024 tube is shown in Figure 131c. The specimen exhibits a nearly uniform material flow, and a good bonding between aluminum chips has been observed, which causes improvement of properties and reduced porosity. This is due to the sufficient heat provided by the tool's rotational speed and sufficient extrusion force, causing the extruded material to bond properly, which results in defect-free extruded tubes. The EDS mapping and analysis of the corresponding case study are shown in Figure 131d. These results are in accordance with the main findings concerning global mechanical properties discussed previously.

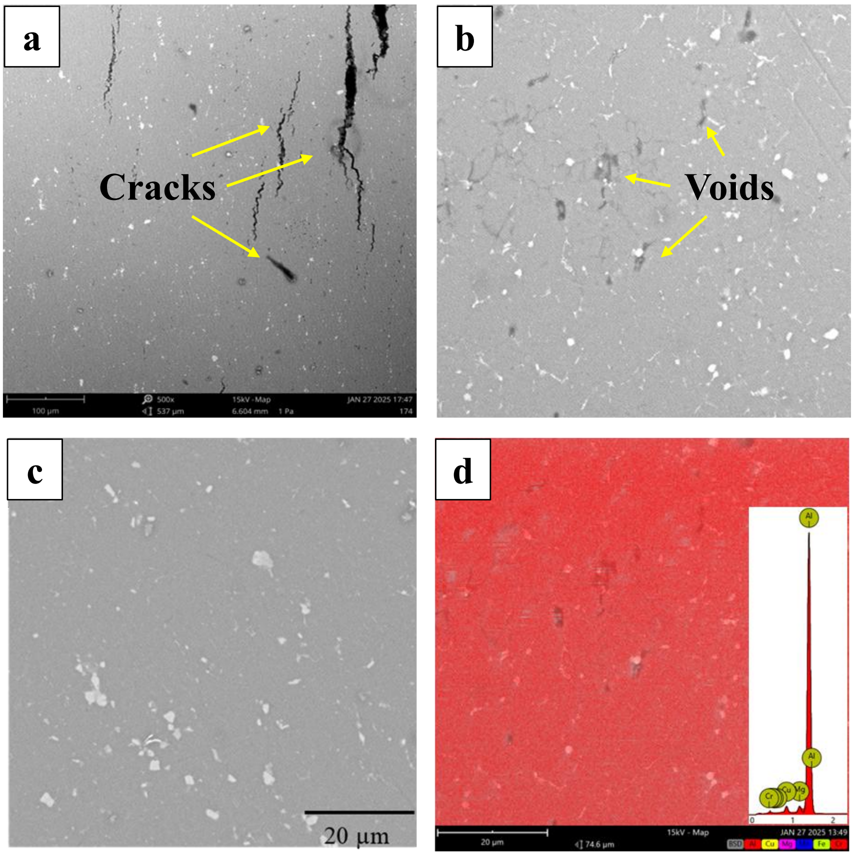

Figure 131. *a-b) SEM image of the cross-section of the sample ID C1, c) SEM image of the cross-section of the sample ID C5, d) corresponding EDS mapping and analysis.*

4.6.3.2 Numerical results

The numerical simulation is used to provide an insight into the process's mechanics and to motivate the observed experimental results. The first phenomenon discussed here is the change in grain size along the radial direction. In Figure 132 the effective strain distribution across the cross-section of the tube for case study C5 is reported. It is interesting to notice that the recrystallization behavior, previously highlighted in Figure 129, is corroborated by the effective strain evolution along the radial direction predicted by numerical simulation; the internal section of the tube (directly in contact with the tool) underwent higher strain than the external or middle one, resulting in better grain refinement.

Additionally, the evolution of the effective strain from the beginning of the process to the end is depicted in Figure 133. In this figure, two main phases were identified to better describe the curves: the transition phase and the steady state phase. In this phase, the material enters the clearance between tool and die, i.e. reduction zone, and thanks to high deformation levels (see strain rate, Figure 134), it is forced to extrude. Once the material reaches the extrusion channel, the strain level remains almost unchanged.

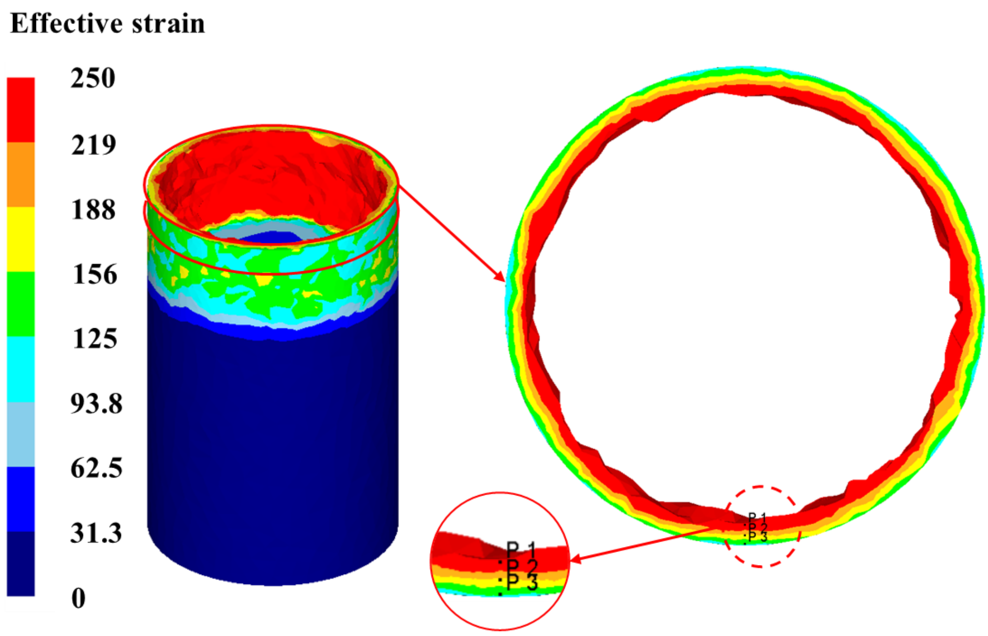

Figure 132. *Strain plot in the circumferential section of the tube, case study C5.*

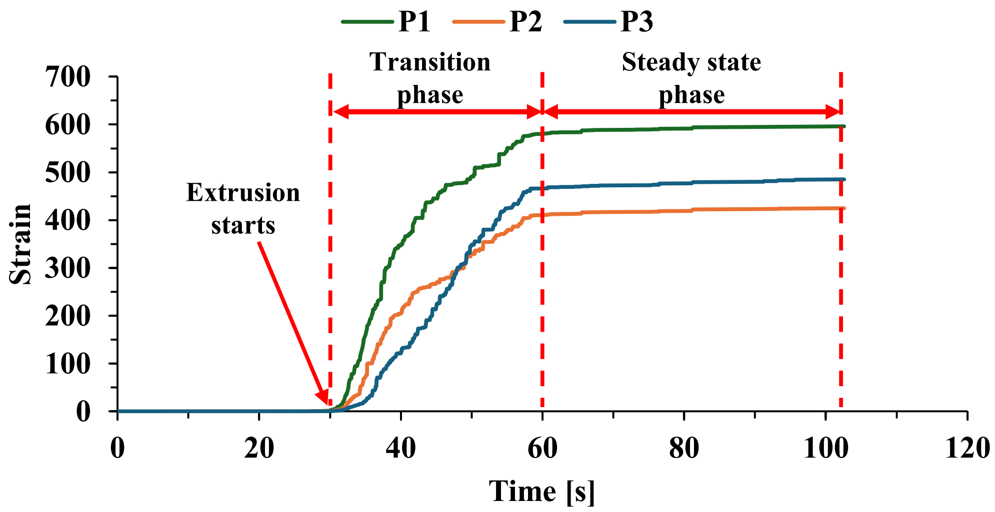

Figure 133. *Strain evolution of the three loci: internal (P1), middle (P2) and external (P3) for the case study C5.*

A more specific explanation of the grain size distribution along the thickness of the tube has been provided by studying the Zener-Hollomon parameter (Z) (Figure 134). It is known that the average grain size decreases with a decrease in the working temperature (T) and an increase in the working strain rate ($\dot{\varepsilon}$) [110]. According to the Zener-Hollomon formulation (Eq. 11), the average grain size decreases when the strain rate increases or the temperature decreases.

Considering as an example the case study C5, in Figure 134, temperature, strain rate, and logarithmic Zener-Hollomon (Log (Z)) parameter are plotted for 40s processing time. This figure shows that the temperature increases near the reduction zone, where the material undergoes high levels of deformation. The combination of high strain rate and temperature resulted in a low value of the Zener-Hollomon parameter, which is an index of big grain size (Eq. 11).

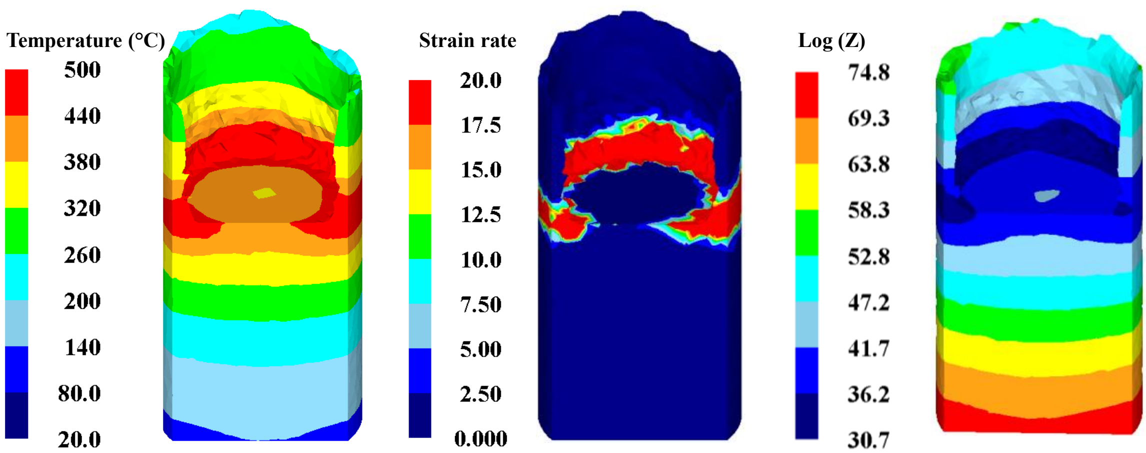

Figure 134. *Temperature, strain rate, and log (Z) distribution at 40 seconds for the case study C5.*

In Figure 135 a detailed view has been proposed by varying the scale value of the Z-parameter. Specifically, in this picture, the upper bound and lower bound (Figure 135a) of the scale was set to catch the small variation of the Z-parameter along the thickness, and the results showed an increase at the external surfaces (namely internal and external) while decreasing moving towards the center of the tube (Figure 135b).

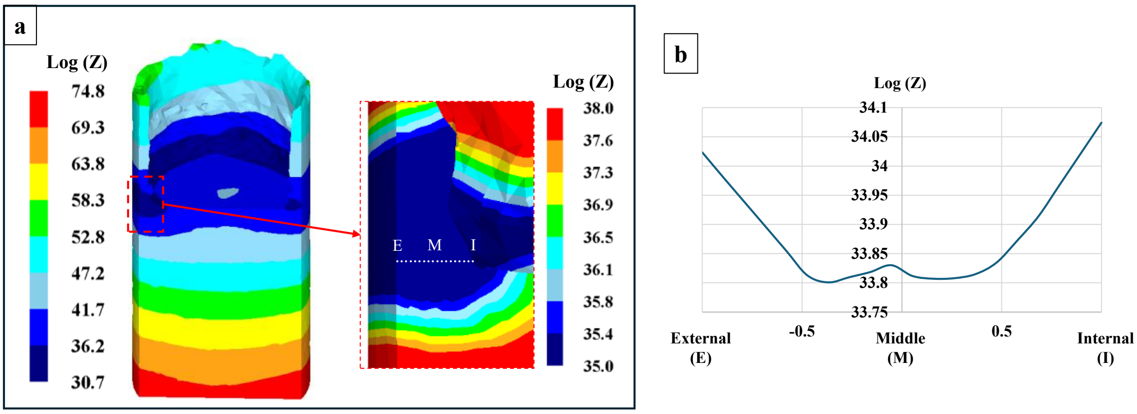

Figure 135. *a) Zener-Hollomon parameter distribution at the extrusion channel and b) Zener-Hollomon analytical distribution along the external (E), middle (M), and internal (I) surface of the extrusion channel.*

4.6.3.3 Limit of the process: extrusion velocity reduction

In Figure 136, the comparison between three different temperature-tool displacement curves has been presented, aiming to describe the limit of the process. Specifically, three case studies were selected to describe the effect of different rotational speeds (IDs C2, C5, and C8) on tube extrusion.

Firstly, looking at the shape of the tool displacement curve for case study ID C2 (Figure 136a), it is possible to note a linear trend. This means that the extrusion rate is quite constant. When looking at the tool displacement trend of case ID C5 (Figure 136b), a different behavior is recorded instead. Specifically, an initial linear trend is visible, at 40s processing time, a slope change occurs, proving an extrusion rate decrease. This phenomenon is even more visible in Figure 136c, where the displacement and temperature trend for case study ID C8 are reported. From this observation, it is possible to state that the process reaches a sort of stuck condition when high temperatures are reached. Actually, for all the tests, the temperature peak was close to 350 °C, but it was reached at different process times, while the maximum displacement was almost the same.

This might appear counterintuitive, as with an increase in temperature, a softening of the material occurs, and the extrusion conditions should be eased. Nevertheless, this phenomenon is to be attributed to the consolidation level of the unextruded chips still in the extrusion chamber rather than to the temperature-enabled softening effect. In fact, the increase in temperature eases the solid bonding occurrence of the material still present in the extrusion chamber. As a given level of consolidation is reached, the extrusion conditions worsen as a higher vertical load should be applied to keep the extrusion rate constant. Moreover, the faster the temperature increases, the faster the material consolidates the earlier the extrusion rate reduction phenomenon occurs (ID C8, Figure 136c). A comparison of the temperature profiles for C2, C5, and C8 is proposed in Figure 136d, to better visualize the heating effect of different rotational speeds at the same load. In this figure, it is clear that higher rotational speed leads to a greater temperature increasing rate, resulting in both excessive consolidation and early process termination.

Figure 137 shows the different Temperature distribution with carrying the rotational speed, and it is possible to note that at higher rotational speed values (ID C8) possibly anticipating the stuck conditions.

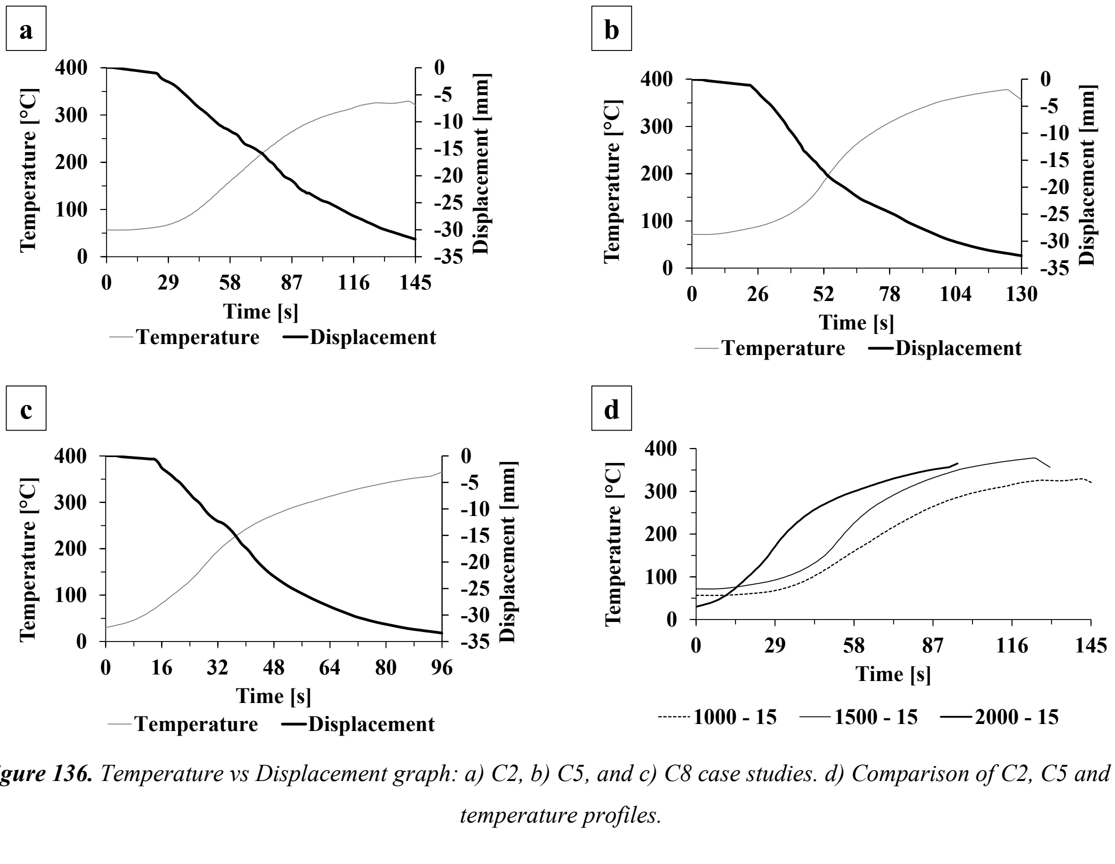

Figure 136. Temperature vs Displacement graph: a) C2, b) C5, and c) C8 case studies. d) Comparison of C2, C5 and C8 temperature profiles.

For a better understanding of the phenomenon, the density evolution during the process has been numerically analyzed, and the results for case study ID C5 are reported in Figure 138. It is possible to notice that the portion of the unextruded chips in the extrusion chamber reaches a density equal to 1 as the processing time increases. After 60 seconds, the entire sample is almost all at a density equal to 1.

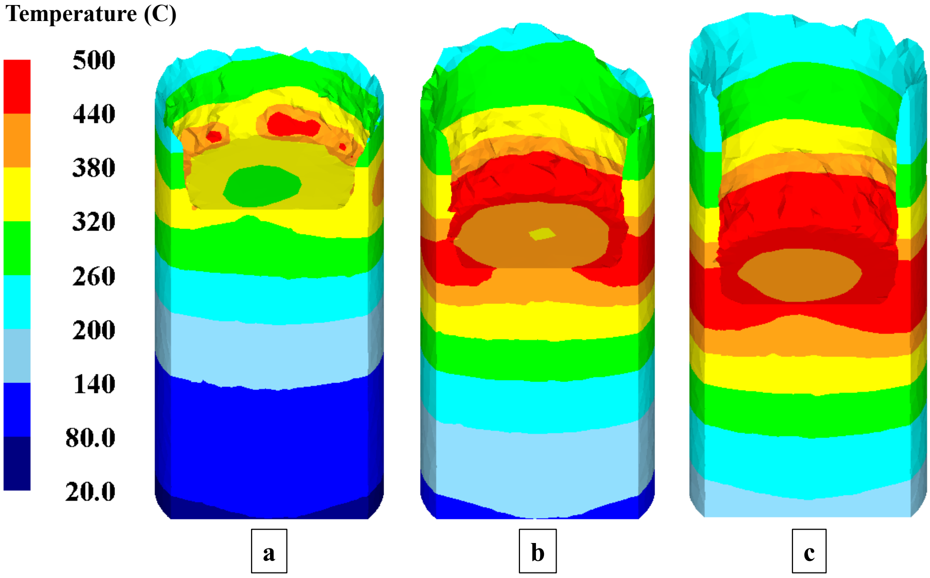

Figure 137. *Temperature plot for the case study IDs a) C2, b) C5 and c) C8 at the process time window (40 s).*

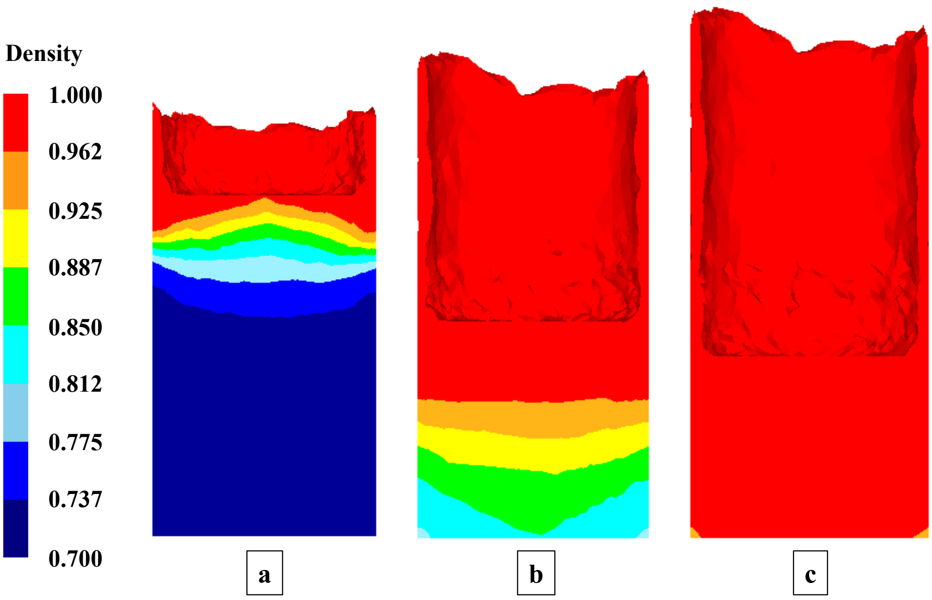

Figure 138. *Density evolution of the case study ID C5 at a) 30, b) 50, and c) 65 seconds.*

To further support this finding, solid bonding was investigated in the material chamber zone. The aim was to study the consolidation occurrence for the material located at the bottom of the extrusion chamber (not extruded material) during the tube extrusion process. This study was carried out by analyzing the bonding condition by varying the processing time over a set of 119 observation loci, as reported in Figure 139a. For monitoring the bonding condition, the Donati and Tomasini criterion was used [77], as it was specifically tuned for the extrusion process. With such kind of approach, the bonding value W in a given observation locus is calculated by using stress and strain values extracted from the numerical simulation, and the value is then compared with a limit value W^{Lim}. When the bonding value (W) of a point is greater than the corresponding bonding limit value (W^{Lim}), that point is considered consolidated. W^{Lim} value changes with material and temperature, proper bonding limit values should be identified for the here used material and for the here recorded process temperatures. In this regard, the W^{lim} expression reported in Eq. 31 is used; this expression was calculated by using the data for AA2024 and the related approach presented by Puleo et al [95].

$$W^{Lim} = -1 \cdot 10^{-4}\, T + 0.0653 \tag{31}$$

Bonding conditions were evaluated at different process times windows, namely 40, 50, 60 and 70 seconds, results are reported in Figure 139b, c, d, e.

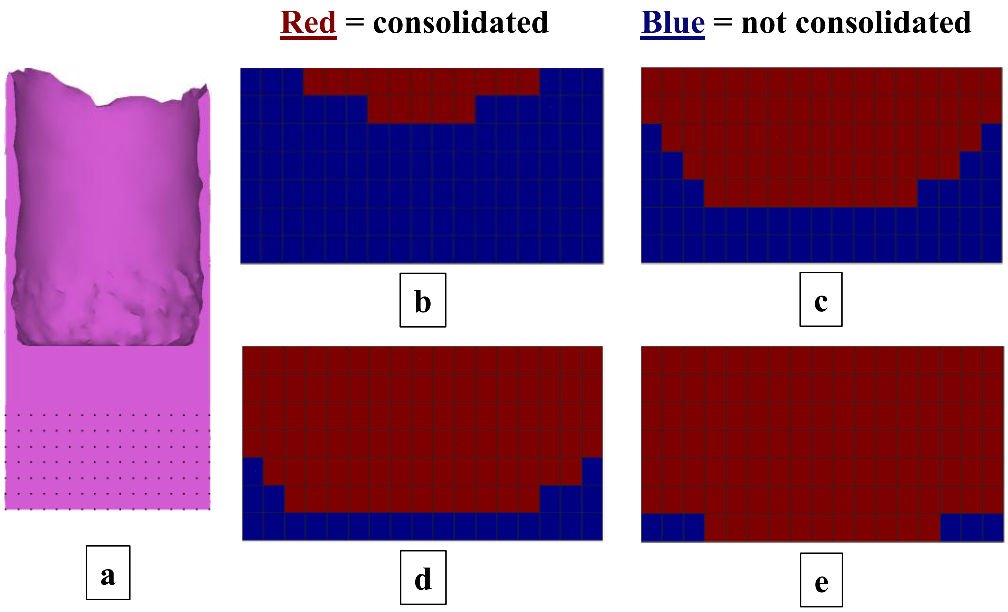

Figure 139. *a) 119 observation loci at the bottom of the cross section of case study C5 at 60 seconds. Solid bonding occurrence maps b) 40 s, c) 50 s, d) 60 s, e) 70 s.*

The bonding maps in Figure 139 revealed that the consolidation phenomenon already begins at 40 seconds. As the process time increased, the consolidation front moved downward, resulting in almost complete material consolidation at around 70 seconds. This bonding condition analysis is consistent with what was reported above concerning density and displacement trends.

As a result of this analysis, different approaches can be considered to mitigate the issue presented. Examples include the use of an active cooling system or a variable tool rotational speed. In the first case, the cooling system could be integrated into the die setup to control the material temperature at the bottom of the die, thereby promoting a slower consolidation of the unprocessed material. The second approach focuses on in-process control of the tool's rotational speed, combined with sensors and thermocouples. This would enable a real-time adaptive system that modulates the rotational speed (reduces the velocity if too hot or increases it if too cold) based on the heat generated by the friction.

4.6.3.4 Electrical energy consumption results

One of the main novelties of the proposed approach concerns the possibility of turning chips directly into tubes by a single-step manufacturing approach. Actually, other approaches already presented are made of a pre-consolidation and/or homogenization step prior to the extrusion process. The single-step nature of the friction stir extrusion approach would allow electrical energy savings to further contribute to reducing the environmental impact of aluminum-based products. In this Chapter, the electrical energy characterization of tube production through friction stir extrusion is provided and compared to that characterizes double-step approaches. The electrical energy was measured by means of a power and energy quality analyzer, Chauvin Arnoux C.A. 8331 (sampling rate of 12.8 kHz, results logged and shown are for averaged values over one-second intervals), connected to the machine input. The entire working cycle was monitored from chips compacting up to tool withdrawal. The typical power consumption profile is plotted in Figure 140a. This figure depicts the power consumption of the entire process, starting from the cold pre-compaction at 35 kN (needed to ensure filling the extrusion chamber) up to the extrusion process. This process was carried out by switching from a position control phase to a force control phase. The first one, the position control phase, is a brief phase where the tool moves downward for a few millimeters (at 5 kN) to ensure adequate contact with the material. The second one, the force control phase, is the actual extrusion process where the force increases from 5 kN to the required force (12, 15 or 18 kN) and the tube is extruded. Moreover, the first part of the process, namely chips preparation, was the same for each test, while the second part, friction stir extrusion, is characterized by a similar shape with different power levels depending on the process parameters used. The power absorbed by the machine was recorded and plotted against the process time for the three considered values of tool rotation

(1000 rpm, 1500 rpm, and 2000 rpm) (Figure 140b, c, d). It is noteworthy that variations in force have no significant impact on power consumption. However, the processing time decreases (and therefore the electrical energy consumed) with increasing both tool force and tool rotation. As previously discussed, this behavior can be attributed to reduced heat generation at lower rpm and force, which results in low extrusion rate and, consequently, long processing times.

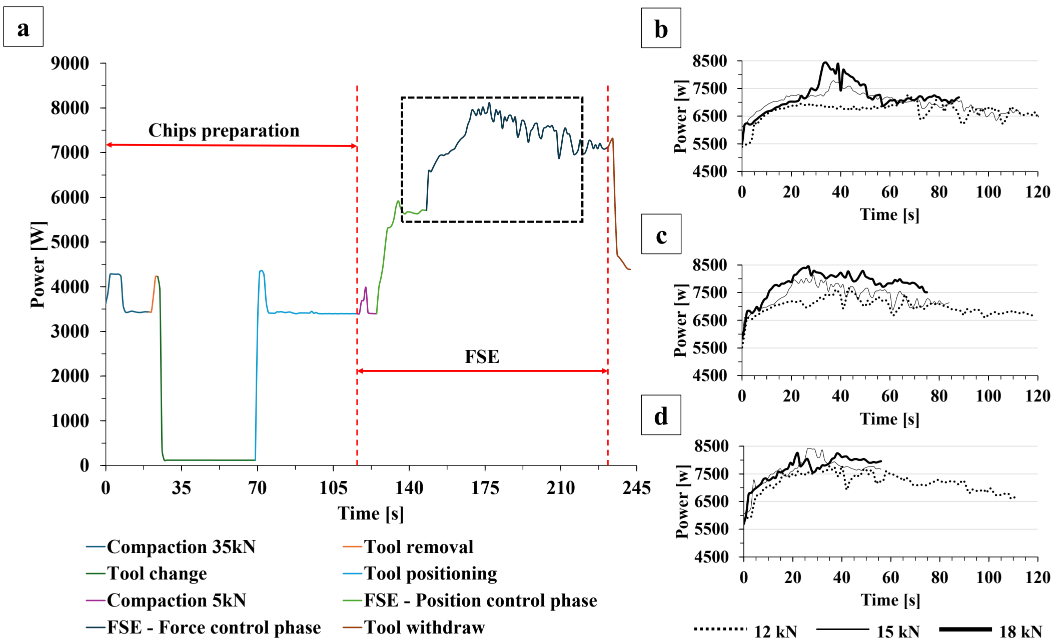

Figure 140. *a) Power consumption profile across processing phases and comparative analysis of the force control window (black dashed window) at b) 1000 rpm, c) 1500 rpm and d) 2000 rpm.*

Looking at Figure 140, it is visible that the power needed for the extrusion exhibits a starting increasing trend followed by a decreasing trend. The reason behind this phenomenon can be attributed to the material flow. Specifically, at the beginning of the process, the temperature increases due to the friction between the rotating tool and chips. When the material is plasticized and extrusion starts, the hot material extrudes, leaving the cold one behind, which causes a decrease in temperature. At this point, less power is required for extrusion, resulting in a comparatively decrease in power.

A further investigation on specific energy consumption (SEC) was carried out to quantitatively assess the influence of different process parameters. The SEC evaluation was performed by considering the same height of tube produced, therefore the same mass, as a functional unit. Specifically, the extrusion speed at steady state was employed to calculate the time required for extruding a fixed height of tube. Consequently, the average energy absorbed was then divided by the mass to obtain SEC values. The results are summarized in Figure 141.

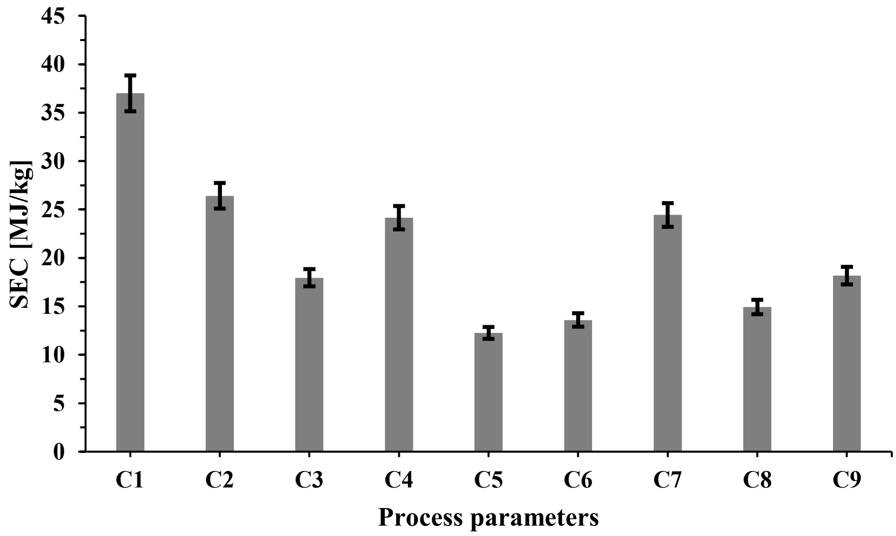

Figure 141. *SEC evaluation for all case studies.*

From Figure 141, it can be observed that the process duration has a stronger effect on SEC than energy consumption. In this regard, comparing the SEC results of 1000 rpm samples and the process times (visible in Figure 140b) it is clear that although the power required for extruding is lower for C2, the specific energy consumption is the highest due to the process duration. When the process time is reduced, the SEC is lower, as demonstrated for C4 and C7. Additionally, energy plays a significant role in tests with comparable process time (C5 and C6 or C8 and C9). In these scenarios, the higher the energy, the higher the SEC. Lastly, concerning the comparison between C2, C5, and C8 which was proposed in different chapters, it is evident that both tube quality obtained in C5 and the lower SEC led to this parameter combination as the optimal solution.

When compared to the conventional remelting process, the efficiency of this approach becomes evident. Cooper et al. [111] report that the total primary energy required for chip recycling (melting), recovery of melting losses (10% of primary aluminum), and extrusion is about 40 MJ/kg. These results clearly demonstrate that FSE, at the optimal parameters (C5), provides significant energy saving.

In order to provide insight into the single-step extrusion efficiency in terms of less power demanding, a comparison between two scenarios was carried out. Specifically, a case study where the tube was directly extruded from chips and a case study where the chips were first consolidated into a billet and then extruded were studied. For consolidating the chips into a billet, a friction stir consolidation process was selected. This process is a suitable option because it shares the same setup and mechanism as the process dynamics of friction stir extrusion, but no extrusion is provided during FSC. In fact, the FSC involves the use of a die, a backing plate, and a tool which, in this study, were the same as the compacting phase. The process parameters selected for the billet consolidation (FSC) were chosen based on previous research [88, 95]. Specifically, 1500 rpm (rotational speed) and 15 kN (vertical load) were selected. Results of the comparison between the two scenarios applied to the C5 case study are depicted in Figure 142. It is clear that the single step is more energy efficient as the consolidation step is skipped. Moreover, in the single-step process, the material is less consolidated at the beginning, resulting in a lower power required for extruding the tube. In fact, looking only at the extrusion step, it is possible to notice that the double step demands a lower power level with respect to the single step approach. In conclusion, the proposed single-step approach is an environmentally friendly solution with respect to the double step, as it requires both a reduced power level and shorter processing time.

Concerning the temperature profiles, the extrusion step performed after the FSC process resulted in an excessive temperature increase. This is visible when looking at Figure 142 where the recorded temperature trends of the entire working cycle of the two approaches are reported.

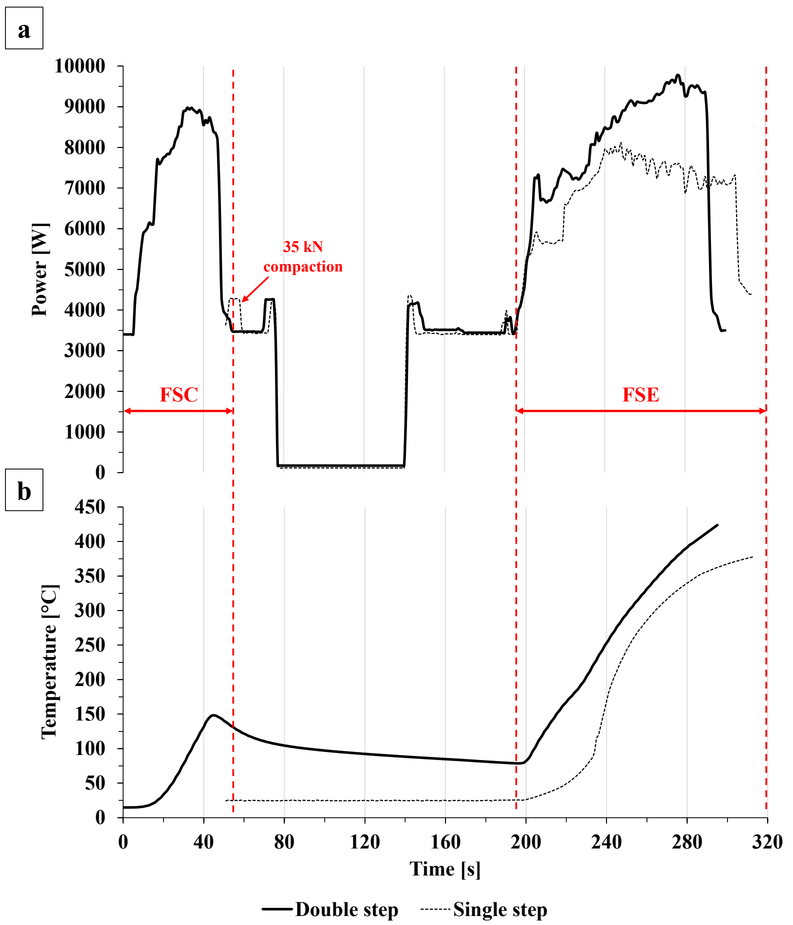

Figure 142. *A) Power consumption and b) temperature comparison between double and single step.*

4.6.4 Summary of the results

This work aimed to produce aluminum tubes directly from chips using a single-step friction stir extrusion process. An experimental campaign was performed to successfully produce a consolidated tube from AA2024-O aluminum chips under various process conditions, and a numerical approach was employed to better explore the process mechanics. The mechanical and metallurgical properties of the tubes were analyzed, and the following conclusions can be drawn:

- This study successfully demonstrated the single-step production of aluminum tubes, directly from chips, achieving excellent mechanical and microstructural properties while ensuring superior energy efficiency compared to conventional multi-step routes.
- The microstructural analysis shows that strong grain refinement is obtained with small grain size variation in radial direction (average grain size equal to 4): 3.4 µm close to the inner surface, 4.4 µm at the middle of the thickness, and 3.5 µm close to the outer surface.
- Defects such as porosity and cracks have been observed on low heat input conditions (1000 rpm – 12 kN). On the contrary, hot crack phenomena were observed at high heat input (2000 rpm – 15 kN). A quantitative study demonstrated that the porosity of the extruded tube under the worst condition (1000 rpm) resulted in 1.8% of porosity.
- Microhardness increased significantly compared to the base material (from 61.5 HV to an average 140 HV). Moreover, it has been observed that the hardness increases with increasing vertical load.
- Compression and flattening tests confirmed that the 1500 rpm – 15 kN condition yielded the best bonding and mechanical performance, compared to 1000 and 2000 rpm, showing no separation of the layers during the flattening of the tubes, and good bonding efficacy of the process.
- The numerical simulation corroborated the finding concerning grain size. The Zener-Hollomon parameter was calculated, and high Zener-Hollomon values were observed at the internal and external surfaces of the tube, which is in accordance with the experimental grain size measurements. Moreover, the tool's stirring effect on the recrystallization phenomenon was successfully explained and justified by a strain study thanks to numerical simulations.

- Energy analysis confirmed that the single-step approach is more efficient and environmentally friendly than the traditional two-step route, as it requires both reduced power level and shorter processing time. Additionally, the FSE revealed an SEC of about 15 MJ/kg at C5 conditions, which is lower than the traditional melting + extrusion process.
- Experimental and numerical results revealed that excessive consolidation of the material in the bottom region of the extrusion chamber may represent a process limit. A solid bonding analysis demonstrated that the unprocessed material is affected by pressure and temperature, leading to earlier consolidation. As a matter of fact, the required extrusion force increases as the material consolidates, leading to an excessive temperature increase and a reduction in the extrusion rate.

4.7 AA7075-AA2024 bi-metallic tube manufacturing

In many industrial sectors, the mechanical and thermal properties of a single material are often insufficient to meet the diverse property requirements of a component. For this reason, after the feasibility study on tube manufacturing via FSE, a new research question arose on the capability of this process to produce a bi-metallic tube: “Is it possible to manufacture a multilayer tube by FSE?”.
In this chapter, this question will be answered and the results discussed.

4.7.1 Experimental methodology

For the experimental campaign, AA7075 aluminium alloy chips were used as the outer tube, whereas AA2024 aluminium alloy chips were considered for the inner one because of the different material ductility. Table 28 shows the chemical compositions of the starting material, i.e., AA7075-T6 and AA2024-T3 aluminium alloy, used in this work. The recycling chips were produced from the milling operation of AA7075-T6 round bar and the turning operation of AA2024-T3 bar. Additionally, the chips were submerged in the acetone for effective cleaning before processing.

Table 28. *Chemical composition analysis of AA2024-T3 [112] and AA7075-T6 [113] aluminum alloys.*

Material	Al	Cu	Mn	Mg	Si	Fe	Cr	Zn
2024-T3	Bal.	4.91	0.54	1.31	0.145	0.31	0.09	0.10
7075-T6	Bal.	1.5	0.3	2.6	0.4	0.5	0.22	5.4

As well as in Chapter 4.6, the experimental tests were performed on an ESAB LEGIO machine, but the process steps were slightly different. The FSE process was structured in four different steps: AA7075 chips loading, AA7075 tube extrusion, AA2024 chips loading, and AA2024 tube extrusion. A schematic diagram of the FSE-based bimetallic tube extrusion process is presented in Figure 143.

In the first step, 20 grams of AA7075 aluminium alloy chips were placed into a custom-designed split die (Figure 144a), which had an internal diameter of 25 mm and a height of 76 mm. The die was manufactured and securely assembled to a backing plate using bolts and nuts. The chips were compacted using a 25 mm diameter flat-head H13 steel tool (Figure 144b) under an axial force of 5 kN to ensure uniform density and avoid scattering during extrusion. The outer tube was then extruded using a 23 mm diameter tool with a 20° conical taper profile (Figure 144c). It is noteworthy to mention that the conical profile was used instead of a flat one to promote smooth material flow and easy tool insertion [107]. After the outer tube was extruded, 20 grams of AA2024 aluminium alloy chips were poured into the internal cavity of the previously extruded tube. These chips were compacted using a flat tool of 23 mm diameter, again under a force of 5 kN. The inner tube was subsequently extruded using a 21 mm diameter tool with the same 20° conical taper profile. The tests were performed at 15 kN vertical load and three rotational speeds equal to 500 (low), 750 (medium), and 1000 (high) rpm.

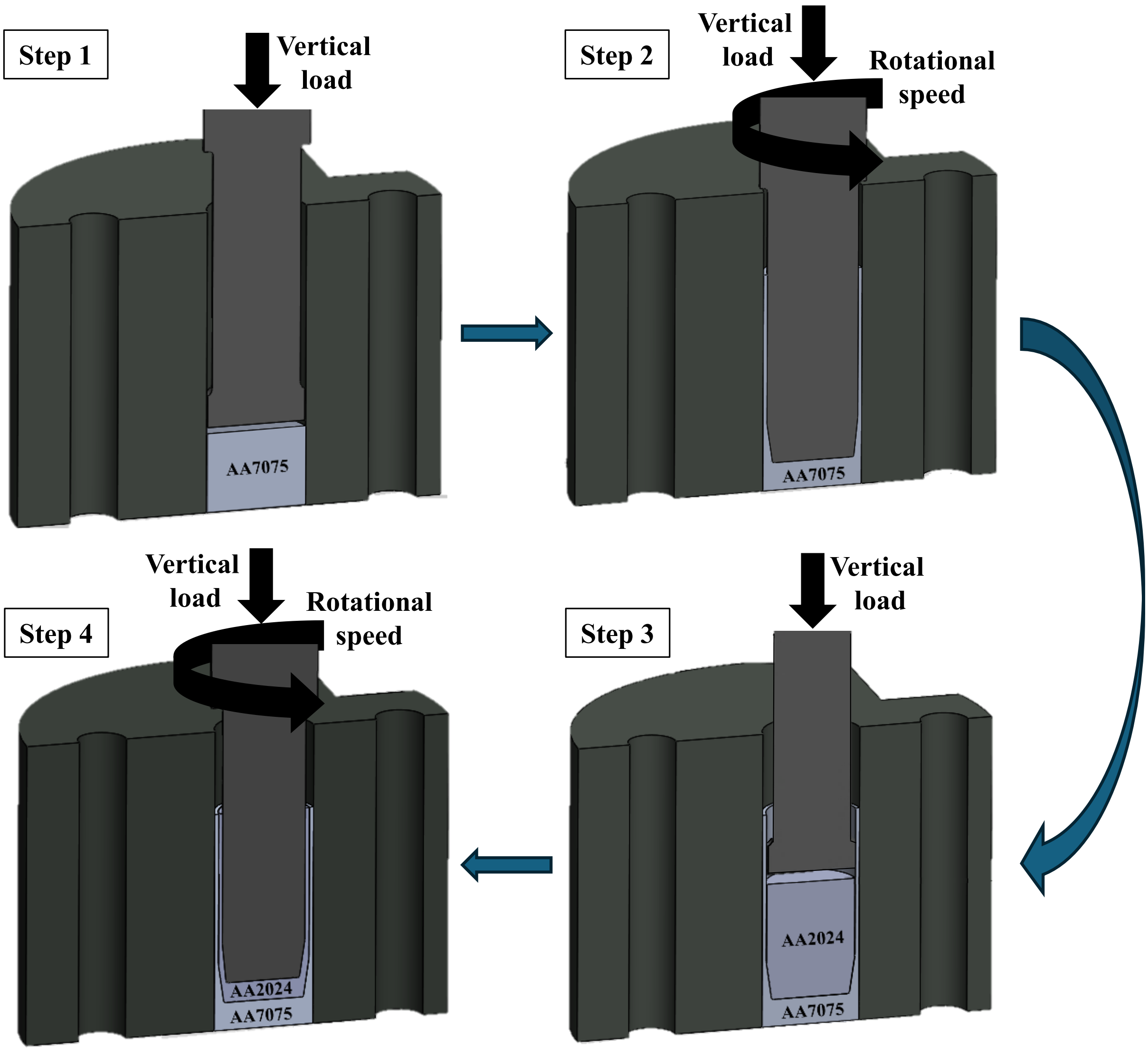

Figure 143. *Schematic diagram of FSE bimetallic tube extrusion process: AA7075 chips compaction (Step 1), AA7075 tube extrusion (Step 2), AA2024 chips loading and compaction (Step 3), and AA2024 tube extrusion (Step 4).*

In the current study, the outer layer of the bimetallic tube (AA7075) had an average thickness of approximately 1.0 mm, as well as the inner layer (AA2024). Details of the tool geometries are shown in Table 29, while process parameters, including rotational speed and axial extrusion force, are summarized in Table 30.

It is worth mentioning that for monitoring temperature during the extrusion process and for tuning the numerical simulations, a K-type thermocouple was inserted into a hole drilled at 1/3-height of the die, positioned 1 mm away from the inner die wall (Figure 144a, A-A section).

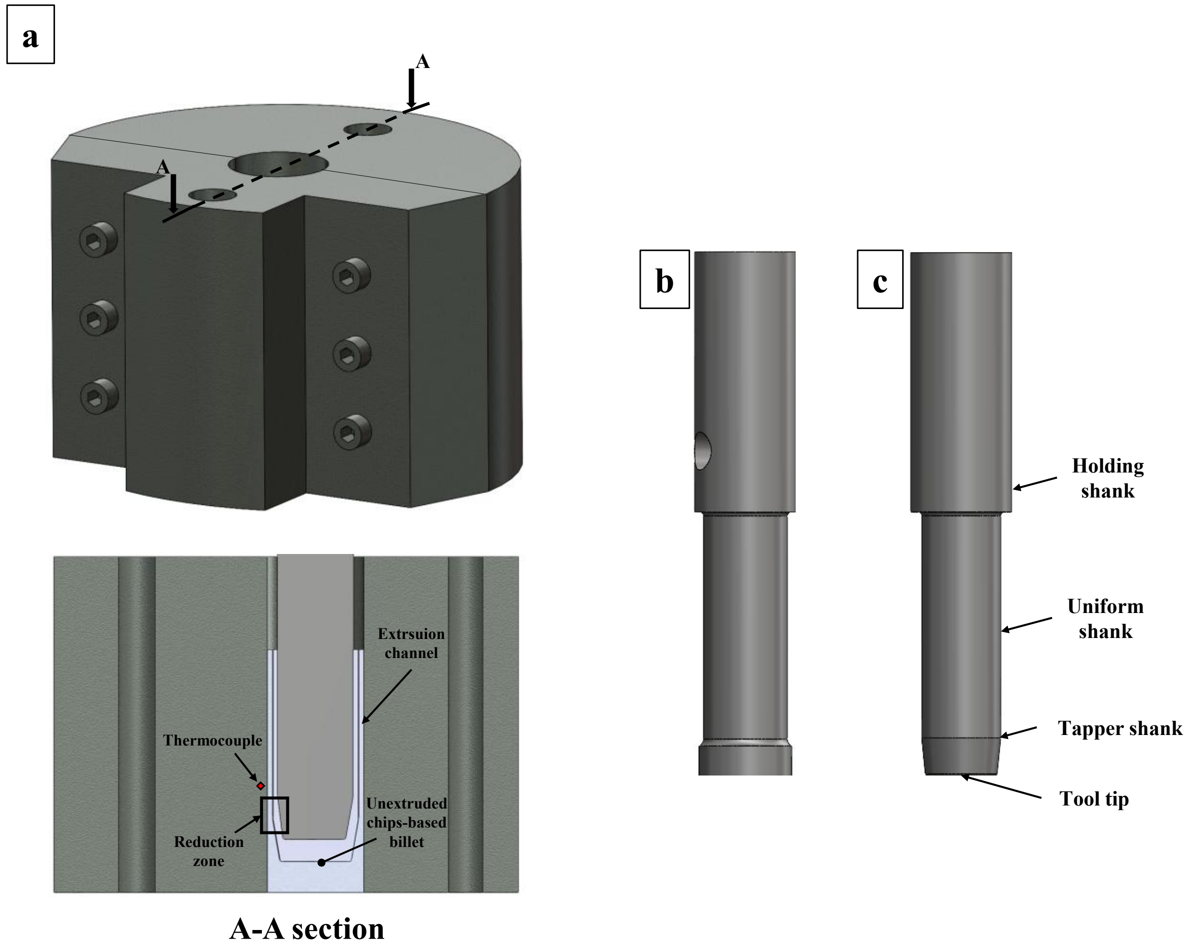

Figure 144. *Sketches of the (a) designed die with section, (b) compacting tool, and (c) 20° tapered tool.*

Table 29. *Geometry characterization of tapered tools.*

Tool	Material	Uniform shank (Ø)	Tool tip	Holding shank	Tapered length	Uniform shank
For AA7075	H-13 tool steel	23 mm	22 mm	Ø 30 mm	10 mm	70 mm
For AA2024	H-13 tool steel	21 mm	20 mm	Ø 30 mm	10 mm	70 mm

Table 30. *FSE process parameters and tube material layers disposition.*

ID	Rotational speed [rpm]	Force [kN]	Total tube thickness [mm]	Outer tube	Inner tube
ID1	500	15	2	7075	2024
ID2	750	15	2	7075	2024
ID3	1000	15	2	7075	2024

Consequently, the bimetallic tubes were cut longitudinally to the extrusion direction to prepare samples for mechanical and microstructural evaluation. For mechanical assessment, Vickers microhardness tests were conducted using a 0.5 kg load and a 15-second dwell time. Hardness measurements were taken across the wall thickness of the tube, starting from the outer diameter toward the inner surface, at intervals of approximately 0.2 mm. Each point was tested three times, and the average of the results was used to ensure consistency and reliability.

4.7.2 Numerical methodology

A numerical campaign was performed using the commercial finite element software SFTC DEFORM 3D. The numerical setup involves five components: a die, a backing plate, two tools, and material chips (Figure 145). The modelling of the chips batch is complex and for this reas,on the aluminium chips were considered as a single block porous material, following the material formulation of Shima-Oyane [86]. Specifically, an initial relative density value of 0.7 was assigned to the porous billet, calculated experimentally considering the mass of the loaded chips and the geometry of the die's chamber. The porous billet was characterized by a mesh size of 35000 elements with a refining mesh window close to the tool-material contact (Figure 145, A-A section).

The other components were considered as rigid material made of H-13 steel. The two tools were defined by a mesh size of 60000 elements, while for both the die and backing plate, the mesh size was 30000 elements. A tuning approach was performed for calculating the proper thermal and frictional coefficients. In this regard, the experimental data of the thermocouple were tuned to the numerical one, and the following values were obtained: shear factor of 0.2 and interface heat transfer coefficients (IHTC) of 11, 45, and 45 W/mm²/K for the tool-material, die-material, and backing plate-material contacts, respectively.

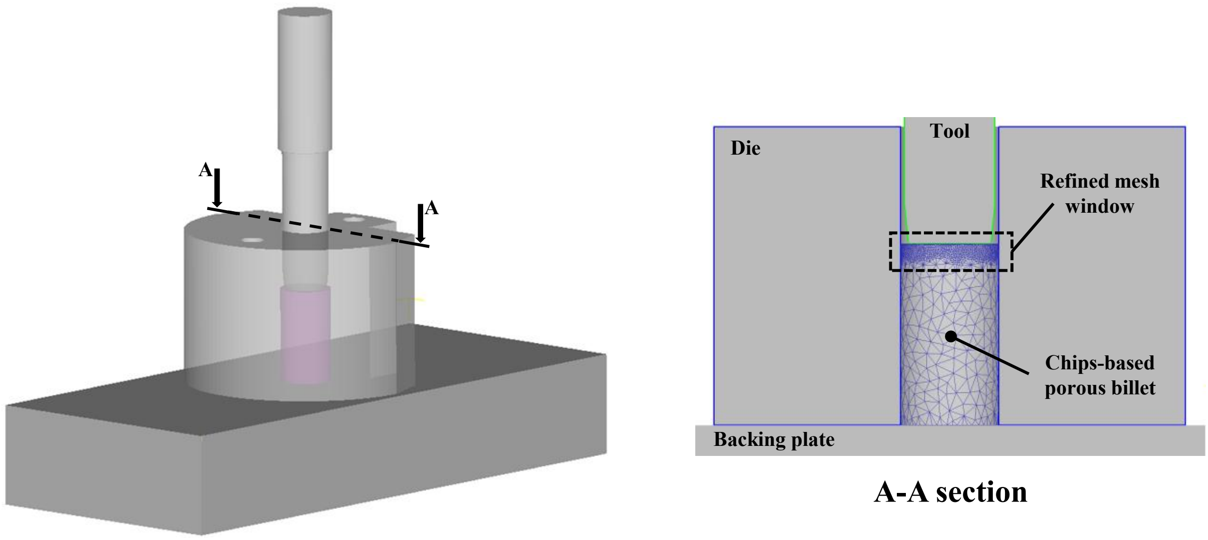

Figure 145. *Numerical setup for the FSE bimetallic process and section of the parts.*

4.7.3 Results and discussion

Figure 4 depicts the bimetallic tubes fabricated from AA7075 and AA2024 aluminum alloy chips using the FSE process under various process parameters. All tubes were successfully extruded, demonstrating the viability of the FSE technique. However, surface quality and material consolidation varied with processing conditions.

At the beginning of the process, the material is compressed and heated up thanks to the initial stirring and frictional actions of the tool. In these early stages, proper process parameters are crucial for obtaining optimal chips bonding and high surface quality. In this regard, when the heat generated is too low (ID1, Figure 146a), a lack of consolidation of the first extruded layers is visible near the top surface of the tube. On the other hand, at a high rotational speed (ID3, Figure 146c), excessive heat led to early softening of the material, which resulted in the surface deteriorating and uneven surface roughness in large parts of the extruded tube. At a medium rotational speed (ID2, Figure 146b), optimal surface conditions were achieved. At process parameters ID2, the tube exhibited a uniform and quite smooth outer surface with no visible cracks at the top. Additionally, the bottom surface showed no signs of adhesion between the backing plate and the workpiece material, indicating effective material flow.

It is worth remarking that the material behavior of AA7075 recycling chips plays an important role in material bonding; high mechanical properties may hinder proper consolidation. Difficulty in chips bonding for AA7075 recycling chips was also experienced by Puleo et al. [88] in the friction stir consolidation process.

The final length of the bimetallic tube, after trimming both top unconsolidated chips and bottom consolidated billet, was approximately 40 mm.

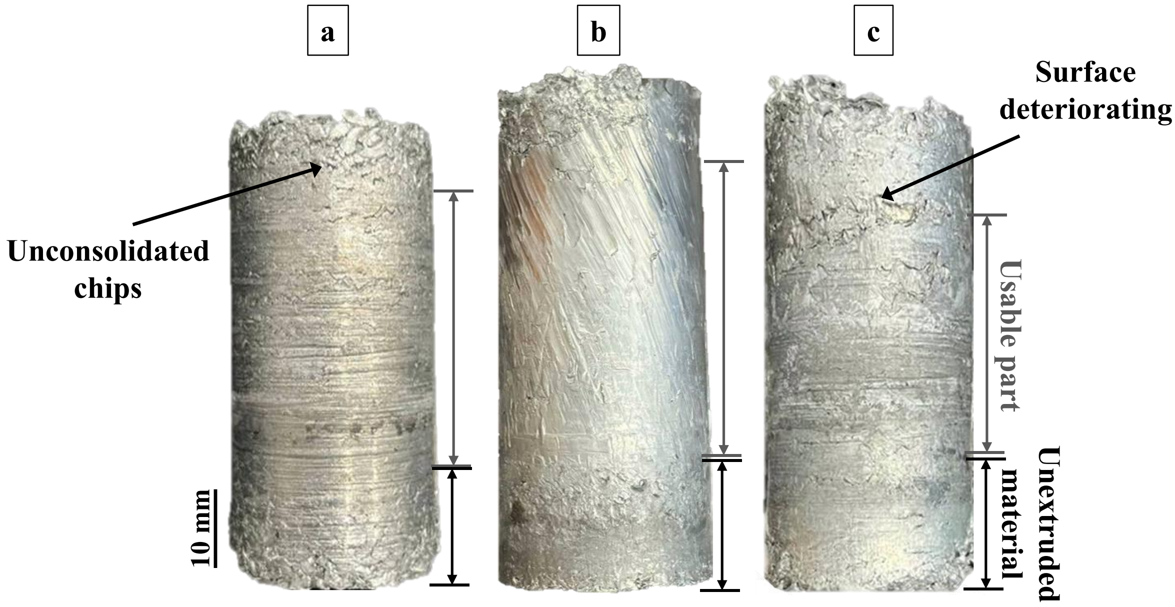

Figure 146. *Macroscopical observations of bimetallic tubes through FSE process for (a) ID1, (b) ID2 and (c) ID3.*

4.7.3.1 Microstructural Investigations

Figure 147 illustrates the cross-sectional microstructure of the AA7075/AA2024 bimetallic tube fabricated under different process parameters. In Figure 147a, corresponding to the low rotational speed condition (ID1), insufficient bonding is observed at the interface of the two materials. A distinct separation indicates that inadequate heat was generated during the process, preventing effective metal-to-metal bonding. High-resolution imaging of the interface further confirms the presence of unbonded regions. In contrast, Figure 147b and Figure 147c, corresponding to medium (ID2) and high (ID3) rotational speeds, show no visible surface defects in the cross-section. The interface appears continuous and free from voids or delamination, indicating successful consolidation and a structurally sound bimetallic tube.

Looking at the third column of Figure 147 (higher magnification), a distinct interfacial region, commonly referred to as the diffusion layer, is clearly visible and outlined by two yellow dashed lines. This zone represents a transition area where the AA2024 and AA7075 interface bonding occurs. The presence of this diffusion layer confirms atomic interdiffusion between the two alloys, which contributes to the formation of a strong metallurgical bond. The gradual transition in composition within this layer (i.e., EDS images) further supports the effectiveness of the FSE process in achieving solid-state bonding without the formation of defects or interfacial discontinuities.

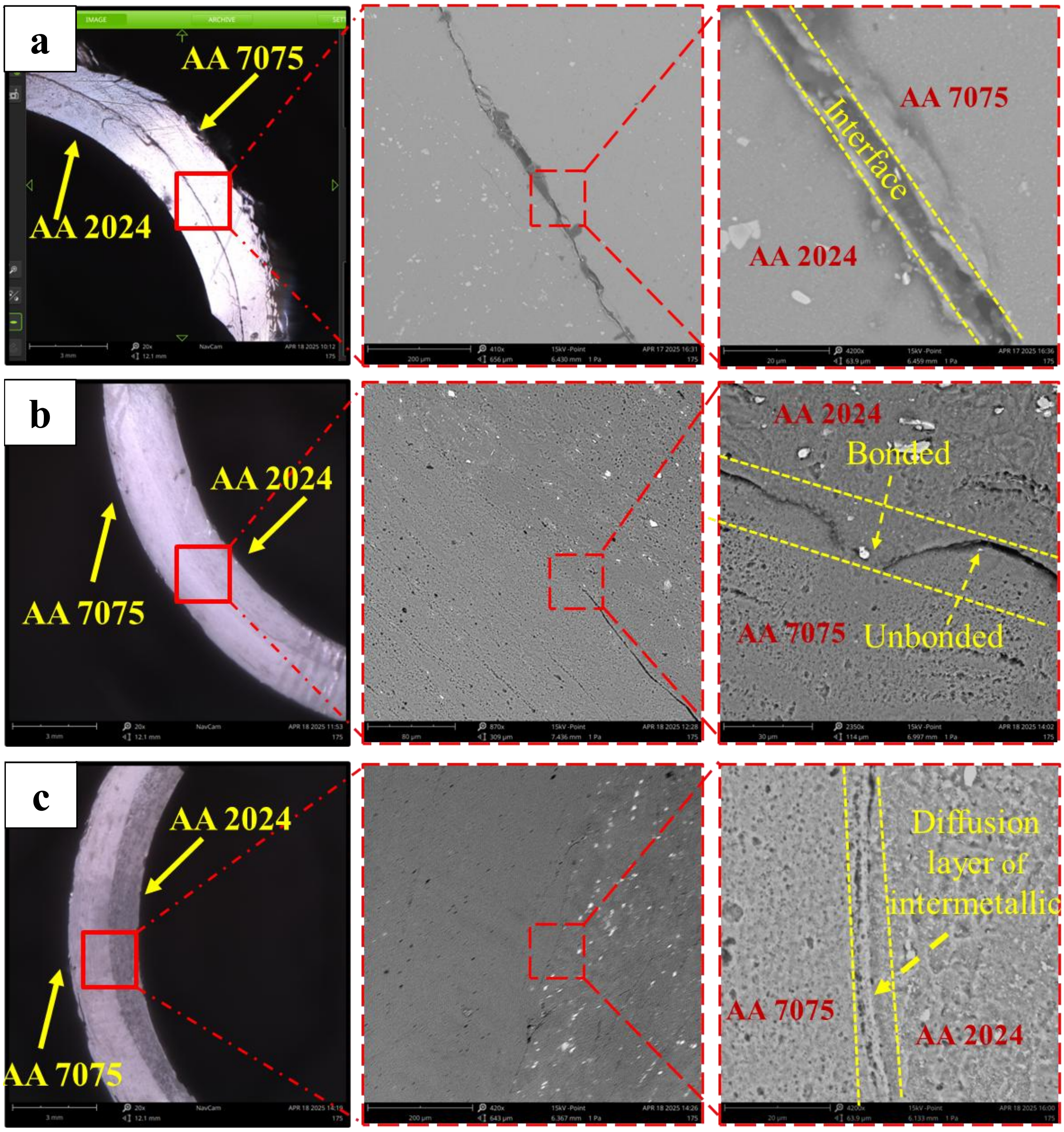

Figure 147. *Microstructure of the cross-section of the bonding layer in AA7075/2024 bimetallic tube prepared by different process methods (a) ID1, (b) ID2, and (c) ID3.*

For investigating the microstructure of the bimetallic tubes at the interface, SEM analysis was performed. Figure 148 presents SEM micrographs along with corresponding EDS results, focusing on the transition zone between AA2024 and AA7075, marked by a red dashed line. Figure 148a (ID1), at low rotational speed displays discontinuity and areas of insufficient bonding, indicating that the heat generated during the process was not adequate to achieve full metallurgical joining. It is important to note that the darker areas near the interface are not voids or porosity. In contrast, the samples extruded at medium and high rotational speeds (ID2 and ID3) haven't shown any signs of discontinuity in the transition region.

Additionally, the EDS mapping presented in Figure 148 further validates and supports the quality of the bond. In this regard, the images of ID1 clearly delineate the transition zone between the AA7075 and AA2024 alloys, with an elemental distribution that matches the expected chemical composition of each material. Specifically, zinc (Zn) was predominantly detected in the AA7075 region, while copper (Cu) was more concentrated in the AA2024 region. On the contrary, ID2 and ID3 show more elemental diffusion. This elemental distribution provides strong evidence of alloying elements' diffusion across the interface and metallurgical bonding between the two aluminium alloys, processed via the FSE process.

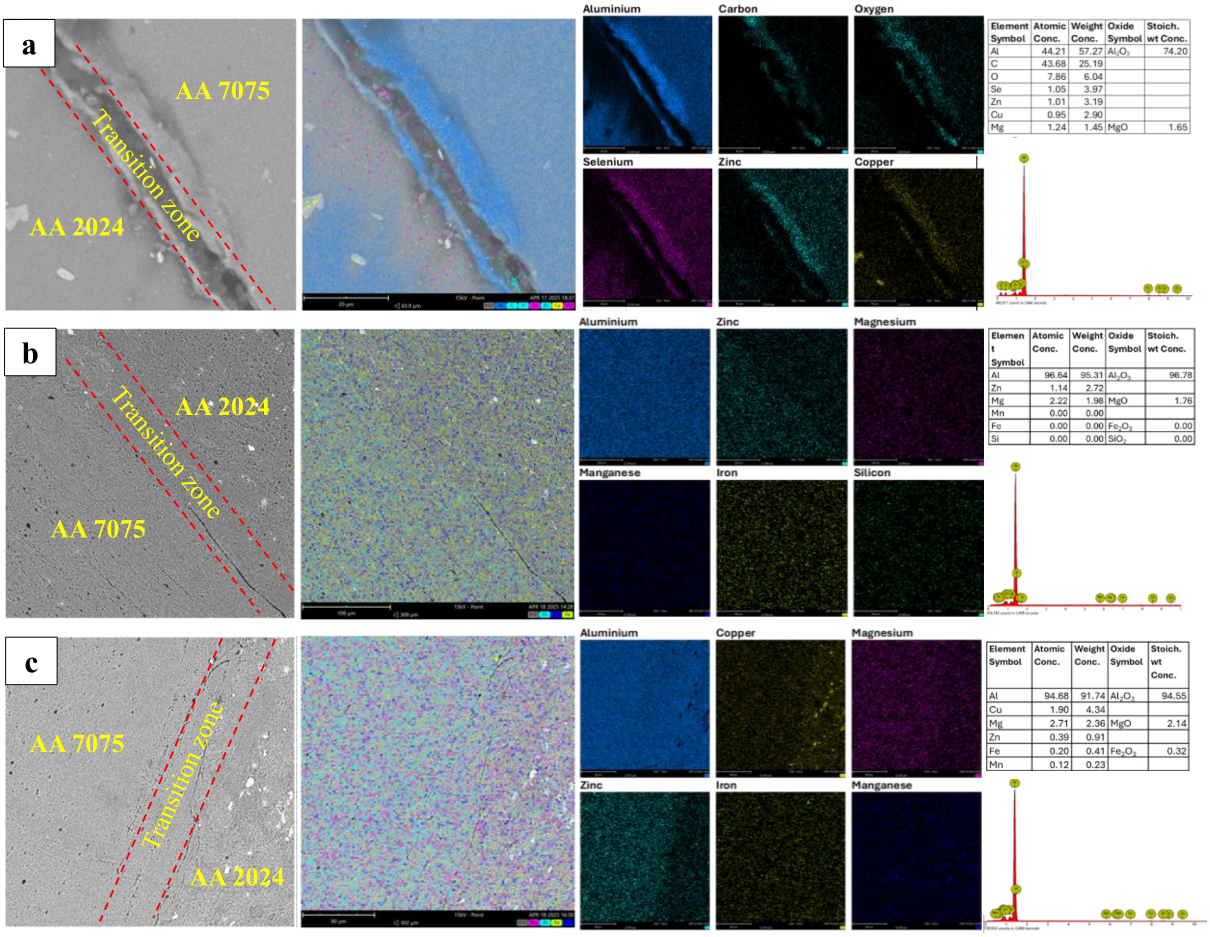

Figure 148. *SEM microstructure of the transition zone of the bimetallic tube, along with EDS mapping for (a) ID1, (b) ID2, and (c) ID3.*

Further grain size analysis was performed on the cross-section of the bimetallic tube to enhance microstructural characterization. Specifically, the grain dimension was measured along the cross section of the tube, from the outer (AA7075) to the inner tube (AA2024), and images of the microstructure were acquired in three specific observation zones: the outer surface of the AA7075 tube (Figure 149a), the AA7075/AA2024 interface (Figure 149b), and the inner surface of the AA2024 tube (Figure 149c). A better refiguration of the selected surfaces and observation zones is given in Figure 149.

Results of tube micrography are presented in Figure 149 for the ID1 sample. Specifically, fine grains (avg. 4.64 μm) were observed near the outer surface of the AA7075 tube (Figure

149a), with a gradual increase toward the interface (avg. 5.60 µm). At the interface (Figure 149b), grain size slightly increased from the AA7075 to the AA2024 side (avg. 5.65 µm). Lastly, close to the inner surface of the AA2024 tube (Figure 149c), a fine and equiaxed structure was again observed (avg. 4.60 µm).

These variations in grain size are mainly attributed to the stirring action of the tool. As already experienced by Baffari et al. [55] during wire production through the FSE process, the material directly in contact with the tool, which is forced through the extrusion reduction zone, undergoes high pressure and temperature, promoting dynamic recrystallization and grain refinement. For this reason, the grain dimension of the inner surface of both AA7075 and AA2024 tubes is smaller than the outer surface (Figure 150).
Similar behavior was observed in samples ID2 and ID3 (Figure 150), with an overall decrease in average grain size at higher rotational speeds.

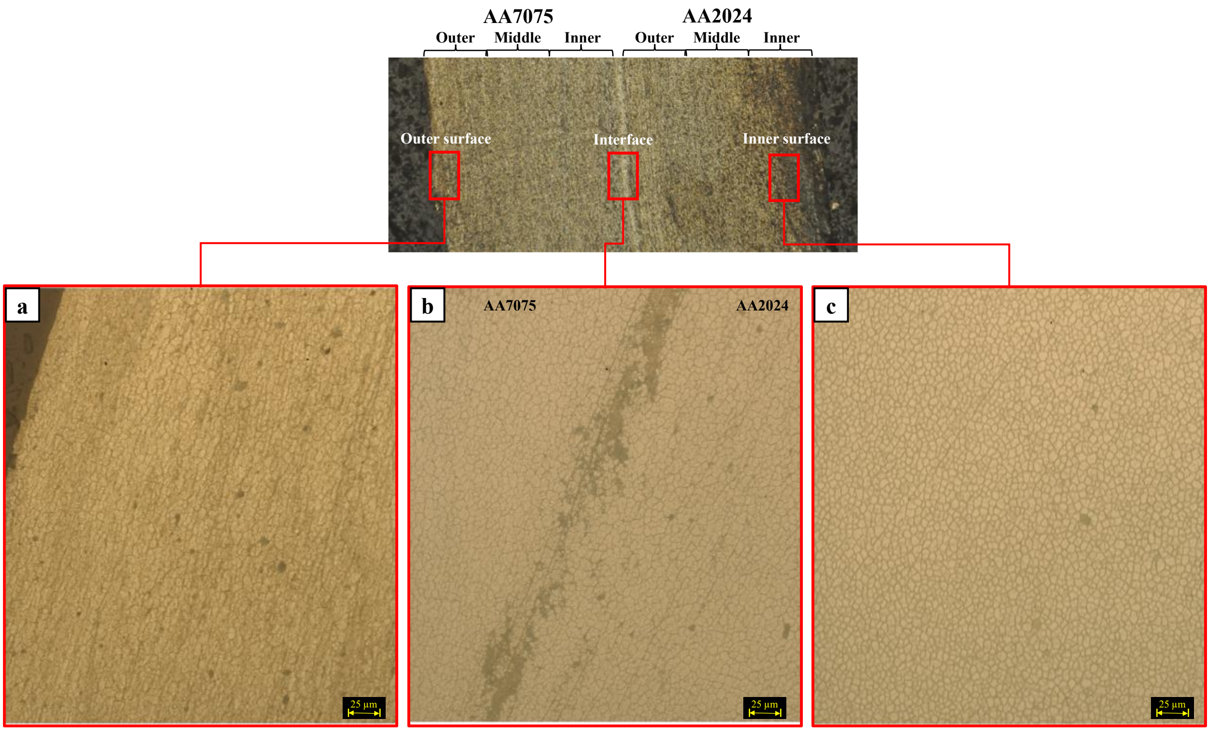

Figure 149. *Microstructure of bimetallic tube representing grain size variation in the (a) outer surface of AA7075 tube, (b) AA7075/AA2024 tube interface and (c) inner surface of AA2024 tube, ID1.*

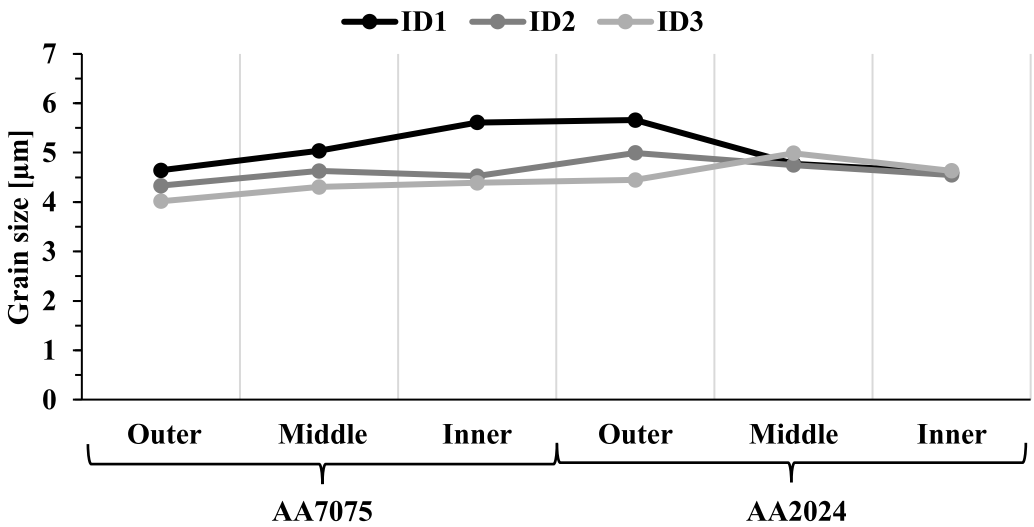

Figure 150. *The average grain size of the bimetallic tube from the outer to the inner surface, for each ID.*

4.7.3.2 Numerical results and microstructural comparison

To support the findings of the experimental campaign, numerical simulations were carried out, aiming to give an overview of the temperature (Figure 151a) and strain (Figure 151b) behavior during FSE tube processing. In this regard, a plot of the temperature and strain profile, at the end of the AA7075 tube production, has been proposed in Figure 9 for the case study ID3. The results reveal that high strain levels occurred both across the tube thickness and under the tool. Furthermore, the detailed cross-sectional view in Figure 9b indicates that the strain is not uniformly distributed through the tube's thickness; instead, it visibly increases from the outer surface toward the inner one. This strain distribution demonstrates that the tool stirring action is more emphasized at the inner tube's surfaces than the external one, corroborating the observation regarding the occurrence of recrystallization phenomena in the inner surface, previously discussed.

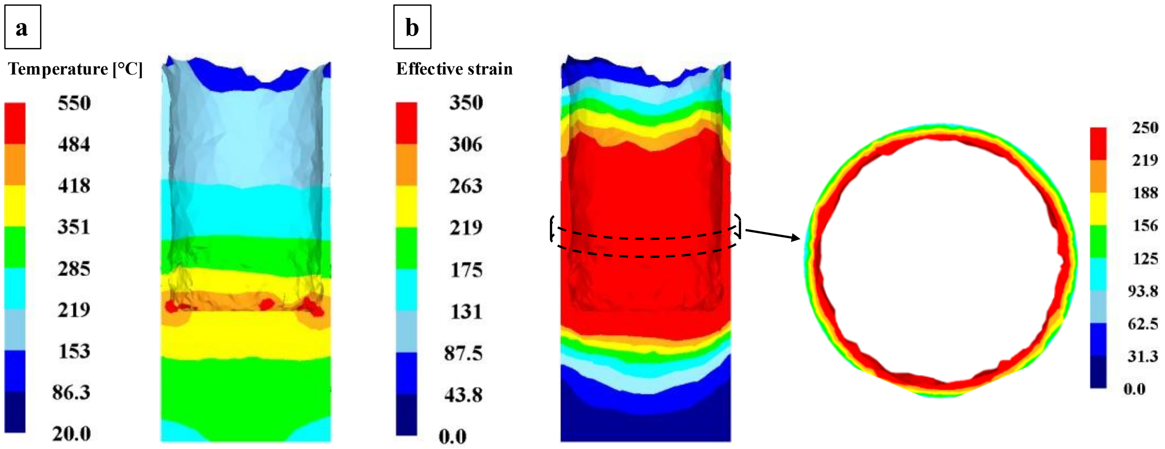

Figure 151. *(a) Temperature and (b) effective strain results (with a zoomed view of the cross-section) at the end of AA7075 extrusion for ID3.*

Numerical simulations were also employed to further investigate and explain the grain growth phenomena observed at the interface of the bi-metallic tube (Figure 150). A point-tracking approach was adopted to track the temperature evolution of a selected point over the entire process. In particular, a point initially located at the interface of the AA7075 extruded tube, was tracked from the considered process time backward to the beginning of the process (Figure 152).

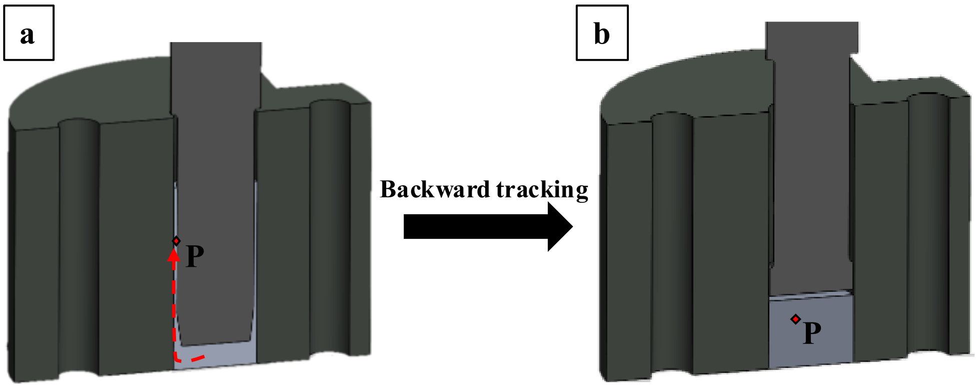

Figure 152. *Point tracking approach from the (a) final position (tube extrusion), backward to the (b) initial position.*

The results of the point tracking showed that, during the FSE process, the material in contact with the tool, particularly near the extrusion channel, was subjected to the highest temperature levels, ranging between 480 and 550 °C (Figure 153). During the AA7075 extrusion stage (Figure 153a), the tracked point moved from the initial position (under the tool) toward the tube wall, experiencing a peak temperature of approximately 400 °C, which lies within the recrystallization temperature range for aluminium alloys. Under these conditions, the combined effect of high strain and elevated temperature promoted recrystallization, resulting in grain refinement of the AA7075 alloy. During the production of the AA2024 tube, point-tracking analysis revealed that the temperature at the monitored location increased again to approximately 350 °C (Figure 153b), partly due to thermal exchange with the already processed AA7075 tube. This secondary temperature peak, located within the recrystallization range, acted as an additional thermal cycle, leading to grain coarsening at the interface in both materials. For this reason, the grain size in correspondence to the AA7075 inner zone resulted in being bigger than the outer (Figure 150), despite the tool stirring refined the inner portion of the AA7075 tube.

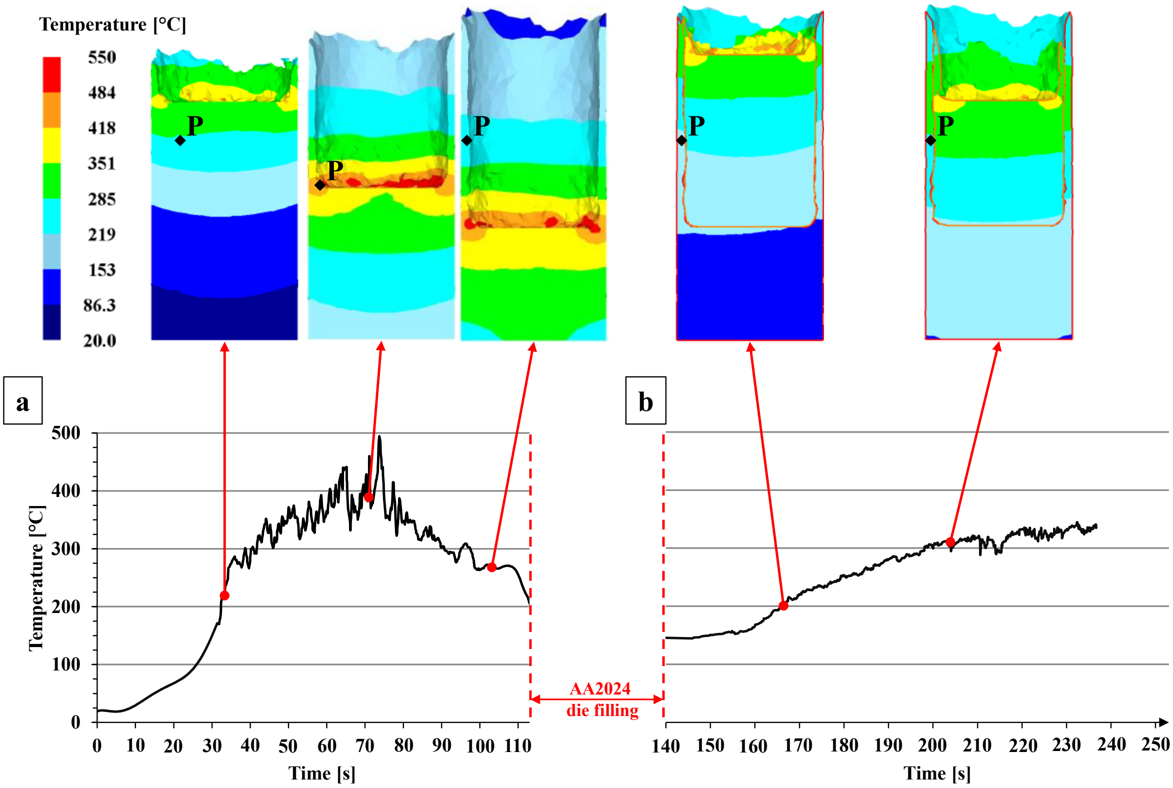

Figure 153. *Numerical simulation results: (a) recording point location for temperature acquisition, (b) strain distribution of the cross section of the numerical AA7075 tube, and (c) temperature evolution of the extruded tubes, for ID3.*

4.7.3.3 Hardness characterization

The mechanical properties of the obtained bimetallic tube were investigated through Vickers microhardness measurements by performing twelve indentation points (Figure 154b) along the cross-section of the tube. The results of these measurements are reported in Figure 154a. Typically, regions containing unbonded or poorly bonded chips exhibit lower hardness compared to areas where strong metallurgical bonding has occurred. Data shows noticeable variation in hardness along different paths across the thickness of the tube. Compared to the average Vickers hardness of the base material, all measured values were higher, indicating that the FSE process enhances the mechanical properties of the extruded material. A consistent trend was observed: microhardness values increased progressively from the outer surface toward the inner surface. For instance, considering ID1, the hardness at point 1 (outer surface) was 87 HV, which increased to 149 HV at point 12 (inner surface). Similar trends were noted for other process conditions. This improvement is in accordance with what was observed by Baffari et al. [55]; in his work, the authors found out that after the FSE process, the hardness of the product was close to the T3 heat treatment hardness value. The AA7075 and AA2024 T3 hardness values are typically about 150 and 145 HV, respectively.

Additionally, an overall increase in hardness has been reported with the increase in rotational speed; at the same vertical load, the increase in rotational speed results in an increase of frictional heating, which enhances chip consolidation, reduces internal voids, and promotes grain refinement, as already shown in Chapter 3.3.

These observations are consistent with the microstructural analysis, which demonstrated grain size refinement from the AA7075 toward the AA2024 layers of the bimetallic tube. However, in the transition zone between AA7075 and AA2024, a localized decrease in microhardness was noted. This reduction resulted from minor defects such as porosity or unbonded regions, which act as stress concentrators, reducing the overall hardness. Similarly, the external surface of the AA7075 tube exhibited low hardness values due to the roughness and poor quality of the surface [55], especially for ID1.

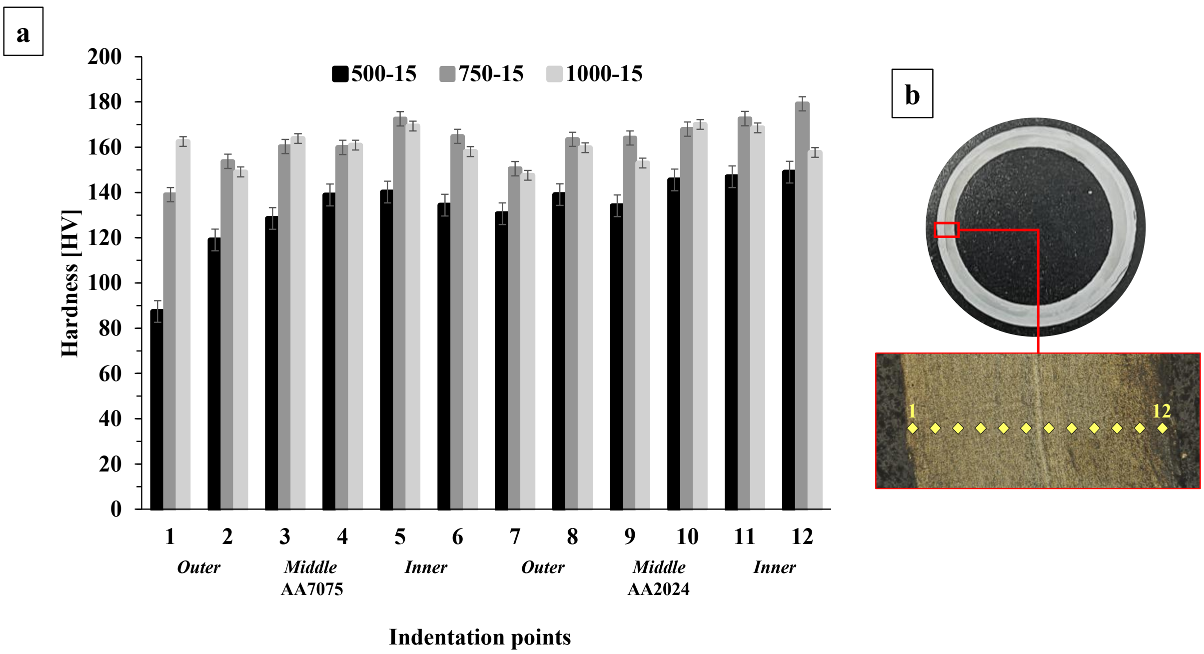

Figure 154. *(a) Average hardness of bimetallic tube for ID1, ID2, and ID3, and (b) indentation lines considered for the hardness measurement.*

4.7.4 Summary of the results

In this study, it was proved that FSE can be successfully applied to produce AA7075/AA2024 bimetallic tubes in a single-step process directly from recycled aluminium chips, demonstrating the effectiveness of this upcycling route. Enhanced microstructural and hardness characteristics were observed across the thickness of the tube, along with a detailed SEM analysis of the bonding quality at the tube interface. The key findings are summarized as follows:

- The results demonstrated that the FSE process is a viable method for fabricating bimetallic tubes. Among the evaluated conditions, the tube produced at 750 rpm and 15 kN exhibited superior surface finish, refined microstructure, and enhanced mechanical properties.
- Optical microscopy and grain size analysis revealed uniformly distributed equiaxed grains, and an overall gradual decrease in grain size was observed toward the inner wall, resulting from the tool's thermal and stirring actions. Moreover, microstructural analysis confirmed that adequate process conditions led to dynamic recrystallization, resulting in fine-grained structures (avg. 4.62 μm, at the outer and inner surface of the bi-metallic tube) and effective bonding between dissimilar aluminum alloys, thus contributing to improved mechanical performance.
- The hardness characterization revealed an overall increase from the outer layer (AA7075) to the inner layer (AA2024). The average hardness for the AA7075 layer was about 150 HV, while a value of nearly 160 HV was obtained for the AA2024 one. At the interface between the two layers, a drop in hardness was observed (around 140 Hv).
- Numerical simulations showed that the material located under the tool and near the extrusion channel experiences high temperatures and strains, conditions that promote recrystallization during FSE. Moreover, a point tracking approach for temperature monitoring at the interface showed that the inner surface of the AA7075 tube is subjected to a secondary heating effect, due to the extrusion of the second tube, which affected the grain size at the tube's interface.
- SEM and EDS analyses verified the presence of a metal-to-metal bonded interface at proper process parameters (750 rpm -15 kN and 1000 rpm – 15 kN). The thermal and mechanical input during FSE was sufficient to facilitate elemental diffusion across the interface, leading to strong interlayer bonding.

4.8 Overcoming process discontinuity in friction stir extrusion techniques

This last chapter explored one research question born due to the limitations of traditional FSE recycling processes: "*Is it possible to produce wire, overcoming the typical discontinuity of the FSE processes?"*. In this regard, wire manufacturing via FSE was investigated by proposing a study using a dedicated continuous extruding machine, developed at the University of Palermo [72].

Note: the images reported in this chapter are taken from the following published work [87].

4.8.1 Experimental methodology

The study of wire manufacturing was carried out using aluminum alloy A356-T6 as the starting material for Continuous Friction Stir Extrusion (CFSE). Table 31 shows the mechanical properties and chemical composition of the material used [114, 115]. For its distinctive properties, extensive research has been conducted over the past few years to explore its use in various manufacturing processes, including Selective Laser Melting (SLM) 3D printing [116]. In this way, the amount of chips produced by the industry for this material is considerable.

Table 31. *Mechanical, physical properties, and chemical composition of A356.*

Heat Treatment	YS [MPa]	UTS [MPa]	HV	Elongation				
F	83	159	67	6%				
T6	207	278	108	6%				
			Chemical composition (% w/w)					
Al	Cu	Fe	Mg	Mn	Si	Ti	Zn	Each
91.1-93.3	≤ 0.2	≤ 0.2	≤ 0.25 - 0.45	≤ 0.1	6.5 - 7.5	≤ 0.2	≤ 0.1	≤ 0.2

The sizes and shapes of the chips that were used to perform the process are highly variable as they are produced by both turning and milling in different processing conditions (Figure 155). However, as observed by Tekkaya et al. [117], extrusion is not affected by the different shapes of chips of introduced material if the correct pressure, strain, and temperature values are reached.

Figure 155. *Shape and dimensions of metal chips used during the experimental campaign.*

Figure 156a shows the geometry of the rotating tool used, made of H13 steel. The rotating tool has an extrusion hole size of 2.4 mm and an extrusion channel length of 0.4 mm. Figure 156b illustrates a redesigned cochlea made of H13 steel.

The redesigned cochlea has a core diameter of 32 mm to ensure robustness and prevent failure caused by deformations during the process. The outer diameter is 42 mm, resulting in an extrusion ratio of 17.5. The redesign of the cochlea was needed to decrease the volume of material introduced during each cochlea's rotation: this was achieved through a larger core diameter (i.e., 32 mm) compared to the previous one (i.e., 26 mm). Previous experimental studies have shown that when the extrusion chamber is set at a fixed dimension of 30 mm and the same rotation parameters are used as in the present study, the volume of material introduced exceeds the volume of extruded material. This indicates a need to reassess the extension of the extrusion chamber, as material accumulation occurs without extrusion. To overcome this problem, the thread pitch characterizing the cochlea was changed from 16 mm to 12 mm without changing the distance between two adjacent threads, which is 8 mm.

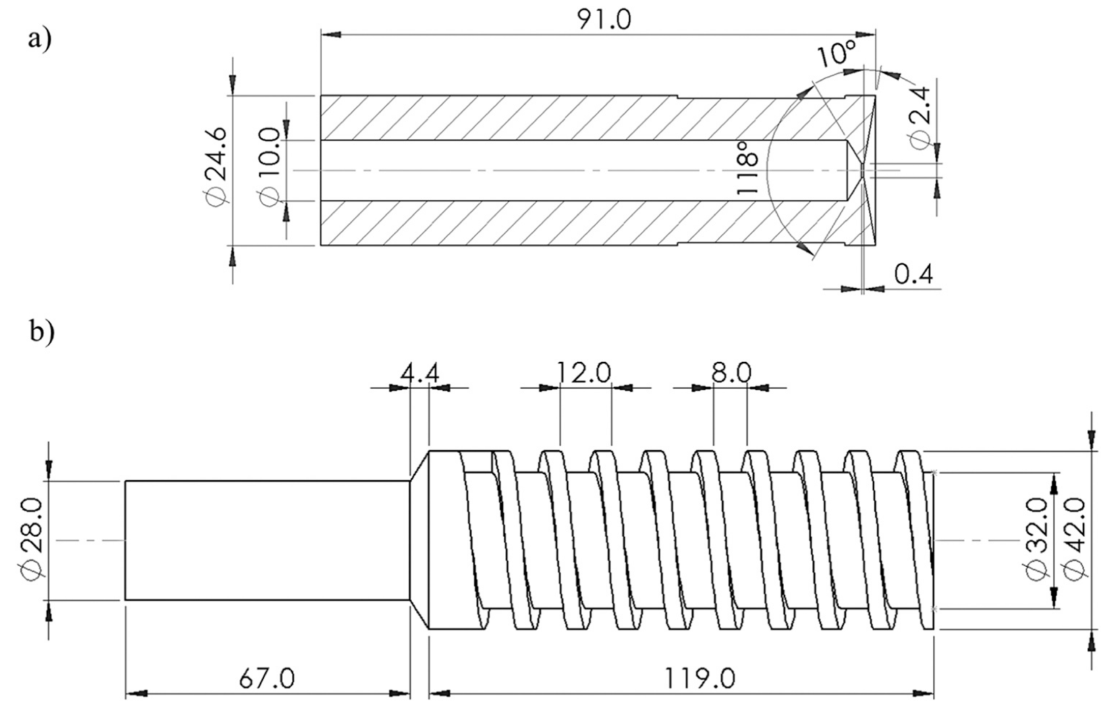

Figure 156. *(a) Geometry dimensions of the rotating tool and (b) geometry dimensions of the redesigned cochlea.*

Figure 157 shows how the volume of chips introduced decreases with each rotation of the cochlea.

The relative density (ρ_r) of the chips deposited by simple gravity fall is 0.44. To determine this value, a cylinder with a diameter of 75 mm and a height of 95 mm was used, with a volume of 419,697 mm^3. The chips were deposited by gravity until the cylinder was filled. The material introduced into the volume was then weighed. The experiment was repeated five times, and the average weight recorded was 495 g. It is possible to calculate the mass of chips introduced for each rotation (m_r), considering the density of the A356-T6 (ρA356-T6), the previously measured relative density (ρ_r), and the ideal volume (V_i) calculated through CAD techniques.

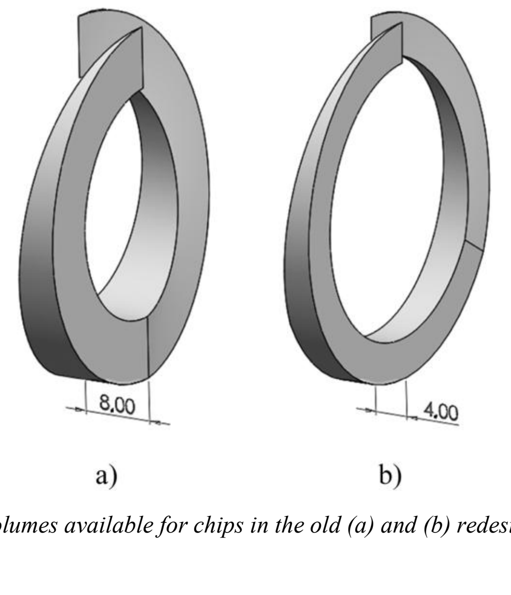

Figure 157. *Different volumes available for chips in the old (a) and (b) redesigned geometry cochlea.*

The actual volume of material introduced for each rotation for the two geometries, given the discrete nature of the chips (V_r) can be calculated with Eq. 32:

$$Vr = Vi \cdot \rho r \qquad (32)$$

Table 32 shows the ideal volume available for chips (Vi), the mass of chips introduced for each rotation (m_r), and the volume occupied by the chips introduced (V_r).
Based on the results of a preliminary campaign, aimed at demonstrating the feasibility of the process and highlighting the role of the main process parameters [72], three different values of rotation of the cochlea (84 rpm, 42 rpm, and 21 rpm) and three different values of the rotation speed of the tool (1600 rpm, 1250 rpm, and 915 rpm) were selected (Table 33). Three tests were performed for each combination of process parameters.

Table 32. *Volume of chips for every rotation of cochlea.*

	v_i (mm^3)	mass, m_r (g)	v_r (mm^3)
Old design	3355	3.9	1452
New design	1356	1.6	596

Table 33. *Process parameter combinations.*

ID	ω tool [rpm]	ω cochlea [rpm]
a	915	21
b		42
c		84
d	1250	21
e		42
f		84
g	1600	21
h		42
i		84

All the tests were carried out with a distance between the cochlea head and the tool equal to 30 mm. The hydraulic system, which causes longitudinal movement of the cochlea, applied a constant load of 5 kN during the productive phase. To overcome typical issues during the run-up phase, a systematic procedure was established (Figure 158). In particular, after the introduction of a pre-determined amount of chips (i.e. 55 g), the cochlea was put in rotation with a speed equal to 10 % of the assigned speed. At the same time, the tool was put in rotation with the assigned speed, and a load equal to 50 kN, constant for all the case studies, was given to the cochlea.

It is worth noting that the start-up load of 50 kN is fundamental to increasing the relative density of the material confined in the extrusion chamber; as already shown in literature, the extrusion process starts only when the relative density of the material close to the tool surface is equal to 1 [118]. After the material reaches the correct conditions of temperature, pressure, and deformation, the start of extrusion is observed.

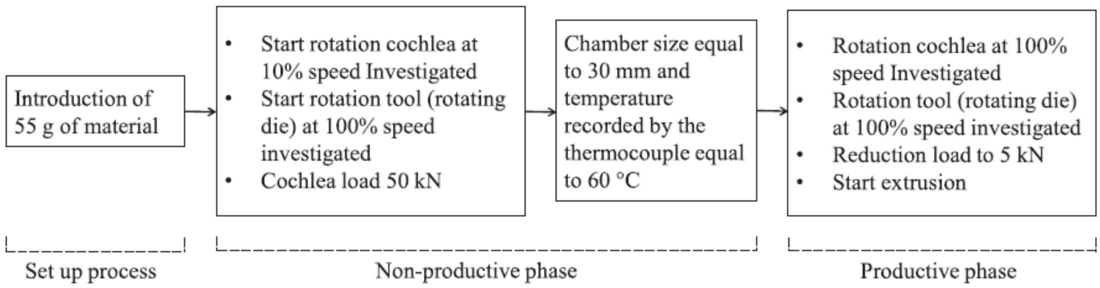

Figure 158. *Systematic experimental procedure.*

A first evaluation of the quality of the product was made by visual inspection of the outer surface of the extrudates. The longitudinal view of wires far from the transient start-up zone was analyzed. Specimens were taken from each wire to evaluate the mechanical properties through quasi-static tensile tests, following ASTM D2256, using a Galdabini Sun 5. Further samples underwent characterization using an Olympus GX 51 optical microscope (OM), and a Phenom ProX Desktop was utilized for scanning electron microscopy (SEM) analyses. Micromechanical characterization in terms of microhardness was determined using a Remet HBV 30. Standard metallographic techniques, such as polishing (alumina diluted in distilled water) and grinding, were employed to prepare the samples. The specimens were then etched for 30 s using Weck’s reagent (1 g NaOH, 4 g KMnO4, and 100 ml H2O) to expose the microstructure. To conduct microhardness testing, a 500 g weight was used to make an indentation in the center of the wires. Additionally, four indentations were made at 0.6 mm intervals from the center, equally spaced on the circumference.

4.8.2 Numerical Methodology

The numerical model of the CFSE process, already validated [72], was established using the commercial software SFTC DEFORM 3D™. The tool, cochlea, and chamber were modeled as rigid parts with a mesh of 25,000, 20,000, and 20,000 elements, respectively. For simplicity, the chips were modeled as a porous billet, characterized through the Shime and

Oyane plastic model, having an initial relative density of 0.44 and a mesh of 15,000 elements; a refined mesh window was generated in the tool-billet surface contact and along the extrusion hole. A constant shear factor equal to 0.4 was used to model the friction between the rigid parts and the porous billet [119] The interface heat transfer coefficient was considered equal to 11 N/sec/mm/C for the billet while as the exchange with the environment is concerned, the temperature and the convection coefficient were imposed equal to 20 ◦C and 0.02 N/sec/mm/C, respectively. The process parameters used in the numerical simulations were defined referring to the experimental tests. Figure 159 shows the developed model with the meshed "workpiece" at the beginning of the simulation. was generated in the tool-billet surface contact and along the extrusion hole. A constant shear factor equal to 0.4 was used to model the friction between the rigid parts and the porous billet [55, 119].

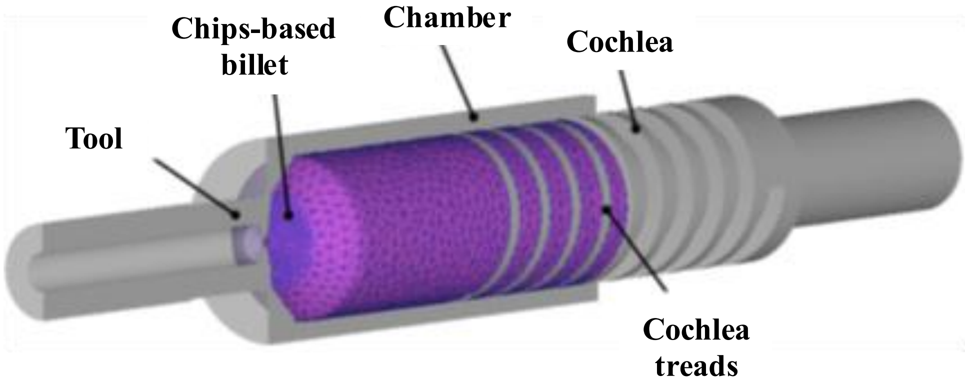

Figure 159. *3D FEM model of the CFSE process: section of the tool, chips-based billet, chamber, and treads of the cochlea.*

4.8.3 Results and discussion

Figure 160 shows the process window obtained from the proposed experimental campaign. As can be seen, all the combinations of process parameters selected allowed the production of a wire, case study *i* being the only exception. For this condition, the cochlea required an excessive amount of torque, overcoming the machine's limiting value. The causes of this behavior will be discussed in the next paragraphs. For all the sound case studies, the extrusion process was stopped after an average wire length of 700 mm was extruded.
Early assessment of product quality is possible by observing the outer surface of the wires (Figure 161).

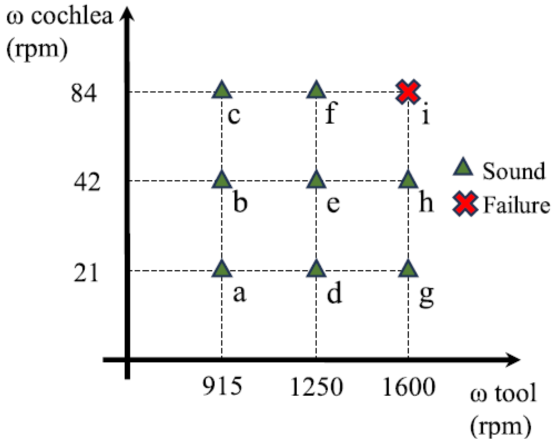

Figure 160. *Process window highlighting sound and failed tests.*

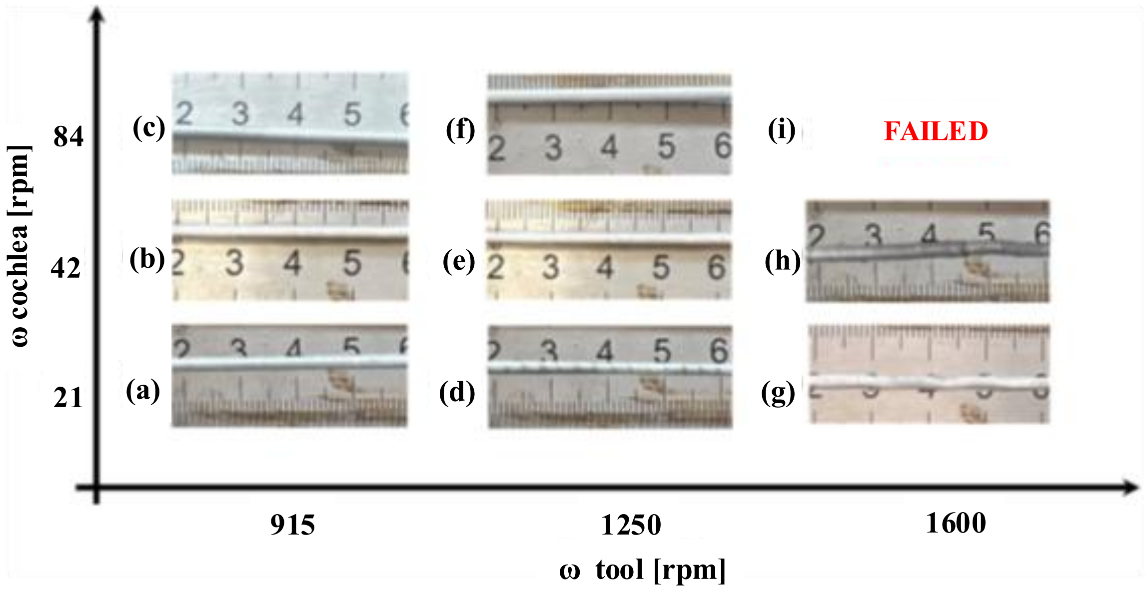

Figure 161. *Longitudinal view (a) ID-a, (b) ID-b, (c) ID-c, (d) ID-d, (e) ID-e, (f) ID-f, (g) ID-g, (h) ID-h, and (i) the failure of ID-i*

It is possible to notice distortions when the tool rotation increases at a set cochlea rotation, e.g., when cochlea rotation is equal to 21 rpm (Figure 161a-d-g), or 42 rpm (Figure 161b-e-h). In turn, with fixed tool rotation of 915 rpm and 1250 rpm, and increasing cochlea rotation, it is possible to observe a more consistent external surface. Finally, as the tool rotation increases up to 1600 rpm, an extremely irregular surface as well as the beginning of hot cracking can be observed (Figure 161g-h).

First, the mechanical properties of the wires were investigated. Figure 162 illustrates the Ultimate Tensile Strength (UTS) of the manufactured wires, correlating with both the rotational speed of the cochlea and the rotational speed of the rotating die.

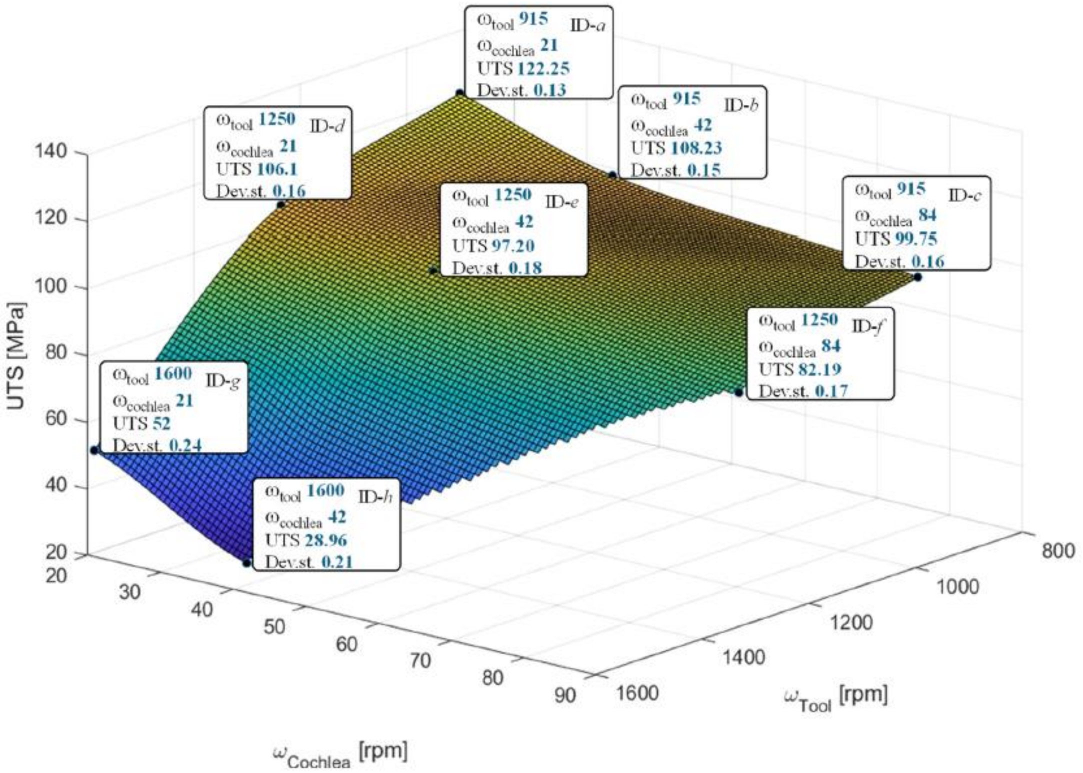

Figure 162. *Ultimate Tensile Strength (UTS) of the produced wires correlates with both the rotational speed of the cochlea and the rotational speed of the rotating die.*

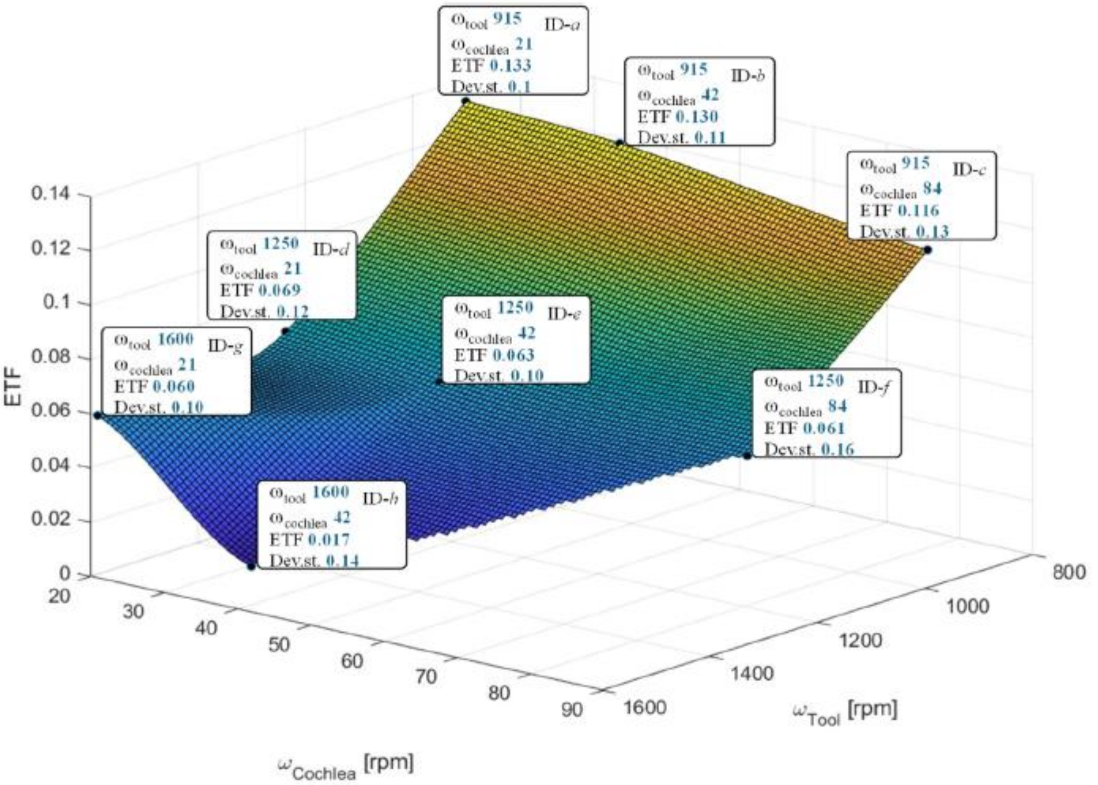

Figure 163. *The elongation to fracture of the produced wires varies with both the rotational speed of the cochlea and the rotational speed of the tool.*

As far as the sound extrudates are concerned, it is possible to observe decreasing UTS values as the rotational speed of the cochlea increases with fixed tool rotation. This trend holds true for the three considered tool rotation values. It is also observed that the reduction in UTS is

more significant when the tool rotation increases from 1250 rpm to 1600 rpm. Moreover, a decreasing trend is also observed for increasing cochlea rotation with fixed tool rotation. The maximum value of UTS, equal to 122 MPa, corresponds to 77 % of the UTS of the as-cast material (A356-F). As a matter of fact, similarly to FSW, the CFSE process induces a local thermal treatment of the material, resulting in the loss of the initial T6 condition [55]. The maximum value is found for the combination of the slowest process parameters of the proposed campaign, i.e., tool rotation of 1200 rpm and cochlea rotation of 21 rpm. As the tool rotation increases, the UTS drastically drops, reaching the minimum value with tool rotation equal to 1600 rpm.
The elongation to fracture was also examined in relation to the rotational speed of the cochlea and the tool (Figure 163).
A similar trend to the one observed by UTS, as a rapid decrease in the ETF occurs with increasing tool rotation and fixed cochlea rotation for all three values considered in this study. As the best-performing case studies are considered, it is noted that ETF is higher than the parent materials.

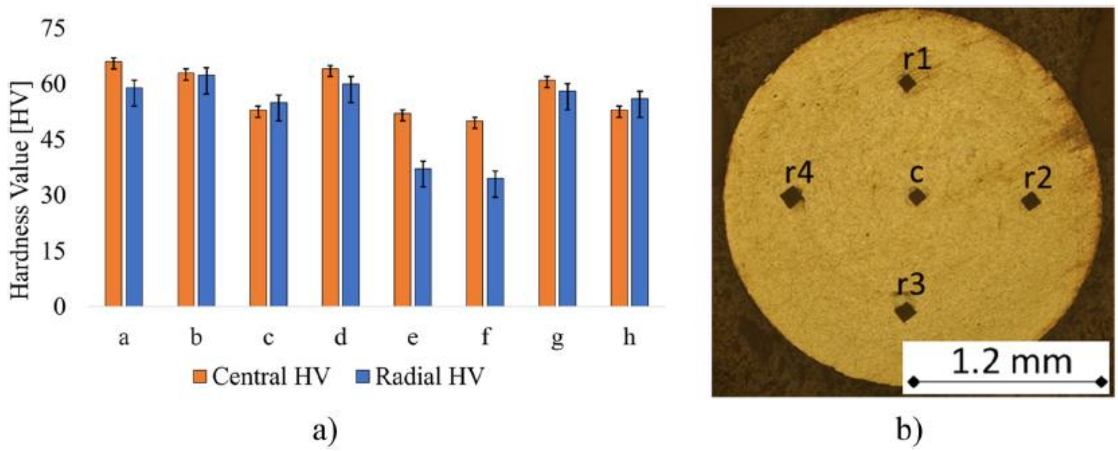

Figure 164. *(a) Micro Hardness results for the tested wires, (b) OM image of the indentations.*

To understand the results and trends obtained during the tensile tests, further characterization was carried out. Figure 164 shows, for each wire produced, the Vickers' hardness value measured at the center of the cross-section and the average value of the hardness measured over a circumference of a radius of 0.6 mm (indentations are indicated in the figure).
Consistent with what was found for UTS, decreasing hardness values are observed as the tool rotation increases with fixed cochlea rotation. It is also noted that radial hardness is characterized by a higher variability than the center hardness. This is due to the peculiar material flow that occurs during the process. It has already been demonstrated that a helicoidal material flow takes place, caused by concurrent effects of the tool rotation and the

extrusion speed. [70, 72]. In this way, the material advancing front moves on a plane with a certain angle, depending on the process parameters considered, with respect to the cross-section plane [70, 72]. It is also noted that relatively high hardness is found for the ID-d, ID-g, and ID-h case studies, which, in turn, are characterized by low UTS and ETF. SEM analyses of the fracture surfaces have been carried out for specimens obtained with increasing tool rotation and fixed cochlea rotation. Figure 165 shows the fracture surfaces of ID-a, ID-d, and ID-g tests.

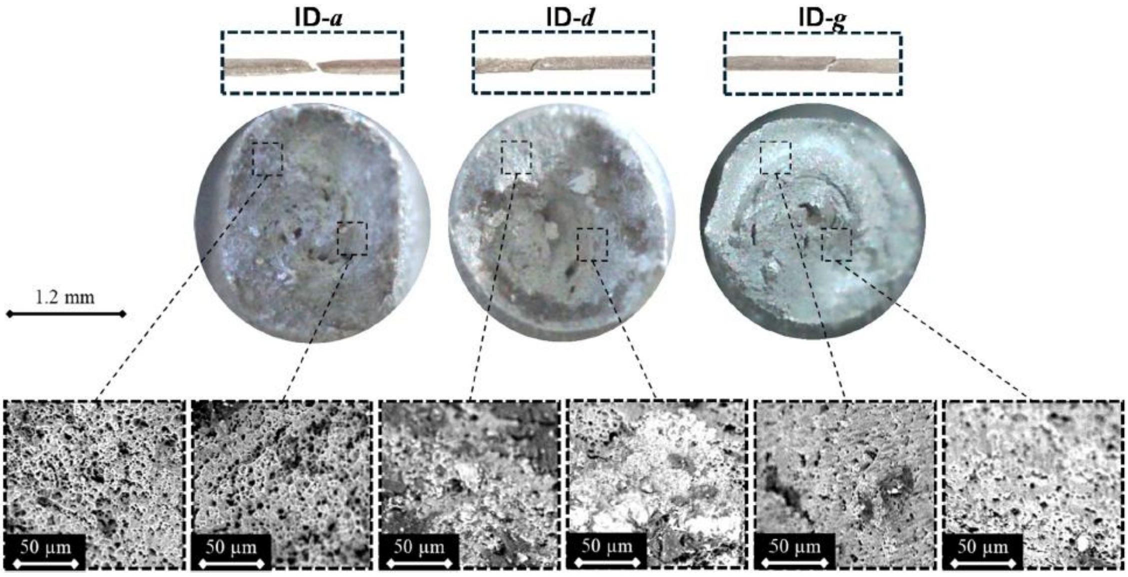

Figure 165. *Failure mode image and associated SEM image for ID-a, ID-d, and ID-g.*

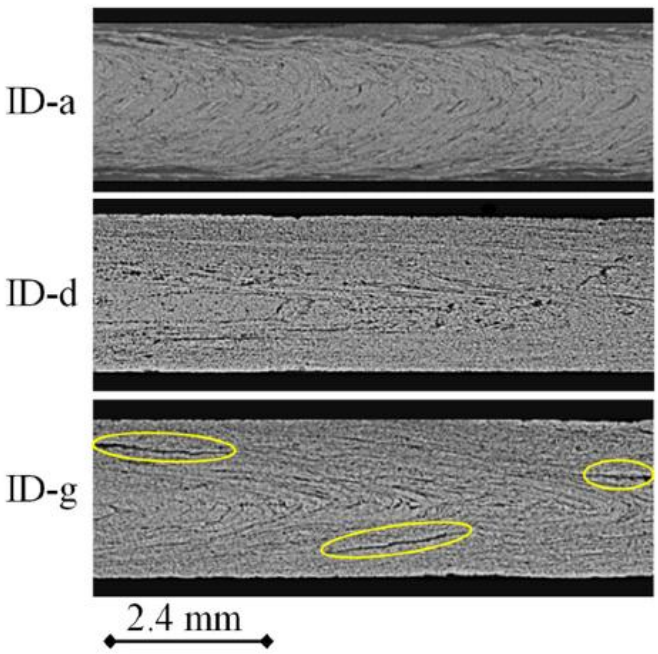

Figure 166. *Longitudinal section of the obtained wires for case studies ID-a, ID-d, and ID-g.*

The ID-a case experienced a ductile fracture, as shown by the presence of dimples, while the ID-d case showed ductile and brittle fracture zones, and the ID-g case showed an entirely brittle fracture surface. Additionally, the presence of internal defects in the longitudinal section (Figure 166), consisting of large void areas (yellow line in Figure 166), makes clear why, with increasing tool rotation, high hardness, and low UTS and ETF are obtained. During the tensile test, the internal cracks propagate rapidly, resulting in the brittle failure of the cases considered. The causes for the UTS decrease when tool rotation and cochlea rotation increase will be discussed in the FEM results section.

Finally, for the same case studies, SEM analysis was conducted to determine the average grain size (Figure 167a), through the intercept method, in both the central area and the external one (Figure 167b). It is noted (Figure 167c) that increasing grain size is obtained with increasing tool rotation, due to the higher heat input. The external area is characterized by a slightly lower average grain size due to the thermal exchange with the tool. It is worth noting that a similar trend, i.e., increasing average grain size with increasing tool rotation and fixed cochlea rotation, was found for the other cochlea rotation values.

The obtained results highlighted that the Ultimate Tensile Strength (UTS) decreases with increasing tool rotation and cochlea rotation. Notably, the highest UTS value achieved was approximately 77 % of that of the parent material in its F state. Additionally, the maximum Elongation to Failure (ETF) recorded was 11 %, surpassing that of the parent material. This enhancement in ETF can primarily be attributed to the formation of recrystallized grains that emerged after the processing phase, contrasting markedly with the structure of the as-fabricated parent material. Moreover, the hardness (HV) trends mirrored those of the UTS. Specifically, at elevated tool rotation speeds, the material exhibits a more brittle behavior. This brittleness is due to the presence of significant void defects, which, in spite of the corresponding higher HV values, lead to poor mechanical resistance. Such observations emphasize the complex interplay between mechanical properties and parameters controlling the manufacturing process, revealing crucial insights into material behavior under varied processing conditions. What has been found is consistent as comparable with the results observed by Gumaste et al. [74] in the study of continuous extrusion of feedstock.

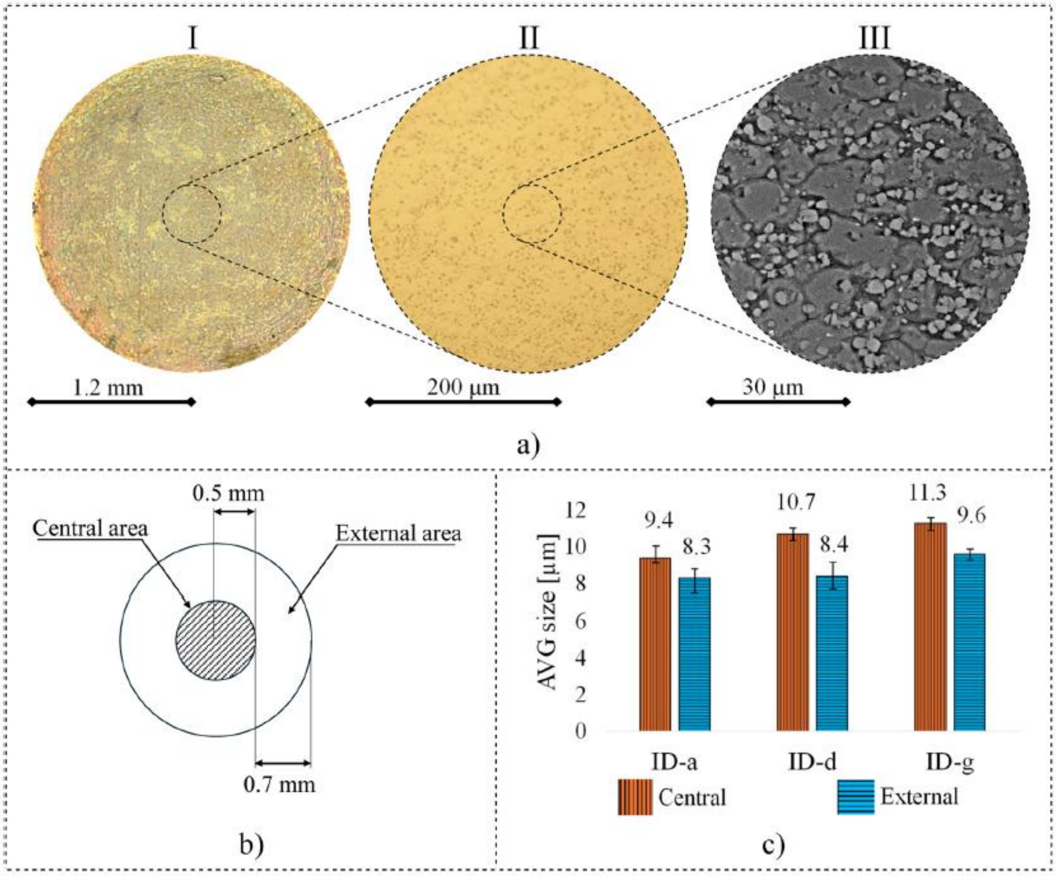

Figure 167. *(a) Microstructural analysis with (a.I) Optical microscope 5x (a.II) Optical microscope 20x, and (a.III) SEM 2000x, (b) scheme of the analyzed zones, and (c) average grain size was measured for case studies ID-a, ID-d, and ID-g.*

In order to better highlight the effect of the considered process parameters and their interaction on the main mechanical properties, ANOVA analyses were carried out for UTS, ETF, and microhardness. Table 34 shows the ANOVA analysis results. It is observed that tool rotation (ω tool) and cochlea rotation (ω cochlea) have a significant impact on UTS, with a p-value much lower than the common significance level of 0.05. Hence, variations in these parameters determine a significant difference in UTS levels. Also, the interaction between ω tool and ω cochlea is significant, as demonstrated by the p-value, indicating that the effect of one factor depends on the level of the other factor.

Table 34. *ANOVA analysis results for UTS value.*

Source	DF	Adj SS	Adj MS	F-Value	P-Value
ω tool	2	35323.2	17661.6	626792.5	0.00000
ω cochlea	2	4849.3	2424.6	86048.02	0.00000
ω tool * ω cochlea	4	875.2	218.8	7764.61	0.00000
Error	18	0.5	0		
Total	26	41048.2			

Figure 168 shows the interaction between the ω tool and the ω cochlea for UTS. Non-parallel lines indicate an interaction between the two factors, i.e., the effect of increasing ω cochlea depends on the level of ω tool. At low levels of ω tool, UTS is higher with low levels of ω cochlea, whereas at high levels of ω tool, UTS is significantly lower for all levels of ω cochlea.

Table 35 shows ANOVA analysis results performed on the ETF obtained from the mechanical analysis. The same p-values are obtained for the three factors. This suggests that there are significant differences in ETF% for different levels of ω tool and ω cochlea. The interaction between ω tool and ω cochlea is significant, again indicating that the effect of one factor depends on the level of the other factor.

Table 35. *ANOVA analysis results for ETF% value.*

Source	DF	Adj SS	Adj MS	F-Value	P-Value
ω tool	2	464.187	232.093	17612.48	0
ω cochlea	2	36.727	18.363	1393.51	0
ω tool * ω cochlea	4	26.633	6658	505.27	0
Error	18	0.237	0.0013		
Total	26	527.784			

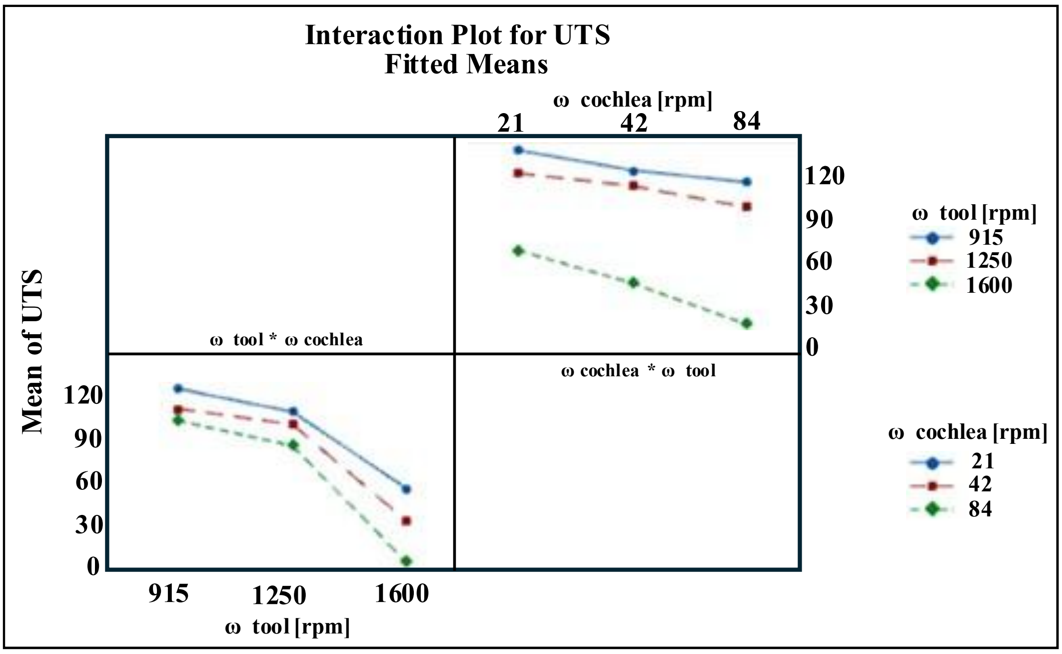

Figure 168. *ANOVA results: interaction between ω tool and ω cochlea for UTS.*

The non-parallel lines in the interaction plot suggest a significant interaction between the two factors (Figure 169). For instance, the effect of increasing ω cochlea varies depending on the level of the ω tool. At lower levels of ω tool, ETF% is higher for lower levels of ω cochlea, whereas at higher levels of ω tool, ETF% significantly decreases for all levels of ω cochlea. The analysis carried out allowed for assessing the high influence of tool and cochlea rotation on the mechanical integrity of the final wire. In this way, the correct choice of these process parameters, as well as the full comprehension of their role in the process mechanics, as will be shown in the next paragraph, is crucial to an effective process design.

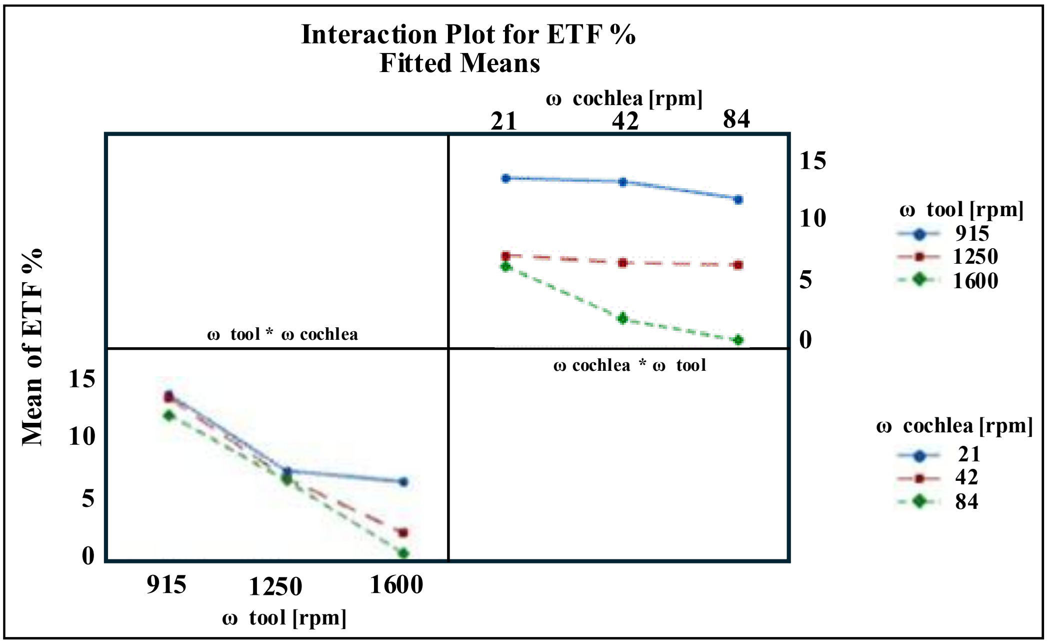

Figure 169. *ANOVA results: interaction between ω tool and ω cochlea for ETF%.*

Finally, Table 36 shows ANOVA analysis results performed on the central and radial HV values measured. As expected, ω tool and ω cochlea significantly affect HV with a p-value far below the conventional significance level of 0.05. The interaction between the ω tool and the ω cochlea is also significant.

Figure 170a and b show the interaction between process variables for central and radial HV, respectively. At lower levels of ω tool, central HV is higher for lower levels of ω cochlea, whereas at higher levels of ω tool, central HV significantly decreases for all levels of ω cochlea.

Table 36. *ANOVA analysis results for central (a) and radial (b) HV value.*

Source (a)	**DF**	**Adj SS**	**Adj MS**	**F-Value**	**P-Value**
ω tool	2	2528	1264	124873.77	0
ω cochlea	2	4166	2083	205784.85	0
ω tool * ω cochlea	4	3050	762.5	75329.31	0
Error	18	0.18	0.01		
Total	26	9744.18			
Source (b)	**DF**	**Adj SS**	**Adj MS**	**F-Value**	**P-Value**
ω tool	2	2061.25	1030.62	27812.92	0
ω cochlea	2	4158.17	2079.08	56107.2	0
ω tool * ω cochlea	4	3603.39	900.85	24310.75	0
Error	18	0.67	0.04		
Total	26	9823.47			

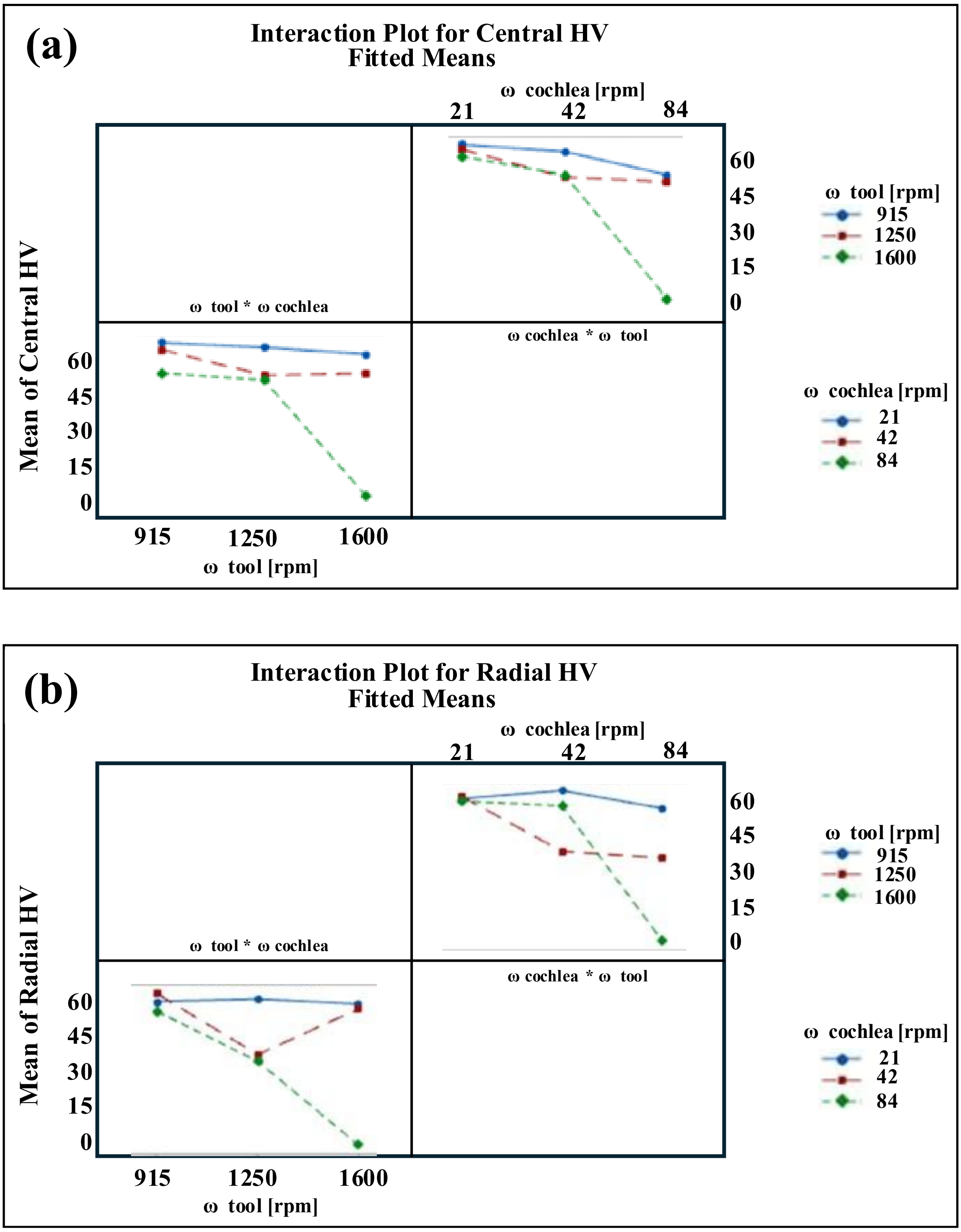

Figure 170. *ANOVA results: interaction between ω tool and ω cochlea for (a) central and (b) radial HV.*

4.8.3.1 Numerical results

The numerical model was used for a more in-depth understanding of the mechanical properties trends experimentally obtained, allowing the analysis of the effect of the process parameters on the main field variables, i.e., temperature, strain, and strain rate. In particular, it is known that the effectiveness of solid bonding phenomena can be quantitatively evaluated through the Piwnik-Plata criterion (Eq. 33) [88], which depends on the temperature and pressure history the material undergoes.

$$Wc = \int p \, \sigma f \, dt \qquad (33)$$

Where p is the contact pressure at the interface between two adjoining chips, and can be considered as the mean stress in the modeled porous material; σf is the flow stress of the material in the given temperature, strain, and strain rate conditions.

Temperatures were calculated along the billet axis during the extrusion process. Figure 171 shows the temperature profile in the billet as a function of the distance from the bottom surface of the tool as well as the temperature distribution in a longitudinal section, for the case studies ID-a, ID-d, and ID-g, i.e., for fixed cochlea rotation equal to 21 rpm and varying tool rotation. As expected, the temperature of the material close to the bottom surface of the tool increases as the cochlea rotation increases, resulting in a significantly larger Heat Affected Zone (HAZ).

In Figure 172a and b it is possible to observe the strain and strain rate profiles, respectively, calculated at the same points considered for temperature in Figure 173a. First, it is noted that, regardless of the considered tool rotation, the material is affected by the tool rotation in an area characterized by a height of about 16 mm. For longer distances from the tool's bottom surface, no significant effective strain is calculated.

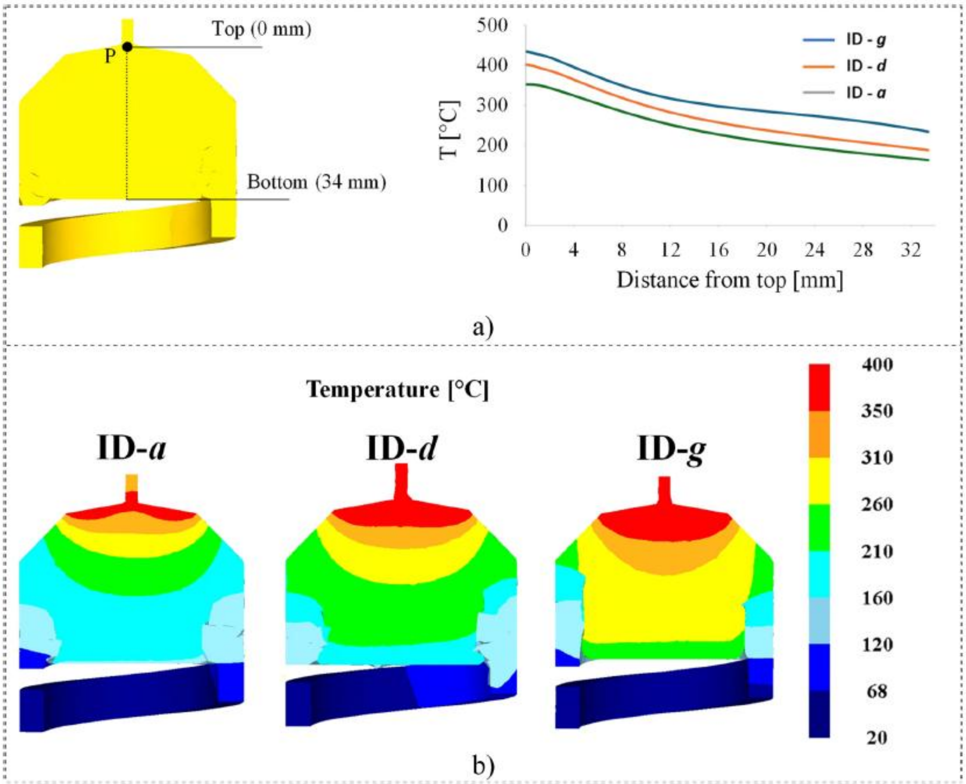

Figure 171. *(a) temperature profile in the billet as a function of the distance from the bottom surface of the tool and (b) temperature distribution in a longitudinal section for case studies ID-a, ID-d, and ID-g.*

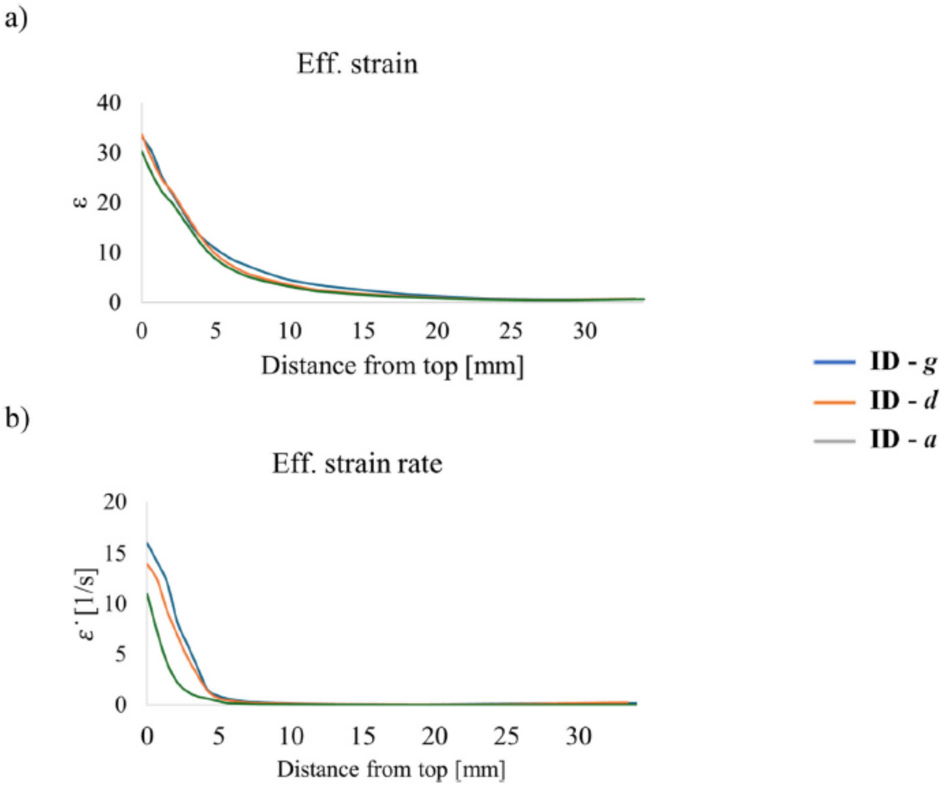

Figure 172. *Comparison of (a) Effective Strain and (b) Effective Strain Rate for Cases ID-a, ID-d, and ID-g.*

Then, a slight increase in both strain and strain rate is observed with increasing tool rotation. The local values of temperature, strain, and strain rate have been used to calculate the material flow stress for each point. The values of W obtained for point P (see again Figure

171a), lying along the wire axis at the tool bottom surface when the extrusion process begins, are 3.55 for ID-a, 3.36 for ID-d, and 3.12 for the ID-g case. It is worth noticing that, in order to calculate these values, the considered point was tracked during the process, recording the history of all the field variable values, according to the procedure followed in [88, 118]. It is worth noting that the Piwnik-Plata criterion was not implemented across the entire analysis field. Instead, field variables were obtained for 10 track points, and these variables were then used to evaluate the weld quality. This approach, focusing on selected track points to derive critical welding parameters, aligns with methodologies previously utilized in the analysis of Friction Stir Welding, as detailed in reference [118].

The experimental and numerical results make clear the decreasing trend obtained for UTS and ETF with fixed cochlea rotation and increasing tool rotation. Indeed, with increasing tool rotation, temperature increases, leading to grain growth. Additionally, with increasing tool rotation, the combined effect of (i) the increasing temperature, resulting in decreasing material flow stress, and (ii) decreasing stress, results in lower values of W, i.e., lower solid bonding quality.

A similar approach was followed to investigate the effect of the cochlea rotation on the mechanical properties. In Figure 173, temperature profiles and distributions are shown for case studies ID-a, ID-b, and ID-c. It can be seen that temperature gradually increases with decreasing cochlea rotation. In particular, higher cochlea rotation leads to a higher extrusion rate. In this way, due to quicker heat dissipation, the material in the region of the extrusion chamber is colder, and thinner thermal layers are observed (Figure 173b).

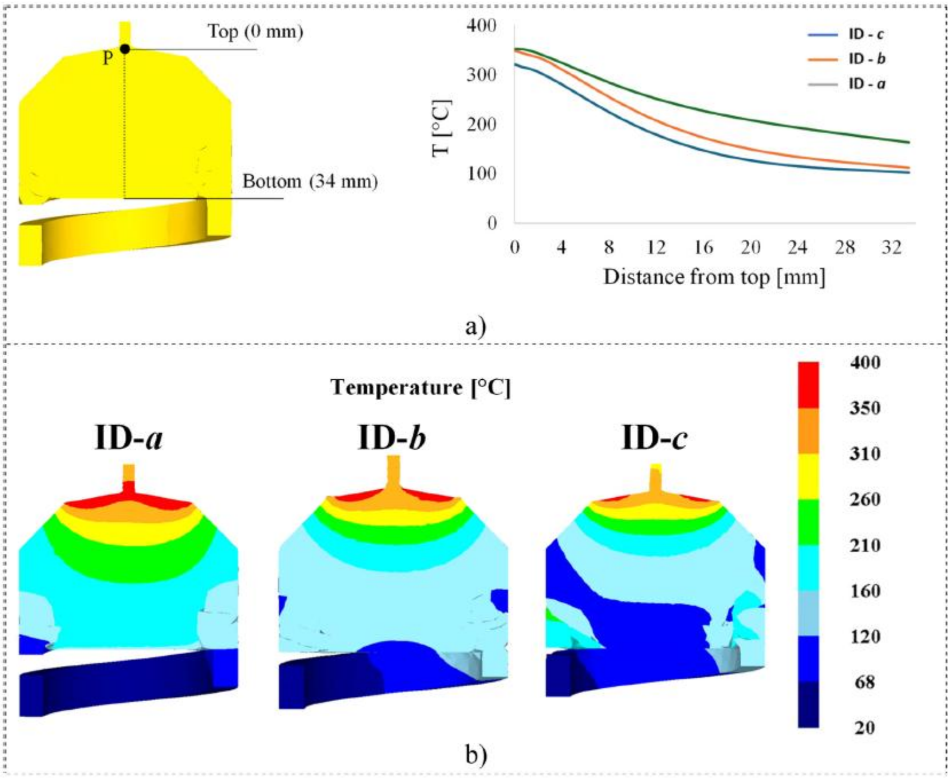

Figure 173. *(a) temperature profile in the billet as a function of the distance from the bottom surface of the tool and (b) temperature distribution in a longitudinal section for case studies ID-a, ID-b, and ID-c.*

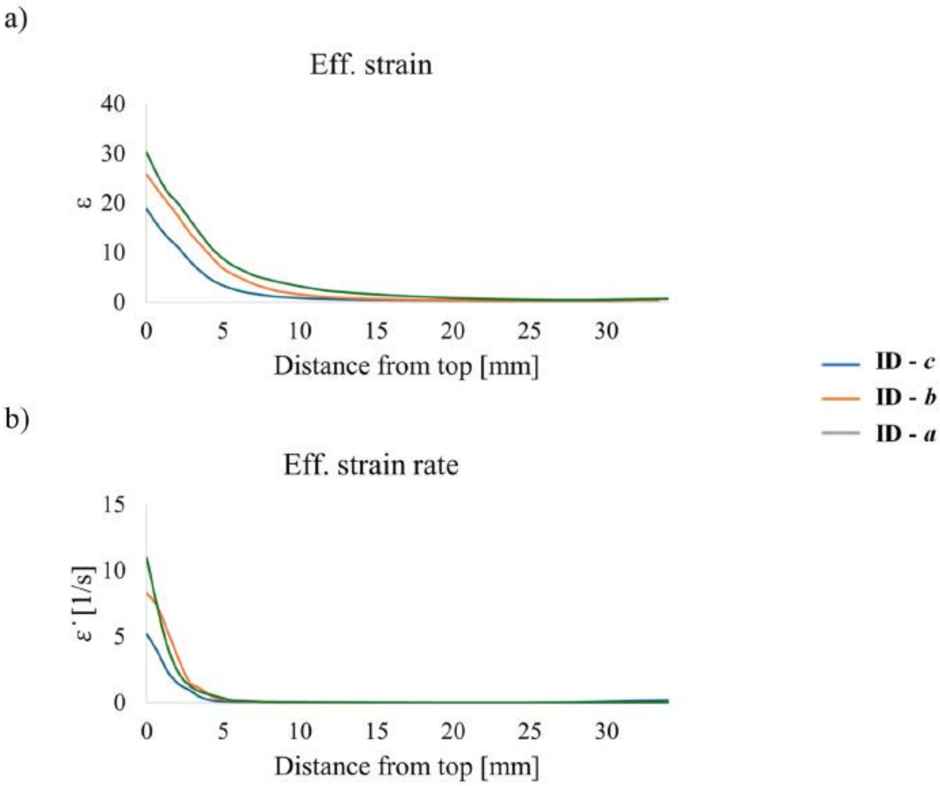

Figure 174. *Comparison of (a) Effective Strain and (b)Effective Strain Rate for Cases ID-a, ID-b, and ID-c.*

In Figure 174a and b, the strain and strain rate profiles, calculated as described for Figure 172, are shown. An increase in the cochlea rotation results in lower values of strain and strain rate all along the billet axis (Figure 172a and b). This is due to the higher extrusion rate caused by the faster material supply from the cochlea. In this way, a single material particle rotates less around the billet longitudinal axis and accumulates less strain. The combined effect of lower temperature and lower time results in lower values of the Piwnik-Plata W. The obtained values of W for point P (Figure 173a) are 3.55 for ID-a, 3.01 for ID-b, and 2.52 for the ID-c case, indicating decreasing bonding quality with increasing cochlea rotation. The reduced material mixing and the lower values of W obtained with higher cochlea rotation can explain the significant drop in the UTS experimentally observed for any given tool rotation.

The numerical model was also used to understand the reasons for the failed test ID-i, for which the maximum tool and cochlea rotation values, among the ones considered in this study, are selected. As the temperature distribution in the cochlea is observed (Figure 175b and c), it is seen that the cochlea top area, i.e., the one close to the extrusion chamber, has a higher temperature. This is due to the concurrent effect of the high tool rotation and high cochlea rotation, whose top surface acts as a "secondary tool", creating heat by friction. In these conditions, the chips do not consolidate close to the tool surface, but rather start close to the cochlea end (Figure 175). This creates a "block" to incoming chips that cannot reach the tool, thus leading to process failure. When such a condition takes place the torque on the cochlea measured by the FSE machine increases reaching the machine limit.

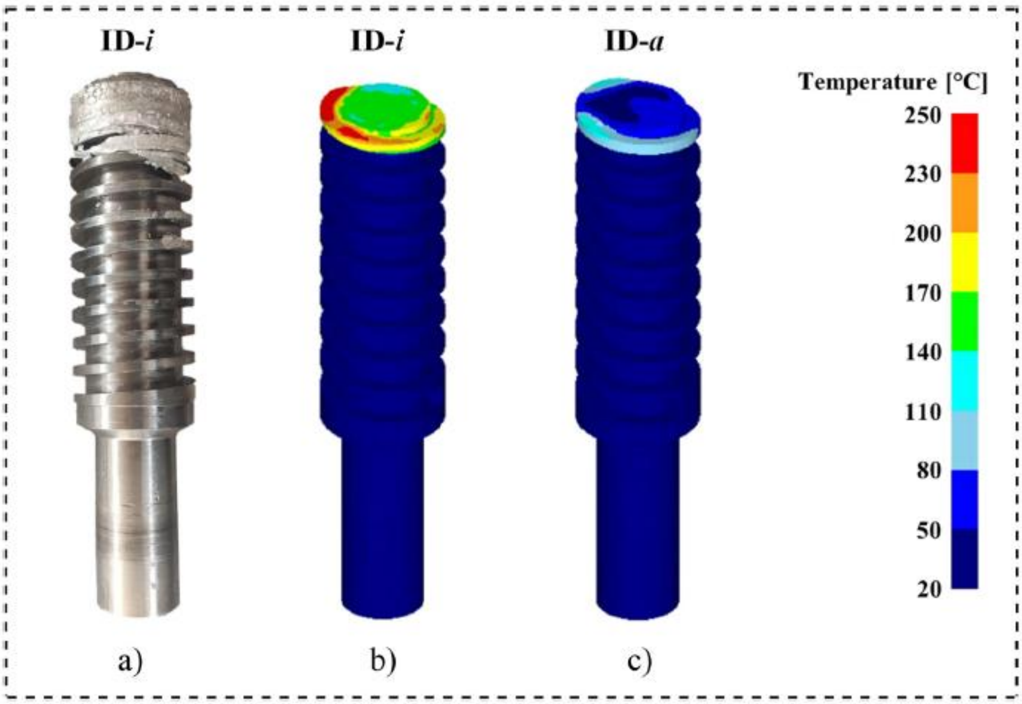

Figure 175. *(a) consolidated material on the cochlea at the end of the process for failed case study. Temperature distribution calculated in the cochlea during (b) failed case study and (c) proper cochlea operation.*

4.8.4 Summary of the results

In this study, A356-T6 aluminum alloy chips were directly recycled through the CFSE solid-state process. An experimental campaign was carried out to investigate the effect of the main CFSE process parameters on the produced wires' mechanical properties. The experimental campaign plan included 9 case studies, each involving three levels of tool rotation and three levels of cochlea rotation.

Based on the results obtained, the following main conclusion can be drawn:

- Decreasing UTS was obtained with increasing tool rotation and cochlea rotation; the maximum UTS obtained was equal to 77 % of the parent material in the F state; the maximum ETF obtained was equal to 11 %, which is larger than that of the parent material. This is due to the recrystallized grain obtained after the process, as compared to the as-cast parent material structure.
- Anova analyses highlighted the strong influence of each considered process parameter as well as their interaction on UTS, ETF, and microhardness.
- The HV trend generally follows the UTS one. For large values of tool rotation, a brittle behavior, characterized by large void defects and larger HV values, is observed.
- With fixed cochlea rotation, increasing tool rotation leads to both larger average grain size and lower calculated Piwnik-Plata parameter W, indicating lower quality of the solid bonding process, explaining the UTS trend observed experimentally.
- With fixed tool rotation, increasing cochlea rotation leads to both low values of strain, i.e., material stirring, and higher extrusion rates. In turn, the latter results in lower process times and hence lower Piwnik-Plata parameter W.
- For the failed case study ID-i, it was found that the combined effect of high tool and cochlea rotation caused the chips' temperature to
- increase close to the cochlea. Consequently, material consolidation occurred in that area, creating an obstacle for the incoming chips and thus leading to cochlea torque increase and process failure.

5 Conclusions and future developments

This thesis has explored the capability to recycle machining metal scraps by means of solid-state recycling processes. Different research questions have arisen in the field of friction stir consolidation and extrusion. In Chapter 4, most of the publication has been presented and discussed, aiming to provide the answer to the research question at the base of this dissertation.

The study in **Chapter 4.1** represents the starting point for the investigation of solid bonding mechanics, showing that the already existing solid bonding criteria are not suitable for the FSC process. In this regard, experimental and analytical criteria were coupled to an iterative workflow in a Matlab environment to create a new formulation able to predict the consolidation level of the FSCed billet. This procedure resulted in a new criterion, named Plata-Piwnik-Weighted (PPW) criterion, which demonstrated higher accuracy and faster evaluation than the other solid bonding criteria.

In **Chapter 4.2**, the proposed criterion (PPW) was applied to different aluminium alloys to assess the applicability and versatility of this formulation to other aluminium alloy chips. Specifically, the same procedure developed in Chapter 4.1 was employed in this study and applied to two more aluminium alloys. The results, which were validated by a third alloy, demonstrated that the PPW criterion still has the best performance and accuracy in solid bonding prediction. Moreover, the proposed generalized model, based on just three material properties (tensile yield strength, specific heat capacity, and elongation to break), can predict the solid bonding threshold curve of an aluminium alloy.

In **Chapter 4.3**, the knowledge on friction stir consolidation techniques was extended to magnesium alloy by combining solid bonding approaches and an energy consumption study. This research demonstrated that the PPW criterion was also suitable for magnesium alloys, and the energy consumption analysis revealed that the transition phase has a high impact compared to the consolidation phase. Moreover, it proved that FSC can enable significant environmental impact reduction with respect to remelting-based routes.

In **Chapters 4.4 and 4.5**, the research questions related to the main variables responsible for the solid bonding occurrence and the possibility of improving the bonding quality were answered. Specifically, in Chapter 4.4, the material flow during the FSC process was investigated using a copper marker, aiming to understand the material flow evolution during billet production. The results showed that the main stirring effects are localized at the top of the billet, which is directly in contact with the tool, and the effective strain and temperature are mainly responsible for an effective solid bonding phenomenon. At the bottom of the billet (especially close to the corners) the effective strain is lower, as well as the temperature, and the comparison with the experimental samples demonstrated that in those parts chips are still visible and are not consolidated. These results were also used as the basis for the research carried out in Chapter 4.5. This second study focused on proposing a new process setup (only with a numerical simulation approach) that could increase the strain and temperature levels at the bottom of the billet, promoting more material softening and, consequently, better consolidation. Numerical simulations were run with a heated backing plate, up to both 300 and 400 °C, to understand the effect of the two-sided heating on consolidation behavior. The results showed that at 300 °C, the temperature of the billet was higher than in the same case study of the traditional FSC process; moreover, the strain had a slight increase. Overall, the solid boning evaluation demonstrated that the combination of these increased strain and temperature led to better consolidation, proving that this setup is effective.

In **Chapter 4.6**, the friction stir extrusion process was investigated for producing tubes from machining chips. Specifically, different process parameters were tested and the optimal one (1500 rpm - 15 kN) was selected as a compromise between surface quality and mechanical properties. Moreover, results revealed that the tubes have mechanical properties improved up to 200 % compared to the base material, and high recrystallization phenomena are observable in the portion of the tube directly in contact with the rotating tool (avg. grain size 4 μm). Additionally, two scenarios were presented to compare the energy requirement of the two-step approach used in literature (compaction + extrusion) and the single step presented here, demonstrating that the single step required reduced energy and lower specific energy consumption than the double-step. Lastly, a reduction in the extrusion rate was observed in each test. This phenomenon was investigated, and the results revealed that excessive consolidation of the material was identified far from the tool action, leading to premature consolidation of the material not yet extruded. This condition makes the process require a higher force to extrude, representing the limit of the process.

In **Chapter 4.7**, the studies of the previous chapter were extended to manufacturing multilayer tubes. The research demonstrated that AA7075-AA2024 bi-metallic tubes were successfully produced at three different process parameters. The bonding at the interface was investigated, and the effect of the process parameters on bonding quality was presented, revealing low bonding at 500 rpm – 15kN. Best performances were obtained at 700 and 1000 rpm – 15 kN. In addition, grain analysis depicted the grain evolution along the thickness of the tube (cross-section), showing decreasing grain dimension going from the outer to the inner tube. Matching the grain results, hardness characterization revealed an increasing trend going from outer to inner tube.

In **Chapter 4.8**, the discontinuity of the friction stir extrusion recycling processes was solved by performing continuous FSE on a dedicated machine. Different process parameters were employed to study the feasibility of this approach and the effect of these parameters on wire quality. Results revealed that with fixed tool rotation, increasing cochlea rotation leads to both low values of strain, i.e., material stirring, and higher extrusion rates. In turn, the latter results in lower process times and hence lower Piwnik-Plata parameter W. With fixed cochlea rotation, increasing tool rotation leads to both larger average grain size and lower calculated Piwnik-Plata parameter W, indicating lower quality of the solid bonding process, explaining the UTS trend observed experimentally. Lastly, numerical investigations demonstrated the role of temperature in this process, highlighting the limitations of the process namely excessive material sticking to the cochlea.

5.1 Outlook on future works

Further development will be addressed to enhance the applicability of such an approach. Specifically, the effectiveness of the PPW criterion and the proposed parametric model will be applied to other material families such as steel. Moreover, future work will be focused on CFSEed wire mechanical properties optimization through the use of AI tools on a wider range of variations of the considered process parameters. Additionally, different approaches can be considered to mitigate the consolidation issues in tube manufacturing via FSE. Examples include the use of an active cooling system or, alternatively, a variable tool rotational speed. In the first case, the cooling system could be integrated into the die setup to control the material temperature at the bottom of the die, thereby promoting a slower consolidation of the unprocessed material. The second approach focuses on in-process control of the tool’s rotational speed, combined with sensors and thermocouples. This would enable a real-time adaptive system that modulates the rotational speed (reduces the velocity if too hot or increases it if too cold) based on the heat generated by the friction.

An interesting future work may concern the study of the oxide dispersion effect in FSCed billets and FSEed tubes. A first approach in this direction was performed on accumulative roll bonding. Specifically, a study was conducted by coupling the theory of precipitates with oxide-related phenomena, with the aim of quantitatively describing the effects of oxide fragmentation on the mechanical properties of the material. This was achieved through the analysis of cutting (K_c) and bowing (K_b) shear yield strengthening (Figure 176 and Figure 177), which represent the stress required to cut (or bow along) the precipitates in the metal matrix. In this research, multiple rolling cycles were performed on aluminium strips, and a MATLAB-based calculation was performed to quantitatively predict the breakage and dispersion of the oxide layer within the aluminium matrix. The expected outcome concerns the role of oxide dispersion in material strengthening.

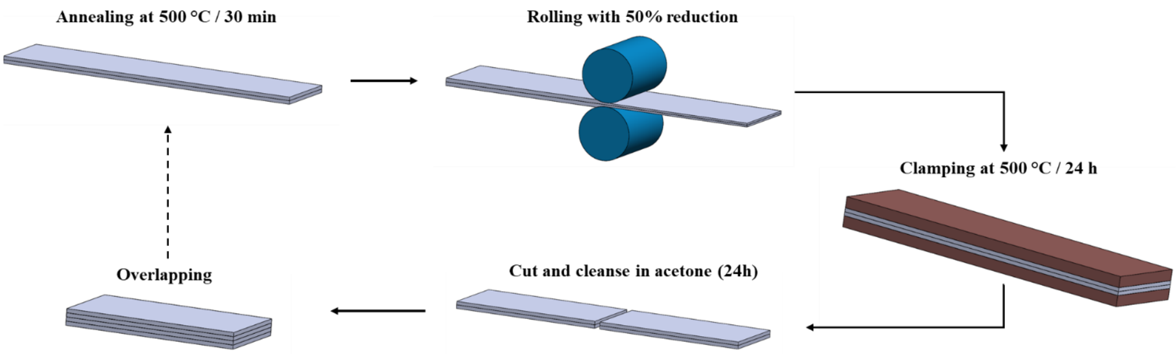

Figure 176. *Loop cycle for rolling the aluminium strips*

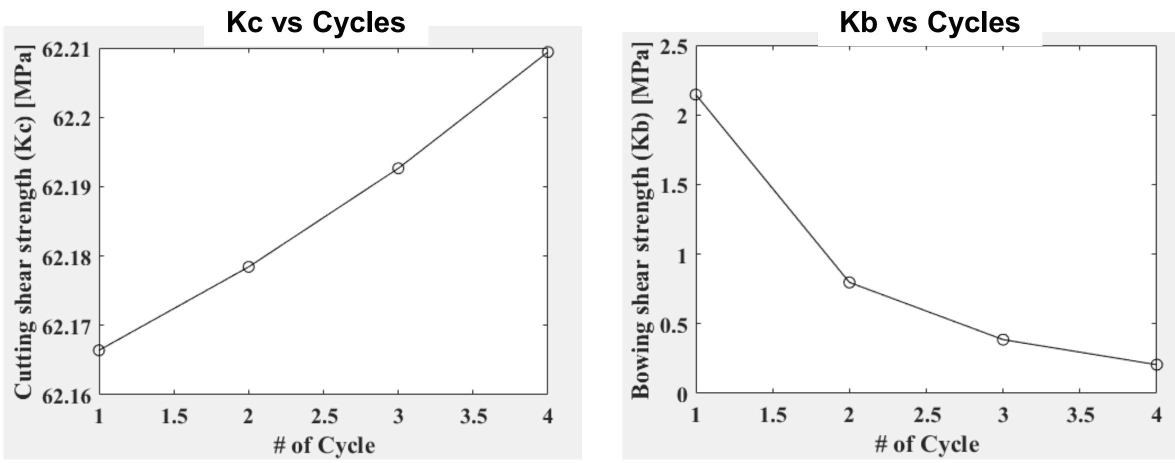

Figure 177. *Example of cutting and bowing shear yield strengthening evaluation, from Matlab calculation.*

Bibliography

1. Seixas J, Ferreira F (2020) Carbon Economy and Carbon Footprint
2. (2024) Recycling of Critical Minerals Strategies to scale up recycling and urban mining A World Energy Outlook Special Report. www.iea.org
3. Graedel TE, Allwood J, Birat JP, et al (2011) Recycling Rates of Metals – A Status Report. A Report of the Working Group on Global Metal Flows to the International Resource Panel. https://www.resourcepanel.org/. Accessed 10 Jun 2025
4. Hertwich EG (2021) Increased carbon footprint of materials production driven by rise in investments. Nat Geosci 14:151–155. https://doi.org/10.1038/s41561-021-00690-8
5. Mastos TD, Nizamis A, Vafeiadis T, et al (2020) Industry 4.0 sustainable supply chains: An application of an IoT enabled scrap metal management solution. J Clean Prod 269:. https://doi.org/10.1016/j.jclepro.2020.122377
6. Paraskevas D, Kellens K, Dewulf W, Duflou JR (2013) Closed and Open Loop Recycling of Aluminium: A Life Cycle Assessment perspective 10.1 Closed and Open Loop Recycling of Aluminium: A Life Cycle Assessment perspective
7. Temjanovski R (2021) The impacts of COVID-19 on the logistic ecosystems and benefit for the circular economy. Journal of Economics 6:8–21. https://doi.org/10.46763/joe216008t
8. (2014) Towards a circular economy: A zero waste programme for Europe. Brussels
9. Kirchherr J, Yang NHN, Schulze-Spüntrup F, et al (2023) Conceptualizing the Circular Economy (Revisited): An Analysis of 221 Definitions. Resour Conserv Recycl 194
10. Jawahir IS, Dillon OW (2007) Sustainable Manufacturing Processes: New Challenges for Developing Predictive Models and Optimization Techniques. In: First International Conference on Sustainable Manufacturing
11. Kutz Myer (2007) Environmentally conscious mechanical design. John Wiley & Sons
12. Recycling of Critical Minerals Strategies to scale up recycling and urban mining A World Energy Outlook Special Report
13. Peiró LT, Nuss P, Mathieux F, Blengini GA (2018) Towards Recycling Indicators based on EU flows and Raw Materials System Analysis data Supporting the EU-28 Raw Materials and Circular Economy policies through RMIS
14. Veliu G, Caslli S (2015) The Material-Energy Binomial in Epicenter of Eco-Design. SEE PROFILE The Material-Energy Binomial in Epicenter of Eco-Design. The Case of Materials for the “Glina” Bottled Water. https://doi.org/10.13140/RG.2.1.2130.8328
15. MatWeb, https://www.matweb.com/.
16. Brough D, Jouhara H (2020) The aluminium industry: A review on state-of-the-art technologies, environmental impacts and possibilities for waste heat recovery. International Journal of Thermofluids 1–2
17. Cusano G, Rodrigo Gonzalo M, Farrell F, et al (2017) Best Available Techniques (BAT) Reference Document for the Non-Ferrous Metals Industries
18. Gunasegaram DR, Molenaar D (2015) Towards improved energy efficiency in the electrical connections of Hall-Héroult cells through Finite Element Analysis (FEA) modeling. J Clean Prod 93:174–192. https://doi.org/10.1016/j.jclepro.2015.01.065
19. Cusano G, Rodrigo Gonzalo M, Farrell F, et al (2017) Best Available Techniques (BAT) Reference Document for the Non-Ferrous Metals Industries

20. Wan B, Chen W, Lu T, et al (2017) Review of solid state recycling of aluminum chips. Resour Conserv Recycl 125:37–47
21. Matsuki K, Aida T, Takeuchi{ T, et al MICROSTRUCTURAL CHARACTERISTICS AND SUPERPLASTIC-LIKE BEHAVIOR IN ALUMINUM POWDER ALLOY CONSOLIDATED BY EQUAL-CHANNEL ANGULAR PRESSING
22. Mabuchi M, Kubota K, Higashi K (1995) New Recycling Process by Extrusion for Machine Chips of AZ91 Magnesium And Mechanical Properties of Extruded Bars. 36:1249–1254
23. Guluzade R, Avci A, Turan Demirci M, Faruk Erkendirci Ö (2013) Fracture toughness of recycled AISI 1040 steel chip reinforced AlMg1SiCu aluminum chip composites. Mater Des 52:345–352. https://doi.org/10.1016/j.matdes.2013.05.025
24. Zhilyaev AP, Gimazov AA, Raab GI, Langdon TG (2008) Using high-pressure torsion for the cold-consolidation of copper chips produced by machining. Materials Science and Engineering: A 486:123–126. https://doi.org/10.1016/j.msea.2007.08.070
25. Bui QH, Dirras G, Ramtani S, Gubicza J (2010) On the strengthening behavior of ultrafine-grained nickel processed from nanopowders. Materials Science and Engineering: A 527:3227–3235. https://doi.org/10.1016/j.msea.2010.02.003
26. Topolski K, Ostachowski P (2021) Solid state processing of titanium chips by an unconventional plastic working. Journal of Materials Research and Technology 13:808–822. https://doi.org/10.1016/j.jmrt.2021.04.037
27. Shamsudin S, Lajis MA, Zhong ZW (2016) Solid-state recycling of light metals: A review. Advances in Mechanical Engineering 8:1–23
28. Munir ZA, Anselmi-Tamburini U, Ohyanagi M (2006) The effect of electric field and pressure on the synthesis and consolidation of materials: A review of the spark plasma sintering method. J Mater Sci 41:763–777
29. Li B, Teng B, Zhu Z (2020) Solid state recycling of Mg–Gd–Y–Zn–Zr alloy chips by spark plasma sintering. Journal of Magnesium and Alloys 8:1154–1165. https://doi.org/10.1016/j.jma.2019.09.014
30. Koch A, Bonhage M, Teschke M, et al (2020) Electrical resistance-based fatigue assessment and capability prediction of extrudates from recycled field-assisted sintered EN AW-6082 aluminium chips. Mater Charact 169:. https://doi.org/10.1016/j.matchar.2020.110644
31. Behrens B, Frischkorn C, Bonhage M (2014) Reprocessing od AW2007, AW6082 and AW7075 aluminium chips by using sintering and forging operations. Production Engineering 8:443–451. https://doi.org/10.1007/s11740-014-0542-2
32. Pei Y, Ma H, Yuan M, Teng B (2024) Solid state recycling of Mg–Gd–Y–Zn–Zr alloy chips by isothermal sintering and equal channel angular pressing. Journal of Magnesium and Alloys 12:2725–2740. https://doi.org/10.1016/j.jma.2022.11.007
33. Duflou JR, Tekkaya AE, Haase M, et al (2015) Environmental assessment of solid state recycling routes for aluminium alloys: Can solid state processes significantly reduce the environmental impact of aluminium recycling? CIRP Ann Manuf Technol 64:37–40. https://doi.org/10.1016/j.cirp.2015.04.051
34. Segal VM (1995) A Materials processing by simple shear
35. Goussous S, Xu W, Wu X, Xia K (2009) Al-C nanocomposites consolidated by back pressure equal channel angular pressing. Compos Sci Technol 69:1997–2001. https://doi.org/10.1016/j.compscitech.2009.05.004
36. Ji ZS, Wen LH, Li XL (2009) Mechanical properties and fracture behavior of Mg-2.4Nd-0.6Zn-0.6Zr alloys fabricated by solid recycling process. J Mater Process Technol 209:2128–2134. https://doi.org/10.1016/j.jmatprotec.2008.05.007

37. Fogagnolo JB, Ruiz-Navas EM, Simón MA, Martinez MA (2003) Recycling of aluminium alloy and aluminium matrix composite chips by pressing and hot extrusion. In: Journal of Materials Processing Technology. pp 792–795
38. Wen L, Ji Z, Li X (2008) Effect of extrusion ratio on microstructure and mechanical properties of Mg-Nd-Zn-Zr alloys prepared by a solid recycling process. Mater Charact 59:1655–1660. https://doi.org/10.1016/j.matchar.2008.03.009
39. Widerøe F, Welo T (2013) Using contrast material techniques to determine metal flow in screw extrusion of aluminium. J Mater Process Technol 213:1007–1018. https://doi.org/10.1016/j.jmatprotec.2012.11.013
40. Latif A, Ingarao G, Fratini L, et al (2023) Characterization of friction stir consolidated recycled billet by uniaxial compression tests with miniaturized cylindrical specimen. In: Materials Research Proceedings. Association of American Publishers, pp 1997–2004
41. Tang W, Reynolds AP (2010) Production of wire via friction extrusion of aluminum alloy machining chips. J Mater Process Technol 210:2231–2237. https://doi.org/10.1016/j.jmatprotec.2010.08.010
42. Li X, Baffari D, Reynolds AP (2018) Friction stir consolidation of aluminum machining chips. International Journal of Advanced Manufacturing Technology 94:2031–2042. https://doi.org/10.1007/s00170-017-1016-4
43. Buffa G, Baffari D, Ingarao G, Fratini L (2020) Uncovering Technological and Environmental Potentials of Aluminum Alloy Scraps Recycling Through Friction Stir Consolidation. International Journal of Precision Engineering and Manufacturing - Green Technology 7:955–964. https://doi.org/10.1007/s40684-019-00159-5
44. Latif A, Ingarao G, Fratini L (2022) Multi-material based functionally graded billets manufacturing through friction stir consolidation of aluminium alloys chips. CIRP Annals 71:261–264. https://doi.org/10.1016/j.cirp.2022.03.035
45. Latif A, Ingarao G, Gucciardi M, Fratini L (2022) A novel approach to enhance mechanical properties during recycling of aluminum alloy scrap through friction stir consolidation. International Journal of Advanced Manufacturing Technology 119:1989–2005. https://doi.org/10.1007/s00170-021-08346-y
46. Behnagh RA, Fathi F, Yeganeh M, et al (2019) Production of seamless tube from aluminum machining chips via double-step friction stir consolidation. International Journal of Advanced Manufacturing Technology 104:4769–4777. https://doi.org/10.1007/s00170-019-04326-5
47. Catalini D, Kaoumi D, Reynolds AP, Grant GJ (2015) Dispersoid Distribution and Microstructure in Fe-Cr-Al Ferritic Oxide Dispersion-Strengthened Alloy Prepared by Friction Consolidation. Metall Mater Trans A Phys Metall Mater Sci 46:4730–4739. https://doi.org/10.1007/s11661-015-3059-1
48. Catalini D, Kaoumi D, Reynolds AP, Grant GJ (2013) Friction consolidation of MA956 powder. Journal of Nuclear Materials 442:. https://doi.org/10.1016/j.jnucmat.2012.11.054
49. Baffari D, Reynolds AP, Masnata A, et al (2019) Friction stir extrusion to recycle aluminum alloys scraps: Energy efficiency characterization. J Manuf Process 43:63–69. https://doi.org/10.1016/j.jmapro.2019.03.049
50. Ingarao G, Baffari D, Bracquene E, et al (2019) Energy demand reduction of aluminum alloys recycling through friction stir extrusion processes implementation. In: Procedia Manufacturing. Elsevier B.V., pp 632–638
51. Buffa G, Campanella D, Fratini L, Micari F (2016) AZ31 magnesium alloy recycling through friction stir extrusion process. International Journal of Material Forming 9:613–618. https://doi.org/10.1007/s12289-015-1247-6
52. Behnagh RA, Mahdavinejad R, Yavari A, et al (2014) Production of wire from AA7277 aluminum chips via friction-stir extrusion (FSE). Metallurgical and

Materials Transactions B: Process Metallurgy and Materials Processing Science 45:1484–1489. https://doi.org/10.1007/s11663-014-0067-2
53. Tahmasbi K, Mahmoodi M (2018) Evaluation of microstructure and mechanical properties of aluminum AA7022 produced by friction stir extrusion. J Manuf Process 32:151–159. https://doi.org/10.1016/j.jmapro.2018.02.008
54. Li L, Gupta V, Li X, et al (2022) Meshfree simulation and experimental validation of extreme thermomechanical conditions in friction stir extrusion. Comput Part Mech 9:789–809. https://doi.org/10.1007/s40571-021-00445-7
55. Baffari D, Reynolds AP, Li X, Fratini L (2017) Influence of processing parameters and initial temper on Friction Stir Extrusion of 2050 aluminum alloy. J Manuf Process 28:319–325. https://doi.org/10.1016/j.jmapro.2017.06.013
56. Whalen S, Olszta M, Roach C, et al (2019) High ductility aluminum alloy made from powder by friction extrusion. Materialia (Oxf) 6:. https://doi.org/10.1016/j.mtla.2019.100260
57. Ansari MA, Behnagh RA, Narvan M, et al (2016) Optimization of Friction Stir Extrusion (FSE) Parameters Through Taguchi Technique. Transactions of the Indian Institute of Metals 69:1351–1357. https://doi.org/10.1007/s12666-015-0686-6
58. Behnagh RA, Shen N, Ansari MA, et al (2016) Experimental analysis and microstructure modeling of friction stir extrusion of magnesium chips. Journal of Manufacturing Science and Engineering, Transactions of the ASME 138:. https://doi.org/10.1115/1.4031281
59. Abdi Behnagh R, Samanta A, Agha Mohammad Pour M, et al (2019) Predicting microstructure evolution for friction stir extrusion using a cellular automaton method. Model Simul Mat Sci Eng 27:. https://doi.org/10.1088/1361-651X/ab044b
60. Darsell JT, Overman NR, Joshi V V., et al (2018) Shear Assisted Processing and Extrusion (ShAPE^{TM}) of AZ91E Flake: A Study of Tooling Features and Processing Effects. J Mater Eng Perform 27:4150–4161. https://doi.org/10.1007/s11665-018-3509-1
61. Zhang H, Zhao X, Deng X, et al (2014) Investigation of material flow during friction extrusion process. Int J Mech Sci 85:130–141. https://doi.org/10.1016/j.ijmecsci.2014.05.011
62. Zhang H, Li X, Tang W, et al (2015) Heat transfer modeling of the friction extrusion process. J Mater Process Technol 221:21–30. https://doi.org/10.1016/j.jmatprotec.2015.01.032
63. Zhang H, Li X, Deng X, et al (2018) Numerical simulation of friction extrusion process. J Mater Process Technol 253:17–26. https://doi.org/10.1016/j.jmatprotec.2017.10.053
64. Li X, Reza-E-Rabby M, Guzman A, et al (2022) Strain and strain rate in friction extrusion. Journal of Materials Research and Technology 20:882–893. https://doi.org/10.1016/j.jmrt.2022.07.116
65. Baffari D, Buffa G, Fratini L (2017) A numerical model for Wire integrity prediction in Friction Stir Extrusion of magnesium alloys. J Mater Process Technol 247:1–10. https://doi.org/10.1016/j.jmatprotec.2017.04.007
66. Baffari D, Buffa G, Campanella D, et al (2017) Process mechanics in Friction Stir Extrusion of magnesium alloys chips through experiments and numerical simulation. J Manuf Process 29:41–49. https://doi.org/10.1016/j.jmapro.2017.07.010
67. Karwa C Finite Element Modelling and Analysis of the Friction Stir Extrusion Process
68. Bocchi S, D'urso G, Giardini C, Maccarini G (2022) A Simulative Method for Studying the Bonding Condition of Friction Stir Extrusion. In: Key Engineering Materials. Trans Tech Publications Ltd, pp 2333–2341

69. Asadi P, Akbari M Numerical modeling and experimental investigation of brass wire forming by friction stir back extrusion. https://doi.org/10.1007/s00170-021-07729-5/Published
70. Widerøe F, Welo T (2013) Using contrast material techniques to determine metal flow in screw extrusion of aluminium. J Mater Process Technol 213:1007–1018. https://doi.org/10.1016/j.jmatprotec.2012.11.013
71. Baffari D, Buffa G, Campanella D, Fratini L (2018) Design of continuous Friction Stir Extrusion machines for metal chip recycling: Issues and difficulties. In: Procedia Manufacturing. Elsevier B.V., pp 280–286
72. Buffa G, Campanella D, Micari F, Fratini L (2023) Design and development of a new machine tool for continuous friction stir extrusion. CIRP J Manuf Sci Technol 41:391–400. https://doi.org/10.1016/j.cirpj.2023.01.004
73. Buffa G, Campanella D, Fratini L, et al (2023) Process mechanics in continuous friction stir extrusion process of aluminum alloy. In: Materials Research Proceedings. Association of American Publishers, pp 719–724
74. Gumaste A, Haridas RS, Gupta S, et al (2023) Solid Stir Extrusion: Innovating friction stir technology for continuous extrusion process. J Mater Process Technol 316:. https://doi.org/10.1016/j.jmatprotec.2023.117952
75. Akeret R (1992) Extrusion welds-quality aspects are now center stage. In: Proceedings of the 5th International Aluminum Extrusion Technology Seminar. pp 319–336
76. Plata M, PJ (2000) Theoretical and experimental analysis of seam weld formation in hot extrusion of aluminium alloys. In: Proceedings of the 7th International Aluminium Extrusion Seminar . pp 205–212
77. Donati L, Tomesani L (2004) The prediction of seam welds quality in aluminum extrusion. J Mater Process Technol 153–154:366–373. https://doi.org/10.1016/j.jmatprotec.2004.04.215
78. Ceretti E, Fratini L, Gagliardi F, Giardini C (2009) A new approach to study material bonding in extrusion porthole dies. CIRP Ann Manuf Technol 58:259–262. https://doi.org/10.1016/j.cirp.2009.03.010
79. Güley V, Güzel A, Jäger A, et al (2013) Effect of die design on the welding quality during solid state recycling of AA6060 chips by hot extrusion. Materials Science and Engineering: A 574:163–175. https://doi.org/10.1016/j.msea.2013.03.010
80. Baffari D, Buffa G, Campanella D, et al (2017) Process mechanics in Friction Stir Extrusion of magnesium alloys chips through experiments and numerical simulation. J Manuf Process 29:41–49. https://doi.org/10.1016/j.jmapro.2017.07.010
81. Bay N (1979) Cold pressure welding—the mechanisms governing bonding
82. Cooper DR, Allwood JM (2014) The influence of deformation conditions in solid-state aluminium welding processes on the resulting weld strength. J Mater Process Technol 214:2576–2592. https://doi.org/10.1016/j.jmatprotec.2014.04.018
83. Kolpak F, Schulze A, Dahnke C, Tekkaya AE (2019) Predicting weld-quality in direct hot extrusion of aluminium chips. J Mater Process Technol 274:. https://doi.org/10.1016/j.jmatprotec.2019.116294
84. Oberhausen G, Cooper DR (2024) Modeling the strength of aluminum extrusion transverse welds using the film theory of solid-state welding. J Mater Process Technol 324:. https://doi.org/10.1016/j.jmatprotec.2023.118254
85. Tang W., Reynolds A. P. (2011) Friction consolidation of aluminum chips. In: TMS Annual Meeting. pp 289–298
86. Shima S OM (1976) Plasticity theory for porous metals. Int J Mech Sci 18:286–291
87. Amantia S, Campanella D, Puleo R, et al (2024) Effect of process parameters on the mechanical properties of wires produced from A356 aluminum alloy chips by

Continuous Friction Stir Extrusion: Experiments and numerical simulation. CIRP J Manuf Sci Technol 54:28–42. https://doi.org/10.1016/j.cirpj.2024.08.001
88. Puleo R, Latif A, Ingarao G, et al (2023) Solid bonding criteria design for aluminum chips recycling through Friction Stir Consolidation. J Mater Process Technol 319:. https://doi.org/10.1016/j.jmatprotec.2023.118080
89. Latif A, Gucciardi M, Ingarao G, Fratini L (2022) Outlining the Limits of Friction Stir Consolidation as Used as an Aluminum Alloys Recycling Approach. In: Smart Innovation, Systems and Technologies. Springer Science and Business Media Deutschland GmbH, pp 169–180
90. Latif A, Ingarao G, Fratini L, Micari F (2023) Progresses in multi-materials billet manufacturing out of metal scraps through friction stir consolidation. In: Materials Research Proceedings. Association of American Publishers, pp 713–718
91. Rofman O V., Prosviryakov AS, Mikhaylovskaya A V., et al (2019) Processing and Microstructural Characterization of Metallic Powders Produced from Chips of AA2024 Alloy. JOM 71:2986–2995. https://doi.org/10.1007/s11837-019-03581-x
92. Huda Z, Zaharinie T (2009) Kinetics of grain growth in 2024-T3: An aerospace aluminum alloy. J Alloys Compd 478:128–132. https://doi.org/10.1016/j.jallcom.2008.11.071
93. El-Danaf EA, Almajid AA, Soliman MS (2008) Hot deformation of AA6082-T4 aluminum alloy. J Mater Sci 43:6324–6330. https://doi.org/10.1007/s10853-008-2895-4
94. Mcqueen HJ, Fry E, Belling J (2001) Comparative Constitutive Constants for Hot Working of Al-4.4Mg-0.7Mn (AA5083). ASM International
95. Puleo R, Latif A, Ingarao G, Fratini L (2024) A generalized parametric model for the bonding occurrence prediction in friction stir consolidation of aluminum alloys chips. J Manuf Process 131:604–618. https://doi.org/10.1016/j.jmapro.2024.09.049
96. Adnan M, Amantia S, Puleo R, et al Recycling Magnesium Alloy AZ31B Chips via Friction Stir Consolidation: A Sustainable Approach
97. Friedrich HE, Schmid S, Friedrich E, Ehrenberger S (2013) Title Life Cycle Assessment of Magnesium Components in Vehicle Construction
98. Ehrenberger, Simone (2020) Carbon Footprint of Magnesium Production and its Use in Transport Applications Update of the IMA Report "Life Cycle Assessment of Magnesium Components in Vehicle Construction (2013)"
99. Cooper DR, Song J, Gerard R (2018) Metal recovery during melting of extruded machining chips. J Clean Prod 200:282–292. https://doi.org/10.1016/J.JCLEPRO.2018.07.246
100. Granta Design Limited 2023. https://www.ansys.com/it-it/products/materials/granta-edupack. Accessed 4 Jan 2025
101. Latif A, Puleo R, Ingarao G, et al (2024) Material flow analysis in friction stir consolidation during recycling aluminum alloy chips. pp 158–166
102. Li X, Reza-E-Rabby M, Ryan M, et al (2021) Evaluation of orthogonal strain components in friction extrusion. Journal of Materials Research and Technology 15:3357–3364. https://doi.org/10.1016/j.jmrt.2021.10.001
103. Ingarao G, Amato M, Latif A, et al (2023) Life Cycle Assessment of aluminum alloys chips recycling through single and multi-step Friction Stir Consolidation processes. J Manuf Syst 68:651–659. https://doi.org/10.1016/j.jmsy.2023.05.021
104. Puleo R, Ingarao G, Fratini L Friction Stir Consolidation of Aluminium chips: A New Approach to Overcome the Inhomogeneous Properties of The Consolidated Billet
105. Abu-Farha F (2012) A preliminary study on the feasibility of friction stir back extrusion. Scr Mater 66:615–618. https://doi.org/10.1016/j.scriptamat.2012.01.059
106. Swarnkar R, Karmakar S, Pal SK (2023) An investigation of bimetallic tube fabrication through a novel friction stir extrusion based technology for automotive

applications. Mater Today Commun 35:. https://doi.org/10.1016/j.mtcomm.2023.106363
107. Asadi P, Akbari M, Sadowski T, et al (2024) Examining the impact of tool taper angle in Al-Si tube manufacturing by friction stir extrusion. J Manuf Process 131:532–544. https://doi.org/10.1016/j.jmapro.2024.09.047
108. Whalen S, Taysom BS, Overman N, et al (2023) Porthole die extrusion of aluminum 6063 industrial scrap by shear assisted processing and extrusion. Manuf Lett 36:52–56. https://doi.org/10.1016/j.mfglet.2023.01.005
109. Li X, Wang T, Ma X, et al (2022) Manufacture aluminum alloy tube from powder with a single-step extrusion via ShAPE. J Manuf Process 80:108–115. https://doi.org/10.1016/j.jmapro.2022.05.060
110. Chang CI, Lee CJ, Huang JC (2004) Relationship between grain size and Zener-Holloman parameter during friction stir processing in AZ31 Mg alloys. Scr Mater 51:509–514. https://doi.org/10.1016/j.scriptamat.2004.05.043
111. Cooper DR, Song J, Gerard R (2018) Metal recovery during melting of extruded machining chips. J Clean Prod 200:282–292. https://doi.org/10.1016/j.jclepro.2018.07.246
112. Ahn J, Chen L, He E, et al (2017) Effect of filler metal feed rate and composition on microstructure and mechanical properties of fibre laser welded AA 2024-T3. J Manuf Process 25:26–36. https://doi.org/10.1016/j.jmapro.2016.10.006
113. Saravanan V, Banerjee N, Amuthakkannan R, Rajakumar S (2015) Microstructural Evolution and Mechanical Properties of Friction Stir Welded Dissimilar AA2014-T6 and AA7075-T6 Aluminum Alloy Joints. Metallography, Microstructure, and Analysis 4:178–187. https://doi.org/10.1007/s13632-015-0199-z
114. Davis J.R., Allen P., Lampman S.R., et al (2012) Properties and Selection: Nonferrous Alloys and Special- Purpose materials
115. Davis JR (1993) Aluminum and Aluminum Alloys.
116. Kimura T, Nakamoto T (2016) Microstructures and mechanical properties of A356 (AlSi7Mg0.3) aluminum alloy fabricated by selective laser melting. Mater Des 89:1294–1301. https://doi.org/10.1016/j.matdes.2015.10.065
117. Tekkaya AE, Schikorra M, Becker D, et al (2009) Hot profile extrusion of AA-6060 aluminum chips. J Mater Process Technol 209:3343–3350. https://doi.org/10.1016/j.jmatprotec.2008.07.047
118. Baffari D, Buffa G, Fratini L (2017) A numerical model for Wire integrity prediction in Friction Stir Extrusion of magnesium alloys. J Mater Process Technol 247:1–10. https://doi.org/10.1016/j.jmatprotec.2017.04.007
119. Buffa G, Hua J, Shivpuri R, Fratini L (2006) A continuum based fem model for friction stir welding - Model development. Materials Science and Engineering: A 419:389–396. https://doi.org/10.1016/j.msea.2005.09.040

Università
Degli Studi
Di Palermo